National Aeronautics and
Space Administration

SLS-SPEC-159

REVISION G

EFFECTIVE DATE: DECEMBER 11, 2019

CROSS-PROGRAM DESIGN SPECIFICATION FOR NATURAL ENVIRONMENTS (DSNE)

HISTORY PAGE

Status	Revision No.	Change No.	Description	Effective Date
	Baseline		Initial baseline per CECBD SV-02-0004, dated 8/8/12; (CR SLS-00034) PCN SV00077	8/8/12
			Category 1 Applicable Document Assessment per PCBD SV2-01-0100R1, dated 8/22/13; CR SLS-00162; PCN SV00305	8/22/13
		A	Update SLS-SPEC-159, Cross-Program Design Specification for Natural Environments (DSNE) to Revision A, per JICBD SV2-02-0063, dated 12/18/13; CR SLS-00193; PCN SV00450	12/18/13
		B	Update SLS-SPEC-159, Cross-Program Design Specification for Natural Environments (DSNE) to Revision B to close out a forward work item and change specifications due to model and database updates that are being applied by ESD per JICBD SV2-02-0133, dated August 27, 2014; CR SLS-00293; PCN SV00668	8/27/14
		C	Revise SLS-SPEC-159, Cross-Program Design Specification for Natural Environments (DSNE) to Revision C, per JICBD SV2-02-0194, dated March 25, 2015; CR SLS-00370; PCN SV00801	03/25/15
		D	Revise SLS-SPEC-159, Cross-Program Design Specification for Natural Environments (DSNE) to Revision D, per JICBD SV2-02-0257, dated November 4, 2015; CR SLS-00407-X; PCN SV00895	11/4/15
		E	Revise SLS-SPEC-159, Cross-Program Design Specification for Natural Environments (DSNE), to Revision E per JICBD SV2-02-0476, dated July 12, 2017; CR SLS-00633-X; PCN SV01341	07/12/17
		F	Revise SLS-SPEC-159, Cross-Program Design Specification for Natural Environments (DSNE) to Revision F per JICBD SV2-02-0707, dated May 8, 2019; CR SLS-00833-X; PCN SV01922	05/08/19
		G	Revise SLS-SPEC-159, Cross-Program Design Specification for Natural Environments (DSNE) to Revision G per JICBD SV2-02-0828, dated	12/11/19

			December 11, 2019; CR SLS-00903-X; PCN SV02184	

NOTE: Updates to this document, as released by numbered changes (Change XXX), are identified by a black bar on the right margin.

TABLE OF CONTENTS

PARAGRAPH **PAGE**

APPENDIX

TABLE

FIGURE

1.0 INTRODUCTION

1.1 Background

This document is derived from the former National Aeronautics and Space Administration (NASA) Constellation Program (CxP) document CxP 70023, titled "The Design Specification for Natural Environments (DSNE), Revision C." The original document has been modified to represent updated Design Reference Missions (DRMs) for the NASA Exploration Systems Development (ESD) Programs.

1.2 Purpose

The DSNE completes environment-related specifications for architecture, system-level, and lower-tier documents by specifying the ranges of environmental conditions that must be accounted for by NASA ESD Programs. To assure clarity and consistency, and to prevent requirements documents from becoming cluttered with extensive amounts of technical material, natural environment specifications have been compiled into this document. The intent is to keep a unified specification for natural environments that each Program calls out for appropriate application.

1.3 Scope

This document defines the natural environments parameter limits (maximum and minimum values, energy spectra, or precise model inputs, assumptions, model options, etc.), for all ESD Programs. These environments are developed by the NASA Marshall Space Flight Center (MSFC) Natural Environments Branch (MSFC organization code: EV44). Many of the parameter limits are based on experience with previous programs, such as the Space Shuttle Program. The parameter limits contain no margin and are meant to be evaluated individually to ensure they are reasonable (i.e., do not apply unrealistic extreme-on-extreme conditions).

The natural environments specifications in this document should be accounted for by robust design of the flight vehicle and support systems. However, it is understood that in some cases the Programs will find it more effective to account for portions of the environment ranges by operational mitigation or acceptance of risk in accordance with an appropriate program risk management plan and/or hazard analysis process.

The DSNE is not intended as a definition of operational models or operational constraints, nor is it adequate, alone, for ground facilities which may have additional requirements (for example, building codes and local environmental constraints).

"Natural environments," as the term is used here, refers to the environments that are not the result of intended human activity or intervention. It consists of a variety of external environmental factors (most of natural origin and a few of human origin) which impose restrictions or otherwise impact the development or operation of flight vehicles and destination surface systems. These natural environments include the following types of environments:

a. Terrestrial environments at launch, abort, and normal landing sites (winds, temperatures, pressures, surface roughness, sea conditions, etc.).

b. Space environments (ionizing radiation, orbital debris, meteoroids, thermosphere density, plasma, solar, Earth, and lunar-emitted thermal radiation, etc.).

Destination environments (Lunar surface and orbital, Mars atmosphere and surface, near Earth asteroids, etc.).

Many of the environmental specifications in this document are based on models, data, and environment descriptions contained in the NASA/TM 2016-218229, Natural Environment Definition for Design (NEDD). The NEDD provides additional detailed environment data and model descriptions to support analytical studies for ESD Programs. For background information on specific environments and their effects on spacecraft design and operations, the environment models, and the data used to generate the specifications contained in the DSNE, the reader is referred to the NEDD.

Validation of the models, data, and design limits in this document are provided in Appendix B. The intent is to provide validity of the specified natural environments for use in design assessment, which includes background of the inputs, physics, and methodology used in development of the various models and databases, as well as use in previous NASA programs. Verification of the natural environments is accomplished by confirming the intended specifications are identified in this document. This confirmation is carried out through review by the Natural Environments Integrated Ad Hoc Team, and review, approval, and configuration control by the applicable ESD Programs.

Also, most of the environmental specifications in this document are tied specifically to the ESD DRMs in ESD-10012, Revision E, Exploration Systems Development Concept of Operations (ConOps). Coordination between these environment specifications and the DRMs must be maintained. This document should be compatible with the current ESD DRMs, but updates to the mission definitions and variations in interpretation may require adjustments to the environment specifications.

Table 1.3-1 provides the mapping of the DRMs in ESD-10012, Revision E to the corresponding sections in the DSNE.

Table 1.3-1. DRM ConOps/DSNE Matrix

Exploration Systems ConOps		DSNE	
Section No.	**Title**	**Section No.**	**Title**
7	**Operations And Interfaces (Comm. Interfaces not included)**	N/A	N/A
7.1	Pre-flight Preparation Operations	3.1	Prelaunch-Ground Processing Phases
7.2	Ground Operations		
7.2.4	Pad and Launch Operations	3.1 3.2	Prelaunch-Ground Processing Phases Launch Countdown and Earth Ascent Phases
7.2.6	Launch Scrub	3.2	Launch Countdown and Earth Ascent Phases
7.3.1	Ascent Operations	3.2 3.5	Launch Countdown and Earth Ascent Phases Entry and Landing Phases
7.4.2	Cargo	3.3 3.4 3.12	In-Space Phases Lunar Surface Operational Phases NEA Specification
7.5.1	Secondary Payloads	3.3	In-Space Phases
7.5.2	Orion NEA DRM Operations	3.12	In-Space Phases NEA Specification
7.5.3	Orion Quiescent Mode Docked with Initial Cis-Lunar Habitat (ICH)/Deep Space Habitat (DSH)	3.3 3.12	In-Space Phases NEA Specification
7.6.1	Entry, Descent, and Landing	3.5 3.6	Entry and Landing Phases Contingency and Off-Nominal Landing Phases
7.6.2	Crew and Spacecraft Recovery and Post Flight Processing	3.7	Recovery and Post-Flight Processing Phases
7.7.1	Pad Contingency Operations	3.2	Launch Countdown and Earth Ascent Phases
7.7.2	Orion Cabin Leak/Depressurization	3.3	In-Space Phases
7.7.3	Orion Cis-Lunar Auxiliary Return	3.3 3.4 3.6	In-Space Phases Lunar Surface Operational Phases Contingency and Off-Nominal Landing Phases
7.7.4	Off-Nominal Crew Rescue	3.6	Contingency and Off-Nominal Landing Phases
7.7.5	Ascent Abort	3.6	Contingency and Off-Nominal Landing Phases

1.4 Change Authority/Responsibility

The NASA Office of Primary Responsibility (OPR) for this document is EV44.

Proposed changes to this document will be submitted by a SLS Program Change Request (CR) to the appropriate SLS control board for disposition. The CR process is described in SLS-PLAN-008, SLSP Configuration Management Plan (CMP).

Proposed changes to this document should be vetted through the Cross-Program Natural Environments Integration Ad-Hoc Team (NEIAHT) prior to the submission of an SLS Program CR. Requests for clarification, interpretation, or questions concerning this document should be addressed to the Cross-Program NEIAHT, or the MSFC Natural Environments Branch.

2.0 DOCUMENTS

2.1 Applicable Documents, Models, and Data Sets

2.1.1 Applicable Documents

The following data items include specifications, models, standards, guidelines, handbooks, and other special publications. The data items listed in this paragraph are applicable in the current approved baseline as specified in the SLS Master List of Baselined Data Items to the extent specified herein. Specific revisions of SLS controlled or jointly controlled documents will not be annotated unless required to specify the boundaries of an incorporated agreement or requirement. Data items not controlled by SLS will be annotated by revision.

Document Number	Document Revision	Document Title
ESD 10012	E	Exploration Systems Development Concept of Operations
MIL-STD-810	G, Change 1	Test Method Standard for Environmental Engineering Considerations and Laboratory Tests
MPCV 70024	A	Orion MPCV Program Human-Systems Integration Requirements
SAE ARP5412	B	Aircraft Lightning Environment and Related Test Waveforms
SAE ARP5414	A	Aircraft Lightning Zoning
DSG-RQMT-002	Baseline	Gateway Human Systems Requirements (HSR)

2.1.2 Applicable Models/Data Sets

The following models and data bases are used for specifications. Their application is described in the appropriate sections of this document.

Model/Data Set Identification	Model/Data Set Name/Description
Earth-GRAM	Earth Global Reference Atmosphere Model (GRAM) As of January 1, 2012 the latest version of this model is Earth-GRAM 2010. Any previous analyses performed using a prior version do not require rework.
GGM02C	Gravity Recovery and Climate Experiment (GRACE) Gravity Model 02 C
GRAIL	Gravity Recovery and Interior Laboratory (GRAIL) Lunar Gravity Model
MEM 3	Meteoroid Engineering Model 3
ORDEM 3.0	Orbital Debris Engineering Model 3.0
KSC Jimsphere Wind Profile Database	Kennedy Space Center Jimsphere Wind Profile Database
MVWPM	Monthly Vector Wind Profile Model
KSC Ground Wind Models	Kennedy Space Center Ground Wind Models
KSC Doppler Radar Wind Profiler Database	Kennedy Space Center Doppler Radar Wind Profiler Database

3.0 NATURAL ENVIRONMENT SPECIFICATION

3.1 Prelaunch – Ground Processing Phases

3.1.1 Transportation Environments to the Launch Site KSC (Reserved)

Description

This section is reserved for special environmental requirements for shipping flight hardware to Kennedy Space Center (KSC) not covered by other standard shipping requirements documents. Examples might include monitoring for lightning discharge or electromagnetic irradiation and monitoring of temperature and pressure extremes. At this time, no special requirements have been identified.

Design Limits

Maximum: Reserved

Minimum: Reserved

Model Inputs

Reserved

Limitations

Reserved

Technical Notes

Reserved

3.1.2 Reserved

3.1.3 Ground Winds for Transport and Launch Pad Environments

Description

This section specifies ground wind environments (altitude range 0 to 150 meters (m) [0 to 492 feet (ft)]), up to and including the maximum design limits for flight hardware that will be exposed during ground operations at KSC, including transportation to and from the pad and on-pad operations. Design specifications include peak wind-speed profile, steady state wind-speed profile, frequency of occurrence of peak winds, and spectral gust environments. “Storage” applies to on-pad or outside storage only.

Design Limits

Table 3.1.3-1 provides the design peak wind profiles, in meters per second (m/s) and feet per second (ft/s), for the various operational phases at selected altitudes. The design steady state wind profiles associated with the design peak wind profiles are provided in Table 3.1.3-2. The steady state wind profile is that profile that could produce the instantaneous peak winds (gusts)

in Table 3.1.3-1, over a 10-minute period. Peak wind profile values between those altitudes given in Tables 3.1.3-1 are determined by:

$$u(z) = u_{18.3}\left(\frac{z}{18.3}\right)^{1.6(u_{18.3})^{-3/4}}$$

where *u(z)* is the peak wind (m/s) at height *z* (m) and $u_{18.3}$ is the peak wind speed (m/s) at 18.3 m. Steady state profile values between those altitudes given in Table 3.1.3-2 are determined by:

$$\bar{U}(z) = u(z)\left(1 + \left(\frac{\left(\frac{18.3}{z}\right)^{\left(0.283 - 0.435e^{-0.2u_{18.3}}\right)}}{1.98 - 1.887e^{-0.2u_{18.3}}}\right)\right)^{-1}$$

where *u(z)* is the peak wind (m/s) at height *z* (m) and $u_{18.3}$ is the peak wind (m/s) at 18.3 m. Note that metric units (m/s and m) must be used in the above two equations. Once *u(z)* and $\bar{U}(z)$ are determined, they can be converted to English units (ft/s).

Table 3.1.3-1. Design Peak Wind-Speed Profile

Height		Peak Wind-Speed Profile					
		Transport To/From Pad		On-Pad (Unfueled)		On-Pad (Intermediate and Fully Fueled)	
m	ft	m/s	ft/s	m/s	ft/s	m/s	ft/s
10	32	28.6	93.8	36.0	118.1	22.1	72.5
18.3	60	30.8	101.1	38.3	125.7	24.2	79.4
30	98	32.7	107.3	40.3	132.2	26.0	85.3
60	197	35.6	116.8	43.3	142.1	28.8	94.5
90	295	37.4	122.7	45.2	148.3	30.6	100.4
120	394	38.8	127.3	46.6	152.9	31.8	104.3
150	492	39.8	130.6	47.7	156.5	32.9	107.9

Table 3.1.3-2. Steady State Wind-Speed Profile Associated with the Design Peak Wind-Speed Profile

Height		Steady State Wind-Speed Profile					
		Transport To/From Pad		On-Pad (Unfueled)		On-Pad (Intermediate and Fully Fueled)	
m	ft	m/s	ft/s	m/s	ft/s	m/s	ft/s
10	32	17.9	58.7	22.5	73.8	13.8	45.3
18.3	60	20.5	67.3	25.4	83.3	16.0	52.5
30	98	22.7	74.5	28.0	91.9	18.0	59.1
60	197	26.1	85.6	31.8	104.3	21.1	69.2
90	295	28.3	92.9	34.2	112.2	23.0	75.5
120	394	29.9	98.1	35.9	117.8	24.5	80.4
150	492	31.1	102.0	37.3	122.4	25.7	84.3

For fatigue load analyses, the design frequency of occurrence of 30 s peak winds at the 18.3 m (60 ft) reference height is provided in Table 3.1.3-3. Any analysis should contain at least one occurrence of the design peak wind of 38.3 m/s (125.7 ft/s). The number of occurrences of a selected 30 s peak wind range for any time period ≥30 s can be determined by multiplying the probability of occurrence by the number of 30 s intervals in the chosen time period. For example, there are approximately 1,238 occurrences of 30 s peak winds in the range 4.75 to 5.25 m/s (15.6 to 17.2 ft/s) in a 5-day period (number of 30 s intervals in 5 days is 14,400, 14,400 * 0.08598149 = 1,238.13).

Table 3.1.3-3. Occurrence Probabilities of 30 s Peak Wind Speed in 0.5 m/s Intervals (Centered at Value x) at the 18.3 m Reference Height

Peak Wind Speed x		Probability	Peak Wind Speed x		Probability
m/s	ft/s		m/s	ft/s	
0.5	1.6	0.003246387	20.0	65.6	0.00003324119
1.0	3.2	0.01116703	20.5	67.3	0.00002514178
1.5	4.9	0.02681171	21.0	68.9	0.00001901570
2.0	6.6	0.04885758	21.5	70.5	0.00001438224
2.5	8.2	0.07209810	22.0	72.2	0.00001087772
3.0	9.8	0.09057693	22.5	73.8	0.000008227152
3.5	11.5	0.1006679	23.0	75.5	0.000006222421
4.0	13.1	0.1019312	23.5	77.1	0.000004706180
4.5	14.8	0.09616256	24.0	78.7	0.000003559402

Peak Wind Speed x		Probability	Peak Wind Speed x		Probability
m/s	ft/s		m/s	ft/s	
5.0	16.4	0.08598149	24.5	80.4	0.000002692063
5.5	18.0	0.07381466	25.0	82.0	0.000002036071
6.0	19.7	0.06144696	25.5	83.7	0.000001539928
6.5	21.3	0.04997189	26.0	85.3	0.000001164683
7.0	23.0	0.03992827	26.5	86.9	0.0000008808765
7.5	24.6	0.03147963	27.0	88.6	0.0000006662268
8.0	26.3	0.02456889	27.5	90.2	0.0000005038823
8.5	27.9	0.01902905	28.0	91.1	0.0000003810975
9.0	29.5	0.01465325	28.5	93.5	0.0000002882325
9.5	31.2	0.01123435	29.0	95.1	0.0000002179967
10.0	32.8	0.008584661	29.5	96.8	0.0000001648757
10.5	34.5	0.006543492	30.0	98.4	0.0000001246991
11.0	36.1	0.004978202	30.5	100.1	0.00000009431272
11.5	37.7	0.003781923	31.0	101.7	0.00000007133080
12.0	39.4	0.002869999	31.5	103.4	0.00000005394906
12.5	41.0	0.002176178	32.0	105.0	0.000000040802862
13.0	42.5	0.001649065	32.5	106.6	0.00000003086010
13.5	44.3	0.001249042	33.0	108.3	0.000000023340178
14.0	45.9	0.0009457197	33.5	109.9	0.00000001765269
14.5	47.6	0.0007158649	34.0	111.6	0.00000001335112
15.0	49.2	0.0005417658	34.5	113.2	0.00000001009775
15.5	50.9	0.0004099448	35.0	114.8	0.000000007637148
16.0	52.5	0.0003101621	35.5	116.5	0.000000005776143
16.5	54.1	0.0002346464	36.0	118.1	0.000000004368624
17.0	55.8	0.0001775048	36.5	119.8	0.000000003304087
17.5	57.4	0.0001342717	37.0	121.4	0.000000002498954
18.0	59.1	0.0001015647	37.5	123.0	0.000000001890014
18.5	60.7	0.00007682245	38.0	124.7	0.000000001429459
19.0	62.3	0.00005810643	38.5	126.3	0.000000001081131
19.5	64.0	0.00004394942			

For thermal assessments involving wind effects, use the following guidelines:

1) For components with time constants less than an hour, or for minimum winds conditions, use the steady-state wind speeds in Table 3.1.3-4

2) For components with time constants on the order of hours, use the steady-state wind speeds in Table 3.1.3-5

3) For components with time constants on the order of days, use the diurnal profile of steady-state wind speeds in Table 3.1.3-6. For the design low case, assume the values in Table 3.1.3-6 are constant with altitude from 10 m (32 ft) up to 150 m (492 ft). For the design high case, the wind speed with altitude from 10 m (32 ft) up to 150 m (492 ft) is determined by:

$$\overline{U}(z) = \overline{U}_{ref} \frac{\ln(z/0.3)}{4.11}$$

where $\overline{U}(z)$ is the steady-state wind speed (m/s) at height z (m) and $\overline{U}_{ref}$ is the design high steady-state wind speed (m/s) from Table 3.1.3-6. Inputs into the above equation must be in metric units (m/s and m).

Table 3.1.3-4. Design High and Low Steady State Wind-Speed Profiles for use in Thermal Assessments with Time Constants Less Than an Hour

Height		Steady State Wind-Speed Profile for Thermal Assessments (Component Time Constants Less Than an Hour)			
		Design Low		Design High	
m	ft	m/s	ft/s	m/s	ft/s
10	32	0	0	9.8	32.2
18.3	60	0	0	11.7	38.4
30	98	0	0	13.3	43.6
60	197	0	0	16.0	52.5
90	295	0	0	17.8	58.4
120	394	0	0	19.1	62.7
150	492	0	0	20.2	66.3

Table 3.1.3-5. Design High and Low Steady State Wind-Speed Profiles for use in Thermal Assessments with Time Constants on the Order of Hours

Height		Steady State Wind-Speed Profile for Thermal Assessments (Component Time Constants on the Order of Hours)			
		Design Low		Design High	
m	ft	m/s	ft/s	m/s	ft/s
10	32	0.4	1.3	9.8	32.2
18.3	60	0.8	2.6	11.7	38.4
30	98	0.8	2.6	13.3	43.6
60	197	0.8	2.6	16.0	52.5
90	295	0.8	2.6	17.8	58.4
120	394	0.8	2.6	19.1	62.7
150	492	0.8	2.6	20.2	66.3

Table 3.1.3-6. Design High and Low Steady State Wind-Speed Profiles for use in Thermal Assessments with Time Constants on the Order of Days

Time of Day	Steady State Wind-Speed Diurnal Profile for Thermal Assessments (Component Time Constants on the Order of Days)			
	Design Low		Design High	
Hour (LST)	m/s	ft/s	m/s	ft/s
00:00	0.6	2.0	10.6	34.7
01:00	0.7	2.2	10.2	33.5
02:00	0.7	2.2	10.3	33.8
03:00	0.6	2.0	10.1	33.2
04:00	0.5	1.6	9.9	32.6
05:00	0.5	1.6	9.9	32.4
06:00	0.5	1.6	9.8	32.3
07:00	0.6	2.0	9.9	32.5
08:00	0.8	2.6	10.1	33.1
09:00	1.1	3.5	10.2	33.6
10:00	1.4	4.8	10.2	33.6
11:00	1.9	6.1	10.4	34.0
12:00	1.8	6.0	10.7	35.0
13:00	2.0	6.4	10.8	35.5
14:00	1.8	6.0	10.5	34.5
15:00	1.8	5.9	10.8	35.3
16:00	1.5	4.9	10.6	34.7

Time of Day	Steady State Wind-Speed Diurnal Profile for Thermal Assessments (Component Time Constants on the Order of Days)			
	Design Low		Design High	
Hour (LST)	m/s	ft/s	m/s	ft/s
17:00	1.1	3.7	10.6	34.8
18:00	1.1	3.5	10.4	34.2
19:00	1.0	3.3	10.6	34.6
20:00	0.9	2.8	10.6	34.7
21:00	0.7	2.2	10.6	34.9
22:00	0.7	2.4	10.4	34.0
23:00	0.7	2.2	10.6	34.6

The design gust environment is characterized by either the spectral gust model or the discrete gust model. The spectral model produces fluctuations from all periods producing significant response of the vehicle. Spectral gusts are to be varied to identify the maximum system response. The spectral gust environment at height z consists of longitudinal, lateral, and vertical turbulence spectra. The turbulence components are applied to the steady state wind profiles given in Table 3.1.3-2. The longitudinal component of turbulence is parallel to the steady state wind vector with the lateral component in the horizontal plane and perpendicular to the longitudinal and vertical components. These components are given by:

$$S(f) = \frac{C_1\left(\frac{z}{18.3}\right)^{C_3} z\left(\frac{\overline{U}_{18.3}^2}{\overline{U}_z}\right)}{\left(1 + C_2\left(\left(\frac{18.3}{z}\right)^{C_5}\left(\frac{fz}{\overline{U}_z}\right)\right)^{C_6}\right)^{C_4}}$$

where the values for the various non-dimensional constants C_1, C_2, C_3, C_4, C_5, and C_6 given in Table 3.1.3-7 are a function of the turbulent components, z is height in meters, $\overline{U}_z$ is the steady state wind speed (m/s) at height z, and $\overline{U}_{18.3}$ is the steady state wind speed (m/s) at 18.3 m. The quantity $S(f)$ is a spectral density function of frequency f with units of $m^2\ sec^{-2}\ (cycles/sec)^{-1}$ and the units of f are cycles/sec. The spectral density function is one-sided in the sense that the root mean square value of the corresponding time history is given by the integral of the function from $f = 0$ to $f =$ infinity. Note that metric units (m/s and m) must be used in the above equation.

Table 3.1.3-7. Non-dimensional Constants for the Longitudinal, Lateral and Vertical Components of Turbulence

Component	C_1	C_2	C_3	C_4	C_5	C_6
Longitudinal	1.350	29.035	-1.10	1.972	1.00	0.845
Lateral and Vertical	0.258	9.059	-0.93	2.134	0.580	0.781

Coherence is a non-dimensional term that describes the similarity between two signals. It can vary between 0 (completely dissimilar) and 1 (identical other than a scaling factor and/or lag time). The coherence function associated with the spectral gust model is given by:

$$coh(f, z_1, z_2) = \exp\left[-\frac{0.693f}{k}\left(\frac{z_2}{\bar{u}(z_2)} - \frac{z_1}{\bar{u}(z_1)}\right)\right]$$

where f is frequency (cycles/sec), $\bar{u}$ is the steady-state wind speed (m/sec) at heights z_1 and z_2, and k is the non-dimensional constant given in Table 3.1.3-8. The coherence function will spatially correlate turbulent time series at heights z_1 and z_2.

Table 3.1.3-8. Non-dimensional Constant for the Coherence Function

Component	k
Longitudinal	0.036
Lateral and Vertical	0.045

The discrete model produces periods of gusts which are varied over the range of critical periods, and the gusts are applied individually. Discrete gusts are to be varied to identify the maximum system response. The discrete gust model has the 1-cosine shape defined by

$$V = \frac{V_m}{2}\left[1 - cos\frac{2\pi t}{T}\right]$$

where V is the gust magnitude at time t, V_m is the maximum gust magnitude, and T is the gust duration. The discrete gusts are applied to the steady state wind profiles given in Table 3.1.3-2. The total wind (steady state plus discrete gust) should not exceed the peak wind given in Table 3.1.3-1. A sufficiently wide range of values of T should be selected to encompass the significant periods of response of the system.

For the various operational phases, the design wind shear is determined by subtracting the steady state wind (from Table 3.1.3-2) at the altitude corresponding to the base of the vehicle from the peak wind (from Table 3.1.3-1) at the altitude corresponding to the top of the vehicle, and then dividing the difference by the vehicle length. If the locations of the top and bottom of the vehicle are not available, use a design wind shear of 0.2 s^{-1}.

Model Inputs

The peak wind profile model requires a peak wind value at a reference height of 18.3 m (60.0 ft) as input. The steady state wind profile is determined from the peak wind profile.

For transport to and from the pad, use $u_{18.3}$ = 30.8 m/s (101.1 ft/s) for construction of the maximum design limit peak wind-speed profile up to 150 m (492.1 ft).

For the on-pad stay (unfueled) phase, use $u_{18.3}$ = 38.3 m/s (125.7 ft/s) for construction of the maximum design limit peak wind-speed profile up to 150 m (492.1 ft).

For the on-pad stay (intermediate and fully fueled) phase, use $u_{18.3}$ = 24.2 m/s (79.4 ft/s) for construction of the maximum design limit peak wind-speed profile up to 150 m (492.1 ft).

Tables 3.1.3-1 and 3.1.3-2 list the peak and steady state wind-speed profiles, respectively, at selected heights for the above phases.

The design high steady state wind profiles for thermal assessments (Tables 3.1.3-4 and 3.1.3-5) are constructed by first determining the peak wind profile with $u_{18.3}$ = 17.7 m/s (58.1 ft/s). This peak wind profile is then used to determine the steady state wind profile.

The steady state profiles are used as input for the spectral gust models.

Limitations

Input into model must be in m/s for wind speed and meters for height. All height levels are with respect to height Above Ground Level (AGL). According to SLS-SPEC-048, vehicle and mobile launcher coordinate system heights are relative to the North American Vertical Datum of 1988 (NAVD 88). The ground level surrounding the launch pad is approximately 4.88 m (16 ft) above the NAVD 88 datum. Engineering assessments requiring ground wind heights relative to the NAVD 88 datum must therefore increase heights by 4.88 m (16 ft). Heights in Tables 3.1.3-1, 3.1.3-2, 3.1.3-4, and 3.1.3-5 would be increased by 4.88 m (16 ft). Input height for all equations must be in height AGL. Once the wind is determined via the equations, the height can be increased by 4.88 m (16 ft).

Technical Notes

The modeled peak wind profile is the 3 sigma (99.865th percentile) peak wind-speed profile associated with the reference level peak wind speed. Ground winds during roll-out and on-pad stay can cause fatigue and reduce structural integrity. The peak wind-speed profile can be used to calculate vehicle on-pad base overturning moments and vortex shedding loads.

The steady state wind-speed profile is the 10-minute mean wind-speed profile that could produce the peak wind-speed profile.

The design limit for the transport to and from the pad of 30.8 m/s (101.1 ft/s) at the 18.3 m (60.0 ft) reference level is the limit used for the Space Shuttle Mobile Launch Platform (MLP) during transport operations (Space Shuttle Operations and Maintenance Requirements and Specifications Document, File II, Volume I, Rule S00L00.010, June 6, 2006). The local weather forecast should be utilized to assure that high wind events, such as thunderstorms or tropical weather, will not be present during transport operations.

The design limit for the unfueled case of 38.3 m/s (125.7 ft/s) at the 18.3 m (60.0 ft) reference level is the 99th percentile peak wind speed for a 180-day exposure period at KSC. This limit protects for extreme gusts from thunderstorms that may develop rapidly in the vicinity of the pad.

The design limit for the fueled case of 24.2 m/s (79.4 ft/s) at the 18.3 m (60.0 ft) reference level is the 99th percentile peak wind speed for a 1-day exposure period at KSC.

The design high steady-state wind speed profiles for thermal assessments in Tables 3.1.3-4 and 3.1.3-5 are the 95th percentile steady-state wind speed for a 1-hour exposure period at KSC. The design low steady-state wind speed profile in Table 3.1.3-5 is the 1st percentile steady-state wind speed for a 1-hour exposure period at KSC. The diurnal steady-state wind speed profile in Table 3.1.3-6 is the 1st percentile steady-state wind at each hour of the day at KSC.

3.1.4 Radiant (Thermal) Energy Environment for Ground Ops at KSC

Description

This section specifies the design radiant (thermal) energy environment and sky temperature limits for ground operations at KSC, including transportation to and from the pad and on-pad operations. “Storage” refers to on-pad or other outside storage only.

Design Limits

Tables 3.1.4-1 through 3.1.4-3 are the radiant energy design environments from the previous version of this document. Any previous design assessments based on these environments are still valid and re-assessments are not required. Radiant energy environments include direct incident, diffuse, and sky temperature. Section 3.1.5 provides the air temperature to be used in conjunction with the design environments in Tables 3.1.4-1 through 3.1.4-3.

Table 3.1.4-1 lists the design high radiant energy as a function of time of day.

Table 3.1.4-2 lists the design low radiant energy as a function of time of day.

Table 3.1.4-3 provides the design high and design low sky temperature design limits for KSC.

Tables 3.1.4-4 through 3.1.4-9 are provided for thermal assessments that require more fidelity of the radiant energy environment, specifically for conditions when the sky is clear, partly cloudy, or cloudy. A clear sky is defined as being completely free of clouds, partly cloudy is defined as having 40 to 60% cloud coverage, and cloudy is defined as 100% cloud coverage. Radiant energy environments include direct incident, diffuse, sky temperature, and air temperature. Air temperature is included in this section because the majority of thermal assessments require a coupling of direct incident, diffuse, sky temperature, air temperature, and other environments not provided here (albedo, etc.). The air temperature provided in this section is to be applied only when coupled to the direct incident, diffuse, and sky temperature environments. Design assessments that only require air temperature should use the environments provided in Section 3.1.5.

Table 3.1.4-4 presents design cold radiant energy and sky temperature environment for a cloudy sky.

Table 3.1.4-5 presents design hot radiant energy and sky temperature environment for a cloudy sky.

Table 3.1.4-6 presents design cold radiant energy and sky temperature environment for a partly cloudy sky.

Table 3.1.4-7 presents design hot radiant energy and sky temperature environment for a partly cloudy sky.

Table 3.1.4-8 presents design cold radiant energy and sky temperature environment for a clear sky.

Table 3.1.4-9 presents design hot radiant energy and sky temperature environment for a clear sky.

For thermal assessments requiring wind speed, use Section 3.1.3, Tables 3.1.3-4, 3.1.3-5, and/or 3.1.3-6, for the appropriate application.

Model Inputs

None

Limitations

None

Table 3.1.4-1. Design High Radiant Energy as a Function of Time of Day

Time of Day	Direct Incident to a Plane Normal to the Sun		Diffuse to a Horizontal Plane	
Hour (LST)	W/m^2	$BTU/hr/ft^2$	W/m^2	$BTU/hr/ft^2$
05:00	0	0.0	0	0.0
06:00	56	17.7	8	2.5
07:00	440	139.5	51	16.2
08:00	613	194.3	82	26.0
09:00	701	222.2	106	33.6
10:00	833	264.1	130	41.2
11:00	823	260.9	161	51.0
12:00	844	267.5	146	46.3
13:00	833	264.1	169	53.6
14:00	835	264.7	203	64.3
15:00	819	259.6	125	39.6
16:00	766	242.8	123	39.0
17:00	753	238.7	91	28.8
18:00	621	196.9	62	19.6
19:00	376	119.2	41	13.0
20:00	20	6.3	3	0.9
21:00	0	0.0	0	0.0

Table 3.1.4-2. Design Low Radiant Energy as a Function of Time of Day

Time of Day	Direct Incident to a Plane Normal to the Sun		Diffuse to a Horizontal Plane	
Hour (LST)	W/m^2	$BTU/hr/ft^2$	W/m^2	$BTU/hr/ft^2$
08:00	0	0.0	0	0.0
09:00	0	0.0	32	10.1
10:00	0	0.0	61	19.3
11:00	0	0.0	77	24.4
12:00	0	0.0	92	29.2
13:00	0	0.0	96	30.4
14:00	0	0.0	93	29.5
15:00	0	0.0	73	23.1
16:00	0	0.0	47	14.9
17:00	0	0.0	21	6.7
18:00	0	0.0	0	0.0

Table 3.1.4-3. Sky Temperature Design Limits for KSC

	Sky Temperature	
	(°C)	(°F)
Design High	10.0	50
Design Low	-15.0	5

Table 3.1.4-4. Cold Design Radiant Energy and Sky Temperature as a Function of Time of Day, Cloudy Sky

Time of Day	Cold, Cloudy Conditions							
	Air Temperature		Sky Temperature		Direct Incident*		Diffuse	
Hour (LST)	°C	°F	°C	°F	W/m^2	$BTU/hr/ft^2$	W/m^2	$BTU/hr/ft^2$
00:00	12.4	54.4	12.4	54.4	0	0.0	0	0.0
01:00	12.8	55.1	12.8	55.1	0	0.0	0	0.0
02:00	13.1	55.5	13.1	55.5	0	0.0	0	0.0
.03:00	13.3	56.0	13.3	56.0	0	0.0	0	0.0
04:00	13.6	56.5	13.6	56.5	0	0.0	0	0.0
05:00	13.9	57.1	13.9	57.1	0	0.0	0	0.0
06:00	14.2	57.6	14.2	57.6	0	0.0	0	0.0
07:00	14.4	58.0	14.4	58.0	0	0.0	15	4.7
08:00	14.9	58.7	14.9	58.7	0	0.0	64	20.4
09:00	15.5	59.9	15.5	59.9	0	0.0	96	30.5

Time of Day	Cold, Cloudy Conditions							
	Air Temperature		Sky Temperature		Direct Incident*		Diffuse	
Hour (LST)	°C	°F	°C	°F	W/m²	BTU/hr/ft²	W/m²	BTU/hr/ft²
10:00	16.1	60.9	16.1	60.9	0	0.0	140	44.4
11:00	15.7	60.3	15.7	60.3	0	0.0	150	47.5
12:00	15.5	60.0	15.5	60.0	0	0.0	167	52.9
13:00	15.1	59.1	15.1	59.1	0	0.0	143	45.4
14:00	14.8	58.6	14.8	58.6	0	0.0	133	42.1
15:00	14.3	57.7	14.3	57.7	0	0.0	91	28.8
16:00	14.0	57.3	14.0	57.3	0	0.0	57	17.9
17:00	13.5	56.3	13.5	56.3	0	0.0	17	5.2
18:00	13.1	55.5	13.1	55.5	0	0.0	0	0.1
19:00	12.8	55.1	12.8	55.1	0	0.0	0	0.0
20:00	12.6	54.7	12.6	54.7	0	0.0	0	0.0
21:00	12.7	54.8	12.7	54.8	0	0.0	0	0.0
22:00	12.2	54.0	12.2	54.0	0	0.0	0	0.0
23:00	12.2	53.9	12.2	53.9	0	0.0	0	0.0

* Direct Incident is to a plane normal to the sun vector.

Table 3.1.4-5. Hot Design Radiant Energy and Sky Temperature as a Function of Time of Day, Cloudy Sky

Time of Day	Hot, Cloudy Conditions							
	Air Temperature		Sky Temperature		Direct Incident*		Diffuse	
Hour (LST)	°C	°F	°C	°F	W/m²	BTU/hr/ft²	W/m²	BTU/hr/ft²
00:00	24.1	75.4	24.1	75.4	0	0.0	0	0.0
01:00	24.1	75.5	24.1	75.5	0	0.0	0	0.0
02:00	23.9	75.1	23.9	75.1	0	0.0	0	0.0
03:00	24.0	75.2	24.0	75.2	0	0.0	0	0.0
04:00	24.1	75.5	24.1	75.5	0	0.0	0	0.0
05:00	24.0	75.2	24.0	75.2	0	0.0	1	0.2
06:00	23.9	74.9	23.9	74.9	0	0.0	14	4.4
07:00	25.2	77.3	25.2	77.3	0	0.0	60	19.1
08:00	26.0	78.7	26.0	78.7	0	0.0	129	41.0
09:00	25.8	78.5	25.8	78.5	0	0.0	196	62.2
10:00	26.7	80.0	26.7	80.0	0	0.0	223	70.8
11:00	27.2	80.9	27.2	80.9	0	0.0	279	88.5

Time of Day	Hot, Cloudy Conditions							
	Air Temperature		Sky Temperature		Direct Incident*		Diffuse	
Hour (LST)	°C	°F	°C	°F	W/m^2	BTU/hr/ft^2	W/m^2	BTU/hr/ft^2
12:00	27.2	81.0	27.2	81.0	0	0.0	261	82.8
13:00	27.0	80.5	27.0	80.5	0	0.0	236	74.7
14:00	26.8	80.2	26.8	80.2	0	0.0	186	58.8
15:00	26.1	78.9	26.1	78.9	0	0.0	133	42.2
16:00	25.2	77.4	25.2	77.4	0	0.0	72	22.7
17:00	23.9	75.1	23.9	75.1	0	0.0	19	6.2
18:00	23.6	74.4	23.6	74.4	0	0.0	4	1.2
19:00	23.6	74.5	23.6	74.5	0	0.0	0	0.0
20:00	23.1	73.5	23.1	73.5	0	0.0	0	0.0
21:00	23.3	74.0	23.3	74.0	0	0.0	0	0.0
22:00	23.4	74.1	23.4	74.1	0	0.0	0	0.0
23:00	23.4	74.0	23.4	74.0	0	0.0	0	0.0

* Direct Incident is to a plane normal to the sun vector.

Table 3.1.4-6. Cold Design Radiant Energy and Sky Temperature as a Function of Time of Day, Partly Cloudy Sky

Time of Day	Cold, Partly Cloudy Conditions							
	Air Temperature		Sky Temperature		Direct Incident*		Diffuse	
Hour (LST)	°C	°F	°C	°F	W/m^2	BTU/hr/ft^2	W/m^2	BTU/hr/ft^2
00:00	4.2	39.6	-9.8	14.4	0	0.0	0	0.0
01:00	3.6	38.4	-10.3	13.4	0	0.0	0	0.0
02:00	3.3	37.9	-10.3	13.4	0	0.0	0	0.0
03:00	2.8	37.1	-9.6	14.8	0	0.0	0	0.0
04:00	2.5	36.4	-9.0	15.8	0	0.0	0	0.0
05:00	1.9	35.4	-8.1	17.3	0	0.0	0	0.0
06:00	1.9	35.4	-7.0	19.4	0	0.0	0	0.0
07:00	2.4	36.3	-4.6	23.8	100	31.6	11	3.6
08:00	3.4	38.1	-5.2	22.6	301	95.5	69	21.9
09:00	5.1	41.2	-3.2	26.3	441	139.8	102	32.4
10:00	6.4	43.5	-2.2	28.0	481	152.5	159	50.4
11:00	7.9	46.2	-0.9	30.4	546	173.1	164	52.1
12:00	8.5	47.4	-0.4	31.2	586	185.7	147	46.5
13:00	9.0	48.3	0.5	32.9	597	189.1	173	55.0

Time of Day	Cold, Partly Cloudy Conditions							
	Air Temperature		Sky Temperature		Direct Incident*		Diffuse	
Hour (LST)	°C	°F	°C	°F	W/m²	BTU/hr/ft²	W/m²	BTU/hr/ft²
14:00	9.7	49.4	-0.2	31.6	547	173.5	130	41.3
15:00	9.4	48.9	-0.6	30.9	492	155.8	114	36.3
16:00	8.6	47.5	-0.5	31.2	334	106.0	65	20.7
17:00	6.7	44.1	-2.0	28.4	128	40.5	15	4.9
18:00	5.3	41.5	-5.6	22.0	3	1.0	0	0.0
19:00	4.9	40.8	-7.0	19.4	0	0.0	0	0.0
20:00	4.6	40.3	-9.2	15.5	0	0.0	0	0.0
21:00	4.4	40.0	-9.8	14.4	0	0.0	0	0.0
22:00	4.3	39.8	-10.7	12.7	0	0.0	0	0.0
23:00	4.1	39.4	-10.6	12.8	0	0.0	0	0.0

* Direct Incident is to a plane normal to the sun vector.

Table 3.1.4-7. Hot Design Radiant Energy and Sky Temperature as a Function of Time of Day, Partly Cloudy Sky

Time of Day	Hot, Partly Cloudy Conditions							
	Air Temperature		Sky Temperature		Direct Incident*		Diffuse	
Hour (LST)	°C	°F	°C	°F	W/m²	BTU/hr/ft²	W/m²	BTU/hr/ft²
00:00	28.0	82.3	21.2	70.1	0	0.0	0	0.0
01:00	27.6	81.7	21.4	70.4	0	0.0	0	0.0
02:00	27.3	81.2	20.7	69.3	0	0.0	0	0.0
03:00	27.2	81.0	22.0	71.6	0	0.0	0	0.0
04:00	27.1	80.7	21.0	69.8	0	0.0	0	0.0
05:00	26.9	80.4	20.4	68.7	22	7.1	3	1.0
06:00	28.1	82.5	21.9	71.4	96	30.5	66	20.9
07:00	29.6	85.3	23.1	73.6	394	124.9	128	40.5
08:00	31.3	88.4	25.7	78.3	590	187.0	153	48.4
09:00	32.5	90.5	27.3	81.2	644	204.1	184	58.3
10:00	33.5	92.4	28.2	82.7	658	208.5	218	69.0
11:00	34.6	94.4	29.6	85.2	638	202.1	245	77.6
12:00	34.7	94.5	30.9	87.6	603	191.2	282	89.3
13:00	34.3	93.7	30.6	87.1	531	168.4	259	82.2
14:00	34.1	93.4	30.3	86.5	415	131.7	239	75.8
15:00	33.7	92.7	29.9	85.8	399	126.5	214	67.7

Time of Day	Hot, Partly Cloudy Conditions							
	Air Temperature		Sky Temperature		Direct Incident*		Diffuse	
Hour (LST)	°C	°F	°C	°F	W/m²	BTU/hr/ft²	W/m²	BTU/hr/ft²
16:00	32.7	90.8	28.7	83.7	376	119.1	167	52.8
17:00	31.7	89.1	27.7	81.8	272	86.1	124	39.3
18:00	30.3	86.5	26.1	79.0	74	23.3	52	16.4
19:00	29.1	84.4	24.4	76.0	10	3.3	2	0.5
20:00	28.8	83.8	24.1	75.4	0	0.0	0	0.0
21:00	27.9	82.2	22.6	72.6	0	0.0	0	0.0
22:00	27.7	81.8	21.6	70.9	0	0.0	0	0.0
23:00	27.1	80.8	21.3	70.3	0	0.0	0	0.0

* Direct Incident is to a plane normal to the sun vector.

Table 3.1.4-8. Cold Design Radiant Energy and Sky Temperature as a Function of Time of Day, Clear Sky

Time of Day	Cold, Clear Conditions							
	Air Temperature		Sky Temperature		Direct Incident*		Diffuse	
Hour (LST)	°C	°F	°C	°F	W/m²	BTU/hr/ft²	W/m²	BTU/hr/ft²
00:00	6.2	43.2	-13.7	7.3	0	0.0	0	0.0
01:00	6.3	43.4	-13.7	7.4	0	0.0	0	0.0
02:00	6.2	43.1	-13.8	7.2	0	0.0	0	0.0
03:00	6.1	43.0	-14.1	6.7	0	0.0	0	0.0
04:00	5.8	42.4	-14.4	6.1	0	0.0	0	0.0
05:00	5.8	42.4	-14.4	6.1	0	0.0	0	0.0
06:00	6.0	42.8	-14.3	6.3	0	0.0	0	0.0
07:00	6.7	44.0	-13.6	7.5	144	45.5	12	3.9
08:00	9.7	49.4	-9.8	14.4	580	184.0	58	18.5
09:00	12.1	53.8	-8.9	16.0	787	249.3	70	22.3
10:00	13.9	57.0	-7.6	18.4	858	272.1	81	25.6
11:00	15.4	59.8	-6.2	20.8	886	280.9	86	27.4
12:00	16.3	61.4	-5.8	21.6	894	283.3	90	28.4
13:00	16.6	61.8	-5.7	21.7	880	279.1	87	27.6
14:00	16.8	62.2	-4.5	23.8	858	271.8	75	23.7
15:00	16.4	61.6	-5.6	22.0	773	245.0	65	20.7
16:00	15.4	59.8	-6.3	20.6	577	182.8	50	16.0
17:00	10.9	51.6	-9.5	14.9	137	43.4	9	2.9

Time of Day	Cold, Clear Conditions							
	Air Temperature		Sky Temperature		Direct Incident*		Diffuse	
Hour (LST)	°C	°F	°C	°F	W/m²	BTU/hr/ft²	W/m²	BTU/hr/ft²
18:00	7.7	45.8	-12.5	9.5	2	0.7	0	0.0
19:00	7.1	44.8	-12.7	9.1	0	0.0	0	0.0
20:00	6.6	43.8	-13.3	8.0	0	0.0	0	0.0
21:00	6.8	44.2	-13.1	8.4	0	0.0	0	0.0
22:00	6.9	44.4	-13.1	8.4	0	0.0	0	0.0
23:00	6.2	43.2	-14.0	6.9	0	0.0	0	0.0

* Direct Incident is to a plane normal to the sun vector.

Table 3.1.4-9. Hot Design Radiant Energy and Sky Temperature as a Function of Time of Day, Clear Sky

Time of Day	Hot, Clear Conditions							
	Air Temperature		Sky Temperature		Direct Incident*		Diffuse	
Hour (LST)	°C	°F	°C	°F	W/m²	BTU/hr/ft²	W/m²	BTU/hr/ft²
00:00	17.1	62.7	2.0	35.7	0	0.0	0	0.0
01:00	16.9	62.4	1.4	34.6	0	0.0	0	0.0
02:00	16.7	62.1	1.3	34.3	0	0.0	0	0.0
03:00	16.6	61.9	1.0	33.9	0	0.0	0	0.0
04:00	16.6	61.9	1.1	34.0	0	0.0	0	0.0
05:00	16.5	61.6	0.9	33.6	0	0.0	0	0.0
06:00	16.7	62.1	1.0	33.8	75	23.7	3	1.0
07:00	18.9	65.9	3.6	38.5	330	104.6	57	18.2
08:00	20.7	69.2	5.4	41.6	605	191.9	104	32.9
09:00	22.4	72.3	7.0	44.6	747	236.7	110	34.8
10:00	23.9	75.0	7.9	46.3	837	265.3	108	34.3
11:00	24.5	76.1	8.6	47.5	862	273.3	113	35.9
12:00	25.0	77.1	8.8	47.8	873	276.9	114	36.0
13:00	24.5	76.1	8.1	46.6	870	275.7	106	33.5
14:00	24.1	75.3	7.7	45.9	822	260.6	103	32.6
15:00	23.4	74.1	7.3	45.2	753	238.8	89	28.2
16:00	22.5	72.4	6.6	43.8	584	185.0	74	23.6
17:00	20.6	69.0	5.5	41.9	229	72.7	28	8.8
18:00	19.2	66.5	3.6	38.5	15	4.6	1	0.2
19:00	18.7	65.7	3.3	37.9	0	0.0	0	0.0
20:00	18.3	65.0	2.7	36.9	0	0.0	0	0.0

Time of Day	Hot, Clear Conditions							
	Air Temperature		Sky Temperature		Direct Incident*		Diffuse	
Hour (LST)	°C	°F	°C	°F	W/m^2	BTU/hr/ft^2	W/m^2	BTU/hr/ft^2
21:00	17.9	64.2	2.5	36.4	0	0.0	0	0.0
22:00	17.5	63.4	2.0	35.6	0	0.0	0	0.0
23:00	17.4	63.4	1.9	35.5	0	0.0	0	0.0

* Direct Incident is to a plane normal to the sun vector.

Technical Notes

Direct incident is the solar radiant energy to a plane normal to the sun vector. The actual radiant energy absorbed by a surface would be a function of the surface optical properties and the surface geometry relative to the Sun vector. Diffuse radiant energy represents the accumulation on a horizontal surface of the scattered solar radiant energy from all directions, not including the direct incident. Sky temperature represents the temperature of the sky assuming it is radiating as a blackbody.

Tables 3.1.4-1 through 3.1.4-3

The design high radiant energy presents clear day direct incident radiant energy to a plane normal to the Sun and diffuse radiant energy to a horizontal plane. The actual radiant energy absorbed by a surface would be a function of the surface optical properties and the surface geometry relative to the Sun vector. The design high is based on extreme high values for the month of June. Diffuse values are those associated with the extreme direct incident values. The design low radiant energy presents cloudy day diffuse radiant energy that would apply to all surfaces. The design low is based on extreme low values for the month of December. These data should be used in conjunction with the sky temperature.

Tables 3.1.4-4 through 3.1.4-9

Design limits are developed from the National Solar Radiation Database (http://rredc.nrel.gov/solar/old_data/nsrdb/1991-2010/) for the Shuttle Landing Facility, KSC. Cold and hot diurnal profiles are the average of the 10 coldest and warmest days for the given sky conditions (cloudy, partly cloudy, and clear). Since surface air temperature, direct incident radiant energy, diffuse radiant energy, and sky temperature are coupled and depend on sky conditions, it is recommended that each case be used as input into thermal models to determine the worst case.

3.1.5 Air Temperature Environment for Ground Operations at KSC

Description

This section specifies the design maximum and minimum surface air temperature, design hot and cold diurnal profiles, and design hot and cold monthly averaged diurnal profiles for ground operations at KSC, including transportation to and from the pad and on-pad operations.

Design Limits

Maximum: 38.0 °C (100.4 °F)

Minimum: -6.0 °C (21.2 °F)

Table 3.1.5-1 provides the design hot and cold diurnal temperature profiles for KSC.

Table 3.1.5-2 provides the design hot and cold monthly averaged diurnal temperature profiles for KSC.

Table 3.1.5-1. Design Hot and Cold Diurnal Temperature Profile

Time of Day Hour	Design Hot Diurnal Profile		Design Cold Diurnal Profile	
LST	°C	°F	°C	°F
00:00	28.0	82.4	1.0	33.8
01:00	27.0	80.6	0.0	32.0
02:00	27.0	80.6	0.0	32.0
03:00	27.0	80.6	0.0	32.0
04:00	27.0	80.6	0.0	32.0
05:00	26.0	78.8	-1.0	30.2
06:00	27.0	80.6	-1.0	30.2
07:00	28.0	82.4	-1.0	30.2
08:00	30.0	86.0	-1.0	30.2
09:00	32.0	89.6	0.0	32.0
10:00	33.0	91.4	2.0	35.6
11:00	34.0	93.2	3.0	37.4
12:00	34.0	93.2	5.0	41.0
13:00	35.0	95.0	6.0	42.8
14:00	35.0	95.0	7.0	44.6
15:00	35.0	95.0	7.0	44.6
16:00	34.0	93.2	7.0	44.6
17:00	34.0	93.2	7.0	44.6
18:00	32.0	89.6	4.0	39.2
19:00	31.0	87.8	3.0	37.4
20:00	29.0	84.2	2.0	35.6
21:00	29.0	84.2	1.0	33.8
22:00	28.0	82.4	0.0	32.0
23:00	28.0	82.4	1.0	33.8

Table 3.1.5-2. Design Hot and Cold Monthly Averaged Diurnal Temperature Profile

Time of Day Hour	Design Hot Monthly Averaged Diurnal Profile		Design Cold Monthly Averaged Diurnal Profile	
LST	°C	°F	°C	°F
00:00	26.2	79.2	8.6	47.5
01:00	26.0	78.8	8.4	47.1
02:00	25.9	78.6	8.0	46.4
03:00	25.6	78.1	7.8	46.0
04:00	25.3	77.5	7.6	45.7
05:00	25.2	77.4	7.4	45.3
06:00	25.1	77.2	7.2	45.0
07:00	26.9	80.4	7.2	45.0
08:00	28.8	83.8	7.7	45.9
09:00	30.0	86.0	9.8	49.6
10:00	31.3	88.3	11.9	53.4
11:00	32.2	90.0	13.3	55.9
12:00	32.6	90.7	14.1	57.4
13:00	32.8	91.0	14.7	58.5
14:00	32.5	90.5	14.7	58.5
15:00	32.1	89.8	14.7	58.5
16:00	31.5	88.3	14.2	57.6
17:00	30.6	87.1	13.5	56.3
18:00	29.8	85.6	11.9	53.4
19:00	28.6	83.5	10.7	51.3
20:00	27.5	81.5	9.9	49.8
21:00	27.0	80.6	9.5	49.1
22:00	26.7	80.1	8.9	48.0
23:00	26.5	79.7	8.7	47.7

Model Inputs

None

Limitations

The design maximum and minimum limits are appropriate for thermal assessments with short durations (no more than 3 hours). The design hot and cold diurnal profiles are appropriate for assessments with a duration on the order of days (Table 3.1.5-1). The design hot and cold monthly averaged diurnal profiles are appropriate for thermal assessments on the order of a month, for example, determination of Propellant Mean Bulk Temperature (PMBT).

Technical Notes

Temperature data for KSC were obtained from hourly surface observations for the period of record (POR) 1957-2001. Design limits represent the maximum and minimum air temperature over the POR. Design hot and cold diurnal profiles are the 99th percentile temperatures for each hour in the hot month (July) and cold month (January), respectively. Design hot and cold monthly averaged diurnal profiles are the 99th and 1st percentile monthly averaged temperatures for each hour in the hot month (July) and cold month (January), respectively.

Atmospheric temperature is used for defining the thermal conditions acting on the vehicle. Icing on fueled cryogenic tanks can occur due to exposure to ambient air temperatures. Once fuel tank loading has been initiated, the temperature of the air surrounding the other vehicle elements may be affected by chilling from the cold surfaces of the fuel tank and from the main engine drain purges and can be colder than the air temperature.

3.1.6 Air Pressure Environment for Ground Operations at KSC

Description

This section specifies the design maximum and minimum sea-level air pressure for ground operations at KSC, including transportation to and from the pad and on-pad operations.

Design Limits

Maximum: 1,037.4 hectoPascals (hPa) (15.1 pounds per square inch (psi)) at sea level

Minimum: 973.9 hPa (14.1 psi) at sea level

Altitude correction may be necessary for sensitive applications. The total variation of pressure from day to day is relatively small. A gradual rise or fall in pressure of 3.0 hPa (0.04 psi) and then a return to original pressure can be expected within a 24-hour period. Typically, a maximum pressure change of 6.0 hPa (0.09 psi) can be expected within a 1-hour period. [100 Pascals = 1 hPa = 1 millibar (mbar) = 0.01450377 psi]

Model Inputs

None

Limitations

Design limits represent the air pressure at a reference level specified by sea level. The design limit, along with temperature and humidity information, can be used to derive air pressure at other desired altitudes.

Technical Notes

Design limits represent the maximum and minimum sea-level air pressure from hourly surface observations at the ER for the POR 1957-2002.

Testing for critical systems may involve pressures higher than those listed in this document. Refer to the appropriate test and verification plan for specific systems.

3.1.7 Humidity Environment for Ground Operations at KSC

Description

This section specifies the design environment of surface humidity for ground operations at KSC, including transportation to and from the pad and on-pad operations.

Design Limits

Design Limits for Surface Dew Point:

Figure 3.1.7-1 contains a graphical depiction of the psychrometric data for the dew point temperature versus temperature envelope for KSC.

Psychrometric data for the dew point temperature versus temperature envelope for KSC are contained in Table 3.1.7-1.

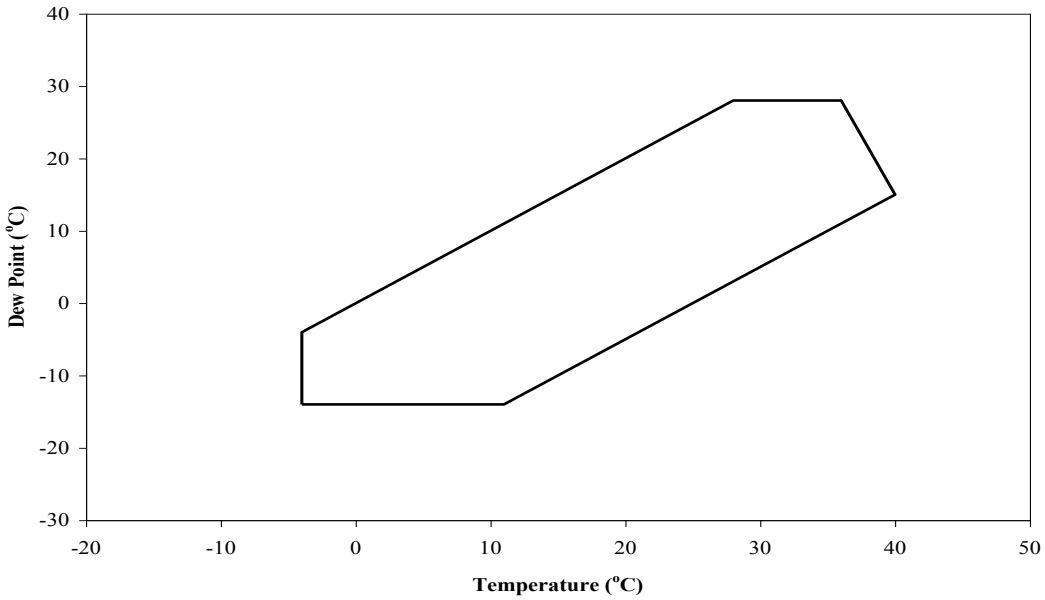

Figure 3.1.7-1. Psychrometric Data, Dew Point Temperature Versus Temperature Envelope for KSC

Table 3.1.7-1. Psychrometric Data, Dew Point Temperature Versus Temperature Envelope for KSC

Temperature		Dew Point	
(°C)	(°F)	(°C)	(°F)
-4.0	24.8	-14.0	6.8
-4.0	24.8	-4.0	24.8
28.0	82.4	28.0	82.4
36.0	96.8	28.0	82.4
40.0	104.0	15.0	59.0
11.0	51.8	-14.0	6.8

Model Inputs

None

Limitations

None

Technical Notes

Atmospheric humidity is used for defining the thermal and dry/moist conditions acting on the vehicle. The surface psychrometric data are based on hourly surface observations for the ER from 1957 to 2002. Figure 3.1.7-1 shows the limits in Table 3.1.7-1. The range of dew point temperatures and associated air temperatures from Table 3.1.7-1 represents the worst case environment to be used in design studies. Values chosen between these limits must be within the envelope in Figure 3.1.7-1.

3.1.8 Aerosol Environment for Ground Operations at KSC

Description

This section specifies the aerosol environment for ground operations at KSC, including transportation to and from the pad and on-pad operations. The natural environment in the launch area is conducive to sea salt, sand, and dust.

Design Limits

Methods for testing of materials for salt fog and sand/dust are given in MIL-STD-810G, Test Method Standard for Environmental Engineering Considerations and Laboratory Tests. The testing of materials for effects of salt fog exposure is described in Method 509.6. The testing of materials for effects of sand/dust exposure is described in Method 510.6, Procedure 1, for particle sizes less than or equal to 150 microns. The particle concentration to be used with Method 510.6, Procedure 1, is 0.177 g/m^3 as specified in Part 3, Section 5.7 of MIL-STD-810G.

Limitations

The aerosol environment for the launch site is poorly defined. The test methods in MIL-STD-810G do not attempt to duplicate the complex environment. They provide generally stressful situations that may reveal potential problem areas in material. Testing in the natural environment, whenever practical, may provide more valuable results.

Technical Notes

Due to the launch site being in a coastal region, systems and material will be exposed to salt fog and suspended sand/dust. The detrimental effects of these aerosols include material corrosion and clogging/binding of moving parts of mechanical components.

3.1.9 Precipitation Environment for Ground Operations at KSC

This section specifies the precipitation environment (rain and hail) for ground operations at KSC, including transportation to and from the pad, on-pad operations, and on-pad or outside storage.

Design Limits

Tables 3.1.9-1 and 3.1.9-2 list the design rainfall and hail characteristics at KSC. Steady state and peak winds given in Section 3.1.3, Ground Winds for Transport and Launch Pad Environments, will be used for studies that require coupling of hail and/or rainfall with wind.

Table 3.1.9-1. Design Rainfall, KSC, Based on Yearly Largest Rate for Stated Durations

Time Period	Rainfall Rate		Rainfall Total Accumulation		Raindrop Size			
					Average		Largest	
	mm/hr	in/hr	mm	in	mm	in	mm	in
1 min	492	19.4	8.0	0.3	2.0	0.079	6.0	0.24
5 min	220	8.7	18	0.7	2.0	0.079	5.8	0.23
15 min	127	5.0	32	1.3	2.0	0.079	5.7	0.22
1 hr	64	2.5	64	2.5	2.0	0.079	5.0	0.20
6 hr	26	1.0	156	6.1	1.8	0.071	5.0	0.20
12 hr	18	0.7	220	8.7	1.6	0.063	4.5	0.18
24 hr	13	0.5	311	12.2	1.5	0.059	4.5	0.18

Table 3.1.9-2. Design Hail Characteristics for KSC

Hailstone Diameter Size	2.2 cm (0.87 in)
Terminal Velocity	17.0 m/s (55.8 ft/s)
Number of Hailstones per Hail Fall	260 m^{-2} (24 ft^{-2})
Duration of Hail Fall	5 min
Horizontal Velocity	15.0 m/s (49.2 ft/s)
Density of Hailstone	0.9 g/cm^3 (0.03 lb/in^3)

Model Inputs

None

Limitations

The rainfall amounts should not be interpreted to mean that the rain fell uniformly for the entire referenced time periods. The average terminal velocity for raindrops is 6.5 m/s for all time periods.

Technical Notes

Hailstone diameter size and horizontal velocity in Table 3.1.9-2 are the 5% risk values based on hail fall studies conducted in Illinois (Changnon, 1977).

3.1.10 Flora and Fauna Environment for Ground Operations

Description

This section specifies the flora and fauna environment for ground operations at KSC, including transportation to and from the launch pad and on-pad operations.

Design Limits

The natural environment in the launch area is conducive to fungus growth. The specific environment is dependent upon material selection. Wildlife and insects in the KSC area include, but are not limited to birds (woodpeckers, buzzards), rodents (mice, rats), insects (bees, cockroaches), wild boar, and alligators.

Model Inputs

None

Limitations

None

Technical Notes

Currently, design specification addresses only fungus growth and common pests. Additional work is required to address other flora and fauna. Consideration may be given to addressing flora and fauna, operationally. Methods for testing of materials for fungus growth are given in MIL-STD-810G, Test Method Standard for Environmental Engineering Considerations and Laboratory Tests, Method 508.

3.1.11 Lightning Environment for Ground Operations at KSC

Description

This section specifies the lightning environment for ground operations at KSC, including transportation to and from the launch pad and stationary storage of the vehicle on the launch pad. Design specifications include standardized voltage and current waveforms derived or characterized to represent the lightning environment at specific zones established on the vehicle.

Design Limits

The environment in the launch area is such that systems will be exposed to the direct and indirect effects of lightning. Descriptions and conditions for the application of lightning environment waveforms are detailed in SAE ARP5414, Aircraft Lightning Zones, and must be defined and

evaluated for each applicable vehicle configuration. SAE ARP5412, Aircraft Lightning Environment and Related Test Waveforms is an applicable document.

Model Inputs

Vehicle lightning strike zones are defined for each configuration of the vehicle and ground support equipment.

Limitations

Waveforms used for analysis are selected based on vehicle attachment profile and electromagnetic regions.

The most important characteristics of the standard lightning waveforms used for analysis and test are the peak current, continuing current, peak rate of rise, and the action integral, or coulomb content, of the waveform. Secondary characteristics of significance are the time to peak, and the time to fall to 50% of the peak. Peak current and continuing current levels are important for direct attachment assessment. The action integral is the amount of energy contained in the flash event and is most important for determining damage related to direct attachment effects. Rise and fall times are important for indirect effects assessment and analysis.

Technical Notes

None

3.2 Launch Countdown and Earth Ascent Phases

3.2.1 Ground Winds Environments During Launch

Description

This section specifies ground wind environments (altitude range 0 to 270 m (886 ft) AGL), up to and including the maximum design limits, for vehicle launch at KSC. Design specifications include peak wind-speed profile, steady state wind-speed profile, and spectral gust environment.

Design Limits

Table 3.2.1-1 provides the design peak wind profiles for the vehicle launch phase. The design steady state wind profiles associated with the design peak wind profiles are provided in Table 3.2.1-2. The steady state wind profile is that profile that could produce the instantaneous peak winds (gusts) in Table 3.2.1-1. Peak wind profile values between those altitudes given in Tables 3.2.1-1 are determined by:

$$u(z) = u_{18.3}\left(\frac{z}{18.3}\right)^{1.6(u_{18.3})^{-3/4}}$$

where $u(z)$ is the peak wind (m/s) at height z (m) and $u_{18.3}$ is the peak wind speed (m/s) at 18.3 m. Steady state profile values between those altitudes given in Table 3.2.1-2 are determined by:

$$\bar{U}(z) = u(z)\left(1 + \left(\frac{\left(\frac{18.3}{z}\right)^{\left(0.283 - 0.435e^{-0.2u_{18.3}}\right)}}{1.98 - 1.887e^{-0.2u_{18.3}}}\right)\right)^{-1}$$

where $u(z)$ is the peak wind (m/s) at height z (m) and $u_{18.3}$ is the peak wind (m/s) at 18.3 m. Note that metric units (m/s and m) must be used in the above two equations. Once $u(z)$ and $\bar{U}(z)$ are determined, they can be converted to English units (ft/s).

Table 3.2.1-1. Peak Wind Speed Profile for Vehicle Launch

Height		Peak Wind-Speed Profile for Vehicle Launch	
m	**ft**	**m/s**	**ft/s**
10	32	15.8	51.8
18.3	60	17.7	58.1
30	98	19.4	63.7
60	197	22.1	72.5
90	295	23.8	78.1
120	394	25.1	82.4
150	492	26.1	85.6
180	591	27.0	88.6
210	689	27.8	91.2
240	787	28.5	93.5
270	886	29.1	95.5

Table 3.2.1-2. Steady State Wind Speed Profile for Vehicle Launch

Height		Steady State Wind-Speed Profile for Vehicle Launch	
m	**ft**	**m/s**	**ft/s**
10	32	9.8	32.2
18.3	60	11.7	38.4
30	98	13.3	43.6
60	197	16.0	52.5
90	295	17.8	58.4
120	394	19.1	62.7
150	492	20.2	66.3
180	591	21.1	69.2

Height		Steady State Wind-Speed Profile for Vehicle Launch	
m	**ft**	**m/s**	**ft/s**
210	689	21.9	71.9
240	787	22.6	74.2
270	886	23.3	76.4

The design gust environment is characterized by either the spectral gust model or the discrete gust model. The spectral model produces fluctuations from all periods producing significant response of the vehicle. Spectral gusts are to be varied to identify the maximum system response. The spectral gust environment at height *z* consists of longitudinal, lateral, and vertical turbulence spectra. The turbulence components are applied to the steady state wind profiles given in Table 3.2.1-2. The longitudinal component of turbulence is parallel to the steady state wind vector with the lateral component in the horizontal plane and perpendicular to the longitudinal and vertical components. These components are given by:

$$S(f) = \frac{C_1\left(\frac{z}{18.3}\right)^{C_3} z\left(\frac{\overline{U}_{18.3}^2}{\overline{U}_z}\right)}{\left(1 + C_2\left(\left(\frac{18.3}{z}\right)^{C_5}\left(\frac{fz}{\overline{U}_z}\right)\right)^{C_6}\right)^{C_4}}$$

where the values for the various non-dimensional constants C_1, C_2, C_3, C_4, C_5, and C_6 given in Table 3.2.1-3 are a function of the turbulent components, *z* is height in meters, $\overline{U}_z$ is the steady state wind speed (m/s) at height *z*, and $\overline{U}_{18.3}$ is the steady state wind speed (m/s) at 18.3 m. The quantity *S(f)* is a spectral density function of frequency *f* with units of m^2 sec^{-2} $(cycles/sec)^{-1}$ and the units of *f* are cycles/sec. The spectral density function is one-sided in the sense that the root mean square value of the corresponding time history is given by the integral of the function from *f* = 0 to *f* = infinity. Note that metric units (m/s and m) must be used in the above equation.

Table 3.2.1-3. Non-dimensional Constants for the Longitudinal, Lateral and Vertical Components of Turbulence

Component	C_1	C_2	C_3	C_4	C_5	C_6
Longitudinal	1.350	29.035	-1.10	1.972	1.00	0.845
Lateral and Vertical	0.258	9.059	-0.93	2.134	0.580	0.781

Coherence is a non-dimensional term that describes the similarity between two signals. It can vary between 0 (completely dissimilar) and 1 (identical other than a scaling factor and/or lag time). The coherence function associated with the spectral gust model is given by:

$$coh(f, z_1, z_2) = \exp\left[-\frac{0.693f}{k}\left(\frac{z_2}{\bar{u}(z_2)} - \frac{z_1}{\bar{u}(z_1)}\right)\right]$$

where f is frequency (cycles/sec), $\bar{u}$ is the steady-state wind speed (m/sec) at heights z_1 and z_2, and k is the non-dimensional constant given in Table 3.2.1-4. The coherence function will spatially correlate turbulent time series at heights z_1 and z_2.

Table 3.2.1-4. Non-dimensional Constant for the Coherence Function

Component	k
Longitudinal	0.036
Lateral and Vertical	0.045

The discrete model produces periods of gusts which are varied over the range of critical periods, and the gusts are applied individually. Discrete gusts are to be varied to identify the maximum system response. The discrete gust model has the 1-cosine shape defined by

$$V = \frac{V_m}{2}\left[1 - cos\frac{2\pi t}{T}\right]$$

where V is the gust magnitude at time t, V_m is the maximum gust magnitude, and T is the gust duration. The discrete gusts are applied to the steady state wind profiles given in Table 3.2.1-2. The total wind (steady state plus discrete gust) should not exceed the peak wind given in Table 3.2.1-1. A sufficiently wide range of values of T should be selected to encompass the significant periods of response of the system.

The design launch wind shear is determined by subtracting the steady state wind (from Table 3.2.1-2) at the altitude corresponding to the base of the vehicle from the peak wind (from Table 3.2.1-1) at the altitude corresponding to the top of the vehicle, and then dividing the difference by the vehicle length. If the locations of the top and bottom of the vehicle are not available, use a design wind shear of 0.2 s^{-1}.

Model Inputs

The peak wind profile model requires a peak wind value at a reference height of 18.3 m (60 ft) as input. For vehicle launch, use $u_{18.3}$ = 17.7 m/s (58.1 ft/s) for construction of the maximum design limit wind-speed profile up to 270 m (886 ft) AGL.

The steady state wind profile is determined from the peak wind profile, and is used as input for the spectral gust model.

Limitations

Input into model must be in m/s for wind speed and meters for height. All height levels are with respect to height Above Ground Level (AGL). According to SLS-SPEC-048, vehicle and mobile launcher coordinate system heights are relative to the North American Vertical Datum of 1988 (NAVD 88). The ground level surrounding the launch pad is approximately 4.88 m (16 ft) above the NAVD 88 datum. Engineering assessments requiring ground wind heights relative to the NAVD 88 datum must therefore increase heights by 4.88 m (16 ft). Heights in Tables 3.2.1-1 and 3.2.1-2 would be increased by 4.88 m (16 ft). Input height for all equations must be in height AGL. Once the wind is determined via the equations, the height can be increased by 4.88 m (16 ft).

Technical Notes

The design limit for vehicle launch of 17.7 m/s (58.1 ft/s) at the 18.3 m (60 ft) reference level is the 99th percentile peak wind speed for the windiest hour of the windiest month based on hourly surface observations for the ER from 1957 to 2001. The modeled profile is the 3 sigma (99.865th percentile) peak wind-speed profile associated with the reference level peak wind speed. Ground winds during launch must be considered to assure tower clearance on lift-off. The peak wind-speed profile can be used to calculate vehicle on-pad base overturning moments and vortex shedding loads.

3.2.2 Surface Air Temperature Environment During Launch

Description

This section specifies the design maximum and minimum surface air temperature for vehicle launch at KSC.

Design Limits

Maximum: 37.2 °C (99.0 °F)

Minimum: 0.6 °C (33.1 °F)

Model Inputs

None

Limitations

For thermal assessments involving wind effects, winds must be assumed to be steady state from any direction, with horizontal speeds in the design range given in Table 3.2.1-2.

Technical Notes

Design limits represent the range of temperatures as described in NSTS 07700, Vol. X, Book 2, Space Shuttle Flight and Ground System Specification-Environment Design, Weight and Performance, and Avionics Events, Appendix 10.10, Section 11.1.4.2. These limits are also

defined in NSTS 16007, Space Shuttle Launch Commit Criteria (LCC) and Background, Section 4, Weather Rules. The rationale for choosing this design range for launch is that redesign, retesting, recertification, etc., of legacy hardware would not be necessary.

3.2.3 Surface Air Pressure Environment During Launch

Description

This section specifies the design maximum and minimum sea-level air pressure for vehicle launch at KSC.

Design Limits

Maximum: 1,037.4 hPa (15.1 psi) at sea level

Minimum: 973.9 hPa (14.1 psi) at sea level

[100 Pa = 1 hPa = 1 millibar (mb) = 0.01450377 pound/in^2 (psi)]

Model Inputs

None

Limitations

Design limits represent the air pressure at a reference level specified by sea level. The design limit, along with temperature and humidity information, can be used to derive air pressure at other desired altitudes.

Technical Notes

Design limits represent the maximum and minimum sea-level air pressure from hourly surface observations at the ER for the POR 1957-2002. Air pressure can affect tank pressures and vent size selections.

3.2.4 Surface Humidity Environment During Launch

Description

This section specifies the design environment of surface humidity for vehicle launch at KSC.

Design Limits

See Design Limits for Section 3.1.7, Humidity Environment for Ground Operations at KSC.

Model Inputs

None

Limitations

None

Technical Notes

See for Section 3.1.7.

3.2.5 Aloft Wind Environment for Vehicle Ascent

Description

This section specifies aloft wind environments and dispersions (altitude range 0 to 90 kilometers (km) (295,276 ft)) for vehicle ascent at KSC.

Design Limits

System performance will be evaluated through the use of the following wind databases, which can be used individually or by combination of any of the three. The following models/databases can be obtained by contacting the MSFC Natural Environments Branch (MSFC organization code: EV44).

1) Earth-GRAM 2010: Monte Carlo analysis of 1,000 or more Earth-GRAM 2010 (see note in 2.1.2 Applicable Models/Data Sets) random profiles per month. Each profile is for a 0 to 90 km (295,276 ft) altitude range with Earth-GRAM 2010 inputs per Table 3.2.5-1. Atmospheric wind, temperature, pressure, and density should be evaluated simultaneously in each simulation. Earth-GRAM 2010 can be used up to the desired altitude.

2) Monthly Vector Wind Profile Model (MVWPM): For the altitude range of 0 to 27 km (88,583 ft), use the 99th percentile monthly and conditional wind vector ellipses from the MVWPM. For the altitude range of 28 to 90 km (91,864 to 295,276 ft), monthly mean wind profiles from Earth-GRAM 2010 will be appended to the MVWPM profiles. Appending of profiles will be accomplished by linear interpolation from the top of the MVWPM (at 27 km (88,583 ft)) to the Earth-GRAM 2010 monthly mean profile at 35 km. The Earth-GRAM 2010 monthly mean profile will be used above 35 km (114,829 ft). Table 3.2.5-2 lists the Earth-GRAM 2010 inputs to generate the monthly mean profile which will be appended to MVWPM profiles.

3) Measured Wind Databases (KSC Jimsphere Wind Profile Database and KSC Doppler Radar Wind Profiler Database): The KSC measured wind databases provide wind dispersions for a 200 m to 18 km (656 to 59,055 ft) altitude range. If wind data are needed below 200 m (656 ft), the higher fidelity option is to use KSC 150-m Wind Tower data. If higher fidelity is not needed, then it is recommended the wind be linearly ramped from zero at the surface to the value of the first measured wind. If ramping is done, the wind direction in the surface to 200 m (656 ft) altitude range should be held constant and equal to the value of the first measured wind direction. For the altitude range of 19 to 90 km (62,336 to 295,276 ft), monthly mean wind profiles from Earth-GRAM 2010 will be appended to the measured wind profiles. Appending of profiles will be accomplished by linear interpolation from the top of the measured wind (at 18 km (59,055 ft)) to the Earth-GRAM 2010 monthly mean profile at 26 km (85,302 ft). The Earth-GRAM 2010 monthly mean profile will be used above 26 km (85,302 ft). Table 3.2.5-2 lists the Earth-GRAM 2010 inputs to generate the monthly mean profile that will be appended to measured wind profiles.

This design limit also applies to any Launch Abort System (LAS) analyses.

The design gust environment for aloft winds is characterized by either the continuous gust model or the discrete gust model. The continuous gust model is developed from the KSC Jimsphere Wind Profile Database and consists of profiles of high-passed filtered U (east/west) and V (north/south) wind components. The profiles contain wind features ranging from the Nyquist wavelength (2 times the Jimsphere sampling interval) to the filter cutoff wavelength, which is determined based on engineering needs (for example, assessing non-persistent wind features on day of launch). The continuous gust profiles can be obtained by contacting the MSFC Natural Environments Branch (MSFC organization code: EV44).

Discrete gusts that produce the desired vehicle response will be individually applied to the wind profiles. The discrete gust model has the 1-cosine shape defined by

$$V = 0, \qquad d < 0 \text{ or } d > 2d_m$$

$$V = \frac{V_m}{2}\left(1 - \cos\left(\frac{\pi d}{d_m}\right)\right), \qquad 0 \le d \le 2d_m$$

where V is the gust magnitude at distance d and V_m is the gust magnitude at the gust half-width d_m. Discrete gust magnitudes (V_m) as a function of altitude and gust half-width (d_m) are provided in Tables 3.2.5-1 (m/s) and 3.2.5-2 (ft/s) for moderate turbulence and in Tables 3.2.5-3 (m/s) and 3.2.5-4 (ft/s) for severe turbulence. It is recommended to use the severe turbulence values (Tables 3.2.5-3 and 3.2.5-4) for all engineering assessments. The moderate turbulence values (Tables 3.2.5-1 and 3.2.5-2) can be used when load relief is needed, given the affected program understands the risk and has provided approval.

Table 3.2.5-1. Discrete Longitudinal Gust Magnitude (m/s) as a Function of Altitude (km) and Gust Half-width d_m (m) Based on Moderate Turbulence

Gust Magnitude (m/s)										
Alt. (km)	Gust Half-Width (m)									
	30.0	60.0	90.0	120.0	150.0	180.0	210.0	240.0	270.0	300.0
1.0	1.12	1.56	1.87	2.13	2.34	2.52	2.68	2.81	2.94	3.05
2.0	1.08	1.50	1.81	2.05	2.26	2.44	2.59	2.73	2.85	2.96
4.0	1.24	1.73	2.09	2.39	2.63	2.84	3.03	3.19	3.34	3.48
6.0	1.30	1.81	2.19	2.49	2.75	2.97	3.16	3.34	3.49	3.63
8.0	1.31	1.83	2.21	2.51	2.77	3.00	3.19	3.37	3.52	3.67
10.0	1.25	1.75	2.12	2.42	2.67	2.89	3.09	3.27	3.42	3.57
12.0	1.15	1.62	1.96	2.25	2.49	2.71	2.90	3.08	3.24	3.39
14.0	0.98	1.38	1.68	1.93	2.14	2.34	2.51	2.67	2.82	2.95
16.0	0.83	1.17	1.43	1.64	1.83	1.99	2.14	2.28	2.41	2.53
18.0	0.62	0.88	1.07	1.23	1.37	1.50	1.62	1.72	1.82	1.91
20.0	0.48	0.68	0.84	0.96	1.08	1.18	1.27	1.35	1.43	1.51

Gust Magnitude (m/s)										
Alt. (km)	Gust Half-Width (m)									
	30.0	60.0	90.0	120.0	150.0	180.0	210.0	240.0	270.0	300.0
25.0	0.49	0.70	0.85	0.98	1.10	1.20	1.29	1.38	1.46	1.54
30.0	0.44	0.62	0.76	0.88	0.98	1.07	1.16	1.24	1.31	1.38
35.0	0.49	0.69	0.84	0.97	1.09	1.19	1.28	1.37	1.45	1.53
40.0	0.51	0.72	0.88	1.02	1.13	1.24	1.34	1.43	1.52	1.60
45.0	0.55	0.78	0.96	1.11	1.24	1.36	1.46	1.56	1.66	1.75
50.0	0.60	0.85	1.04	1.20	1.35	1.47	1.59	1.70	1.80	1.90
55.0	0.68	0.96	1.17	1.35	1.51	1.65	1.78	1.91	2.02	2.13
60.0	0.74	1.04	1.28	1.48	1.65	1.81	1.95	2.09	2.21	2.33
65.0	0.78	1.11	1.35	1.56	1.75	1.91	2.07	2.21	2.34	2.47
70.0	1.04	1.48	1.81	2.09	2.33	2.56	2.76	2.95	3.13	3.30
75.0	1.20	1.70	2.08	2.40	2.68	2.94	3.17	3.39	3.59	3.79
80.0	1.35	1.91	2.34	2.71	3.02	3.31	3.58	3.82	4.06	4.27
85.0	1.57	2.21	2.71	3.13	3.50	3.83	4.14	4.42	4.69	4.95
90.0	1.82	2.58	3.16	3.64	4.07	4.46	4.82	5.15	5.46	5.76

Table 3.2.5-2. Discrete Longitudinal Gust Magnitude (ft/s) as a Function of Altitude (kft) and Gust Half-width d_m (ft) Based on Moderate Turbulence

Gust Magnitude (ft/s)										
Alt. (Kft)	Gust Half-Width (ft)									
	98.4	196.9	295.3	393.7	492.1	590.6	688.9	787.4	885.8	984.3
3.3	3.67	5.12	6.14	6.99	7.68	8.27	8.79	9.22	9.65	10.01
6.6	3.54	4.92	5.94	6.73	7.41	8.01	8.50	8.96	9.35	9.71
13.1	4.07	5.68	6.86	7.84	8.63	9.32	9.94	10.47	10.96	11.42
19.7	4.27	5.94	7.19	8.17	9.02	9.74	10.37	10.96	11.45	11.91
26.2	4.30	6.00	7.25	8.23	9.09	9.84	10.47	11.06	11.55	12.04
32.8	4.10	5.74	6.96	7.94	8.76	9.48	10.14	10.73	11.22	11.71
39.4	3.77	5.31	6.43	7.38	8.17	8.89	9.51	10.10	10.63	11.12
45.9	3.22	4.53	5.51	6.33	7.02	7.68	8.23	8.76	9.25	9.68
52.5	2.72	3.84	4.69	5.38	6.00	6.53	7.02	7.48	7.91	8.30
59.1	2.03	2.89	3.51	4.04	4.49	4.92	5.31	5.64	5.97	6.27
65.6	1.57	2.23	2.76	3.15	3.54	3.87	4.17	4.43	4.69	4.95
82.0	1.61	2.30	2.79	3.22	3.60	3.94	4.23	4.53	4.79	5.05
98.4	1.44	2.03	2.49	2.89	3.22	3.51	3.81	4.07	4.30	4.53
114.8	1.61	2.26	2.76	3.18	3.58	3.90	4.20	4.49	4.76	5.02

Gust Magnitude (ft/s)										
Alt. (Kft)	Gust Half-Width (ft)									
	98.4	196.9	295.3	393.7	492.1	590.6	688.9	787.4	885.8	984.3
131.2	1.67	2.36	2.89	3.35	3.70	4.07	4.40	4.69	4.99	5.25
147.6	1.80	2.56	3.15	3.64	4.07	4.46	4.79	5.12	5.45	5.74
164.0	1.97	2.79	3.41	3.94	4.43	4.82	5.22	5.58	5.91	6.23
180.4	2.23	3.15	3.84	4.43	4.95	5.41	5.84	6.27	6.63	6.99
196.9	2.43	3.41	4.20	4.86	5.41	5.94	6.40	6.86	7.25	7.64
213.3	2.56	3.64	4.43	5.12	5.74	6.27	6.79	7.25	7.68	8.10
229.7	3.41	4.86	5.94	6.86	7.64	8.40	9.06	9.68	10.27	10.83
246.1	3.94	5.58	6.82	7.87	8.79	9.65	10.40	11.12	11.78	12.43
262.5	4.43	6.27	7.68	8.89	9.91	10.86	11.75	12.53	13.32	14.01
278.9	5.15	7.25	8.89	10.27	11.48	12.57	13.58	14.50	15.39	16.24
295.3	5.97	8.46	10.37	11.94	13.35	14.63	15.81	16.90	17.91	18.90

Table 3.2.5-3. Discrete Longitudinal Gust Magnitude (m/s) as a Function of Altitude (km) and Gust Half-width d_m (m) Based on Severe Turbulence

Gust Magnitude (m/s)										
Alt. (km)	Gust Half-Width (m)									
	30.0	60.0	90.0	120.0	150.0	180.0	210.0	240.0	270.0	300.0
1	2.65	3.68	4.43	5.03	5.53	5.95	6.32	6.65	6.94	7.20
2	2.84	3.95	4.77	5.42	5.96	6.43	6.84	7.20	7.52	7.81
4	3.81	5.31	6.41	7.30	8.05	8.69	9.26	9.77	10.23	10.64
6	4.37	6.09	7.35	8.37	9.23	9.98	10.63	11.21	11.74	12.21
8	4.63	6.45	7.79	8.88	9.79	10.58	11.27	11.89	12.44	12.94
10	4.34	6.06	7.34	8.37	9.25	10.02	10.70	11.30	11.85	12.36
12	3.68	5.16	6.27	7.18	7.96	8.65	9.27	9.83	10.35	10.82
14	2.59	3.64	4.44	5.10	5.67	6.18	6.64	7.06	7.45	7.81
16	1.70	2.40	2.92	3.36	3.74	4.08	4.39	4.67	4.94	5.18
18	1.14	1.61	1.97	2.27	2.53	2.76	2.98	3.17	3.35	3.53
20	0.82	1.16	1.42	1.64	1.83	2.00	2.16	2.31	2.44	2.57
25	0.79	1.12	1.36	1.57	1.76	1.92	2.07	2.21	2.35	2.47
30	0.66	0.93	1.14	1.32	1.47	1.61	1.74	1.86	1.97	2.08
35	0.73	1.03	1.26	1.46	1.63	1.79	1.93	2.06	2.18	2.30
40	0.76	1.08	1.32	1.52	1.70	1.86	2.01	2.15	2.28	2.40
45	0.83	1.18	1.44	1.66	1.86	2.03	2.20	2.35	2.49	2.62
50	0.90	1.28	1.56	1.81	2.02	2.21	2.39	2.55	2.71	2.85
55	1.01	1.43	1.76	2.03	2.27	2.48	2.68	2.86	3.04	3.20
60	1.10	1.56	1.91	2.21	2.47	2.70	2.92	3.12	3.31	3.49
65	1.17	1.65	2.02	2.34	2.61	2.86	3.09	3.30	3.50	3.69
70	1.56	2.21	2.71	3.12	3.49	3.82	4.13	4.42	4.68	4.93
75	1.79	2.53	3.10	3.58	4.01	4.39	4.74	5.07	5.37	5.66
80	2.02	2.86	3.50	4.05	4.52	4.95	5.35	5.72	6.07	6.39

Gust Magnitude (m/s)										
Alt. (km)	Gust Half-Width (m)									
	30.0	60.0	90.0	120.0	150.0	180.0	210.0	240.0	270.0	300.0
85	2.35	3.32	4.06	4.69	5.24	5.74	6.20	6.63	7.03	7.41
90	2.73	3.87	4.74	5.47	6.11	6.69	7.23	7.73	8.20	8.64

Table 3.2.5-4. Discrete Longitudinal Gust Magnitude (ft/s) as a Function of Altitude (kft) and Gust Half-width d_m (ft) Based on Severe Turbulence

Gust Magnitude (ft/s)										
Alt. (Kft)	Gust Half-Width (ft)									
	98.4	196.9	295.3	393.7	492.1	590.6	688.9	787.4	885.8	984.3
3.3	8.69	12.07	14.53	16.50	18.14	19.52	20.73	21.82	22.77	23.62
6.6	9.32	12.96	15.65	17.78	19.55	21.10	22.44	23.62	24.67	25.62
13.1	12.50	17.42	21.03	23.95	26.41	28.51	30.38	32.05	33.56	34.91
19.7	14.34	19.98	24.11	27.46	30.28	32.74	34.88	36.78	38.52	40.06
26.2	15.19	21.16	25.56	29.13	32.12	34.71	36.98	39.01	40.81	42.45
32.8	14.24	19.88	24.08	27.46	30.35	32.87	35.10	37.07	38.88	40.55
39.4	12.07	16.93	20.57	23.56	26.12	28.38	30.41	32.25	33.96	35.50
45.9	8.50	11.94	14.57	16.73	18.60	20.28	21.78	23.16	24.44	25.62
52.5	5.58	7.87	9.58	11.02	12.27	13.39	14.40	15.32	16.21	16.99
59.1	3.74	5.28	6.46	7.45	8.30	9.06	9.78	10.40	10.99	11.58
65.6	2.69	3.81	4.66	5.38	6.00	6.56	7.09	7.58	8.01	8.43
82.0	2.59	3.67	4.46	5.15	5.77	6.30	6.79	7.25	7.71	8.10
98.4	2.17	3.05	3.74	4.33	4.82	5.28	5.71	6.10	6.46	6.82
114.8	2.40	3.38	4.13	4.79	5.35	5.87	6.33	6.76	7.15	7.55
131.2	2.49	3.54	4.33	4.99	5.58	6.10	6.59	7.05	7.48	7.87
147.6	2.72	3.87	4.72	5.45	6.10	6.66	7.22	7.71	8.17	8.60
164.0	2.95	4.20	5.12	5.94	6.63	7.25	7.84	8.37	8.89	9.35
180.4	3.31	4.69	5.77	6.66	7.45	8.14	8.79	9.38	9.97	10.50
196.9	3.61	5.12	6.27	7.25	8.10	8.86	9.58	10.24	10.86	11.45
213.3	3.84	5.41	6.63	7.68	8.56	9.38	10.14	10.83	11.48	12.11
229.7	5.12	7.25	8.89	10.24	11.45	12.53	13.55	14.50	15.35	16.17
246.1	5.87	8.30	10.17	11.75	13.16	14.40	15.55	16.63	17.62	18.57
262.5	6.63	9.38	11.48	13.29	14.83	16.24	17.55	18.77	19.91	20.96
278.9	7.71	10.89	13.32	15.39	17.19	18.83	20.34	21.75	23.06	24.31
295.3	8.96	12.70	15.55	17.95	20.05	21.95	23.72	25.36	26.90	28.35

The design should be developed against the above models to maximum vehicle responses.

Model Inputs

Earth-GRAM 2010 (see note in 2.1.2 Applicable Models/Data Sets) inputs for Monte Carlo analyses are listed in Table 3.2.5-3 for each monthly reference period. The spatial and temporal increments are chosen to optimize vehicle response for performance analyses. A large increment may not capture the frequencies (and/or wavelengths) necessary to excite appropriate vehicle responses, while too small an increment can produce very large relative derivatives along the

flight path. It is suggested to choose increments that result in spatial steps no smaller than the length of the vehicle.

The inputs given below provide random profiles with random perturbations that can be used to determine envelopes for trajectory and load variables for ascent analyses. An "rpscale" setting of 1.0 represents perturbation scaling equivalent to the climatological environment. If additional analyses to study the effects of more severe perturbations/turbulence are desired, the "rpscale" can be set to a higher value, which should not exceed 2.0. For thermal and aeroheating studies, it may be desirable to design to extreme profiles (for example, 2 or 3 sigma climatological profiles) which Earth-GRAM 2010 also has the capability to produce.

Table 3.2.5-3. Earth-GRAM 2010 Input to Generate 1,000 or More Perturbed Profiles (0 to 90 km) of Wind, Temperature, Pressure, and Density Per Monthly Reference Period

Parameter	Earth-GRAM 2010 Variable Name	Value
RRA data set	iyrrra	3 = 2013 RRA
RRA limits – use if near site with an RRA	sitenear	0.5
	sitelim	2.5
Random output	iopr	1= random
Non-RRA sites	NCEPyr	9008 = period of record
Random perturbations	rpscale, ruscale, rwscale	1.0
Small scale perturbations	patchy	0

Table 3.2.5-4. Earth-GRAM 2010 Input to Generate Monthly Mean Profiles to be Appended to MVWPM Profiles

Parameter	Earth-GRAM 2010 variable name	Value
RRA data set	iyrrra	3 = 2013 RRA
RRA limits – use if near site with an RRA	sitenear	0.5
	sitelim	2.5
Random output	iopr	2= none
Non-RRA sites	NCEPyr	9008 = period of record

Limitations

Earth-GRAM 2010 (see note in 2.1.2 Applicable Models/Data Sets) and MVWPM perturbations in the aloft region are statistically derived. Large-scale perturbations in Earth-GRAM 2010 follow a cosine wave model, while small-scale perturbations are normally distributed. MVWPM dispersions are developed with the quadravariate normal model, with the assumption that measured wind components are normally distributed at each altitude. The MVWPM, KSC Jimsphere Wind Profiles, and KSC Doppler Radar Wind Profiler databases only contain wind

data. Profiles of temperature, pressure, and density dispersions for use with these models/databases will need to be acquired from other measured databases, or from Earth-GRAM 2010. Discrete gusts may be adjusted (tuned) and applied by the engineer for vehicle response analyses.

Technical Notes

The MVWPM approximates the dispersion in the vector wind, relative to the monthly mean, at a reference altitude. It is suggested that the vehicle ascent guidance steering commands be designed to the monthly mean wind profile, which will produce the baseline aerodynamic load indicators at each altitude for a selected month. The aerodynamic load indicators derived from trajectory simulations using the modeled vector wind profiles for a selected reference altitude represent the dispersion from the baseline at that altitude. The KSC Jimsphere Wind Profiles and KSC Doppler Radar Wind Profiler databases can be used to evaluate flight simulations to determine the operational capability of the launch vehicle.

3.2.6 Aloft Air Temperature Environment for Vehicle Ascent

Description

This section specifies the aloft air temperature environments (altitude range 0 to 90 km (295,276 ft)) for vehicle ascent at KSC.

Design Limits

System performance will be evaluated through the use of the following database. The model/database can be obtained by contacting the MSFC Natural Environments Branch (MSFC organization code: EV44).

1) Earth-GRAM 2010: Monte Carlo analysis of 1,000 or more Earth-GRAM 2010 (see note in 2.1.2 Applicable Models/Data Sets) random profiles per month. Each profile is for a 0 to 90 km altitude range with Earth-GRAM 2010 inputs per Table 3.2.5-1. Atmospheric temperature, pressure, and density should be evaluated simultaneously in each simulation.

Model Inputs

Earth-GRAM 2010 (see note in 2.1.2 Applicable Models/Data Sets) input is listed in Table 3.2.5-1 for each monthly reference period. The spatial and temporal increments are chosen to optimize vehicle response for performance analyses. A large increment may not capture the frequencies (and/or wavelengths) necessary to excite appropriate vehicle responses, while too small an increment can produce very large relative derivatives along the flight path. It is suggested to choose increments that result in spatial steps no smaller than the length of the vehicle.

The inputs given in Table 3.2.5-1 provide random profiles with random perturbations that can be used to determine envelopes for trajectory and load variables for ascent analyses. An “rpscale” setting of 1.0 represents perturbation scaling equivalent to the climatological environment. If additional analyses to study the effects of more severe perturbations/turbulence are desired, the “rpscale” can be set to a higher value, which should not exceed 2.0. For thermal and aeroheating

studies, it may be desirable to design to extreme profiles (for example, 2 or 3 sigma climatological profiles), which Earth-GRAM 2010 also has the capability to produce.

Limitations

Perturbations in the aloft region are statistically derived and are generated using the input variables in Table 3.2.5-1.

Technical Notes

Thermodynamic parameters during ascent drive vehicle venting rates, aeroheating/aerodynamic loads, and trajectory design. It is suggested that at least 1,000 Earth-GRAM 2010 random profiles be analyzed for vehicle design limit development.

3.2.7 Aloft Air Pressure Environment for Vehicle Ascent

Description

This section specifies the aloft air pressure environments (altitude range 0 to 90 km (295,276 ft)) for vehicle ascent at KSC.

Design Limits

See Section 3.2.6, Aloft Air Temperature Environment for Vehicle Ascent.

Model Inputs

See Section 3.2.6.

Limitations

See Section 3.2.6.

Technical Notes

See Section 3.2.6.

3.2.8 Aloft Air Density Environment for Vehicle Ascent

Description

This section specifies the aloft air density environments (altitude range 0 to 90 km (295,276 ft)) for vehicle ascent at KSC.

Design Limit

See Section 3.2.6, Aloft Air Temperature Environment for Vehicle Ascent.

Model Inputs

See Section 3.2.6.

Limitations

See Section 3.2.6.

Technical Notes

See Section 3.2.6.

3.2.9 Cloud Environment for Launch

Description

This section defines the cloud environments within which the vehicle must be capable of launching.

Design Limits

The design range for cloud cover is up to and including 100% cloud cover, excluding convective clouds and thunderstorms. The size distribution of liquid cloud particles is given by:

$$N = \frac{N_o}{\Gamma(\nu)}\left(\frac{D}{D_n}\right)^{\nu-1}\frac{1}{D_n}\exp\left(\frac{-D}{D_n}\right)$$

where N is the cloud droplet size spectra (m^{-3} μm^{-1}), defined as the number of cloud droplets in a cubic meter, within a droplet size interval, ΔD (μm), N_o, ν, and D_n are the gamma distribution parameters, D is the droplet diameter (μm), and Γ is the gamma function. This equation is applicable for a cloud thickness of 3 km (9,843 ft) in the altitude range of 0.5 to 4.5 km (1,640 to 14,764 ft).

The size distribution of frozen cloud particles is given by:

$$N = 100N_o\left(\frac{D}{10000}\right)^{\mu}\exp\left(\frac{-\lambda D}{10000}\right)$$

where N is the ice particle size spectra ($m^{-3}\cdot\mu m^{-1}$), defined as the number of ice particles in a cubic meter, within a particle size interval, ΔD (μm), N_o, μ, and λ are the gamma distribution parameters, and D is the particle diameter (μm). This equation is applicable for a cloud thickness of 2 km (6,562 ft) in the altitude range of 6 to 15 km (19,685 to 49,213 ft).

Model Inputs

For liquid cloud droplet diameters ≤ 19.3 μm (0.000760 in), use:

$$N_0 = 2.88\text{x}10^8\ m^{-3}$$

$$\nu = 8.7$$

$$D_n = 1.3\ \mu m$$

For liquid cloud droplet diameters > 19.3 μm (0.00760 in), use:

$$N_0 = 7.4 \times 10^7 \text{ m}^{-3}$$

$$\nu = 8.6$$

$$D_n = 2.7 \text{ μm}$$

For frozen cloud particles, the parameter λ is a function of temperature given by:

$\lambda = 5.80 \exp(-0.114T)$ for T > -18°C (-0.4 °F)

$\lambda = 20.25 \exp(-0.042T)$ for T < -18°C (-0.4 °F)

Temperature T, in °C, is related to altitude Z, in km, with:

$$T = 0.0506Z^3 - 1.4202Z^2 + 5.7035Z - 4.5349$$

Once λ is determined, the other parameters are given by:

$$\mu = 0.076\lambda^{0.8} - 2$$

$$N_o = 0.0586 \exp(0.077\lambda)$$

Limitations

None

Technical Notes

The size distribution for liquid cloud particles is obtained from Miles, et al (2000). The reference gives size distributions for clouds originating in both marine and continental environments. The design limits given here envelop both of these distributions, with a crossover between the two environments at 19.3 μm (0.000760 in) (continental environment at diameters <19.3 μm (0.000760 in), and marine environment at diameters >19.3 μm (0.000760 in)). The size distribution for liquid cloud particles allows the vehicle to traverse stratiform clouds and rain in non-convective situations.

Traversing convective type clouds, such as thunderstorms, could expose the vehicle to ice particles (hail or graupel) with diameters of several centimeters (cm) or larger. Flight path avoidance of thunderstorms is assumed to protect the vehicle from extreme environments such as lightning, hail, and extreme turbulence.

The size distribution for frozen cloud particles (obtained from Heymsfield (2003)) allows for traverse through mid- and high-altitude layer clouds (alto and cirrus type). Temperature as a function of altitude is determined by applying a 3rd order polynomial fit to the yearly average temperature profile from the KSC Range Reference Atmosphere (RRA) between 6 and 15 km.

3.2.10 Rain and Precipitation Environment for Launch

Description

This section specifies the precipitation environment for vehicle launch at KSC.

Design Limits

The maximum design rainfall rate is 7.6 mm/hr (0.30 in/hr) from non-convective clouds.

The raindrop size distribution is given by:

$$N = 1\times10^{5} N_o \left(\frac{D}{10}\right)^{\alpha} \exp\left(\frac{-\Lambda D}{10}\right)$$

where N is the raindrop size spectra (m^{-3} mm^{-1}), defined as the number of raindrops in a cubic meter, within a raindrop size interval, ΔD (mm), N_o, α, and Λ are the gamma distribution parameters, and D is the raindrop diameter (mm). This equation is applicable from raindrops from the surface to 4.5 km (14,764 ft).

Model Inputs

$$R = 7.6 \text{ mm/hr}$$

$$\Lambda = \frac{5.588}{0.0984R^{0.1535}}$$

$$\alpha = 2.16$$

$$N_o = \frac{5.1285\times10^{-4}\left(0.062R^{0.913}\right)}{\left(0.0984R^{0.1535}\right)^{4}}\left(\frac{1}{0.0984R^{0.1535}}\right)^{\alpha}$$

Limitations

None

Technical Notes

The design rainfall rate is the National Oceanic and Atmospheric Administration (NOAA) maximum observational reporting value for moderate rainfall NOAA (2005). This rate was chosen to exclude operations during heavy rainfall produced by convective clouds (thunderstorms). The raindrop size distribution function is obtained from Tattelman and Willis (1985) Tattelman, P. and Willis, P., Model Vertical Profiles of Extreme Rainfall Rate, Liquid Water Content, and Drop-Size Distribution, AFGL-TR-85-0200, September 6, 1985. Flight path avoidance of thunderstorms is desired to protect the vehicle from extreme environments such as lightning, hail, and extreme turbulence.

3.2.11 Flora and Fauna Environments during Launch and Ascent

Description

This section specifies the flora and fauna environment for vehicle ascent at KSC.

Design Limits

In the KSC area, the most common larger species of birds, with a maximum mass of 2.2 kg (4.9 pounds (lbs)) may be found with decreasing number density up to 7.6 km (25,000 ft). Table 3.2.11-1 presents the avian number density with respect to height AGL.

Table 3.2.11-1. Avian Number Density up to 7.62 km (25,000 ft).

Height AGL		Avian Number Density	
m	ft	# per m^3	#per ft^3
30.5 – 99.9	100.0 – 328.0	6.28E-08	1.78E-09
100.0 – 199.9	328.1 – 656.0	3.28E-08	9.29E-10
200.0 – 299.9	656.1 – 984.1	1.49E-08	4.23E-10
300.0 – 399.9	984.2 – 1312.2	8.17E-09	2.31E-10
400.0 – 499.9	1312.3 – 1640.3	4.96E-09	1.40E-10
500.0 - 999.9	1640.4 – 3280.7	1.57E-09	4.45E-11
1000.0 – 1499.9	3280.8 - 4921.2	4.68E-10	1.32E-11
1500.0 – 1999.9	4921.3 – 6561.6	4.52E-10	1.28E-11
2000.0 – 2499.9	6561.7 – 8202.0	4.82E-10	1.36E-11
2500.0 – 2999.9	8202.1 – 9842.4	5.14E-10	1.46E-11
3000.0 – 3499.9	9842.5 – 11482.8	4.45E-10	1.26E-11
3500.0 – 3999.9	11482.9 – 13123.3	3.21E-10	9.09E-12
4000.0 – 4499.9	13123.4 – 14763.7	1.97E-10	5.58E-12
4500.0 – 4999.9	14763.8 – 16404.1	7.30E-11	2.07E-12
5000.0 – 5499.9	16404.2 – 18044.5	3.70E-12	1.05E-13
5500.0 – 7620.0	18044.6 – 25000.0	3.48E-12	9.85E-14

Model Inputs

None

Limitations

None

Technical Notes

Studies over the past twenty years in the KSC area have been consistent with respect to bird populations, however they only provide coarse detail about bird number densities with respect to height and migratory patterns. The most common larger species of birds in the KSC area are black vultures (mass 1.6 to 2.2 kg (3.5 to 4.9 lbs)), turkey vultures (mass ~2.0 kg (4.4 lbs)) and osprey (mass 1.4 to 2.0 kg) (3.1 to 4.4 lbs). Much less common, but also present in the KSC area are bald eagles (mass 4.5 to 6.4 kg) (9.9 to 14.1 lbs). Data used to derive Table 3.2.11-1 can be found in NASA MSFC Memo EV44 (15-007), titled 'KSC Avian Environment Report'.

3.2.12 Natural and Triggered Lightning during Launch and Ascent

Description

This section specifies the lightning environment for launch and ascent from KSC. Design specifications include standardized voltage and current waveforms derived or characterized to represent the lightning environment at specific zones established on the vehicle.

Design Limits

The environment in the launch area is such that systems will be exposed to the direct and indirect effects of lightning. Descriptions and conditions for the application of lightning environment waveforms are detailed in SAE ARP5414, Aircraft Lightning Zones, and must be defined and evaluated for each applicable vehicle configuration. SAE ARP5412, Aircraft Lightning Environment and Related Test Waveforms is an applicable document.

Model Inputs

Vehicle lightning strike zones must be defined for each integrated vehicle configuration.

Limitations

Waveforms used for analysis are selected based on vehicle attachment profile and electromagnetic regions.

The most important characteristics of the standard lightning waveforms used for analysis and test are the peak current, continuing current, peak rate of rise, and the action integral, or coulomb content, of the waveform. Secondary characteristics of significance are the time to peak, and the time to fall to 50% of the peak. Peak current and continuing current levels are important for direct attachment assessment. The action integral is the amount of energy contained in the flash event, and is most important for determining damage related to direct attachment effects. Rise and fall times are important for indirect effects assessment and analysis.

Technical Notes

None.

3.2.13 Ionizing Radiation Environment for Launch, Ascent and Re-entry

Description

Environment parameters identified here are applicable for KSC launch trajectories to target orbit inclinations of 51.6° or less. This specification applies to SLS vehicles operating at or below latitude 40°N and a peak altitude of 200 km. The magnetic field intensity values used for geomagnetic shielding calculations were selected based on the 40°N maximum latitude and 200 km altitude at longitudes appropriate for a KSC launch. These parameters are derived from representative ascent trajectories, and provide a reasonable representation of anticipated radiation environment risk to the launch vehicle systems. The same conditions apply during any phases of re-entry conducted within the same altitude and latitude limits.

The environment at and below an altitude of 20 km consists almost entirely of secondary radiation products, primarily atmospheric neutrons.

Total Ionizing Dose (TID) and displacement damage (DD) to flight hardware are negligible for this segment of the environment.

Design Limits

Systems that operate at altitudes above 20 km and at or below 200 km altitude will be exposed to the Galactic Cosmic Ray (GCR) and Design Solar Particle Event (Design SPE) environments of Tables 3.2.13-1, -2, and -3. The low altitude atmospheric neutron environment (Table 3.2.13-4) is not a concern for these systems.

The design limit for systems that operate only at or below 20 km is provided in the Table 3.2.13-4 atmospheric neutron environment for the system maximum operating altitude. The 200 km GCR and Design SPE environments are not applicable.

Figure 3.2.13-1 and Table 3.2.13-1 present 200 km particle flux for a Design SPE, as a function of Linear Energy Transfer (LET), and for solar minimum GCR in stormy magnetic field conditions.

Figures 3.2.13-2 and 3.2.13-3 and Tables 3.2.13-2 and 3.2.13-3 present 200 km differential and integral proton fluxes for a Design SPE and GCR.

Table 3.2.13-4 presents the flux of >10 MeV neutrons at altitudes to 20 km.

Limitations

Probability that the 200 km proton energy and particle flux LET spectra of the Design SPE will not be exceeded is estimated at 97%.

The GCR proton energy and particle flux LET spectra represent a worst case (solar minimum) background environment.

The >10 MeV neutron flux is derived from empirical data. No probability has been determined and specified flux could be exceeded during an anomalously large SPE.

Technical Notes

Particle flux and LET values are obtained using the Cosmic Ray Effects on Microelectronics 96 (CREME96) model. Minimum shielding by earth's magnetic field is applied by using the "sections of orbits" option in the model's Geomagnetic Transmission (GTRN) module, choosing the "stormy" magnetic weather conditions, and further selecting bounding McIlwain L values between 2.4 and 2.55. This represents conditions at the approximately 40°N latitude, 200 km altitude, and appropriate longitudes for the core stage operations.

Proton energy and particle flux spectra are acquired using the FLUX model in CREME96. The Design SPE spectra can be reproduced in more detail using the CREME96 "Worst Week" flare model. Atomic numbers for Z=1 through Z=92 ions are included for definition of the LET spectrum, while the proton fluxes, of course, use only Z = 1. All SPE based flux values are then multiplied by 2 to derive the Design SPE which has twice the flux of the October 1989 solar particle event as represented by the CREME96 model. The x2 multiplier of the 1989 event is needed to simulate a "worst case" SPE exposure at the high 97% probability level appropriate for crewed missions included in the Program defined DRM set. The probability is determined by comparison to the Goddard Spaceflight Center (GSFC) Emission of Solar Proton (ESP) model.

The GCR proton energy and particle flux spectra can be reproduced using the CREME96 FLUX module with the same GTRN module output describe in the previous paragraph and selecting the "Solar Minimum" option for 200 km and the Z=1 or Z=1-92 atomic number range, depending on whether the proton only or full GCR spectrum is desired.

For LET analysis, the particle spectra from the FLUX module are converted using the LETSPEC module, which converts particle flux to LET flux.

For all spectra, appropriate unit conversions must be applied whenever applicable.

The incident spectra will be modified during transport through shielding materials between the environment and equipment inside the vehicle. Modified spectra should be defined using the radiation transport model provided in CREME96 or an alternate approved transport model.

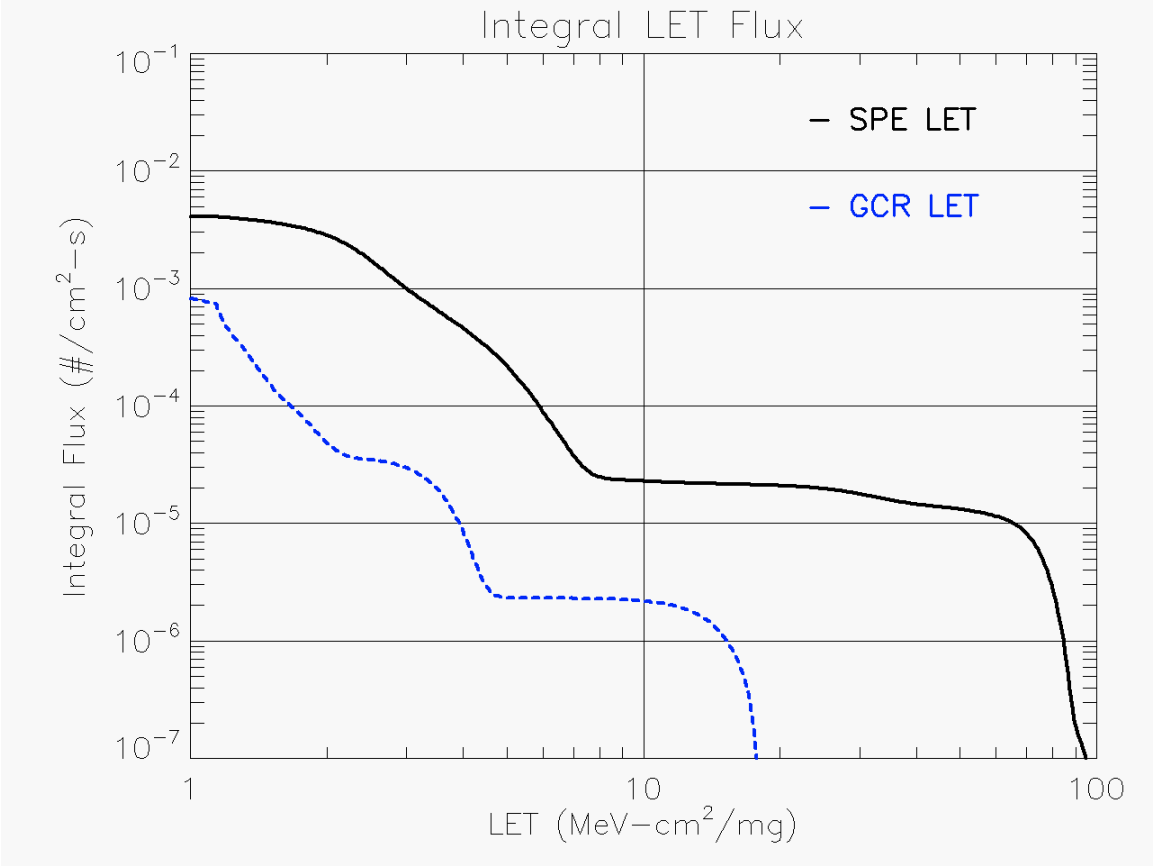

Figure 3.2.13-1. 200 km Integral Flux for a Design SPE and Solar Minimum GCR in a Stormy Magnetic Field for 51.6° Inclination, 200 km Altitude, at 40° North Latitude, as a Function of LET

Table 3.2.13-1. 200 km Integral LET Flux as Shown in Figure 3.2.13-1

	Design SPE (2.55≥ L≥2.4)	GCR (2.55≥L≥2.4)
LET (MeV-cm^2/mg)	Integral Flux (#/cm^2-s)	Integral Flux (#/cm^2-s)
1.06E+00	4.10E-03	7.87E-04
1.17E+00	4.04E-03	5.78E-04
1.28E+00	3.92E-03	3.44E-04
1.41E+00	3.78E-03	2.14E-04
1.54E+00	3.60E-03	1.34E-04
1.69E+00	3.38E-03	9.56E-05
1.86E+00	3.11E-03	6.67E-05
2.04E+00	2.76E-03	4.58E-05
2.23E+00	2.33E-03	3.70E-05
2.45E+00	1.84E-03	3.50E-05
2.69E+00	1.40E-03	3.33E-05
2.95E+00	1.05E-03	3.03E-05
3.24E+00	8.08E-04	2.55E-05
3.55E+00	6.31E-04	1.87E-05
3.90E+00	4.93E-04	1.04E-05
4.28E+00	3.78E-04	4.43E-06
4.69E+00	2.79E-04	2.46E-06
5.15E+00	1.93E-04	2.33E-06
5.65E+00	1.24E-04	2.32E-06
6.20E+00	7.51E-05	2.32E-06
6.80E+00	4.47E-05	2.31E-06
7.46E+00	2.91E-05	2.29E-06
8.19E+00	2.43E-05	2.27E-06
8.99E+00	2.34E-05	2.25E-06
9.86E+00	2.29E-05	2.19E-06
1.08E+01	2.25E-05	2.10E-06
1.19E+01	2.22E-05	1.96E-06
1.30E+01	2.19E-05	1.73E-06
1.43E+01	2.17E-05	1.35E-06
1.57E+01	2.15E-05	8.53E-07
1.72E+01	2.13E-05	2.86E-07
1.89E+01	2.11E-05	1.14E-11
2.07E+01	2.08E-05	4.84E-12
2.27E+01	2.04E-05	1.18E-12
2.49E+01	1.97E-05	8.15E-14
2.74E+01	1.89E-05	
3.00E+01	1.78E-05	
3.29E+01	1.65E-05	
3.61E+01	1.54E-05	
3.96E+01	1.46E-05	

	Design SPE (2.55≥ L≥2.4)	GCR (2.55≥L≥2.4)
LET (MeV-cm²/mg)	Integral Flux (#/cm²-s)	Integral Flux (#/cm²-s)
4.35E+01	1.40E-05	
4.77E+01	1.35E-05	
5.24E+01	1.28E-05	
5.75E+01	1.20E-05	
6.30E+01	1.08E-05	
6.92E+01	8.62E-06	
7.59E+01	5.00E-06	
8.33E+01	1.37E-06	
9.14E+01	1.52E-07	

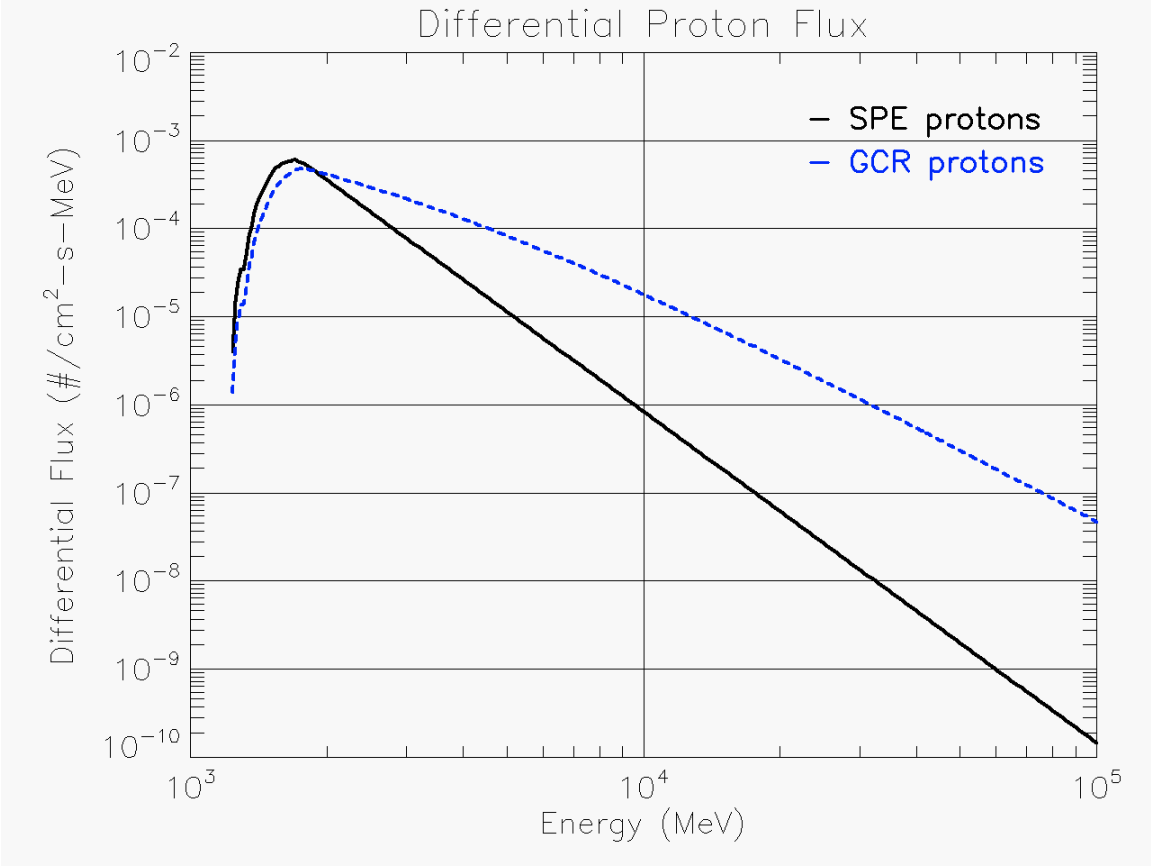

Figure 3.2.13-2. 200 km Differential Design SPE and GCR Proton Flux as a Function of Energy

Table 3.2.13-2. 200 km Differential Proton Flux as Shown in Figure 3.2.13-2.

	Design SPE (2.55≥ L≥2.4)	GCR (2.55≥L≥2.4)
Energy (MeV)	Differential Flux (p+/cm^2-s-MeV)	Differential Flux (p+/cm^2-s-MeV)
1.24E+03	3.97E-06	1.38E-06
1.35E+03	8.28E-05	3.59E-05
1.46E+03	3.24E-04	1.74E-04
1.59E+03	5.52E-04	3.66E-04
1.73E+03	5.85E-04	4.76E-04
1.88E+03	4.55E-04	4.52E-04
2.04E+03	3.33E-04	4.02E-04
2.22E+03	2.44E-04	3.56E-04
2.41E+03	1.79E-04	3.13E-04
2.62E+03	1.31E-04	2.74E-04
2.84E+03	9.58E-05	2.39E-04
3.09E+03	7.02E-05	2.08E-04
3.35E+03	5.14E-05	1.79E-04
3.64E+03	3.76E-05	1.54E-04
3.96E+03	2.76E-05	1.32E-04
4.30E+03	2.02E-05	1.12E-04
4.67E+03	1.48E-05	9.54E-05
5.07E+03	1.08E-05	8.07E-05
5.51E+03	7.93E-06	6.79E-05
5.99E+03	5.81E-06	5.70E-05
6.50E+03	4.26E-06	4.77E-05
7.07E+03	3.12E-06	3.98E-05
7.68E+03	2.28E-06	3.31E-05
8.34E+03	1.67E-06	2.74E-05
9.06E+03	1.22E-06	2.27E-05
9.84E+03	8.97E-07	1.87E-05
1.07E+04	6.57E-07	1.54E-05
1.16E+04	4.81E-07	1.26E-05
1.26E+04	3.52E-07	1.04E-05
1.37E+04	2.58E-07	8.46E-06
1.49E+04	1.89E-07	6.91E-06
1.62E+04	1.38E-07	5.63E-06
1.76E+04	1.01E-07	4.58E-06
1.91E+04	7.42E-08	3.72E-06
2.07E+04	5.44E-08	3.01E-06
2.25E+04	3.98E-08	2.44E-06
2.45E+04	2.92E-08	1.97E-06
2.66E+04	2.14E-08	1.59E-06

	Design SPE (2.55≥ L≥2.4)	GCR (2.55≥L≥2.4)
Energy (MeV)	**Differential Flux (p+/cm^2-s-MeV)**	**Differential Flux (p+/cm^2-s-MeV)**
2.89E+04	1.56E-08	1.29E-06
3.14E+04	1.15E-08	1.04E-06
3.41E+04	8.39E-09	8.35E-07
3.70E+04	6.14E-09	6.72E-07
4.02E+04	4.50E-09	5.40E-07
4.37E+04	3.30E-09	4.34E-07
4.75E+04	2.41E-09	3.48E-07
5.16E+04	1.77E-09	2.80E-07
5.60E+04	1.29E-09	2.24E-07
6.08E+04	9.48E-10	1.80E-07
6.61E+04	6.94E-10	1.44E-07
7.18E+04	5.09E-10	1.15E-07
7.80E+04	3.72E-10	9.23E-08
8.47E+04	2.73E-10	7.38E-08
9.21E+04	2.00E-10	5.90E-08

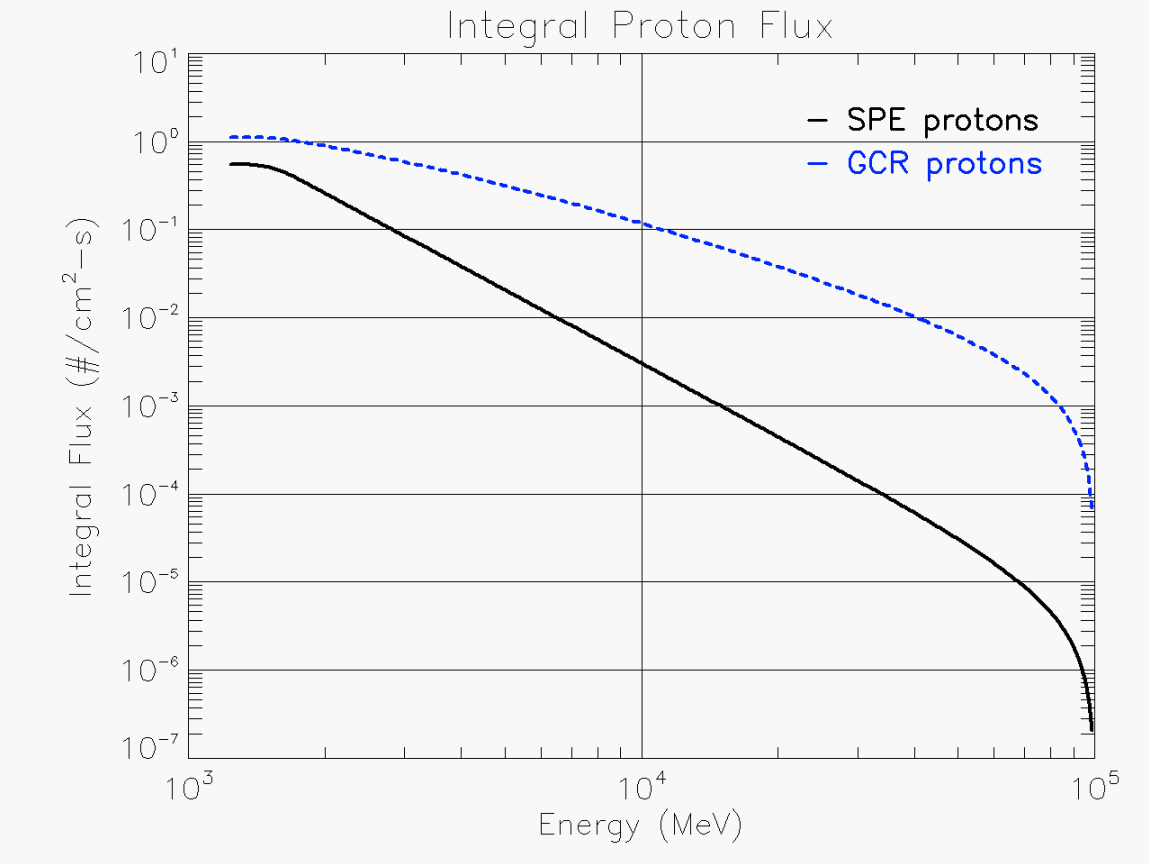

Figure 3.2.13-3. 200 km Integral Proton Flux of Design SPE and Integral GCR Flux as a Function of Energy

Table 3.2.13-3. 200 km Integral Proton Flux as Shown in Figure 3.2.13-3

	Design SPE (2.55≥ L≥2.4)	GCR (2.55≥L≥2.4)
Energy (MeV)	Integral Flux (p+/cm²-s-MeV)	Integral Flux (p+/cm²-s-MeV)
1.24E+03	5.51E-01	1.12E+00
1.35E+03	5.48E-01	1.12E+00
1.46E+03	5.25E-01	1.11E+00
1.59E+03	4.68E-01	1.07E+00
1.73E+03	3.88E-01	1.01E+00
1.88E+03	3.09E-01	9.44E-01
2.04E+03	2.46E-01	8.74E-01
2.22E+03	1.96E-01	8.08E-01
2.41E+03	1.56E-01	7.44E-01
2.62E+03	1.24E-01	6.83E-01
2.84E+03	9.87E-02	6.25E-01

	Design SPE (2.55≥ L≥2.4)	GCR (2.55≥L≥2.4)
Energy (MeV)	**Integral Flux (p+/cm^2-s-MeV)**	**Integral Flux (p+/cm^2-s-MeV)**
3.09E+03	7.85E-02	5.70E-01
3.35E+03	6.24E-02	5.19E-01
3.64E+03	4.97E-02	4.71E-01
3.96E+03	3.95E-02	4.26E-01
4.30E+03	3.14E-02	3.84E-01
4.67E+03	2.50E-02	3.46E-01
5.07E+03	1.99E-02	3.11E-01
5.51E+03	1.58E-02	2.78E-01
5.99E+03	1.26E-02	2.48E-01
6.50E+03	1.00E-02	2.22E-01
7.07E+03	7.97E-03	1.97E-01
7.68E+03	6.34E-03	1.75E-01
8.34E+03	5.04E-03	1.55E-01
9.06E+03	4.01E-03	1.37E-01
9.84E+03	3.19E-03	1.21E-01
1.07E+04	2.54E-03	1.06E-01
1.16E+04	2.02E-03	9.35E-02
1.26E+04	1.60E-03	8.20E-02
1.37E+04	1.28E-03	7.18E-02
1.49E+04	1.01E-03	6.28E-02
1.62E+04	8.05E-04	5.47E-02
1.76E+04	6.40E-04	4.77E-02
1.91E+04	5.08E-04	4.14E-02
2.07E+04	4.03E-04	3.59E-02
2.25E+04	3.20E-04	3.10E-02
2.45E+04	2.53E-04	2.68E-02
2.66E+04	2.00E-04	2.30E-02
2.89E+04	1.58E-04	1.97E-02
3.14E+04	1.25E-04	1.68E-02
3.41E+04	9.83E-05	1.43E-02
3.70E+04	7.71E-05	1.21E-02
4.02E+04	6.03E-05	1.02E-02
4.37E+04	4.69E-05	8.51E-03
4.75E+04	3.62E-05	7.05E-03
5.16E+04	2.77E-05	5.77E-03
5.60E+04	2.10E-05	4.65E-03
6.08E+04	1.56E-05	3.68E-03
6.61E+04	1.13E-05	2.84E-03
7.18E+04	7.93E-06	2.10E-03

	Design SPE (2.55≥ L≥2.4)	GCR (2.55≥L≥2.4)
Energy (MeV)	Integral Flux (p+/cm^2-s-MeV)	Integral Flux (p+/cm^2-s-MeV)
7.80E+04	5.22E-06	1.46E-03
8.47E+04	3.07E-06	9.03E-04

Table 3.2.13-4. Flux of > 10 MeV Neutrons at Altitudes to 20 km

Altitude (km)	Integral Flux (#/cm^2-s)
0.02	6.85E-03
0.05	7.05E-03
0.10	7.38E-03
0.30	8.87E-03
0.50	1.06E-02
1.00	1.64E-02
2.00	3.67E-02
3.00	7.62E-02
4.00	1.47E-01
5.00	2.66E-01
6.00	4.53E-01
7.00	7.28E-01
9.00	1.62E+00
10.00	2.27E+00
12.00	3.94E+00
15.00	6.95E+00
17.00	8.96E+00
18.00	9.91E+00
19.00	1.08E+01
20.00	1.15E+01

3.3 In-Space Phases

Within this section the ionizing radiation environments that lead to Total Dose and Single Event Effect are defined. Within each of these subsections the definition is split into all the phases of the Design Reference Missions (DRMs), as defined in Exploration Systems Development (ESD) Concept of Operations (ESD 10012). As each DRM preliminary design is started, the MSFC Natural Environments Branch/EV44, through the NEIAHT, will generate a memo that details the Ionizing Radiation and Plasma environments for that specific DRM. The memo will use the data provided here and delineate the environments for each DRM mission segment (launch/ascent, staging & injections, mission transit and operations, and return and reentry). Those programs, elements, systems, subsystems and components that will operate during one or more of the DRM mission segments will be responsible for meeting their requirements during and after exposure to the environments as defined in the generated memo.

3.3.1 Total Dose

This section specifies cumulative Total Dose environments. Total Dose consists of two components, Total Ionizing Dose (TID) and Displacement Damage Dose (DDD). To calculate these, the ionizing radiation environments must be defined. TID is determined by transporting these environments through equivalent aluminum thicknesses and determining the deposited energy or dose. TID is given in Systems International derived units of centiGrays [cGy (Si)] for parts and materials exposed to DRM phases at altitudes greater than 150 km. One cGy (Si) equals one rad (silicon). For all regions of space and staging orbits, the TID is calculated using the Space Environment Information System (SPENVIS) version of Shieldose2, which calculates the dose at the center of an aluminum sphere. This does represent a conservative estimate of the TID but a more realistic TID can be calculated by performing three dimensional radiation transport calculations through the structure of the system under consideration.

DDD is determined by transporting the environment fluences and coupling with a damage function to determine the DDD. Since this damage function is material dependent, only the environment fluences are given. Methods for determining the DDD and the material damage functions for Silicon and Gallium Arsenide can be found in Srour, et al., 2003, Johnston, et al., 2013 and Messenger, et al., 2001.

Table 3.3.1-1 gives the applicability matrix for each of the DRMs (down the right-hand column) for each of the regions of space defined in this document (across the top of the Table) for Total Dose Effects. An "X" is placed in each box where the region of space is applicable to that DRM. For the "Staging and Transit Orbits" column, subsections of 3.3.1.2 are called out as applicable, since not all may be applicable for each DRM. A pseudo region of space is added in Section 3.3.1.10 Solar Particle Events (SPE). Since the number of SPE is a function of total mission time, placing SPE events in each region of space section would place multiple events in a DRM when only one may be appropriate. Therefore, the SPE environment, for both geomagnetic shielded and unshielded, is placed in its own subsection and the appropriate number of events will be incorporated into the DRM memo.

All sections and subsections under Total Dose will give the environments as per day environments. To determine the total dose environments for a specific DRM, the environments for all application sections and subsections must be multiplied by the appropriate number of days spent in that environment, then the appropriate number of SPE accounted for, and then all of these summed for the final dose.

Note: Tables may contain abbreviated data as compared to the plotted data. Complete data sets are available in electronic form.

Table 3.3.1-1. Total Dose Applicability Matrix for the Design Reference Mission by Regions of Space

	LEO (3.3.1.1)	Staging and Transit Orbits (3.3.1.2)	GEO (3.3.1.3)	Interplanetary (3.3.1.4)	Lunar Orbit (3.3.1.5)	Lunar Surface (3.3.1.6)	NEA (3.3.1.7)	Mars Orb it (3.3.1.8)	Mars Surface (3.3.1.9)	Solar Particle Event (3.3.1.10)
Distant Retrograde Orbit	X	3.3.1.2.1 3.3.1.2.2		X						X
Crewed Lunar Orbit	X	3.3.1.2.1 3.3.1.2.2		X	X					X
Low Lunar Orbit	X	3.3.1.2.6 3.3.1.2.2		X	X					X
Initial Capability NEA	X	3.3.1.2.4 3.3.1.2.5 3.3.1.2.2		X						X
Advanced NEA	X	3.3.1.2.4 3.3.1.2.5 3.3.1.2.2		X						X
Full Capability NEA	X	3.3.1.2.6 3.3.1.2.7 3.3.1.2.8 3.3.1.2.5 3.3.1.2.2		X						X
Lunar Surface Sortie	X	3.3.1.2.6 3.3.1.2.2		X	X	X				X
ISS Crew Delivery Backup	X	None								X
GEO Vicinity	X	3.3.1.2.6 3.3.1.2.2	X							X
Martian Moon	X	Reserved		X				X		X
Martian Landing	X	Reserved		X				X	X	X

3.3.1.1 Low Earth Orbit (LEO)-International Space Station (ISS) Orbit

Design Limits

Total dose contributions for ISS missions (conducted within Earth's magnetosphere) primarily originate from the Earth's trapped radiation environments. It is assumed that a single Solar Particle Event (SPE) will occur during the mission and it will add to the total dose.

The following Tables and graphs provide the ionizing radiation environment data, external to the spacecraft, that can be used as input for 3-dimensional shielding calculations of total ionizing dose or for the calculation of displacement damage dose: Figure 3.3.1.1-1 and Table 3.3.1.1-1 specify the daily trapped proton, integral and differential, spectra as a function of energy. Figure 3.3.1.1-2 and Table 3.3.1.1-2 specify the daily trapped electron, integral and differential, spectra as a function of energy. Figure 3.3.1.1-3 and Table 3.3.1.1-3 specify the total SPE proton integral and differential spectra as a function of energy.

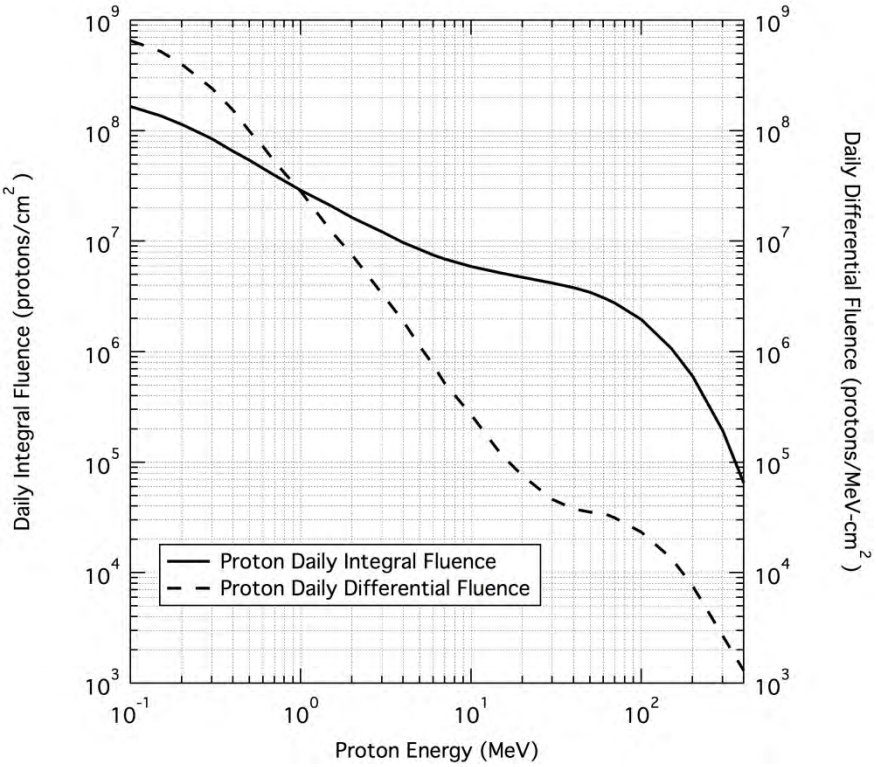

Figure 3.3.1.1-1. Daily Trapped Proton Fluences

Table 3.3.1.1-1. Daily Trapped Proton Fluences

Proton Energy	Daily Integral Trapped Proton Fluence	Daily Differential Trapped Proton Fluence
MeV	protons/cm^2	protons/MeV-cm^2
1.00E-01	1.66E+08	6.56E+08
5.00E-01	5.40E+07	9.89E+07
7.00E-01	3.96E+07	5.27E+07
1.00E+00	2.89E+07	2.83E+07
2.00E+00	1.64E+07	7.55E+06
3.00E+00	1.22E+07	3.34E+06

Proton Energy	Daily Integral Trapped Proton Fluence	Daily Differential Trapped Proton Fluence
MeV	protons/cm^2	protons/MeV-cm^2
4.00E+00	9.76E+06	1.90E+06
5.00E+00	8.44E+06	1.13E+06
6.00E+00	7.50E+06	7.56E+05
7.00E+00	6.92E+06	5.17E+05
1.00E+01	5.90E+06	2.69E+05
2.00E+01	4.72E+06	7.56E+04
3.00E+01	4.20E+06	4.62E+04
4.00E+01	3.79E+06	3.78E+04
5.00E+01	3.44E+06	3.54E+04
6.00E+01	3.08E+06	3.45E+04
7.00E+01	2.75E+06	3.15E+04
1.00E+02	1.95E+06	2.33E+04
1.50E+02	1.07E+06	1.35E+04
2.00E+02	6.04E+05	7.60E+03
3.00E+02	1.94E+05	2.70E+03
4.00E+02	6.46E+04	0.00E+00

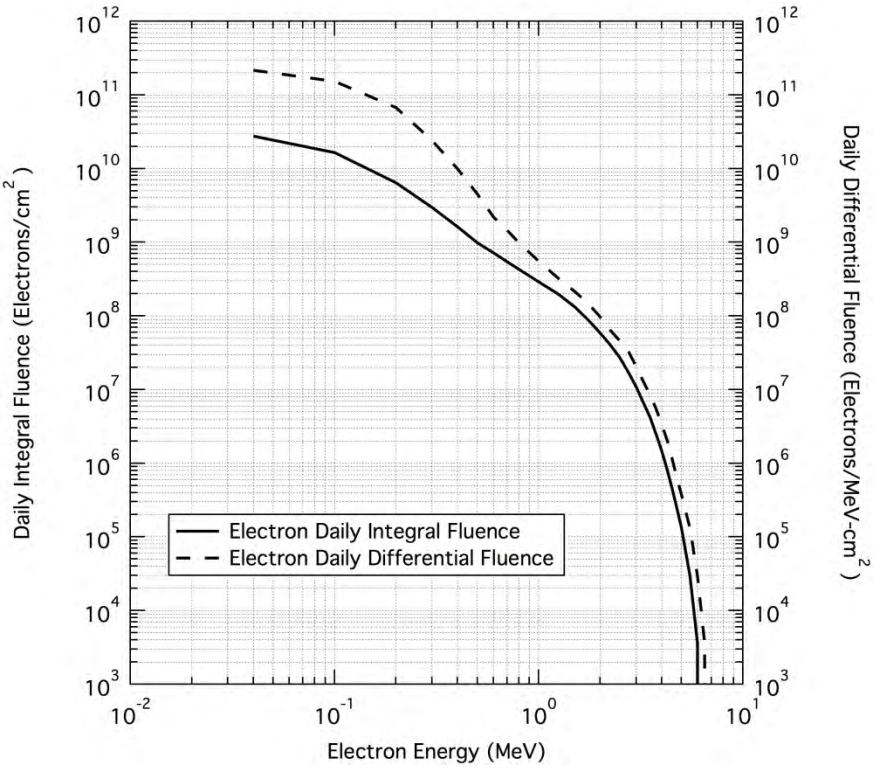

Figure 3.3.1.1-2. Daily Trapped Electron Fluences

Table 3.3.1.1-2. Daily Trapped Electron Fluences

Electron Energy	Daily Integral Trapped Electron Fluence	Daily Differential Trapped Electron Fluence
MeV	electrons/cm^2	electrons/MeV-cm^2
4.00E-02	2.74E+10	2.15E+11
1.00E-01	1.64E+10	1.52E+11
2.00E-01	6.44E+09	6.72E+10
3.00E-01	2.96E+09	2.41E+10
4.00E-01	1.62E+09	9.91E+09
5.00E-01	9.81E+08	4.51E+09
6.00E-01	7.21E+08	2.19E+09
7.00E-01	5.43E+08	1.45E+09
8.00E-01	4.30E+08	9.86E+08
1.00E+00	2.91E+08	5.54E+08
1.25E+00	1.96E+08	3.19E+08
1.50E+00	1.32E+08	2.15E+08

Electron Energy	Daily Integral Trapped Electron Fluence	Daily Differential Trapped Electron Fluence
MeV	electrons/cm^2	electrons/MeV-cm^2
1.75E+00	8.80E+07	1.46E+08
2.00E+00	5.88E+07	9.63E+07
2.25E+00	3.99E+07	6.35E+07
2.50E+00	2.71E+07	4.58E+07
2.75E+00	1.70E+07	3.27E+07
3.00E+00	1.08E+07	2.05E+07
3.25E+00	6.74E+06	1.31E+07
3.50E+00	4.25E+06	8.48E+06
3.75E+00	2.50E+06	5.53E+06
4.00E+00	1.48E+06	3.36E+06
4.25E+00	8.23E+05	2.06E+06
4.50E+00	4.57E+05	1.15E+06
4.75E+00	2.49E+05	6.44E+05
5.00E+00	1.35E+05	3.75E+05
5.50E+00	2.95E+04	1.31E+05
6.00E+00	3.60E+03	2.95E+04
6.50E+00	0.00E+00	3.60E+03
7.00E+00	0.00E+00	0.00E+00

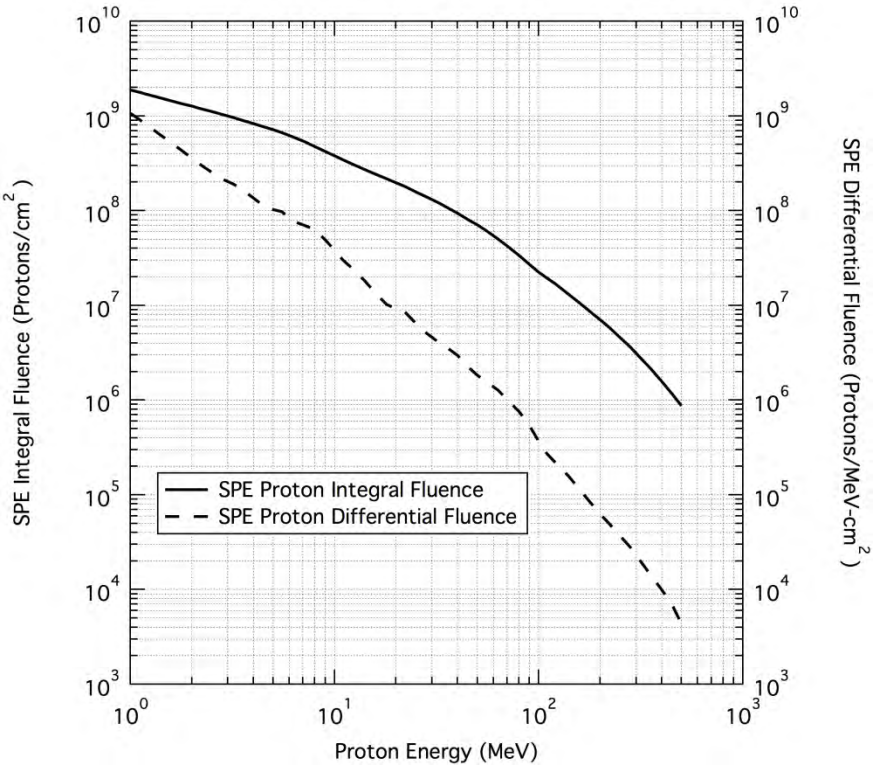

Figure 3.3.1.1-3. Proton Fluences of an ISS SPE

Table 3.3.1.1-3. Proton Fluences of an ISS SPE

Proton Energy	ISS SPE Integral Fluence per event	ISS SPE Differential Fluence per event
MeV	protons/cm^2	protons/MeV-cm^2
1.00E-01	7.11E+09	4.02E+10
2.50E-01	4.18E+09	9.63E+09
5.00E-01	2.80E+09	3.21E+09
1.00E+00	1.88E+09	1.07E+09
2.00E+00	1.27E+09	3.58E+08
3.50E+00	9.09E+08	1.70E+08
5.00E+00	7.16E+08	1.03E+08
7.10E+00	5.37E+08	7.00E+07
8.00E+00	4.77E+08	6.29E+07
9.00E+00	4.21E+08	4.89E+07
1.00E+01	3.78E+08	3.80E+07
1.60E+01	2.41E+08	1.32E+07

Proton Energy	ISS SPE Integral Fluence per event	ISS SPE Differential Fluence per event
MeV	protons/cm^2	protons/MeV-cm^2
1.80E+01	2.18E+08	1.02E+07
2.00E+01	1.98E+08	9.23E+06
2.50E+01	1.58E+08	6.46E+06
3.50E+01	1.10E+08	3.67E+06
4.00E+01	9.38E+07	2.98E+06
4.50E+01	8.07E+07	2.26E+06
5.00E+01	7.05E+07	1.82E+06
7.10E+01	4.15E+07	9.89E+05
8.00E+01	3.36E+07	7.61E+05
9.00E+01	2.71E+07	5.42E+05
1.00E+02	2.25E+07	3.70E+05
1.60E+02	1.04E+07	1.11E+05
1.80E+02	8.48E+06	8.19E+04
2.00E+02	7.04E+06	6.26E+04
2.50E+02	4.61E+06	3.70E+04
4.00E+02	1.58E+06	9.92E+03
5.00E+02	8.74E+05	4.36E+03

Figure 3.3.1.1-4 and Table 3.3.1.1-4 specify the daily TID inside selected thicknesses of spherical aluminum (Al) shielding from the trapped radiation belt protons and electrons. Figure 3.3.1.1-5 and Table 3.3.1.1-5 specify total TID associated with the worst–case as defined in the Emission of Solar Protons (ESP)/ Prediction of Solar particle Yields for Characterizing Integrated Circuits (PSYCHIC) model.

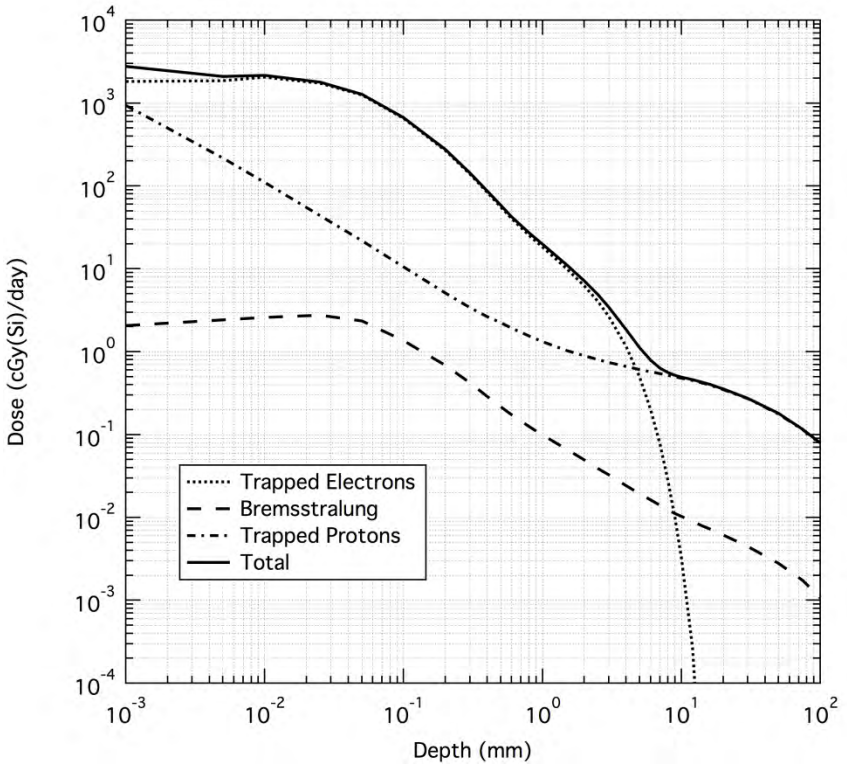

Figure 3.3.1.1-4. Daily Trapped Belts TID Inside Shielding

Table 3.3.1.1-4. Daily Trapped Belts TID Inside Shielding

Aluminum Shield Depth	Trapped Electron Daily TID	Bremsstrahlung Daily TID	Trapped Proton Daily TID	Total Daily TID
mm	cGy(Si)/day	cGy(Si)/day	cGy(Si)/day	cGy(Si)/day
1.00E-03	1.82E+03	2.07E+00	9.42E+02	2.76E+03
5.00E-03	1.87E+03	2.43E+00	2.17E+02	2.09E+03
1.00E-02	2.05E+03	2.61E+00	1.10E+02	2.16E+03
2.50E-02	1.74E+03	2.76E+00	4.38E+01	1.79E+03
5.00E-02	1.25E+03	2.36E+00	2.18E+01	1.28E+03
1.00E-01	6.55E+02	1.36E+00	1.06E+01	6.67E+02
2.00E-01	2.69E+02	6.83E-01	5.12E+00	2.75E+02

Aluminum Shield Depth	Trapped Electron Daily TID	Bremsstrahlung Daily TID	Trapped Proton Daily TID	Total Daily TID
mm	cGy(Si)/day	cGy(Si)/day	cGy(Si)/day	cGy(Si)/day
3.00E-01	1.39E+02	4.19E-01	3.41E+00	1.43E+02
4.00E-01	8.37E+01	2.89E-01	2.66E+00	8.67E+01
5.00E-01	5.58E+01	2.17E-01	2.23E+00	5.83E+01
6.00E-01	4.04E+01	1.74E-01	1.93E+00	4.25E+01
8.00E-01	2.54E+01	1.25E-01	1.55E+00	2.71E+01
1.00E+00	1.82E+01	9.90E-02	1.32E+00	1.97E+01
2.50E+00	4.06E+00	3.92E-02	8.03E-01	4.90E+00
5.00E+00	4.92E-01	1.93E-02	6.08E-01	1.12E+00
1.00E+01	3.18E-03	1.03E-02	4.81E-01	4.94E-01
1.20E+01	2.62E-04	8.92E-03	4.53E-01	4.62E-01
1.40E+01	6.83E-06	7.96E-03	4.21E-01	4.29E-01
1.60E+01	5.24E-08	7.24E-03	3.96E-01	4.03E-01
1.80E+01	5.69E-10	6.64E-03	3.71E-01	3.78E-01
2.00E+01	0.00E+00	6.14E-03	3.50E-01	3.56E-01
3.00E+01	0.00E+00	4.47E-03	2.71E-01	2.75E-01
5.00E+01	0.00E+00	2.81E-03	1.78E-01	1.81E-01
7.50E+01	0.00E+00	1.73E-03	1.14E-01	1.16E-01
1.00E+02	0.00E+00	1.07E-03	7.79E-02	7.89E-02

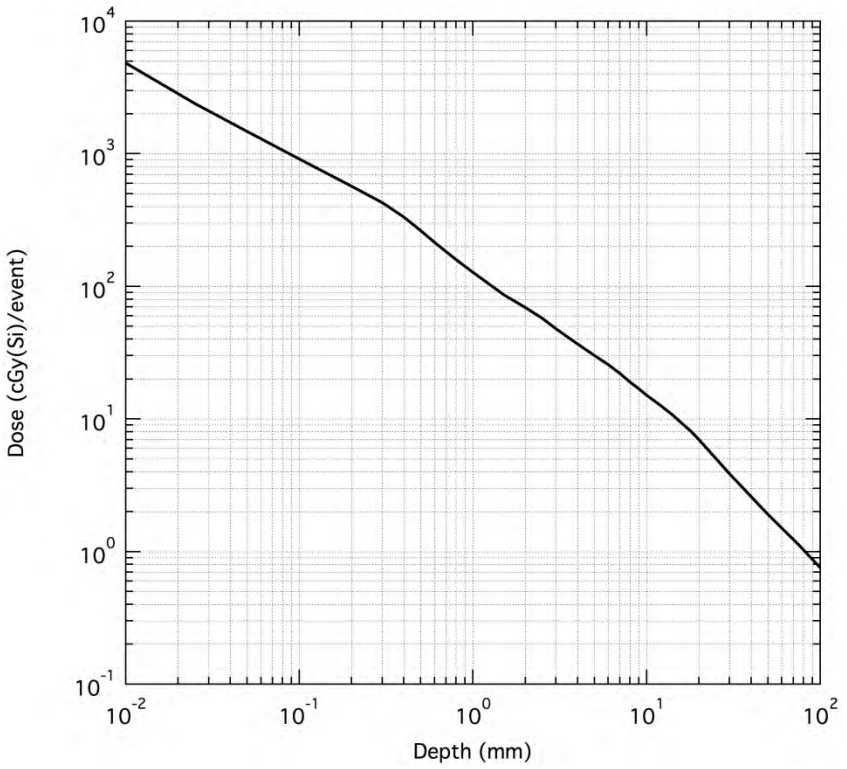

Figure 3.3.1.1-5. Total SPE TID Inside Shielding

Table 3.3.1.1-5. Total SPE TID Inside Shielding

Aluminum Shield Depth	Total ISS SPE TID
mm	cGy(Si)/event
1.00E-03	3.13E+04
5.00E-03	8.40E+03
1.00E-02	4.84E+03
2.50E-02	2.40E+03
5.00E-02	1.47E+03
1.00E-01	9.13E+02
2.00E-01	5.71E+02
3.00E-01	4.28E+02
4.00E-01	3.33E+02
5.00E-01	2.64E+02
6.00E-01	2.15E+02
8.00E-01	1.59E+02
1.00E+00	1.27E+02

Aluminum Shield Depth	Total ISS SPE TID
2.50E+00	5.75E+01
5.00E+00	3.01E+01
1.00E+01	1.51E+01
1.20E+01	1.27E+01
1.40E+01	1.08E+01
1.60E+01	9.26E+00
1.80E+01	8.07E+00
2.00E+01	7.00E+00
3.00E+01	3.86E+00
5.00E+01	1.91E+00
7.50E+01	1.13E+00
1.00E+02	7.53E-01

The final TID specification can either be derived by generating a dose versus depth curve by 3-dimensional shielding transport calculations, using the external environments presented at the beginning of this section, or by using the data given in Figure and Table 3.3.1.1-4. To calculate the final TID specification level for the ISS mission (when no 3-dimensional shielding calculations are done), multiply the daily Total TID in Table 3.3.1.1-4 by the number of days in the mission and add that number to the total SPE TID in Table 3.3.1.1-5. When performing the 3-D shielding calculations, the external trapped ionizing radiation environments (given as daily fluences in the above Tables) are multiplied by the number of mission days. Those trapped electron and proton mission fluences and the SPE proton fluence are then used as inputs to code that will perform the 3-D transport calculations. The output of this code will be the TID specification.

Model Inputs

None.

Limitations

None.

Technical Notes

All environment models were run for the assumed ISS orbit of 500 km circular orbit at 51.6° inclination. The trapped electron environment was defined using the AE8MAX model, as it represents the worst-case electron environment. The mean (50%) model is then scaled by a factor of two to account for the model uncertainty. The trapped proton environment was defined using the AP8MIN model, as it represents the worst-case proton environment. The model is then scaled

by a factor of two to account for the model uncertainty. The SPE TID specification was defined by using the ESP/PSYCHIC model for a one year period during solar maximum conditions with a stormy magnetosphere and a 95% probability of the fluences not being exceeded. The TID shielding calculations were performed using the SPENVIS Shieldose2 code, solid Aluminum sphere option.

3.3.1.2 Staging and Transit Orbits

3.3.1.2.1 LEO 185 x 1806 km

Design Limits

Total dose contributions for this staging orbit primarily originate from the Earth's trapped radiation environments. Since this orbit is part of larger DRM, no SPE environment is needed specific to this orbit except for any segment whose mission ends with this orbit. For those segments only, the ESP/PSYCHIC model was used and it was determined that no solar particles penetrate the Earth's magnetic field in this orbit. Therefore, even for segments that end in this orbit, no SPE will be observed.

The following Tables and graphs provide the ionizing radiation environment data, external to the spacecraft, that can be used as input for 3-dimensional shielding calculations of total ionizing dose or for the calculation of displacement damage dose: Figure 3.3.1.2.1-1 and Table 3.3.1.2.1-1 specify the daily trapped proton, integral and differential, spectra as a function of energy. Figure 3.3.1.2.1-2 and Table 3.3.1.2.1-2 specify the daily trapped electron, integral and differential, spectra as a function of energy.

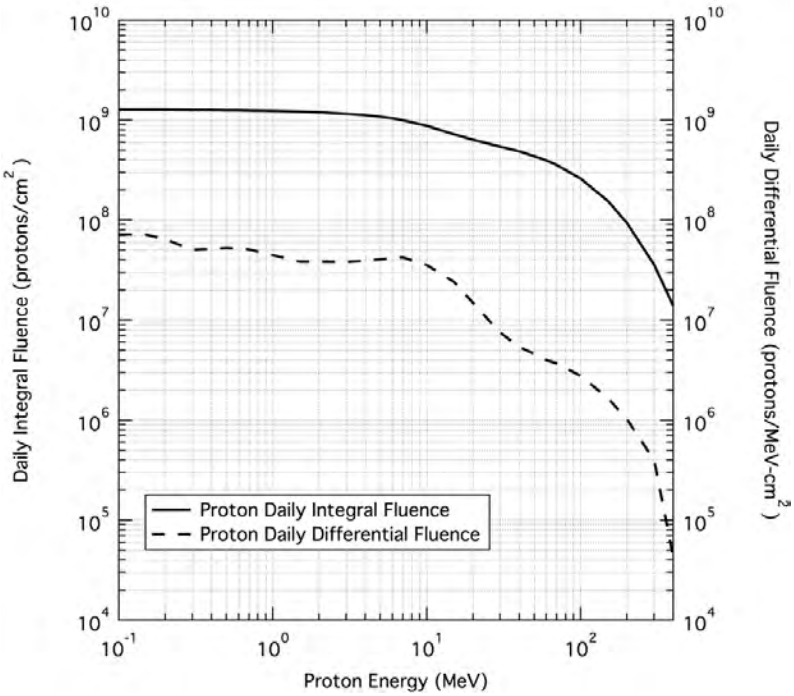

Figure 3.3.1.2.1-1. Daily Trapped Proton Fluences

Table 3.3.1.2.1-1. Daily Trapped Proton Fluences

Proton Energy	Daily Integral Trapped Proton Fluence	Daily Differential Trapped Proton Fluence
MeV	protons/cm^2	protons/MeV-cm^2
1.00E-01	1.28E+09	7.22E+07
5.00E-01	1.26E+09	5.26E+07
7.00E-01	1.25E+09	5.08E+07
1.00E+00	1.24E+09	4.48E+07
2.00E+00	1.20E+09	3.86E+07
3.00E+00	1.16E+09	3.82E+07
4.00E+00	1.12E+09	3.96E+07
5.00E+00	1.08E+09	4.08E+07
6.00E+00	1.04E+09	4.18E+07
7.00E+00	9.96E+08	4.25E+07
1.00E+01	8.81E+08	3.56E+07
2.00E+01	6.37E+08	1.49E+07
3.00E+01	5.44E+08	7.52E+06
4.00E+01	4.87E+08	5.40E+06
5.00E+01	4.36E+08	4.61E+06
6.00E+01	3.95E+08	4.00E+06
7.00E+01	3.56E+08	3.71E+06
1.00E+02	2.61E+08	2.78E+06
1.50E+02	1.56E+08	1.67E+06
2.00E+02	9.35E+07	1.02E+06
3.00E+02	3.59E+07	3.98E+05
4.00E+02	1.39E+07	4.27E+04

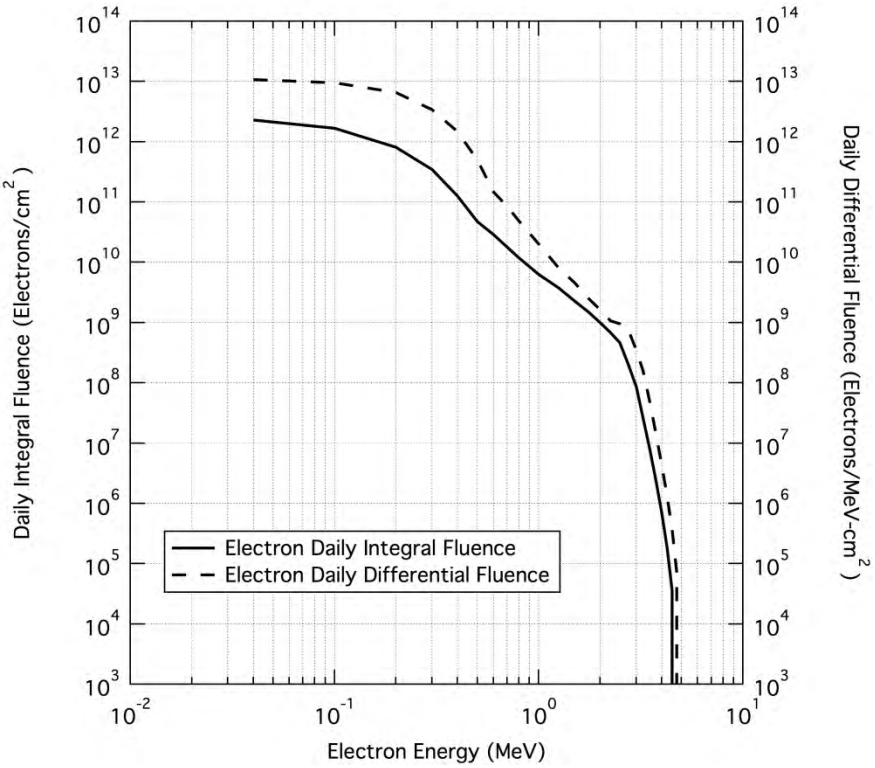

Figure 3.3.1.2.1-2. Daily Trapped Electron Fluences

Table 3.3.1.2.1-2. Daily Trapped Electron Fluences

Electron Energy	Daily Integral Trapped Electron Fluence	Daily Differential Trapped Electron Fluence
MeV	electrons/cm^2	electrons/MeV-cm^2
4.00E-02	2.28E+12	1.07E+13
1.00E-01	1.67E+12	9.55E+12
2.00E-01	8.13E+11	6.62E+12
3.00E-01	3.46E+11	3.43E+12
4.00E-01	1.27E+11	1.49E+12
5.00E-01	4.71E+10	4.93E+11
6.00E-01	2.88E+10	1.47E+11
7.00E-01	1.78E+10	8.44E+10
8.00E-01	1.19E+10	4.83E+10
1.00E+00	6.32E+09	2.01E+10
1.25E+00	3.77E+09	8.13E+09
1.50E+00	2.26E+09	4.55E+09

Electron Energy	Daily Integral Trapped Electron Fluence	Daily Differential Trapped Electron Fluence
MeV	electrons/cm^2	electrons/MeV-cm^2
1.75E+00	1.50E+09	2.52E+09
2.00E+00	9.97E+08	1.64E+09
2.25E+00	6.78E+08	1.07E+09
2.50E+00	4.62E+08	9.59E+08
2.75E+00	1.99E+08	7.51E+08
3.00E+00	8.67E+07	3.46E+08
3.25E+00	2.60E+07	1.58E+08
3.50E+00	7.80E+06	4.73E+07
3.75E+00	2.35E+06	1.42E+07
4.00E+00	7.03E+05	4.32E+06
4.25E+00	1.87E+05	1.33E+06
4.50E+00	3.58E+04	3.74E+05
4.75E+00	0.00E+00	7.16E+04
5.00E+00	0.00E+00	0.00E+00

Figure 3.3.1.2.1-3 and Table 3.3.1.2.1-3 specify the daily TID inside selected thicknesses of spherical aluminum (Al) shielding from the trapped radiation belt protons and electrons. Since no solar protons penetrate the Earth's magnetic field for this orbit, no TID from solar protons is generated.

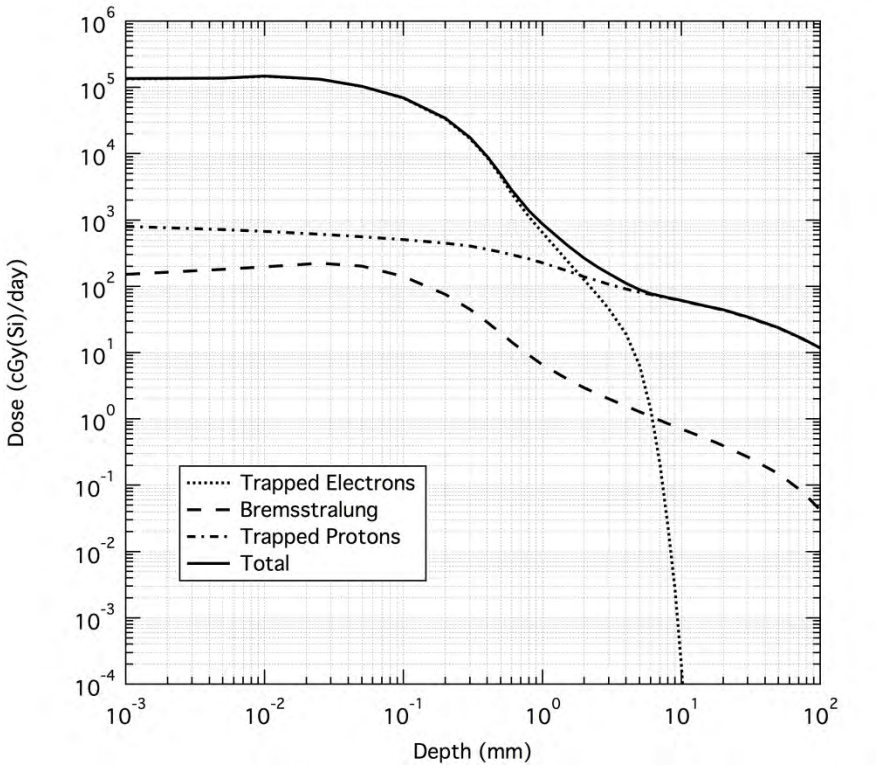

Figure 3.3.1.2.1-3. Daily Trapped Belts TID Inside Shielding

Table 3.3.1.2.1-3. Daily Trapped Belts TID Inside Shielding

Aluminum Shield Depth	Trapped Electron Daily TID	Bremsstrahlung Daily TID	Trapped Proton Daily TID	Total Daily TID
mm	cGy(Si)/day	cGy(Si)/day	cGy(Si)/day	cGy(Si)/day
1.00E-03	1.35E+05	1.53E+02	8.07E+02	1.36E+05
5.00E-03	1.38E+05	1.81E+02	7.23E+02	1.39E+05
1.00E-02	1.48E+05	1.98E+02	6.75E+02	1.49E+05
2.50E-02	1.33E+05	2.24E+02	6.09E+02	1.34E+05
5.00E-02	1.04E+05	2.02E+02	5.62E+02	1.04E+05
1.00E-01	6.90E+04	1.42E+02	5.11E+02	6.97E+04
2.00E-01	3.36E+04	7.60E+01	4.50E+02	3.42E+04
3.00E-01	1.70E+04	4.51E+01	4.05E+02	1.75E+04
4.00E-01	8.72E+03	2.88E+01	3.64E+02	9.12E+03
5.00E-01	4.56E+03	1.98E+01	3.30E+02	4.91E+03
6.00E-01	2.54E+03	1.45E+01	3.02E+02	2.85E+03
8.00E-01	1.11E+03	9.12E+00	2.59E+02	1.37E+03

Aluminum Shield Depth	Trapped Electron Daily TID	Bremsstrahlung Daily TID	Trapped Proton Daily TID	Total Daily TID
mm	cGy(Si)/day	cGy(Si)/day	cGy(Si)/day	cGy(Si)/day
1.00E+00	6.40E+02	6.59E+00	2.27E+02	8.73E+02
2.50E+00	7.29E+01	2.39E+00	1.21E+02	1.96E+02
5.00E+00	6.39E+00	1.29E+00	8.18E+01	8.95E+01
1.00E+01	1.81E-04	7.10E-01	6.06E+01	6.13E+01
1.20E+01	2.62E-07	6.12E-01	5.59E+01	5.66E+01
1.40E+01	0.00E+00	5.39E-01	5.19E+01	5.25E+01
1.60E+01	0.00E+00	4.82E-01	4.89E+01	4.93E+01
1.80E+01	0.00E+00	4.35E-01	4.64E+01	4.68E+01
2.00E+01	0.00E+00	3.95E-01	4.39E+01	4.43E+01
3.00E+01	0.00E+00	2.69E-01	3.44E+01	3.47E+01
5.00E+01	0.00E+00	1.50E-01	2.37E+01	2.39E+01
7.50E+01	0.00E+00	7.97E-02	1.61E+01	1.62E+01
1.00E+02	0.00E+00	4.23E-02	1.17E+01	1.18E+01

The final TID specification can either be derived by generating a dose versus depth curve by 3-dimensional shielding transport calculations, using the external environments presented at the beginning of this section, or by using the data given in Figure and Table 3.3.1.2.1-3. To calculate the final TID specification level for this segment (when no 3-dimensional shielding calculations are done), multiply the daily Total TID in Table 3.3.1.2.1-3 by the number of days in the segment. When performing the 3-D shielding calculations, the external trapped ionizing radiation environments (given as daily fluences in the above Tables) are multiplied by the number of mission days. Those trapped electron and proton segment fluences are then used as inputs to code that will perform the 3-D transport calculations. The output of this code will be the TID specification.

Model Inputs

None.

Limitations

None.

Technical Notes

All environment models were run for the assumed an orbit of 185 km x 1860 km at a 28.5° inclination. The trapped electron environment was defined using the AE8MAX model, as it represents the worst-case electron environment. The mean (50%) model is then scaled by a factor of two to account for the model uncertainty. The trapped proton environment was defined using

the AP8MIN model, as it represents the worst-case proton environment. The model is then scaled by a factor of two to account for the model uncertainty. The SPE TID specification was defined by using the ESP/PSYCHIC model for a one year period during solar maximum conditions with a stormy magnetosphere and a 95% probability of the fluences not being exceeded. The TID shielding calculations were performed using the SPENVIS Shieldose2 code, solid Aluminum sphere option.

3.3.1.2.2 Radiation Belt Transit

Design Limits

Total dose contributions for this staging orbit primarily originate from the Earth's trapped radiation environments. Since this orbit is part of larger DRM, no SPE environment is needed specific to this orbit except for any segment whose mission ends with this orbit. For those segments only, it is assumed that a single Solar Particle Event (SPE) will occur during this stage and it will add to the total dose. That SPE environment is presented in Section 3.3.1.10.2 Geomagnetic Unshielded since this staging orbit ends outside the Earth's magnetic field.

The following Tables and graphs provide the ionizing radiation environment data, external to the spacecraft, that can be used as input for 3-dimensional shielding calculations of total ionizing dose or for the calculation of displacement damage dose: Figure 3.3.1.2.2-1 and Table 3.3.1.2.2-1 specify the trapped proton fluence, integral and differential, spectra as a function of energy. Figure 3.3.1.2.2-2 and Table 3.3.1.2.2-2 specify the trapped electron fluence, integral and differential, spectra as a function of energy.

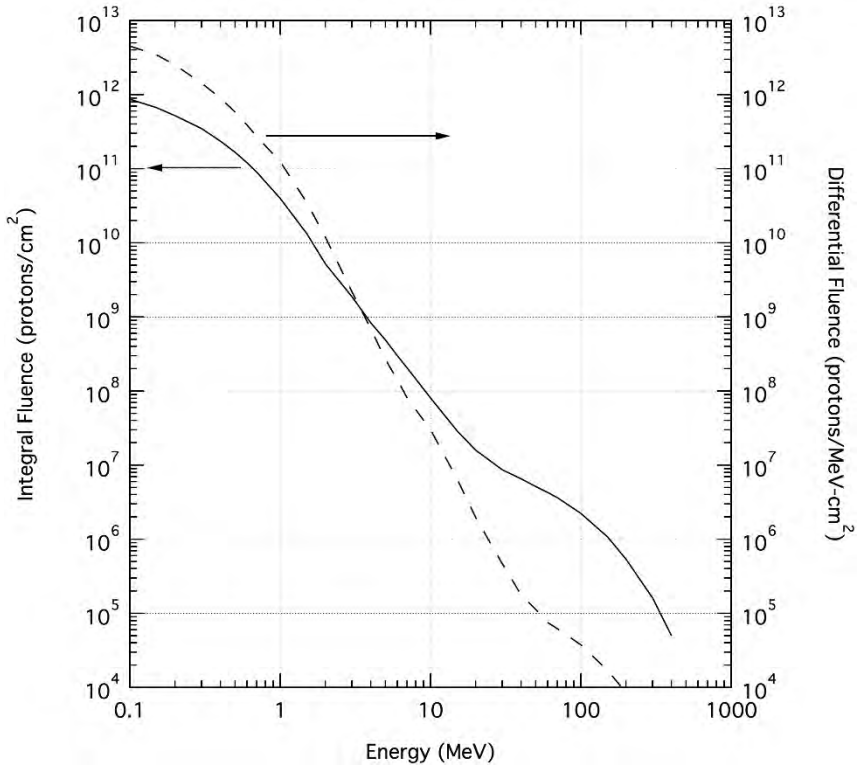

Figure 3.3.1.2.2-1. Trapped Proton Fluences

Table 3.3.1.2.2-1. Trapped Proton Fluences

Proton Energy	Integral Trapped Proton Fluence	Differential Trapped Proton Fluence
MeV	protons/cm^2	protons/MeV-cm^2
0.1	8.67E+11	4.51E+12
0.15	6.69E+11	3.45E+12
0.2	5.22E+11	2.53E+12
0.3	3.48E+11	1.43E+12
0.4	2.37E+11	9.01E+11
0.5	1.67E+11	5.81E+11
0.6	1.20E+11	3.88E+11
0.7	8.96E+10	2.72E+11
1	3.99E+10	1.24E+11
1.5	1.33E+10	3.47E+10
2	5.22E+09	1.19E+10
3	1.87E+09	2.19E+09
4	8.28E+08	6.93E+08

Proton Energy	Integral Trapped Proton Fluence	Differential Trapped Proton Fluence
MeV	protons/cm^2	protons/MeV-cm^2
5	4.86E+08	2.65E+08
6	2.98E+08	1.41E+08
7	2.05E+08	8.01E+07
10	8.07E+07	2.98E+07
15	2.89E+07	6.47E+06
20	1.60E+07	1.96E+06
30	8.70E+06	4.70E+05
40	6.57E+06	1.78E+05
50	5.13E+06	1.13E+05
60	4.30E+06	7.53E+04
70	3.63E+06	6.21E+04
100	2.23E+06	3.77E+04
150	1.08E+06	1.70E+04
200	5.36E+05	8.56E+03
300	1.61E+05	2.43E+03
400	5.01E+04	0.00E+00

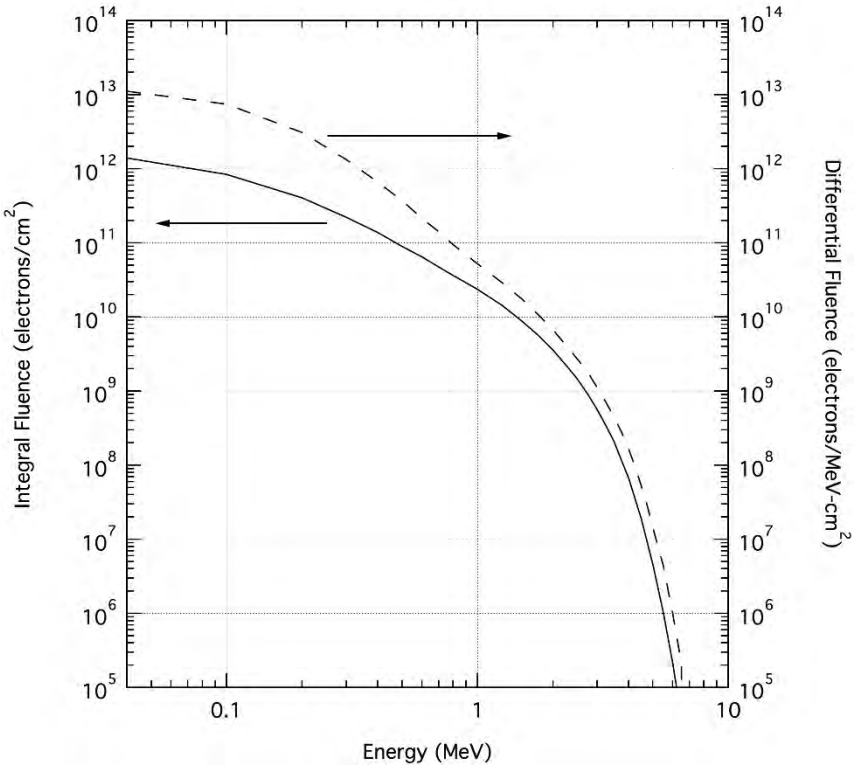

Figure 3.3.1.2.2-2. Trapped Electron Fluences

Table 3.3.1.2.2-2. Trapped Electron Fluences

Electron Energy	Integral Trapped Electron Fluence	Differential Trapped Electron Fluence
MeV	electrons/cm^2	electrons/MeV-cm^2
0.04	1.40E+12	1.12E+13
0.1	8.42E+11	7.49E+12
0.2	4.04E+11	3.10E+12
0.3	2.22E+11	1.32E+12
0.4	1.39E+11	6.62E+11
0.5	9.01E+10	3.73E+11
0.6	6.47E+10	2.14E+11
0.7	4.74E+10	1.42E+11
0.8	3.64E+10	9.45E+10
1	2.35E+10	5.20E+10
1.25	1.44E+10	2.92E+10
1.5	8.90E+09	1.75E+10
1.75	5.61E+09	1.07E+10

Electron Energy	Integral Trapped Electron Fluence	Differential Trapped Electron Fluence
MeV	electrons/cm^2	electrons/MeV-cm^2
2	3.55E+09	6.69E+09
2.25	2.27E+09	4.18E+09
2.5	1.46E+09	2.73E+09
2.75	9.03E+08	1.79E+09
3	5.61E+08	1.12E+09
3.25	3.42E+08	7.03E+08
3.5	2.09E+08	4.47E+08
3.75	1.18E+08	2.84E+08
4	6.72E+07	1.65E+08
4.25	3.56E+07	9.64E+07
4.5	1.90E+07	5.29E+07
4.75	9.16E+06	2.87E+07
5	4.65E+06	1.44E+07
5.5	1.03E+06	4.44E+06
6	2.14E+05	9.91E+05
6.5	3.86E+04	2.10E+05
7	4.29E+03	0.00E+00

Figure 3.3.1.2.2-3 and Table 3.3.1.2.2-3 specify the Translunar Injection (TLI) TID inside selected thicknesses of spherical aluminum (Al) shielding from the trapped radiation belt protons and electrons.

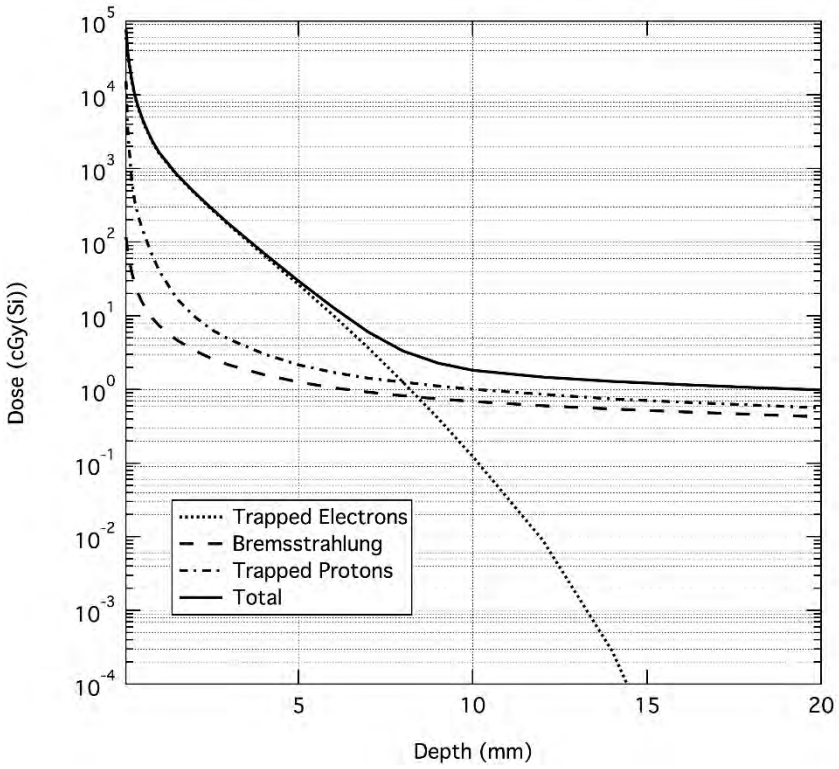

Figure 3.3.1.2.2-3. Trapped Belts TID inside Shielding

Table 3.3.1.2.2-3. Trapped Belts TID inside Shielding

Aluminum Shield Depth	Trapped Electron TID	Bremsstrahlung TID	Trapped Proton TID	Total TID
mm	cGy(Si)/TLI	cGy(Si)/TLI	cGy(Si)/TLI	cGy(Si)/TLI
0.05	6.14E+04	1.18E+02	1.55E+04	7.70E+04
0.1	3.39E+04	7.25E+01	3.26E+03	3.72E+04
0.2	1.64E+04	4.08E+01	7.65E+02	1.72E+04
0.3	9.80E+03	2.74E+01	3.62E+02	1.02E+04
0.4	6.62E+03	2.01E+01	2.26E+02	6.87E+03
0.5	4.78E+03	1.57E+01	1.59E+02	4.96E+03
0.6	3.62E+03	1.29E+01	1.16E+02	3.75E+03
0.8	2.31E+03	9.39E+00	6.69E+01	2.38E+03
1	1.61E+03	7.38E+00	4.16E+01	1.66E+03
1.5	8.18E+02	4.74E+00	1.74E+01	8.40E+02
2	4.69E+02	3.42E+00	9.89E+00	4.82E+02
2.5	2.80E+02	2.65E+00	6.58E+00	2.89E+02
3	1.71E+02	2.16E+00	4.83E+00	1.78E+02

Aluminum Shield Depth	Trapped Electron TID	Bremsstrahlung TID	Trapped Proton TID	Total TID
mm	cGy(Si)/TLI	cGy(Si)/TLI	cGy(Si)/TLI	cGy(Si)/TLI
4	6.70E+01	1.59E+00	3.06E+00	7.16E+01
5	2.64E+01	1.26E+00	2.16E+00	2.98E+01
6	1.01E+01	1.06E+00	1.70E+00	1.29E+01
7	3.69E+00	9.24E-01	1.43E+00	6.04E+00
8	1.26E+00	8.23E-01	1.26E+00	3.34E+00
9	4.06E-01	7.48E-01	1.12E+00	2.28E+00
10	1.23E-01	6.90E-01	1.01E+00	1.83E+00
12	9.12E-03	6.04E-01	8.63E-01	1.48E+00
14	2.84E-04	5.44E-01	7.44E-01	1.29E+00
16	2.18E-06	4.98E-01	6.73E-01	1.17E+00
18	2.59E-08	4.59E-01	6.14E-01	1.07E+00
20	0.00E+00	4.26E-01	5.66E-01	9.92E-01

The final TID specification can either be derived by generating a dose versus depth curve by 3-dimensional shielding transport calculations, using the external environments presented at the beginning of this section, or by using the data given in Figure 3.3.1.2.2-3 and Table 3.3.1.2.2-3.

Model Inputs

None.

Limitations

None.

Technical Notes

All environment models were run for the assumed a trajectory from the SLS Design Analysis Cycle (DAC-2) for the Distant Retrograde Orbit Design Reference Mission. Only the first 6 hours of the trajectory are used as this places the spacecraft in excess of 60,000 km, which is beyond the trapped radiation belts. Additionally, the first 90 minutes of the trajectory are also removed. This removes the Low Earth Orbit section so only the radiation belt transit is considered in these calculations. The trapped electron environment was defined using the AE8MAX model, as it represents the worst-case electron environment. The mean (50%) model is then scaled by a factor of two to account for the model uncertainty. The trapped proton environment was defined using the AP8MIN model, as it represents the worst-case proton environment. The model is then scaled by a factor of two to account for the model uncertainty. TID shielding calculations were performed using the SPENVIS version of Shieldose2 code, solid Aluminum sphere option.

3.3.1.2.3 LEO 241 km Circular

Design Limits

Total dose contributions for this staging orbit primarily originate from the Earth's trapped radiation environments. Since this orbit is part of larger DRM, no SPE environment is needed specific to this orbit except for any segment whose mission ends with this orbit. For those segments only, the ESP/PSYCHIC model was used and it was determined that no solar particles penetrate the Earth's magnetic field in this orbit. Therefore, even for segments that end in this orbit, no SPE will be observed.

The following Tables and graphs provide the ionizing radiation environment data, external to the spacecraft, that can be used as input for 3-dimensional shielding calculations of total ionizing dose or for the calculation of displacement damage dose: Figure 3.3.1.2.3-1 and Table 3.3.1.2.3-1 specify the daily trapped proton, integral and differential, spectra as a function of energy. Figure 3.3.1.2.3-2 and Table 3.3.1.2.3-2 specify the daily trapped electron, integral and differential, spectra as a function of energy.

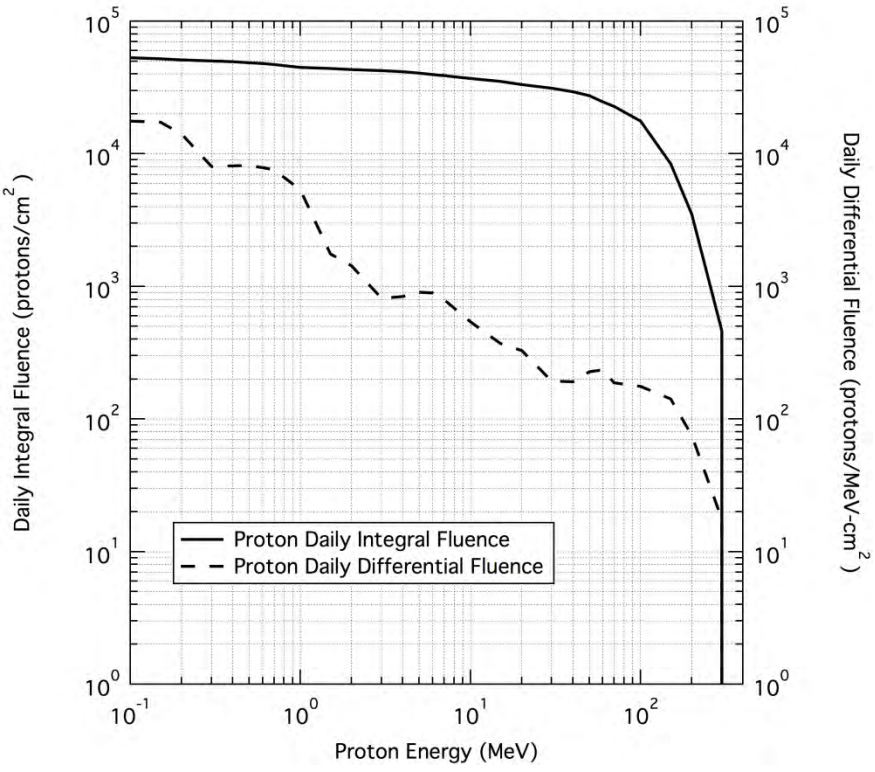

Figure 3.3.1.2.3-1. Daily Trapped Proton Fluences

Table 3.3.1.2.3-1. Daily Trapped Proton Fluences

Proton Energy	Daily Integral Trapped Proton Fluence	Daily Differential Trapped Proton Fluence
MeV	protons/cm^2	protons/MeV-cm^2
1.00E-01	5.29E+04	1.76E+04
5.00E-01	4.87E+04	8.16E+03
7.00E-01	4.71E+04	7.60E+03
1.00E+00	4.49E+04	5.34E+03
2.00E+00	4.31E+04	1.43E+03
3.00E+00	4.23E+04	8.15E+02
4.00E+00	4.15E+04	8.40E+02
5.00E+00	4.06E+04	9.06E+02
6.00E+00	3.97E+04	8.91E+02
7.00E+00	3.89E+04	7.96E+02
1.00E+01	3.69E+04	5.39E+02
2.00E+01	3.32E+04	3.28E+02
3.00E+01	3.13E+04	1.93E+02
4.00E+01	2.93E+04	1.91E+02
5.00E+01	2.75E+04	2.28E+02
6.00E+01	2.47E+04	2.34E+02
7.00E+01	2.28E+04	1.88E+02
1.00E+02	1.77E+04	1.76E+02
1.50E+02	8.40E+03	1.42E+02
2.00E+02	3.51E+03	7.53E+01
3.00E+02	4.62E+02	1.76E+01
4.00E+02	0.00E+00	0.00E+00

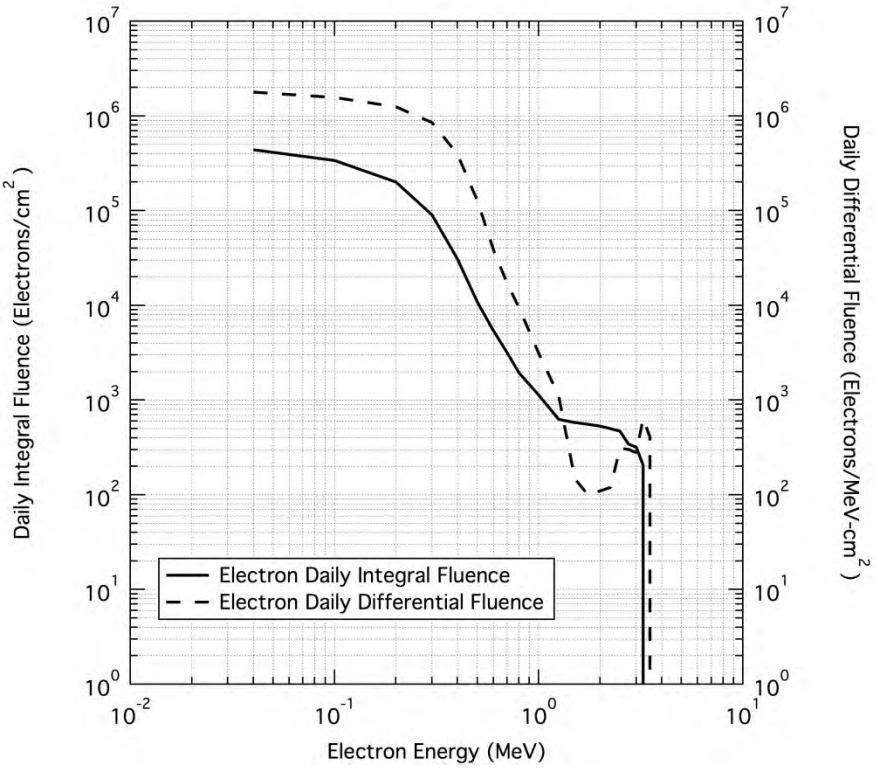

Figure 3.3.1.2.3-2. Daily Trapped Electron Fluences

Table 3.3.1.2.3-2. Daily Trapped Electron Fluences

Electron Energy	Daily Integral Trapped Electron Fluence	Daily Differential Trapped Electron Fluence
MeV	electrons/cm^2	electrons/MeV-cm^2
4.00E-02	4.41E+05	1.78E+06
1.00E-01	3.40E+05	1.57E+06
2.00E-01	2.01E+05	1.25E+06
3.00E-01	9.01E+04	8.53E+05
4.00E-01	3.08E+04	3.96E+05
5.00E-01	1.08E+04	1.27E+05
6.00E-01	5.36E+03	3.83E+04
7.00E-01	3.16E+03	1.71E+04
8.00E-01	1.94E+03	9.50E+03
1.00E+00	1.13E+03	3.14E+03
1.25E+00	6.28E+02	1.11E+03
1.50E+00	5.79E+02	1.48E+02

Electron Energy	Daily Integral Trapped Electron Fluence	Daily Differential Trapped Electron Fluence
MeV	electrons/cm^2	electrons/MeV-cm^2
1.75E+00	5.54E+02	9.94E+01
2.00E+00	5.29E+02	1.10E+02
2.25E+00	4.98E+02	1.20E+02
2.50E+00	4.69E+02	3.09E+02
2.75E+00	3.44E+02	3.01E+02
3.00E+00	3.19E+02	2.78E+02
3.25E+00	2.05E+02	6.38E+02
3.50E+00	0.00E+00	4.09E+02
3.75E+00	0.00E+00	0.00E+00
4.00E+00	0.00E+00	0.00E+00
4.25E+00	0.00E+00	0.00E+00
4.50E+00	0.00E+00	0.00E+00
4.75E+00	0.00E+00	0.00E+00
5.00E+00	0.00E+00	0.00E+00

Figure 3.3.1.2.3-3 and Table 3.3.1.2.3-3 specify the daily TID inside selected thicknesses of spherical aluminum (Al) shielding from the trapped radiation belt protons and electrons.

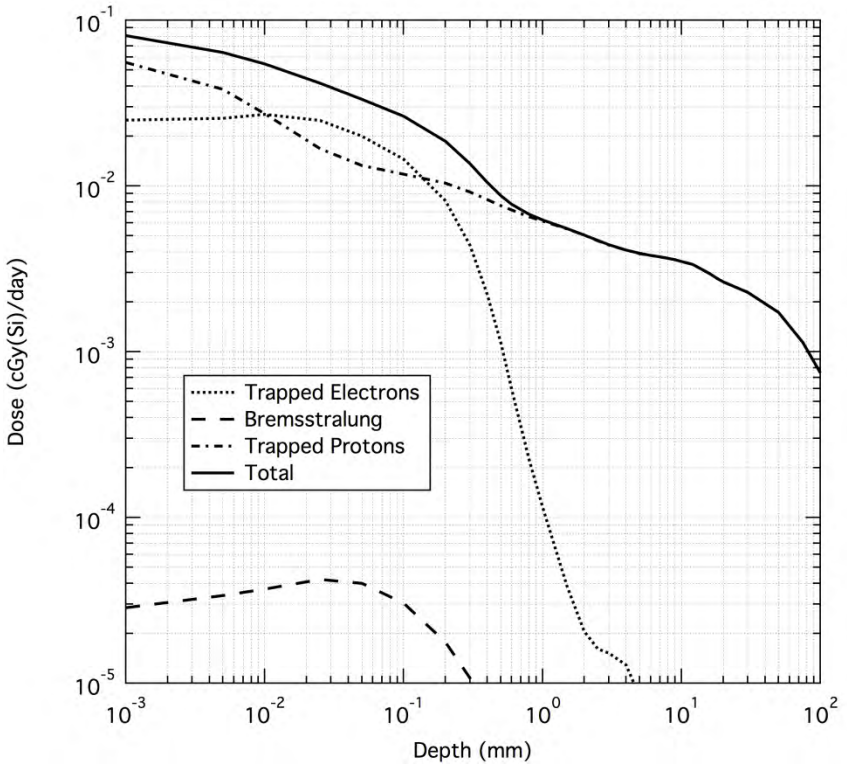

Figure 3.3.1.2.3-3. Daily Trapped Belts TID Inside Shielding

Table 3.3.1.2.3-3. Daily Trapped Belts TID Inside Shielding

Aluminum Shield Depth	Trapped Electron Daily TID	Bremsstrahlung Daily TID	Trapped Proton Daily TID	Total Daily TID
mm	cGy(Si)/day	cGy(Si)/day	cGy(Si)/day	cGy(Si)/day
1.00E-03	2.50E-02	2.85E-05	5.55E-02	8.06E-02
5.00E-03	2.56E-02	3.38E-05	3.83E-02	6.39E-02
1.00E-02	2.71E-02	3.70E-05	2.73E-02	5.45E-02
2.50E-02	2.48E-02	4.23E-05	1.68E-02	4.16E-02
5.00E-02	2.00E-02	4.00E-05	1.33E-02	3.34E-02
1.00E-01	1.45E-02	3.05E-05	1.18E-02	2.64E-02
2.00E-01	8.17E-03	1.77E-05	1.04E-02	1.86E-02
3.00E-01	4.37E-03	1.07E-05	9.19E-03	1.36E-02
4.00E-01	2.22E-03	6.85E-06	8.27E-03	1.05E-02

Aluminum Shield Depth	Trapped Electron Daily TID	Bremsstrahlung Daily TID	Trapped Proton Daily TID	Total Daily TID
mm	cGy(Si)/day	cGy(Si)/day	cGy(Si)/day	cGy(Si)/day
5.00E-01	1.13E-03	4.66E-06	7.62E-03	8.75E-03
6.00E-01	5.96E-04	3.36E-06	7.15E-03	7.75E-03
8.00E-01	2.24E-04	2.04E-06	6.53E-03	6.76E-03
1.00E+00	1.15E-04	1.43E-06	6.13E-03	6.24E-03
2.50E+00	1.61E-05	5.43E-07	4.68E-03	4.69E-03
5.00E+00	8.37E-06	3.13E-07	3.91E-03	3.92E-03
1.00E+01	3.62E-13	1.71E-07	3.51E-03	3.51E-03
1.20E+01	0.00E+00	1.46E-07	3.36E-03	3.36E-03
1.40E+01	0.00E+00	1.29E-07	3.14E-03	3.14E-03
1.60E+01	0.00E+00	1.16E-07	2.95E-03	2.95E-03
1.80E+01	0.00E+00	1.04E-07	2.77E-03	2.77E-03
2.00E+01	0.00E+00	9.48E-08	2.64E-03	2.64E-03
3.00E+01	0.00E+00	6.59E-08	2.28E-03	2.28E-03
5.00E+01	0.00E+00	3.73E-08	1.73E-03	1.73E-03
7.50E+01	0.00E+00	2.15E-08	1.14E-03	1.14E-03
1.00E+02	0.00E+00	1.18E-08	7.44E-04	7.44E-04

The final TID specification can either be derived by generating a dose versus depth curve by 3-dimensional shielding transport calculations, using the external environments presented at the beginning of this section, or by using the data given in Figure and Table 3.3.1.2.3-3. To calculate the final TID specification level for this segment (when no 3-dimensional shielding calculations are done), multiply the daily Total TID in Table 3.3.1.2.3-3 by the number of days in the segment. When performing the 3-D shielding calculations, the external trapped ionizing radiation environments (given as daily fluences in the above Tables) are multiplied by the number of mission days. Those trapped electron and proton segment fluences are then used as inputs to code that will perform the 3-D transport calculations. The output of this code will be the TID specification.

Model Inputs

None.

Limitations

None.

Technical Notes

All environment models were run for the assumed an orbit of 241 km circular at a 28.5° inclination. The trapped electron environment was defined using the AE8MAX model, as it represents the worst-case electron environment. The mean (50%) model is then scaled by a factor of two to account for the model uncertainty. The trapped proton environment was defined using the AP8MIN model, as it represents the worst-case proton environment. The model is then scaled by a factor of two to account for the model uncertainty. The SPE TID specification was defined by using the ESP/PSYCHIC model for a one year period during solar maximum conditions with a stormy magnetosphere and a 95% probability of the fluences not being exceeded. The TID shielding calculations were performed using the SPENVIS Shieldose2 code, solid Aluminum sphere option.

3.3.1.2.4 High Earth Orbit (HEO) 407 x 233,860 km

Design Limits

Total dose contributions for this staging orbit primarily originate from the Earth's trapped radiation environments. Since this orbit is part of larger DRM, no SPE environment is needed specific to this orbit except for any segment whose mission ends with this orbit. For those segments only, it is assumed that a single Solar Particle Event (SPE) will occur during this stage and it will add to the total dose. That SPE environment is presented in Section 3.3.1.10.2 Geomagnetic Unshielded since this staging orbit spends the majority of its time outside the Earth's magnetic field.

The following tables and graphs provide the ionizing radiation environment data, external to the spacecraft, that can be used as input for 3-dimensional shielding calculations of total ionizing dose or for the calculation of displacement damage dose: Figure 3.3.1.2.4-1 and Table 3.3.1.2.4-1 specify the daily trapped proton, integral and differential, spectra as a function of energy. Figure 3.3.1.2.4-2 and Table 3.3.1.2.4-2 specify the daily trapped electron, integral and differential, spectra as a function of energy.

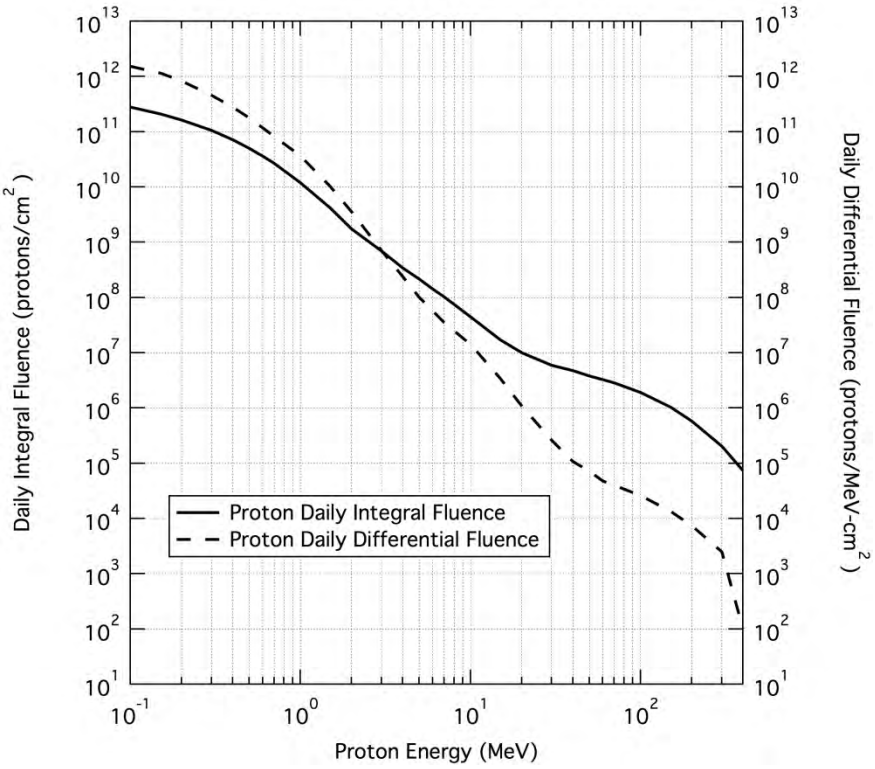

Figure 3.3.1.2.4-1. Daily Trapped Proton Fluences

Table 3.3.1.2.4-1. Daily Trapped Proton Fluences

Proton Energy	Daily Integral Trapped Proton Fluence	Daily Differential Trapped Proton Fluence
MeV	protons/cm^2	protons/MeV-cm^2
1.00E-01	2.77E+11	1.52E+12
5.00E-01	5.02E+10	1.78E+11
7.00E-01	2.67E+10	8.14E+10
1.00E+00	1.20E+10	3.65E+10
2.00E+00	1.74E+09	3.57E+09
3.00E+00	6.94E+08	7.00E+08
4.00E+00	3.44E+08	2.39E+08
5.00E+00	2.16E+08	1.01E+08
6.00E+00	1.42E+08	5.70E+07
7.00E+00	1.02E+08	3.49E+07
1.00E+01	4.43E+07	1.41E+07
2.00E+01	1.00E+07	1.09E+06

Proton Energy	Daily Integral Trapped Proton Fluence	Daily Differential Trapped Proton Fluence
MeV	protons/cm^2	protons/MeV-cm^2
3.00E+01	5.96E+06	2.64E+05
4.00E+01	4.71E+06	1.08E+05
5.00E+01	3.81E+06	7.19E+04
6.00E+01	3.27E+06	4.79E+04
7.00E+01	2.85E+06	3.98E+04
1.00E+02	1.91E+06	2.60E+04
1.50E+02	1.04E+06	1.34E+04
2.00E+02	5.76E+05	7.44E+03
3.00E+02	2.04E+05	2.51E+03
4.00E+02	7.37E+04	1.01E+02

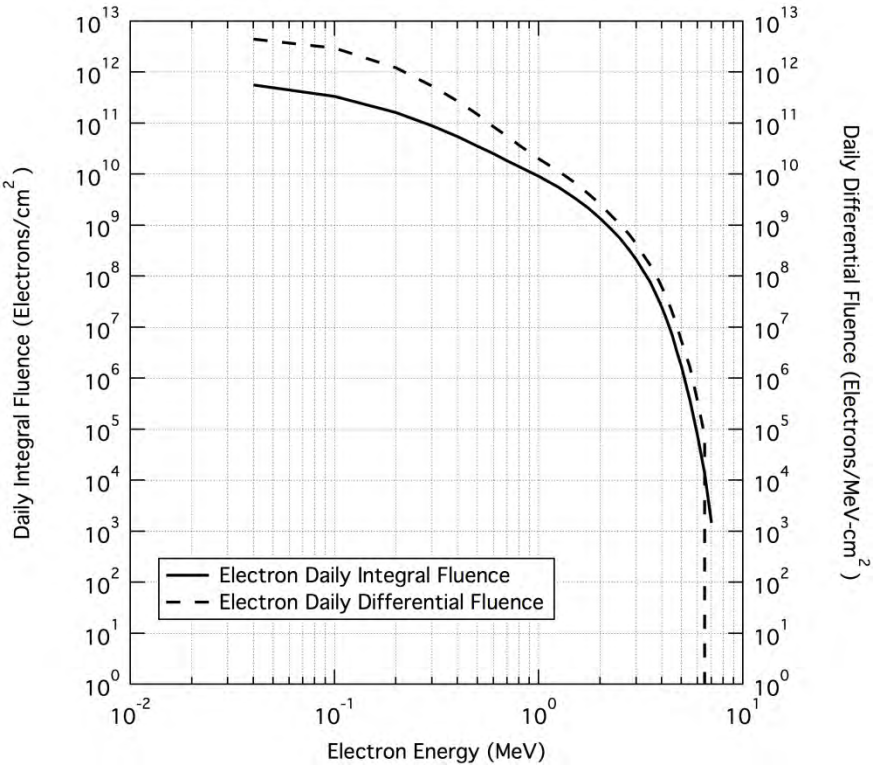

Figure 3.3.1.2.4-2. Daily Trapped Electron Fluences

Table 3.3.1.2.4-2. Daily Trapped Electron Fluences

Electron Energy	Daily Integral Trapped Electron Fluence	Daily Differential Trapped Electron Fluence
MeV	electrons/cm^2	electrons/MeV-cm^2
4.00E-02	5.59E+11	4.48E+12
1.00E-01	3.35E+11	2.97E+12
2.00E-01	1.63E+11	1.23E+12
3.00E-01	8.92E+10	5.39E+11
4.00E-01	5.51E+10	2.70E+11
5.00E-01	3.53E+10	1.49E+11
6.00E-01	2.53E+10	8.43E+10
7.00E-01	1.84E+10	5.57E+10
8.00E-01	1.41E+10	3.71E+10
1.00E+00	9.09E+09	2.03E+10
1.25E+00	5.54E+09	1.14E+10
1.50E+00	3.42E+09	6.78E+09
1.75E+00	2.15E+09	4.12E+09
2.00E+00	1.36E+09	2.57E+09
2.25E+00	8.65E+08	1.60E+09
2.50E+00	5.55E+08	1.04E+09
2.75E+00	3.43E+08	6.86E+08
3.00E+00	2.12E+08	4.27E+08
3.25E+00	1.29E+08	2.67E+08
3.50E+00	7.87E+07	1.69E+08
3.75E+00	4.44E+07	1.07E+08
4.00E+00	2.52E+07	6.22E+07
4.25E+00	1.33E+07	3.62E+07
4.50E+00	7.09E+06	1.99E+07
4.75E+00	3.38E+06	1.08E+07
5.00E+00	1.70E+06	5.36E+06
5.50E+00	3.71E+05	1.63E+06
6.00E+00	7.60E+04	3.57E+05
6.50E+00	1.36E+04	7.45E+04
7.00E+00	1.47E+03	0.00E+00

Figure 3.3.1.2.4-3 and Table 3.3.1.2.4-3 specify the daily TID inside selected thicknesses of spherical aluminum (Al) shielding from the trapped radiation belt protons and electrons.

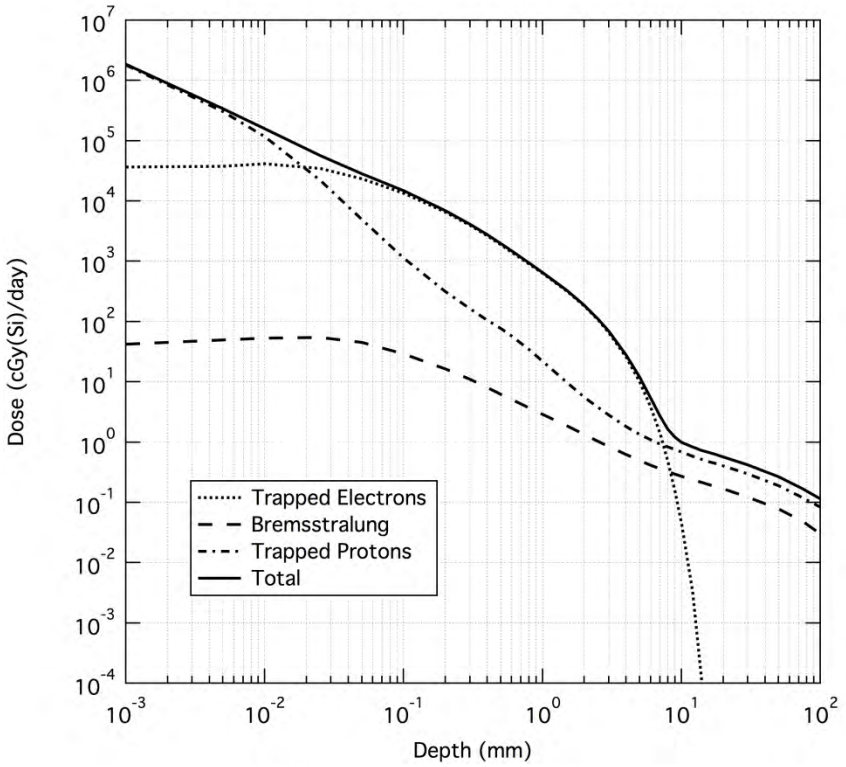

Figure 3.3.1.2.4-3. Daily Trapped Belts TID Inside Shielding

Table 3.3.1.2.4-3. Daily Trapped Belts TID Inside Shielding

Aluminum Shield Depth	Trapped Electron Daily TID	Bremsstrahlung Daily TID	Trapped Proton Daily TID	Total Daily TID
mm	cGy(Si)/day	cGy(Si)/day	cGy(Si)/day	cGy(Si)/day
1.00E-03	3.67E+04	4.23E+01	1.81E+06	1.85E+06
5.00E-03	3.78E+04	4.94E+01	3.04E+05	3.41E+05
1.00E-02	4.14E+04	5.29E+01	1.18E+05	1.59E+05
2.50E-02	3.48E+04	5.50E+01	2.22E+04	5.71E+04
5.00E-02	2.35E+04	4.50E+01	4.94E+03	2.85E+04
1.00E-01	1.36E+04	2.92E+01	1.14E+03	1.48E+04
2.00E-01	6.59E+03	1.63E+01	3.15E+02	6.92E+03
3.00E-01	3.95E+03	1.10E+01	1.64E+02	4.12E+03
4.00E-01	2.64E+03	8.02E+00	1.06E+02	2.76E+03
5.00E-01	1.89E+03	6.25E+00	7.66E+01	1.98E+03

Aluminum Shield Depth	Trapped Electron Daily TID	Bremsstrahlung Daily TID	Trapped Proton Daily TID	Total Daily TID
mm	cGy(Si)/day	cGy(Si)/day	cGy(Si)/day	cGy(Si)/day
6.00E-01	1.42E+03	5.10E+00	5.74E+01	1.49E+03
8.00E-01	9.01E+02	3.70E+00	3.41E+01	9.39E+02
1.00E+00	6.28E+02	2.90E+00	2.20E+01	6.53E+02
2.50E+00	1.08E+02	1.04E+00	3.79E+00	1.12E+02
5.00E+00	1.00E+01	4.96E-01	1.34E+00	1.19E+01
1.00E+01	4.53E-02	2.71E-01	6.85E-01	1.00E+00
1.20E+01	3.32E-03	2.38E-01	5.86E-01	8.27E-01
1.40E+01	1.02E-04	2.14E-01	5.15E-01	7.29E-01
1.60E+01	7.81E-07	1.96E-01	4.68E-01	6.64E-01
1.80E+01	9.25E-09	1.80E-01	4.35E-01	6.15E-01
2.00E+01	0.00E+00	1.67E-01	4.04E-01	5.71E-01
3.00E+01	0.00E+00	1.23E-01	2.97E-01	4.20E-01
5.00E+01	0.00E+00	7.81E-02	1.90E-01	2.68E-01
7.50E+01	0.00E+00	4.82E-02	1.20E-01	1.68E-01
1.00E+02	0.00E+00	2.98E-02	8.41E-02	1.14E-01

The final TID specification can either be derived by generating a dose versus depth curve by 3-dimensional shielding transport calculations, using the external environments presented at the beginning of this section, or by using the data given in Figure and Table 3.3.1.2.4-3. To calculate the final TID specification level for this segment (when no 3-dimensional shielding calculations are done), multiply the daily Total TID in Table 3.3.1.2.4-3 by the number of days in the segment and add that number to the total SPE TID given in Section 3.3.1.10.2. When performing the 3-D shielding calculations, the external trapped ionizing radiation environments (given as daily fluences in the above Tables) are multiplied by the number of mission days. Those trapped electron and proton segment fluences and the SPE proton fluence (found in Section 3.3.1.10.2) are then used as inputs to code that will perform the 3-D transport calculations. The output of this code will be the TID specification.

Model Inputs

None.

Limitations

None.

Technical Notes

All environment models were run for the assumed an orbit of 407 km x 233,860 km at a 28.5° inclination. The trapped electron environment was defined using the AE8MAX model, as it

represents the worst-case electron environment. The mean (50%) model is then scaled by a factor of two to account for the model uncertainty. The trapped proton environment was defined using the AP8MIN model, as it represents the worst-case proton environment. The model is then scaled by a factor of two to account for the model uncertainty. The TID shielding calculations were performed using the SPENVIS Shieldose2 code, solid Aluminum sphere option.

3.3.1.2.5 HEO to NEA transit

It is assumed that for this stage the transit will start at the apogee of the HEO orbit. Therefore, the total dose contributions for this staging orbit will not have contribution from the Earth's trapped radiation environments. Since this orbit is part of larger DRM, no SPE environment is needed specific to this orbit except for any segment whose mission ends with this orbit. For those segments only, it is assumed that a single Solar Particle Event (SPE) will occur during this stage and it will add to the total dose. Since this transit is outside the Earth's magnetic field, the details of this SPE environment for this stage are given in Section 3.3.1.10.2.

3.3.1.2.6 LEO 407 km Circular

The total dose environment model parameters for LEO 407 km circular are bounded by those used for the LEO-ISS. For LEO 407 km circular total dose environments use those presented in Section 3.3.1.1 LEO-ISS Orbit.

3.3.1.2.7 Low Perigee (LP)-HEO 407 x 400,000 km

Design Limits

Total dose contributions for this staging orbit primarily originate from the Earth's trapped radiation environments. Since this orbit is part of larger DRM, no SPE environment is needed specific to this orbit except for any segment whose mission ends with this orbit. For those segments only, it is assumed that a single Solar Particle Event (SPE) will occur during this stage and it will add to the total dose. That SPE environment is presented in Section 3.3.1.10.2 Geomagnetic Unshielded since this staging orbit spends the majority of its time outside the Earth's magnetic field.

The following Tables and graphs provide the ionizing radiation environment data, external to the spacecraft, that can be used as input for 3-dimensional shielding calculations of total ionizing dose or for the calculation of displacement damage dose: Figure 3.3.1.2.7-1 and Table 3.3.1.2.7-1 specify the daily trapped proton, integral and differential, spectra as a function of energy.

Figure 3.3.1.2.7-2 and Table 3.3.1.2.7-2 specify the daily trapped electron, integral and differential, spectra as a function of energy.

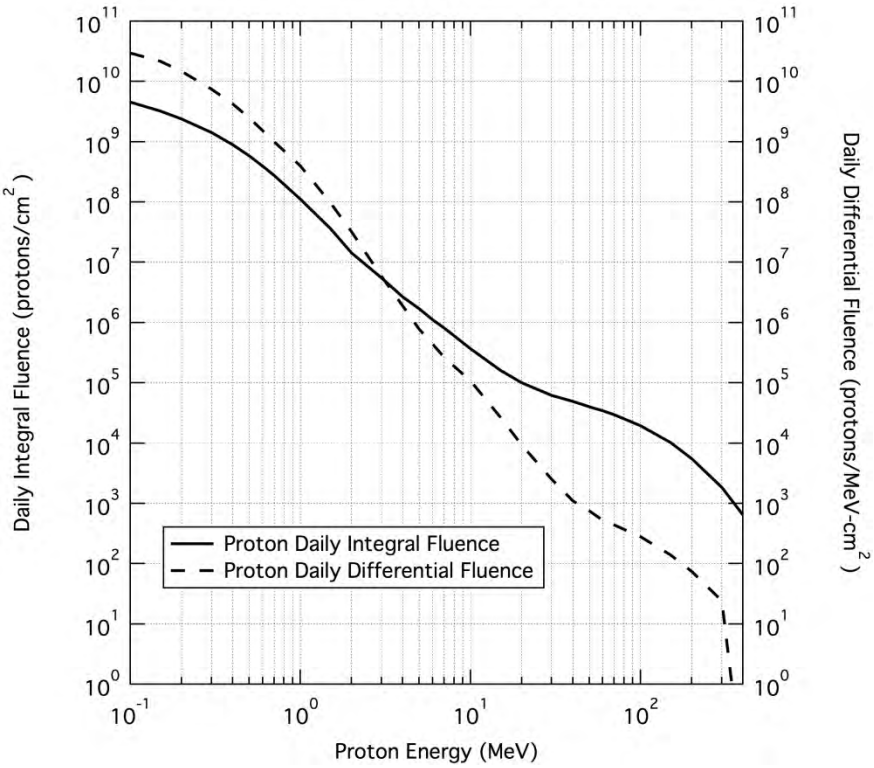

Figure 3.3.1.2.7-1. Daily Trapped Proton Fluences

Table 3.3.1.2.7-1. Daily Trapped Proton Fluences

Proton Energy	Daily Integral Trapped Proton Fluence	Daily Differential Trapped Proton Fluence
MeV	protons/cm^2	protons/MeV-cm^2
1.00E-01	4.53E+09	2.95E+10
5.00E-01	5.83E+08	2.49E+09
7.00E-01	2.77E+08	9.94E+08
1.00E+00	1.12E+08	4.00E+08
2.00E+00	1.44E+07	3.23E+07
3.00E+00	5.50E+06	5.84E+06
4.00E+00	2.67E+06	1.91E+06
5.00E+00	1.69E+06	7.78E+05
6.00E+00	1.12E+06	4.40E+05
7.00E+00	8.13E+05	2.66E+05
1.00E+01	3.70E+05	1.08E+05
2.00E+01	1.00E+05	9.32E+03

Proton Energy	Daily Integral Trapped Proton Fluence	Daily Differential Trapped Proton Fluence
MeV	protons/cm^2	protons/MeV-cm^2
3.00E+01	6.22E+04	2.54E+03
4.00E+01	4.94E+04	1.10E+03
5.00E+01	4.01E+04	7.53E+02
6.00E+01	3.43E+04	5.28E+02
7.00E+01	2.96E+04	4.41E+02
1.00E+02	1.94E+04	2.81E+02
1.50E+02	1.02E+04	1.39E+02
2.00E+02	5.50E+03	7.48E+01
3.00E+02	1.86E+03	2.42E+01
4.00E+02	6.47E+02	3.16E-02

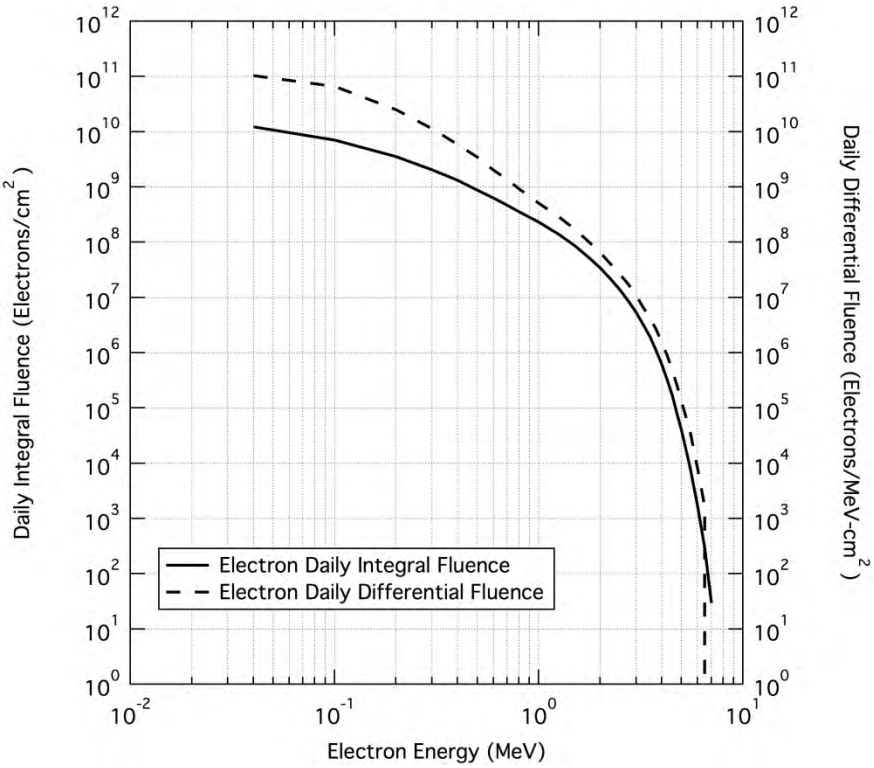

Figure 3.3.1.2.7-2. Daily Trapped Electron Fluences

Table 3.3.1.2.7-2. Daily Trapped Electron Fluences

Electron Energy	Daily Integral Trapped Electron Fluence	Daily Differential Trapped Electron Fluence
MeV	electrons/cm^2	electrons/MeV-cm^2
4.00E-02	1.22E+10	1.04E+11
1.00E-01	7.08E+09	6.63E+10
2.00E-01	3.58E+09	2.51E+10
3.00E-01	2.05E+09	1.13E+10
4.00E-01	1.32E+09	5.92E+09
5.00E-01	8.69E+08	3.44E+09
6.00E-01	6.32E+08	2.02E+09
7.00E-01	4.65E+08	1.37E+09
8.00E-01	3.58E+08	9.25E+08
1.00E+00	2.31E+08	5.14E+08
1.25E+00	1.40E+08	2.90E+08
1.50E+00	8.63E+07	1.73E+08
1.75E+00	5.41E+07	1.04E+08
2.00E+00	3.41E+07	6.49E+07
2.25E+00	2.17E+07	4.05E+07
2.50E+00	1.39E+07	2.62E+07
2.75E+00	8.57E+06	1.72E+07
3.00E+00	5.31E+06	1.07E+07
3.25E+00	3.23E+06	6.69E+06
3.50E+00	1.97E+06	4.24E+06
3.75E+00	1.11E+06	2.68E+06
4.00E+00	6.25E+05	1.55E+06
4.25E+00	3.28E+05	9.02E+05
4.50E+00	1.74E+05	4.93E+05
4.75E+00	8.15E+04	2.66E+05
5.00E+00	4.05E+04	1.31E+05
5.50E+00	8.52E+03	3.88E+04
6.00E+00	1.70E+03	8.22E+03
6.50E+00	3.00E+02	1.67E+03
7.00E+00	2.94E+01	0.00E+00

Figure 3.3.1.2.7-3 and Table 3.3.1.2.7-3 specify the daily TID inside selected thicknesses of spherical aluminum (Al) shielding from the trapped radiation belt protons and electrons.

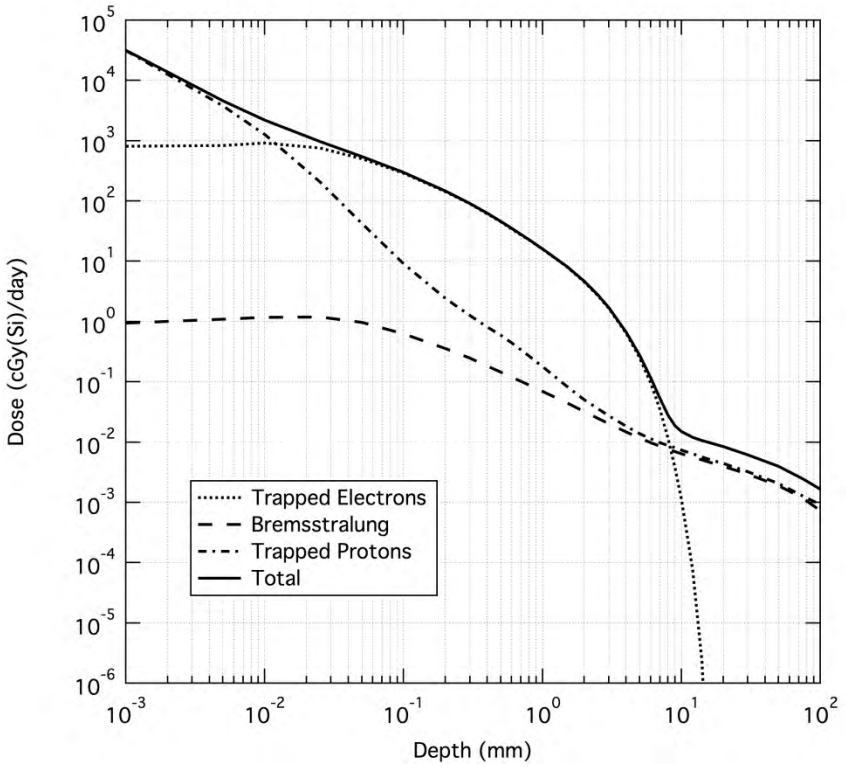

Figure 3.3.1.2.7-3. Daily Trapped Belts TID Inside Shielding

Table 3.3.1.2.7-3. Daily Trapped Belts TID Inside Shielding

Aluminum Shield Depth	Trapped Electron Daily TID	Bremsstrahlung Daily TID	Trapped Proton Daily TID	Total Daily TID
mm	cGy(Si)/day	cGy(Si)/day	cGy(Si)/day	cGy(Si)/day
1.00E-03	8.12E+02	9.39E-01	3.11E+04	3.19E+04
5.00E-03	8.35E+02	1.10E+00	3.81E+03	4.64E+03
1.00E-02	9.20E+02	1.17E+00	1.28E+03	2.21E+03
2.50E-02	7.63E+02	1.19E+00	2.07E+02	9.71E+02
5.00E-02	5.04E+02	9.66E-01	4.21E+01	5.47E+02
1.00E-01	2.89E+02	6.27E-01	9.13E+00	2.98E+02
2.00E-01	1.43E+02	3.58E-01	2.43E+00	1.46E+02
3.00E-01	8.92E+01	2.47E-01	1.26E+00	9.07E+01
4.00E-01	6.16E+01	1.84E-01	8.17E-01	6.26E+01

Aluminum Shield Depth	Trapped Electron Daily TID	Bremsstrahlung Daily TID	Trapped Proton Daily TID	Total Daily TID
mm	cGy(Si)/day	cGy(Si)/day	cGy(Si)/day	cGy(Si)/day
5.00E-01	4.52E+01	1.45E-01	5.94E-01	4.60E+01
6.00E-01	3.46E+01	1.20E-01	4.48E-01	3.52E+01
8.00E-01	2.24E+01	8.82E-02	2.70E-01	2.28E+01
1.00E+00	1.58E+01	6.96E-02	1.78E-01	1.61E+01
2.50E+00	2.72E+00	2.48E-02	3.57E-02	2.78E+00
5.00E+00	2.51E-01	1.17E-02	1.38E-02	2.77E-01
1.00E+01	1.10E-03	6.41E-03	7.38E-03	1.49E-02
1.20E+01	7.76E-05	5.63E-03	6.38E-03	1.21E-02
1.40E+01	2.33E-06	5.07E-03	5.64E-03	1.07E-02
1.60E+01	1.78E-08	4.65E-03	5.14E-03	9.79E-03
1.80E+01	2.10E-10	4.29E-03	4.77E-03	9.06E-03
2.00E+01	0.00E+00	3.99E-03	4.42E-03	8.41E-03
3.00E+01	0.00E+00	2.95E-03	3.23E-03	6.18E-03
5.00E+01	0.00E+00	1.90E-03	2.05E-03	3.95E-03
7.50E+01	0.00E+00	1.18E-03	1.27E-03	2.46E-03
1.00E+02	0.00E+00	7.34E-04	9.22E-04	1.66E-03

The final TID specification can either be derived by generating a dose versus depth curve by 3-dimensional shielding transport calculations, using the external environments presented at the beginning of this section, or by using the data given in Figure and Table 3.3.1.2.7-3. To calculate the final TID specification level for this segment (when no 3-dimensional shielding calculations are done), multiply the daily Total TID in Table 3.3.1.2.7-3 by the number of days in the segment and add that number to the total SPE TID given in Section 3.3.1.10.2. When performing the 3-D shielding calculations, the external trapped ionizing radiation environments (given as daily fluences in the above Tables) are multiplied by the number of mission days. Those trapped electron and proton segment fluences and the SPE proton fluence (found in Section 3.3.1.10.2) are then used as inputs to code that will perform the 3-D transport calculations. The output of this code will be the TID specification.

Model Inputs

None.

Limitations

None.

Technical Notes

All environment models were run for the assumed an orbit of 407 km x 400,000 km at a 28.5° inclination. The trapped electron environment was defined using the AE8MAX model, as it represents the worst-case electron environment. The mean (50%) model is then scaled by a factor of two to account for the model uncertainty. The trapped proton environment was defined using the AP8MIN model, as it represents the worst-case proton environment. The model is then scaled by a factor of two to account for the model uncertainty. The TID shielding calculations were performed using the SPENVIS Shieldose2 code, solid Aluminum sphere option.

3.3.1.2.8 High Perigee (HP)-HEO Spiral to 60,000 x 400,000 km

Reserved.

3.3.1.3 Geosynchronous Earth Orbit (GEO)

Design Limits

Total dose contributions for GEO DRM primarily originate from the Earth's trapped electron environment. It is assumed that a single unshielded Solar Particle Event (SPE) will occur during the mission and it will add to the total dose. The details of the SPE environment for this region of space are given in Section 3.3.1.10.2.

The following Tables and graphs provide the ionizing radiation environment data, external to the spacecraft, that can be used as input for 3-dimensional shielding calculations of total ionizing dose or for the calculation of displacement damage dose: Figure 3.3.1.3-1 and Table 3.3.1.3-1 specify the daily trapped electron, integral and differential, spectra as a function of energy.

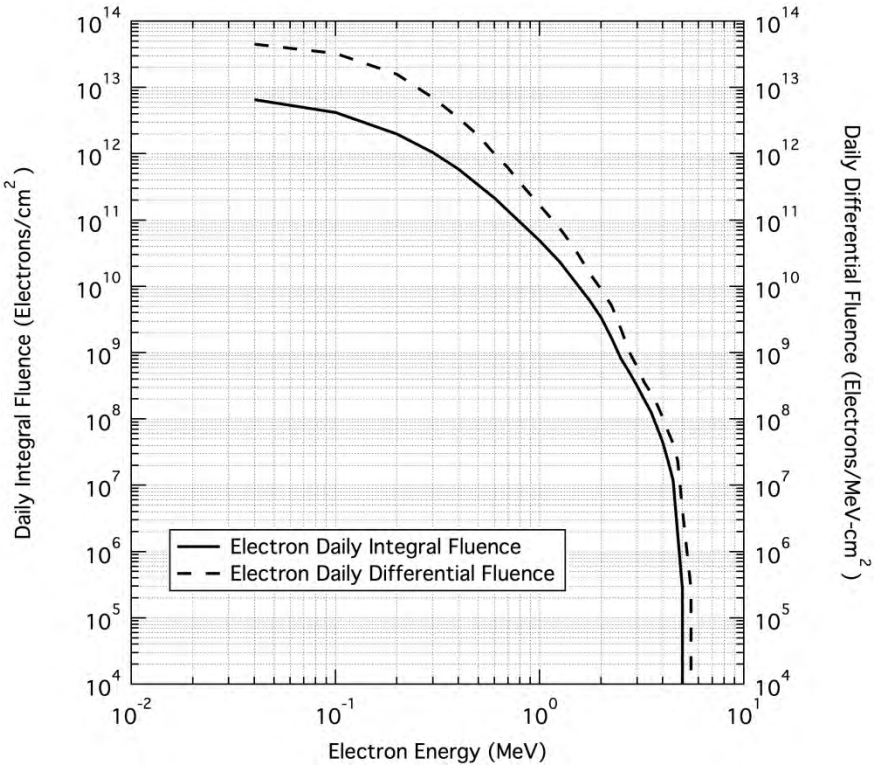

Figure 3.3.1.3-1. Daily Trapped Electron Fluences

Table 3.3.1.3-1. Daily Trapped Electron Fluences

Electron Energy	Daily Integral Trapped Electron Fluence	Daily Differential Trapped Electron Fluence
MeV	electrons/cm^2	electrons/MeV-cm^2
4.00E-02	6.54E+12	4.52E+13
1.00E-01	4.21E+12	3.26E+13
2.00E-01	2.00E+12	1.59E+13
3.00E-01	1.04E+12	7.02E+12
4.00E-01	5.91E+11	3.50E+12
5.00E-01	3.37E+11	1.88E+12
6.00E-01	2.15E+11	9.98E+11
7.00E-01	1.37E+11	6.08E+11
8.00E-01	9.34E+10	3.67E+11
1.00E+00	4.90E+10	1.68E+11
1.25E+00	2.36E+10	7.53E+10
1.50E+00	1.14E+10	3.48E+10

Electron Energy	Daily Integral Trapped Electron Fluence	Daily Differential Trapped Electron Fluence
MeV	electrons/cm^2	electrons/MeV-cm^2
1.75E+00	6.20E+09	1.60E+10
2.00E+00	3.38E+09	9.08E+09
2.25E+00	1.66E+09	5.13E+09
2.50E+00	8.15E+08	2.31E+09
2.75E+00	5.02E+08	1.01E+09
3.00E+00	3.09E+08	6.06E+08
3.25E+00	1.99E+08	3.62E+08
3.50E+00	1.28E+08	2.47E+08
3.75E+00	7.55E+07	1.67E+08
4.00E+00	4.45E+07	1.05E+08
4.25E+00	2.31E+07	6.50E+07
4.50E+00	1.20E+07	4.25E+07
4.75E+00	1.81E+06	2.34E+07
5.00E+00	2.75E+05	4.29E+06
5.50E+00	0.00E+00	2.75E+05
6.00E+00	0.00E+00	0.00E+00

Figure 3.3.1.3-2 and Table 3.3.1.3-2 specify the daily TID inside selected thicknesses of spherical aluminum (Al) shielding from the trapped radiation belt protons and electrons.

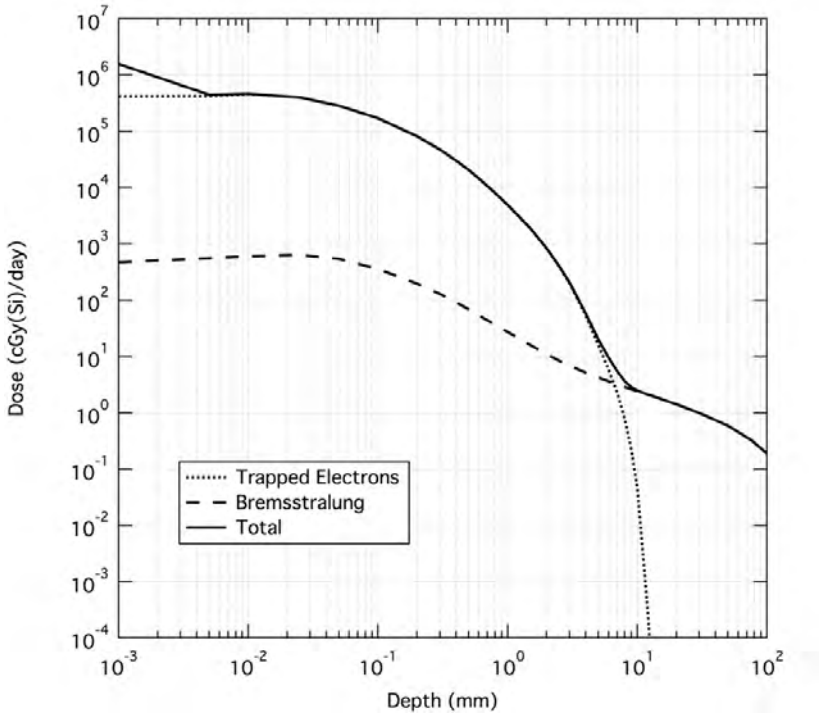

Figure 3.3.1.3-2. Daily Trapped Belts TID Inside Shielding

Table 3.3.1.3-2. Daily Trapped Belts TID Inside Shielding

Aluminum Shield Depth	Trapped Electron Daily TID	Bremsstrahlung Daily TID	Total Daily TID
mm	cGy(Si)/day	cGy(Si)/day	cGy(Si)/day
1.00E-03	4.16E+05	4.76E+02	1.57E+06
5.00E-03	4.27E+05	5.59E+02	4.50E+05
1.00E-02	4.64E+05	6.03E+02	4.68E+05
2.50E-02	4.00E+05	6.44E+02	4.01E+05
5.00E-02	2.84E+05	5.44E+02	2.84E+05
1.00E-01	1.71E+05	3.60E+02	1.72E+05
2.00E-01	8.19E+04	1.99E+02	8.21E+04
3.00E-01	4.74E+04	1.30E+02	4.75E+04
4.00E-01	3.04E+04	9.16E+01	3.04E+04
5.00E-01	2.06E+04	6.88E+01	2.06E+04
6.00E-01	1.45E+04	5.41E+01	1.46E+04

Aluminum Shield Depth	Trapped Electron Daily TID	Bremsstrahlung Daily TID	Total Daily TID
mm	cGy(Si)/day	cGy(Si)/day	cGy(Si)/day
8.00E-01	8.04E+03	3.67E+01	8.08E+03
1.00E+00	4.92E+03	2.71E+01	4.95E+03
2.50E+00	3.92E+02	8.40E+00	4.00E+02
5.00E+00	1.59E+01	4.23E+00	2.01E+01
1.00E+01	4.45E-02	2.42E+00	2.47E+00
1.20E+01	2.96E-04	2.11E+00	2.11E+00
1.40E+01	1.17E-06	1.88E+00	1.88E+00
1.60E+01	1.49E-09	1.70E+00	1.70E+00
1.80E+01	0.00E+00	1.55E+00	1.55E+00
2.00E+01	0.00E+00	1.42E+00	1.42E+00
3.00E+01	0.00E+00	9.97E-01	9.97E-01
5.00E+01	0.00E+00	5.90E-01	5.90E-01
7.50E+01	0.00E+00	3.33E-01	3.33E-01
1.00E+02	0.00E+00	1.91E-01	1.91E-01

The final TID specification can either be derived by generating a dose versus depth curve by 3-dimensional shielding transport calculations, using the external environments presented at the beginning of this section, or by using the data given in Figure and Table 3.3.1.3-2. To calculate the final TID specification level for the GEO region (when no 3-dimensional shielding calculations are done), multiply the daily Total TID in Table 3.3.1.3-2 by the number of days in the mission segment and add that number to the total SPE TID as given in Section 3.3.1.10.2. When performing the 3-D shielding calculations, the external trapped electron environment (given as a daily fluence in the above Table) is multiplied by the number of mission segment days. That trapped electron fluence and the SPE proton fluence (found in Section 3.3.1.10.2) are then used as inputs to code that will perform the 3-D transport calculations. The output of this code will be the TID specification.

Model Inputs

None.

Limitations

None.

Technical Notes

All environment models were run for the GEO of 35600 km at 0° inclination. The trapped electron environment was defined using the AE8MAX model, as it represents the worst-case electron environment. The mean (50%) model is then scaled by a factor of two to account for the

model uncertainty. The GEO is outside the trapped proton belt, so no trapped proton environment exists. The TID shielding calculations were performed using the SPENVIS Shieldose2 code, solid Aluminum sphere option.

3.3.1.4 Interplanetary

While operating at or near in Interplanetary space, the only total dose that will be seen is from a geomagnetic unshielded SPE. That environment is given in Section 3.3.1.10.2.

3.3.1.5 Lunar Orbit

While operating at or near the moon, the only total dose that will be seen is from a geomagnetic unshielded SPE. That environment is given in Section 3.3.1.10.2. While, depending on the orbit altitude, the moon may supply some level of shielding, the unshielded SPE gives a conservative bound. Since other minor radiation sources are not included (e.g., albedo neutrons), it is appropriate to use the conservative bound environment for this region.

3.3.1.6 Lunar Surface

While operating on the lunar surface, the only total dose that will be seen is from a geomagnetic unshielded SPE. That environment is given in Section 3.3.1.10.2. While, depending on the orbit altitude, the moon may supply some level of shielding, the unshielded SPE gives a conservative bound. Since other minor radiation sources are not included (e.g., albedo neutrons), it is appropriate to use the conservative bound environment for this region.

3.3.1.7 Near Earth Asteroid

While operating at or near an NEA, the only total dose that will be seen is from a geomagnetic unshielded SPE. That environment is given in Section 3.3.1.10.2.

3.3.1.8 Mars Orbit

Reserved.

3.3.1.9 Mars Surface

Reserved.

3.3.1.10 Solar Particle Events

3.3.1.10.1 Geomagnetic Shielded

Design Limits

The Earth's geomagnetic field provides a shield for some of the particles from an SPE. In general, for low inclination orbits (28.5° or less), the geomagnetic field completely screens out the particles. For polar orbits, the conservative approach would be to assume the event happens in the unshielded polar regions and using Section 3.3.1.10.2 would be more appropriate. For all other shielded orbits, the calculations done for the ISS orbit provide good bounding data. Therefore, the total dose contributions for a geomagnetic shielded single Solar Particle Event (SPE) is given below, based on the standard ISS orbit.

Figure 3.3.1.10.1-1 and Table 3.3.1.10.1-1 specify the total SPE proton integral and differential spectra as a function of energy.

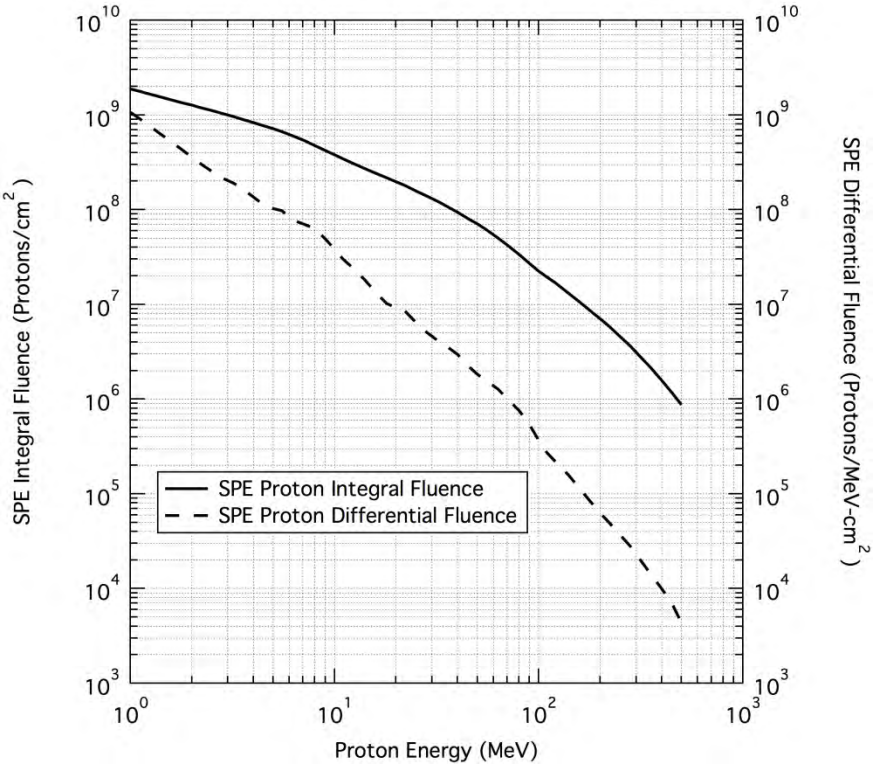

Figure 3.3.1.10.1-1. Integral and Differential Proton Fluences of a Shielded SPE

Table 3.3.1.10.1-1. Integral and Differential Proton Fluences of a Shielded SPE

Proton Energy	ISS SPE Integral Fluence per event	ISS SPE Differential Fluence per event
MeV	protons/cm^2	protons/MeV-cm^2
1.00E-01	7.11E+09	4.02E+10
2.50E-01	4.18E+09	9.63E+09
5.00E-01	2.80E+09	3.21E+09
1.00E+00	1.88E+09	1.07E+09
2.00E+00	1.27E+09	3.58E+08
3.50E+00	9.09E+08	1.70E+08
5.00E+00	7.16E+08	1.03E+08
7.10E+00	5.37E+08	7.00E+07
8.00E+00	4.77E+08	6.29E+07
9.00E+00	4.21E+08	4.89E+07

Proton Energy	ISS SPE Integral Fluence per event	ISS SPE Differential Fluence per event
MeV	protons/cm^2	protons/MeV-cm^2
1.00E+01	3.78E+08	3.80E+07
1.60E+01	2.41E+08	1.32E+07
1.80E+01	2.18E+08	1.02E+07
2.00E+01	1.98E+08	9.23E+06
2.50E+01	1.58E+08	6.46E+06
3.50E+01	1.10E+08	3.67E+06
4.00E+01	9.38E+07	2.98E+06
4.50E+01	8.07E+07	2.26E+06
5.00E+01	7.05E+07	1.82E+06
7.10E+01	4.15E+07	9.89E+05
8.00E+01	3.36E+07	7.61E+05
9.00E+01	2.71E+07	5.42E+05
1.00E+02	2.25E+07	3.70E+05
1.60E+02	1.04E+07	1.11E+05
1.80E+02	8.48E+06	8.19E+04
2.00E+02	7.04E+06	6.26E+04
2.50E+02	4.61E+06	3.70E+04
4.00E+02	1.58E+06	9.92E+03
5.00E+02	8.74E+05	4.36E+03

Figure 3.3.1.10.1-2 and Table 3.3.1.10.1-2 specify total TID inside selected thicknesses of spherical aluminum (Al) shielding from the ISS SPE. 3.3.1.10.1-2 and Table 3.3.1.10.1-2 specify total TID associated with the worst–case as defined in the ESP/PSYCHIC model.

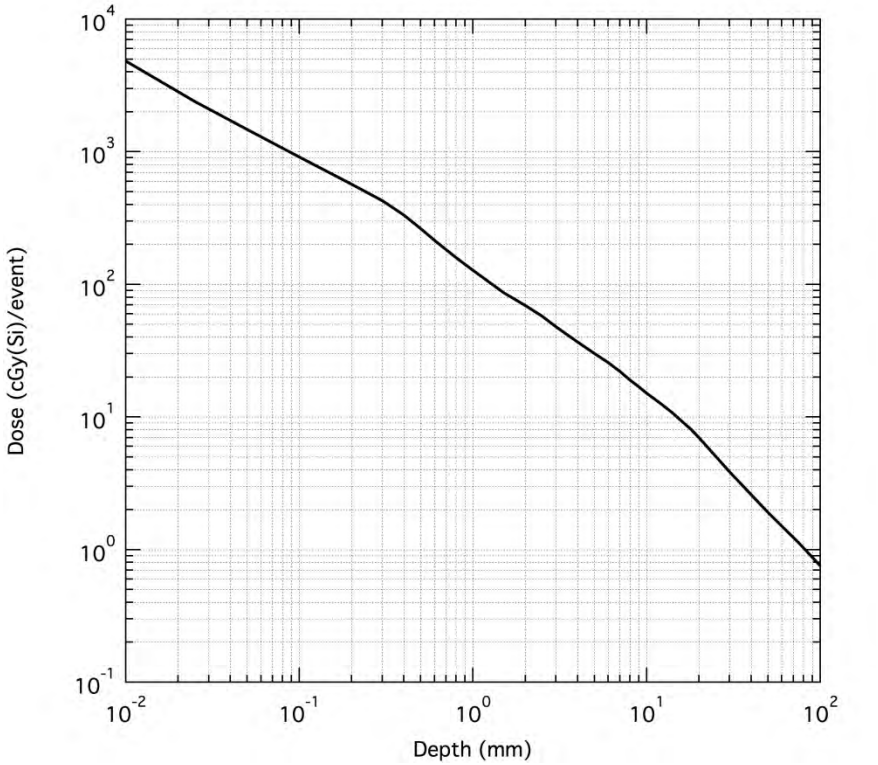

Figure 3.3.1.10.1-2. Total Shielded SPE TID Inside Al Shielding

Table 3.3.1.10.1-2. Total Shielded SPE TID Inside Al Shielding

Aluminum Shield Depth	Total ISS SPE TID
mm	cGy(Si)/event
1.00E-03	3.13E+04
5.00E-03	8.40E+03
1.00E-02	4.84E+03
2.50E-02	2.40E+03
5.00E-02	1.47E+03
1.00E-01	9.13E+02
2.00E-01	5.71E+02
3.00E-01	4.28E+02
4.00E-01	3.33E+02

Aluminum Shield Depth	Total ISS SPE TID
mm	cGy(Si)/event
5.00E-01	2.64E+02
6.00E-01	2.15E+02
8.00E-01	1.59E+02
1.00E+00	1.27E+02
2.50E+00	5.75E+01
5.00E+00	3.01E+01
1.00E+01	1.51E+01
1.20E+01	1.27E+01
1.40E+01	1.08E+01
1.60E+01	9.26E+00
1.80E+01	8.07E+00
2.00E+01	7.00E+00
3.00E+01	3.86E+00
5.00E+01	1.91E+00
7.50E+01	1.13E+00
1.00E+02	7.53E-01

Model Inputs

None.

Limitations

Probability that the shielded SPE dose will not be exceeded during a single SPE event is estimated at 95%.

Technical Notes

All environment models were run for the assumed ISS orbit of 500 km circular orbit at 51.6° inclination. The shielded SPE TID specification was defined by using the ESP/PSYCHIC model for a one year period during solar maximum conditions with a stormy magnetosphere and a 95% probability of the fluences not being exceeded. The TID shielding calculations were performed using the SPENVIS Shieldose2 code, solid Aluminum sphere option.

3.3.1.10.2 Geomagnetic Unshielded

Design Limits

Total dose contributions for a geomagnetic unshielded single Solar Particle Event (SPE) are given below.

Figure 3.3.1.10.2-1 and Table 3.3.1.10.2-1 specify the total unshielded SPE proton integral and differential spectra as a function of energy. Figure 3.3.1.10.2-2 and Table 3.3.1.10.2-2 specify the total unshielded daily GCR proton integral spectra as a function of energy.

Figure 3.3.1.10.2-3 and Table 3.3.1.10.2-3 specify total TID associated with the unshielded SPE environment, and Table 3.3.1.10.2-4 specifies total TID associated with the daily GCR fluence.

Figure 3.3.1.10.2-4 and Table 3.3.1.10.2-5 give the total dose versus shielding depth from solar energetic particles appropriate for a 15 year mission. Figure 3.3.1.10.2-5 and Table 3.3.1.10.2-6 give the fluence of electrons and protons from the solar wind and Earth's magnetotail which should be used for evaluation of thin surface materials on a spacecraft in a near rectilinear halo orbit for 15 years. For mission durations other than 15 years or 1 year, use the 15 year value multiplied by a factor of the mission length divided by 15 years.

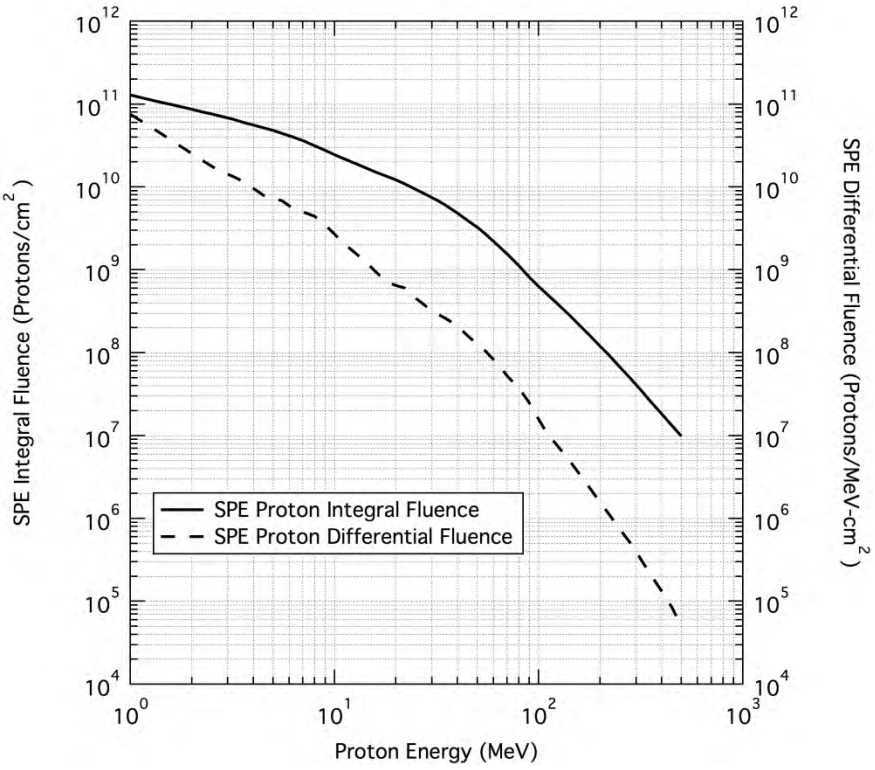

Figure 3.3.1.10.2-1. Integral and Differential Proton Fluence of an Unshielded SPE

Table 3.3.1.10.2-1. Integral and Differential Proton Fluence of an Unshielded SPE

Proton Energy	Unshielded SPE Integral Fluence per year	Unshielded SPE Differential Fluence per year
MeV	protons/cm^2	protons/MeV-cm^2
1.00E-01	4.93E+11	2.83E+12
2.50E-01	2.89E+11	6.79E+11
5.00E-01	1.93E+11	2.26E+11
1.00E+00	1.29E+11	7.56E+10
2.00E+00	8.63E+10	2.53E+10
3.50E+00	6.14E+10	1.20E+10
5.00E+00	4.83E+10	7.28E+09
7.10E+00	3.58E+10	4.94E+09
8.00E+00	3.13E+10	4.43E+09
9.00E+00	2.75E+10	3.45E+09
1.00E+01	2.44E+10	2.68E+09
1.60E+01	1.51E+10	9.33E+08
1.80E+01	1.35E+10	7.17E+08
2.00E+01	1.22E+10	6.51E+08
2.50E+01	9.32E+09	4.55E+08
3.50E+01	6.04E+09	2.59E+08
4.00E+01	4.84E+09	2.10E+08
4.50E+01	3.94E+09	1.59E+08
5.00E+01	3.25E+09	1.26E+08
7.10E+01	1.51E+09	5.10E+07
8.00E+01	1.12E+09	3.72E+07
9.00E+01	8.19E+08	2.48E+07
1.00E+02	6.28E+08	1.57E+07
1.60E+02	2.09E+08	3.31E+06
1.80E+02	1.56E+08	2.23E+06
2.00E+02	1.20E+08	1.56E+06
2.50E+02	6.72E+07	7.44E+05
4.00E+02	1.83E+07	1.33E+05
5.00E+02	9.89E+06	4.94E+04

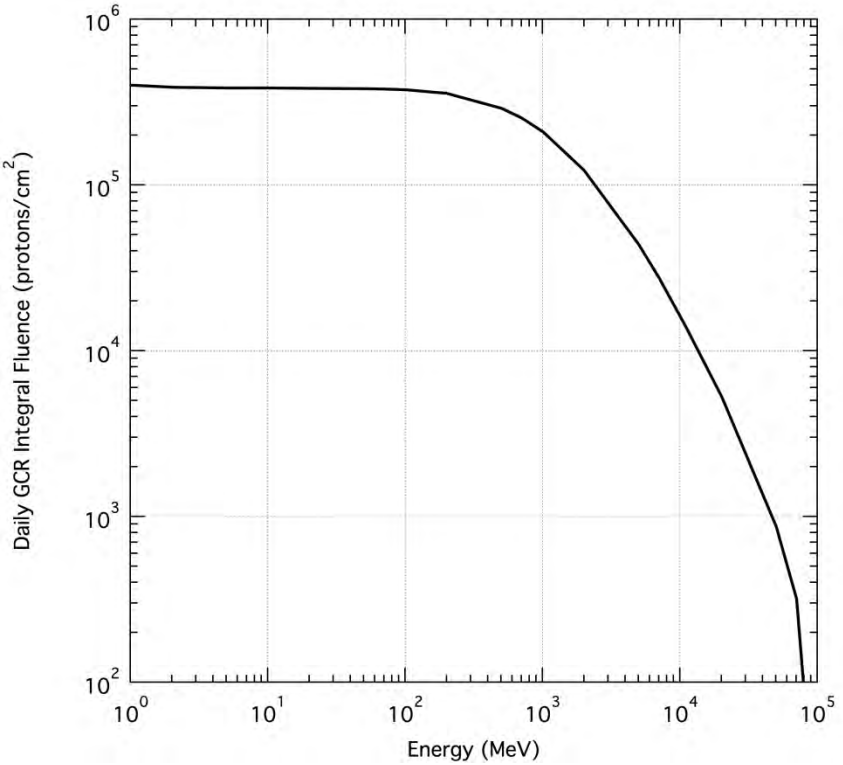

Figure 3.3.1.10.2-2. Daily Unshielded GCR Integral Proton Fluence

Table 3.3.1.10.2-2. Daily Unshielded GCR Integral Proton Fluence

Proton Energy	GCR - Solar Minimum Daily Integral Fluence
MeV	protons/cm^2
1.00E+00	4.007E+05
2.03E+00	3.880E+05
5.04E+00	3.846E+05
7.02E+00	3.844E+05
1.01E+01	3.842E+05
2.00E+01	3.838E+05
5.05E+01	3.819E+05
7.03E+01	3.798E+05
1.01E+02	3.755E+05
2.01E+02	3.564E+05
5.06E+02	2.901E+05
7.05E+02	2.535E+05

Proton Energy	GCR - Solar Minimum Daily Integral Fluence
MeV	protons/cm^2
1.01E+03	2.090E+05
2.01E+03	1.229E+05
5.00E+03	4.399E+04
7.07E+03	2.743E+04
1.11E+04	1.390E+04
2.02E+04	5.256E+03
5.02E+04	8.700E+02
7.08E+04	3.179E+02
1.00E+05	8.986E+00

Figure 3.3.1.10.2-3 and Table 3.3.1.10.2-3 specify total TID associated with the unshielded SPE environment and Table 3.3.1.10.2-4 specify total TID associated with the daily GCR fluence.

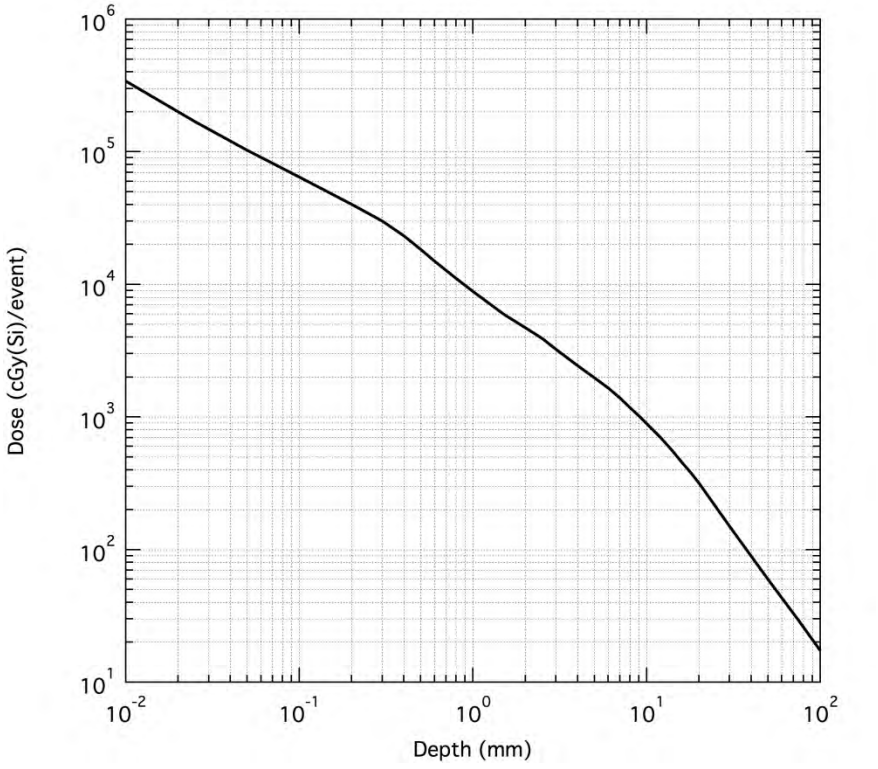

Figure 3.3.1.10.2-3. Total Unshielded SPE TID Inside Al Shielding

Table 3.3.1.10.2-3. Total Unshielded SPE TID Inside Al Shielding

Aluminum Shield Depth	Total SPE TID
mm	cGy(Si)/year
1.00E-02	3.41E+05
2.50E-02	1.69E+05
5.00E-02	1.03E+05
1.00E-01	6.43E+04
2.00E-01	4.01E+04
3.00E-01	3.00E+04
4.00E-01	2.33E+04
5.00E-01	1.84E+04
6.00E-01	1.50E+04
8.00E-01	1.11E+04
1.00E+00	8.83E+03
2.50E+00	3.91E+03
5.00E+00	1.97E+03
1.00E+01	8.87E+02
1.20E+01	7.03E+02
1.40E+01	5.57E+02
1.60E+01	4.53E+02
1.80E+01	3.77E+02
2.00E+01	3.18E+02
3.00E+01	1.50E+02
5.00E+01	5.97E+01
7.50E+01	2.94E+01
1.00E+02	1.73E+01

Table 3.3.1.10.2-4. Total Unshielded Daily GCR TID Inside Al Shielding

Aluminum Shield Depth	Daily GCR TID
cm	cGy(Si)/day
2.54e-02	3.76E-02
1.00e-01	3.56E-02
2.54e-01	3.43E-02
5.08e-01	3.28E-02
1.00e+00	3.11E-02
5.08e+00	2.33E-02
1.02e+01	1.78E-02

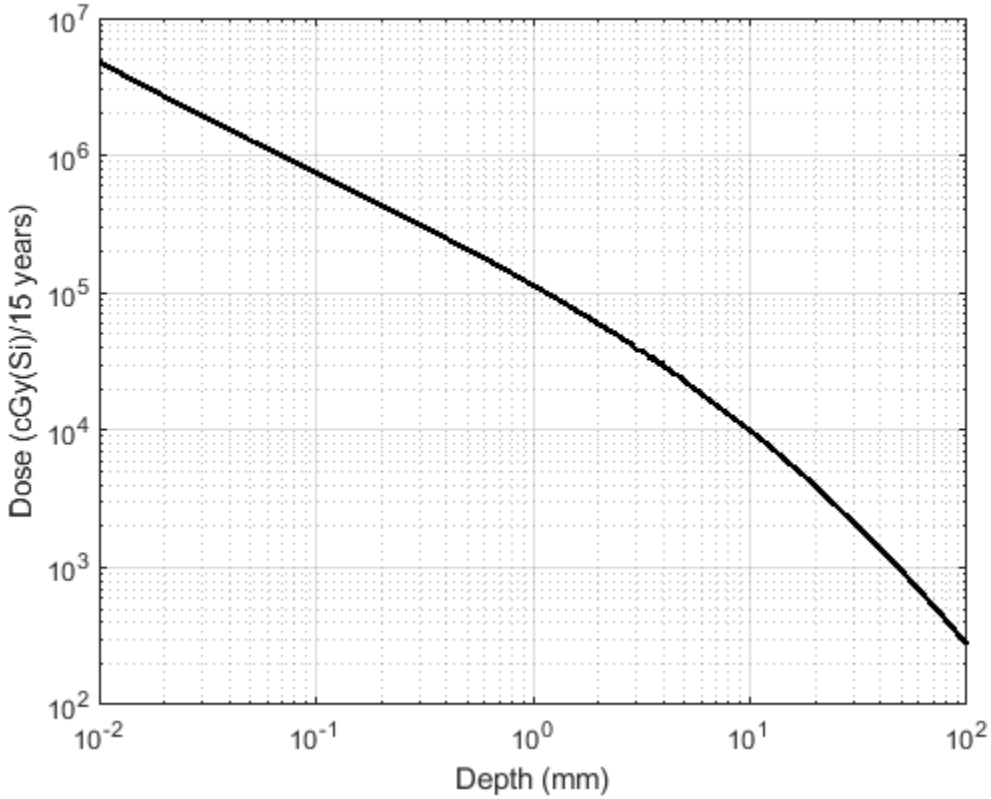

Figure 3.3.1.10.2-4. Total Unshielded SPE TID Inside Al Shielding – 15 Years

Table 3.3.1.10.2-5. Total Unshielded SPE TID Inside Al Shielding – 15 Years

Aluminum Shield Depth	Total SPE TID
mm	cGy(Si)/15 years
1.00E-02	4.79E+06
2.50E-02	2.24E+06
5.00E-02	1.28E+06
1.00E-01	7.47E+05
2.00E-01	4.35E+05
3.00E-01	3.16E+05
4.00E-01	2.48E+05
5.00E-01	2.06E+05
6.00E-01	1.78E+05
8.00E-01	1.38E+05
1.00E+00	1.13E+05
2.50E+00	4.79E+04

Aluminum Shield Depth	Total SPE TID
mm	cGy(Si)/15 years
5.00E+00	2.28E+04
1.00E+01	9.91E+03
1.20E+01	7.93E+03
1.40E+01	6.41E+03
1.60E+01	5.35E+03
1.80E+01	4.56E+03
2.00E+01	3.91E+03
3.00E+01	2.13E+03
5.00E+01	9.47E+02
7.50E+01	4.66E+02
1.00E+02	2.74E+02

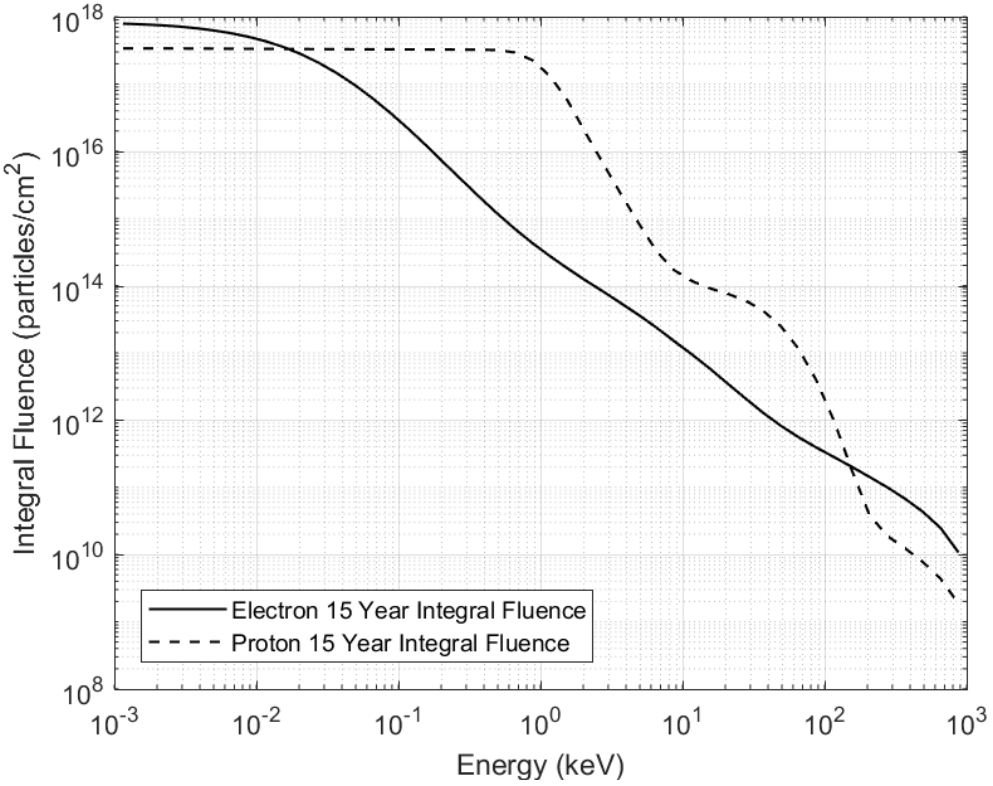

Figure 3.3.1.10.2-5. Integral Electron and Proton Fluence for 15 Year Exposure to Solar Wind and Earth's Magnetotail in a Near Rectilinear Halo Orbit, 95th percentile

Table 3.3.1.10.2-6. Integral Electron and Proton Fluence for 15 Year Exposure to Solar Wind and Earth's Magnetotail in a Near Rectilinear Halo Orbit, 95th percentile

Particle Energy	15 Year Integral Electron Fluence	15 Year Integral Proton Fluence
keV	electrons/cm^2	protons/cm^2
1.15E-03	7.91E+17	3.39E+17
1.55E-03	7.72E+17	3.39E+17
2.10E-03	7.49E+17	3.38E+17
2.80E-03	7.18E+17	3.38E+17
3.70E-03	6.79E+17	3.37E+17
4.90E-03	6.31E+17	3.36E+17
6.55E-03	5.73E+17	3.35E+17
8.75E-03	5.06E+17	3.34E+17
1.17E-02	4.31E+17	3.33E+17
1.56E-02	3.53E+17	3.32E+17
2.08E-02	2.76E+17	3.31E+17
2.77E-02	2.05E+17	3.30E+17
3.69E-02	1.45E+17	3.29E+17
4.92E-02	9.68E+16	3.29E+17
6.56E-02	6.15E+16	3.28E+17
8.75E-02	3.73E+16	3.27E+17
1.17E-01	2.17E+16	3.27E+17
1.56E-01	1.23E+16	3.26E+17
2.07E-01	6.84E+15	3.26E+17
2.77E-01	3.79E+15	3.25E+17
3.69E-01	2.11E+15	3.24E+17
4.92E-01	1.20E+15	3.20E+17
6.56E-01	7.07E+14	2.95E+17
8.75E-01	4.31E+14	2.27E+17
1.17E+00	2.73E+14	1.31E+17
1.56E+00	1.79E+14	5.56E+16
2.07E+00	1.20E+14	1.90E+16
2.77E+00	8.14E+13	6.48E+15
3.69E+00	5.47E+13	2.28E+15
4.92E+00	3.65E+13	8.44E+14
6.56E+00	2.37E+13	3.24E+14
8.75E+00	1.49E+13	1.69E+14
1.17E+01	9.41E+12	1.16E+14

Particle Energy	15 Year Integral Electron Fluence	15 Year Integral Proton Fluence
keV	electrons/cm^2	protons/cm^2
1.56E+01	5.81E+12	9.13E+13
2.07E+01	3.51E+12	7.58E+13
2.77E+01	2.10E+12	6.02E+13
3.69E+01	1.28E+12	4.23E+13
4.92E+01	8.23E+11	2.49E+13
6.56E+01	5.56E+11	1.15E+13
8.75E+01	3.90E+11	3.90E+12
1.17E+02	2.80E+11	9.50E+11
1.56E+02	2.01E+11	1.77E+11
2.07E+02	1.43E+11	3.86E+10
2.77E+02	9.95E+10	1.88E+10
3.69E+02	6.73E+10	1.24E+10
4.92E+02	4.31E+10	7.72E+09
6.56E+02	2.48E+10	4.35E+09
8.75E+02	1.08E+10	1.86E+09

Model Inputs

None.

Limitations

Probability that the unshielded SPE dose will not be exceeded during a single SPE event is estimated at 95%.

Technical Notes

All environment models were run for a near Earth interplanetary orbit which is geomagnetically unshielded. The unshielded SPE TID specification in Table 3.3.1.10.2-3 was defined by running the ESP/PSYCHIC model in SPENVIS in worst case mode, for protons only, with a prediction period of one year, zero offset from solar maximum, and a 95% confidence level. The TID calculations were performed using the SPENVIS Shieldose2 code, with the solid Aluminum sphere option. The GCR daily fluence was defined using CREME96, selecting the NEI option, and solar minimum (GCR maximum) conditions.

For Figure 3.3.1.10.2-4 and Table 3.3.1.10.2-5 the trajectory is a single 15-year long near-earth interplanetary (NEI or geomagnetically unshielded) segment with a distance from the Sun = 1 AU, and a start date of January 1, 1977. This date was chosen because it is close to the start of the 7 year maximum activity period of solar cycle 21, defined in SPENVIS as beginning 2.5 years before the date of the peak sunspot number, and ending 4.5 years after this date. This cycle

had the largest peak sunspot number (220.1) of the cycles within the range of the trajectory start dates allowed in SPENVIS.

ESP/PSYCHIC was run in total fluence mode for protons with the following settings: prediction period = automatic, offset in solar cycle = override, offset from solar maximum = 0 years, confidence level = 95%. Magnetic shielding is automatically switched off since the trajectory is specified as NEI. ESP reports that the specified trajectory spends 12.3 years in two solar maximum periods, and 2.7 years in solar minimum periods for which the fluence is set equal to zero. The TID was computed using Shieldose-2 with shielding configuration of the center of Al spheres, and target material is Si. Shieldose-2 does not compute TID for ions other than protons. The contribution from heavier ions is not significant due to their relatively low flux. The algorithm corresponding to the total fluence mode of ESP is described in Xapsos, M.A. et al., IEEE Transactions on Nuclear Science, vol. 47, no. 3, June 2000.
ESP/PSYCHIC also has a worst case mode. When ESP/PSYCHIC was run in this mode with all other inputs the same as for the run in total fluence mode, described above, the resulting TID was approximately one order of magnitude less than it was for the total fluence mode. The worst case mode uses an event that is not an actual event. It is a hypothetical event calculated from statistics of the ESP event database (Xapsos, M.A. et al., IEEE Transactions on Nuclear Science, vol. 46, no. 5, December 1999).

Figure 3.3.1.10.2-5 and Table 3.3.1.10.2-6 were generated using the L2-Charged Particle Environment (L2-CPE) model (Minow, J.I. et al., AIAA-2007-0910) for a near-rectilinear halo orbit (NRHO) for 15 years. The model includes exposure to the various regions of the Earth's magnetotail as well as the solar wind. These particles could be important for very thin external surface materials with 15 year mission life. Since the environment is directional, the highest fluence of each of the 6 surfaces of a cube was used with the 95th percentile setting of the model. The NRHO trajectory was generated with Copernicus using a SPICE kernel provided by Johnson Space Center/EG5 and was run for Jan. 2020 to Feb. 2035.

3.3.2 Single Event Effects

This section defines the ionizing radiation environments that may produce single event effects in electrical or electronic systems. Peak Galactic Cosmic Radiation (GCR) and Solar Particle Event (SPE) fluxes are encountered inside and outside Earth's magnetic field. In addition to these, inside the Earth's magnetic field, the peak trapped proton flux has to be included. Flux values inside spherical aluminum shielding during exposure to the SPE peak 5-minute average and worst day average fluxes are provided to support evaluation of Single Event Effects (SEE) rate concerns for shielded electronics. GCR and SPE proton fluxes are provided to support evaluation of proton effects on unshielded surface materials external to the Earth's magnetic field. Trapped and SPE proton fluxes are provided to support evaluation of proton effects on unshielded surface materials internal to the Earth's magnetic field.

A *pseudo* region of space is added in Section 3.3.1.10 Solar Particle Events (SPE). Since all the DRM can be considered "near-Earth", once outside the geomagnetic field, all regions of space will have the same SPE environment definition. So the unshielded subsection is a convenient

place to locate this definition, once, and reference it for all the appropriate regions. The shielded SPE environment still remains with and region of space subsection that is inside the Earth's magnetic field, as the shielding levels are dependent on the location within the magnetic field. The appropriate SPE environment will be determined for each DRM mission segment and incorporated into the DRM IR and Plasma memo.

Table 3.3.2-1 gives the applicability matrix for each of the DRMs (down the right hand column) for each of the regions of space defined in this document (across the top of the Table) for Single Event Effects. An "X" is placed in each box where the region of space is applicable to that DRM. For the "Staging and Transit Orbits" column, subsections of 3.3.2.2 are called out as applicable, since not all may be applicable for each DRM.

Unlike the total dose area, for SEE the environments are not summed. For each DRM mission segment, the worst-case environment from that segment will be the design environment incorporated into the DRM memo for that segment. Systems that are required to operate in multiple segments will have to account for all mission segment worst-case environments in their designs.

Note: Tables may contain abbreviated data as compared to the plotted data. Complete data sets are available in electronic form.

Table 3.3.2-1. Single Event Effects Applicability Matrix for the Design Reference Mission by Regions of Space

	LEO (3.3.2.1)	Staging and Transit Orbits (3.3.2.2)	GEO (3.3.2.3)	Interplanetary (3.3.2.4)	Lunar Orbit (3.3.2.5)	Lunar Surface (3.3.2.6)	NEA (3.3.2.7)	Mars Orb it (3.3.2.8)	Mars Surface (3.3.2.9)	GCR & Solar Particle Event (3.3.2.10)
Distant Retrograde Orbit	X	3.3.2.2.1 3.3.2.2.2		X						X
Crewed Lunar Orbit	X	3.3.2.2.1 3.3.2.2.2		X						X
Low Lunar Orbit	X	3.3.2.2.6 3.3.2.2.2		X	X					X
Initial Capability NEA	X	3.3.2.2.4 3.3.2.2.5 3.3.2.2.2		X						X
Advanced NEA	X	3.3.2.2.4 3.3.2.2.5 3.3.2.2.2		X						X
Full Capability NEA	X	3.3.2.2.6 3.3.2.2.7 3.3.2.2.8		X						X

	LEO (3.3.2.1)	Staging and Transit Orbits (3.3.2.2)	GEO (3.3.2.3)	Interplanetary (3.3.2.4)	Lunar Orbit (3.3.2.5)	Lunar Surface (3.3.2.6)	NEA (3.3.2.7)	Mars Orb it (3.3.2.8)	Mars Surface (3.3.2.9)	GCR & Solar Particle Event (3.3.2.10)
		3.3.2.2.5 3.3.2.2.2								
Lunar Surface Sortie	X	3.3.2.2.6 3.3.2.2.2		X	X	X				X
ISS Crew Delivery Backup	X	None								X
GEO Vicinity	X	3.3.2.2.6 3.3.2.2.2	X							X
Martian Moon	X	Reserved		X				X		X
Martian Landing	X	Reserved		X				X	X	X

3.3.2.1 LEO-ISS Orbit

Design Limits

Figure 3.3.2.1-1 and Table 3.3.2.1-1 present the ISS SPE peak rate LET flux inside selected aluminum shield thicknesses as a function of LET. Each thickness value is identical to the radius of the assumed spherical shielding.

Figure 3.3.2.1-2 and Table 3.3.2.1-2 provide the ISS SPE worst day average fluxes for the same shield geometry and thicknesses.

Figure 3.3.2.1-3 and Table 3.3.2.1-3 present integral proton fluxes of an ISS SPE and of the nominal and peak trapped protons.

Figure 3.3.2.1-4 and Table 3.3.2.1-4 present differential proton fluxes of an ISS SPE and of the nominal and peak trapped protons.

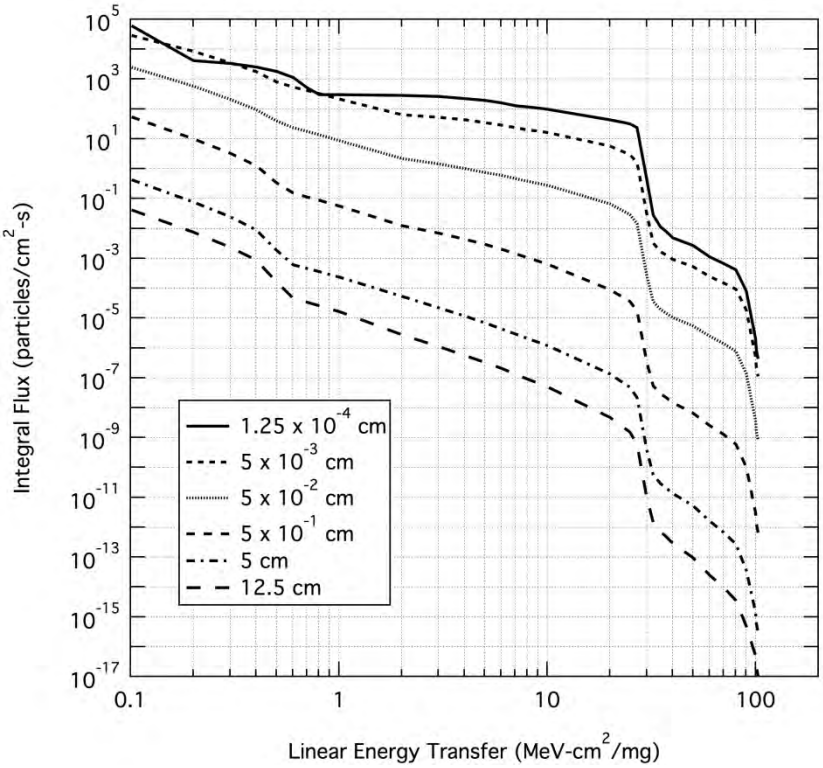

Figure 3.3.2.1-1. ISS SPE Integral Peak LET Flux for Selected Al Shielding Thickness as a Function of LET

Table 3.3.2.1-1. ISS SPE Integral Peak LET Flux for Selected Al Shielding Thickness as a Function of LET

LET	Shield Thickness 1.25 x 10^{-4} cm	Shield Thickness 5 x 10^{-2} cm	Shield Thickness 5 x 10^{-1} cm	Shield Thickness 5 cm	Shield Thickness 12.5 cm
MeV-cm^2/mg	Particles/cm^2-s	Particles/cm^2-s	Particles/cm^2-s	Particles/cm^2-s	Particles/cm^2-s
1.01E-01	6.04E+04	2.48E+03	5.37E+01	4.21E-01	4.12E-02
2.00E-01	4.14E+03	5.76E+02	1.01E+01	7.71E-02	7.52E-03
3.01E-01	3.33E+03	2.12E+02	3.26E+00	2.43E-02	2.34E-03
4.02E-01	2.55E+03	9.47E+01	1.26E+00	8.94E-03	8.56E-04
5.01E-01	1.82E+03	3.98E+01	3.40E-01	1.86E-03	1.65E-04
6.03E-01	1.13E+03	2.38E+01	1.53E-01	6.09E-04	4.61E-05
7.01E-01	5.19E+02	1.78E+01	1.14E-01	4.61E-04	3.40E-05
8.05E-01	3.03E+02	1.35E+01	8.68E-02	3.54E-04	2.57E-05
9.04E-01	3.03E+02	1.07E+01	6.90E-02	2.85E-04	2.04E-05
1.00E+00	3.03E+02	8.75E+00	5.58E-02	2.36E-04	1.66E-05

LET	Shield Thickness 1.25×10^{-4} cm	Shield Thickness 5×10^{-2} cm	Shield Thickness 5×10^{-1} cm	Shield Thickness 5 cm	Shield Thickness 12.5 cm
MeV-cm^2/mg	Particles/cm^2-s	Particles/cm^2-s	Particles/cm^2-s	Particles/cm^2-s	Particles/cm^2-s
2.01E+00	2.85E+02	2.18E+00	1.22E-02	5.23E-05	2.78E-06
3.02E+00	2.59E+02	1.43E+00	6.92E-03	2.20E-05	1.09E-06
4.04E+00	2.24E+02	1.01E+00	4.35E-03	1.15E-05	5.56E-07
5.03E+00	1.90E+02	7.50E-01	2.89E-03	6.81E-06	3.22E-07
6.06E+00	1.60E+02	5.86E-01	1.98E-03	4.33E-06	2.01E-07
7.04E+00	1.26E+02	4.65E-01	1.41E-03	2.92E-06	1.32E-07
8.00E+00	1.18E+02	3.80E-01	1.04E-03	2.07E-06	9.12E-08
8.99E+00	1.08E+02	3.26E-01	8.10E-04	1.56E-06	6.78E-08
1.01E+01	9.75E+01	2.75E-01	6.18E-04	1.15E-06	4.88E-08
2.00E+01	4.35E+01	6.71E-02	9.07E-05	1.36E-07	4.68E-09
2.49E+01	3.17E+01	2.89E-02	3.56E-05	4.88E-08	1.52E-09
2.70E+01	2.34E+01	1.46E-02	1.73E-05	2.17E-08	6.02E-10
3.00E+01	4.44E-01	2.73E-04	3.36E-07	3.89E-10	1.00E-11
3.22E+01	2.85E-02	3.61E-05	5.37E-08	5.58E-11	1.45E-12
3.49E+01	1.12E-02	1.95E-05	2.96E-08	2.89E-11	7.22E-13
3.70E+01	8.19E-03	1.50E-05	2.22E-08	2.09E-11	4.93E-13
4.01E+01	4.88E-03	1.04E-05	1.48E-08	1.34E-11	2.85E-13
5.00E+01	2.66E-03	5.53E-06	6.62E-09	5.28E-12	9.47E-14
6.02E+01	1.11E-03	2.45E-06	2.52E-09	1.59E-12	2.45E-14
7.00E+01	6.83E-04	1.42E-06	1.28E-09	6.81E-13	9.84E-15
8.04E+01	4.10E-04	7.66E-07	6.02E-10	2.75E-13	3.56E-15
9.03E+01	8.03E-05	1.40E-07	1.02E-10	3.63E-14	4.84E-16
1.00E+02	1.95E-06	3.59E-09	2.99E-12	1.39E-15	4.88E-17
1.01E+02	8.68E-07	1.60E-09	1.34E-12	6.00E-16	2.11E-17
1.03E+02	4.28E-07	7.80E-10	6.46E-13	2.89E-16	1.02E-17

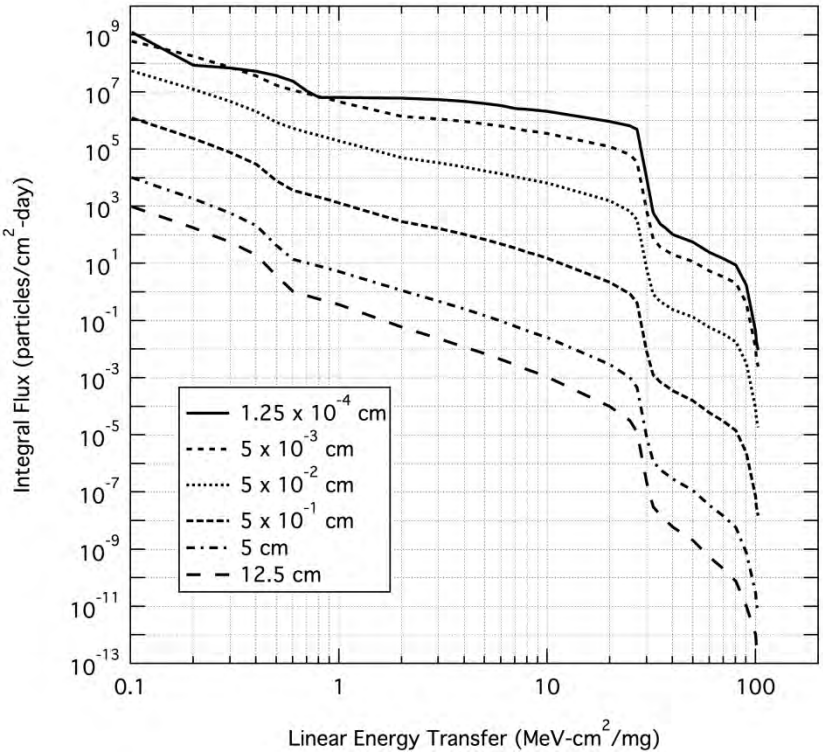

Figure 3.3.2.1-2. ISS SPE Worst Day Integral Flux for Selected Al Shielding Thickness as a Function of LET

Table 3.3.2.1-2. ISS SPE Worst Day Integral Flux for Selected Al Shielding Thickness as a Function of LET

LET	Shield Thickness 1.25 x 10-4 cm	Shield Thickness 5 x 10-2 cm	Shield Thickness 5 x 10-1 cm	Shield Thickness 5 cm	Shield Thickness 12.5 cm
MeV-cm2/mg	Particles/cm2-day	Particles/cm2-day	Particles/cm2-day	Particles/cm2-day	Particles/cm2-day
1.01E-01	1.26E+09	5.45E+07	1.25E+06	1.01E+04	9.72E+02
2.00E-01	8.68E+07	1.27E+07	2.36E+05	1.85E+03	1.77E+02
3.01E-01	6.98E+07	4.66E+06	7.62E+04	5.80E+02	5.51E+01
4.02E-01	5.32E+07	2.09E+06	2.95E+04	2.14E+02	2.00E+01
5.01E-01	3.80E+07	8.79E+05	7.95E+03	4.35E+01	3.79E+00
6.03E-01	2.36E+07	5.29E+05	3.60E+03	1.38E+01	1.02E+00
7.01E-01	1.09E+07	3.95E+05	2.69E+03	1.04E+01	7.50E-01
8.05E-01	6.44E+06	3.00E+05	2.05E+03	7.96E+00	5.65E-01
9.04E-01	6.42E+06	2.40E+05	1.63E+03	6.39E+00	4.47E-01
1.00E+00	6.40E+06	1.96E+05	1.32E+03	5.24E+00	3.62E-01

LET	Shield Thickness 1.25 x 10-4 cm	Shield Thickness 5 x 10-2 cm	Shield Thickness 5 x 10-1 cm	Shield Thickness 5 cm	Shield Thickness 12.5 cm
MeV-cm2/mg	Particles/cm2-day	Particles/cm2-day	Particles/cm2-day	Particles/cm2-day	Particles/cm2-day
2.01E+00	6.04E+06	5.02E+04	2.92E+02	1.13E+00	5.87E-02
3.02E+00	5.46E+06	3.29E+04	1.66E+02	4.75E-01	2.31E-02
4.04E+00	4.72E+06	2.34E+04	1.04E+02	2.48E-01	1.18E-02
5.03E+00	4.00E+06	1.74E+04	6.93E+01	1.47E-01	6.84E-03
6.06E+00	3.36E+06	1.36E+04	4.75E+01	9.29E-02	4.26E-03
7.04E+00	2.66E+06	1.08E+04	3.38E+01	6.25E-02	2.80E-03
8.00E+00	2.50E+06	8.84E+03	2.51E+01	4.42E-02	1.93E-03
8.99E+00	2.28E+06	7.63E+03	1.95E+01	3.33E-02	1.44E-03
1.01E+01	2.06E+06	6.42E+03	1.48E+01	2.45E-02	1.04E-03
2.00E+01	9.18E+05	1.57E+03	2.18E+00	2.89E-03	9.92E-05
2.49E+01	6.64E+05	6.77E+02	8.56E-01	1.04E-03	3.21E-05
2.70E+01	4.88E+05	3.40E+02	4.15E-01	4.60E-04	1.28E-05
3.00E+01	9.28E+03	6.37E+00	8.01E-03	8.23E-06	2.12E-07
3.22E+01	5.96E+02	8.48E-01	1.27E-03	1.18E-06	3.08E-08
3.49E+01	2.36E+02	4.60E-01	7.00E-04	6.15E-07	1.53E-08
3.70E+01	1.73E+02	3.53E-01	5.24E-04	4.44E-07	1.04E-08
4.01E+01	1.04E+02	2.45E-01	3.50E-04	2.83E-07	6.02E-09
5.00E+01	5.66E+01	1.31E-01	1.56E-04	1.12E-07	2.01E-09
6.02E+01	2.38E+01	5.78E-02	5.92E-05	3.36E-08	5.22E-10
7.00E+01	1.46E+01	3.37E-02	2.98E-05	1.44E-08	2.08E-10
8.04E+01	8.76E+00	1.81E-02	1.40E-05	5.84E-09	7.54E-11
9.03E+01	1.73E+00	3.30E-03	2.37E-06	7.72E-10	1.03E-11
1.00E+02	4.20E-02	8.50E-05	6.91E-08	2.94E-11	1.04E-12
1.01E+02	1.87E-02	3.79E-05	3.11E-08	1.27E-11	4.47E-13
1.03E+02	9.20E-03	1.85E-05	1.50E-08	6.12E-12	2.15E-13

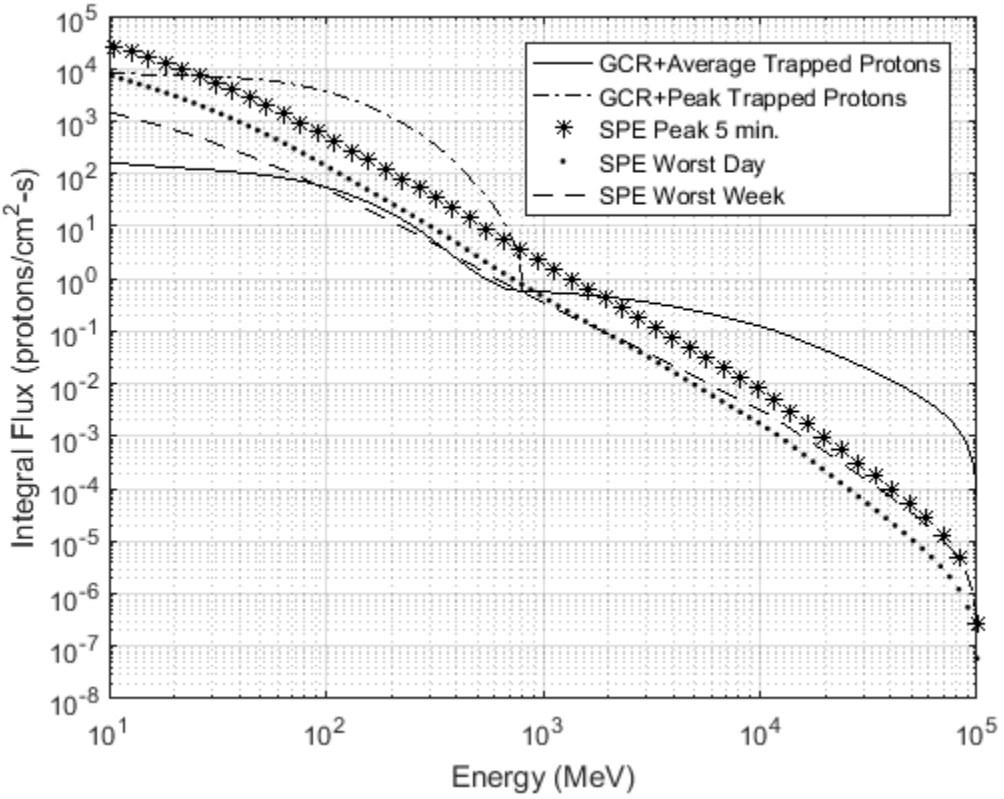

Figure 3.3.2.1-3. Integral Proton Flux of an ISS SPE and GCR

Table 3.3.2.1-3. Integral Proton Flux for an ISS SPE, Solar Minimum GCR, Average Trapped Protons and Peak Trapped Protons

Proton Energy	GCR + Average Trapped	GCR + Peak Trapped	SPE Worst 5 Minutes	SPE Worst Day	SPE Worst Week
MeV	p+/cm^2-s	p+/cm^2-s	p+/cm^2-s	p+/cm^2-s	p+/cm^2-s
1.00E+01	1.61E+02	8.08E+03	2.83E+04	7.44E+03	1.46E+03
1.31E+01	1.48E+02	7.90E+03	2.05E+04	5.44E+03	1.12E+03
1.70E+01	1.37E+02	7.65E+03	1.44E+04	3.85E+03	8.30E+02
2.21E+01	1.27E+02	7.37E+03	9.72E+03	2.63E+03	5.99E+02
2.87E+01	1.18E+02	7.08E+03	6.34E+03	1.73E+03	4.20E+02
3.73E+01	1.08E+02	6.74E+03	3.99E+03	1.10E+03	2.85E+02
4.85E+01	9.68E+01	6.23E+03	2.42E+03	6.68E+02	1.88E+02
6.30E+01	8.33E+01	5.47E+03	1.42E+03	3.92E+02	1.20E+02
8.19E+01	6.78E+01	4.48E+03	8.06E+02	2.22E+02	7.41E+01
1.06E+02	5.11E+01	3.40E+03	4.46E+02	1.22E+02	4.45E+01

Proton Energy	GCR + Average Trapped	GCR + Peak Trapped	SPE Worst 5 Minutes	SPE Worst Day	SPE Worst Week
MeV	p+/cm^2-s	p+/cm^2-s	p+/cm^2-s	p+/cm^2-s	p+/cm^2-s
1.38E+02	3.52E+01	2.37E+03	2.43E+02	6.52E+01	2.61E+01
1.80E+02	2.20E+01	1.49E+03	1.33E+02	3.49E+01	1.52E+01
2.34E+02	1.21E+01	8.43E+02	7.42E+01	1.88E+01	8.86E+00
3.04E+02	5.81E+00	4.10E+02	4.07E+01	9.87E+00	5.02E+00
3.95E+02	2.51E+00	1.61E+02	2.15E+01	5.01E+00	2.76E+00
5.13E+02	1.14E+00	5.03E+01	1.08E+01	2.44E+00	1.47E+00
6.67E+02	6.60E-01	1.15E+01	5.47E+00	1.23E+00	8.24E-01
8.67E+02	5.80E-01	5.80E-01	2.85E+00	6.40E-01	4.75E-01
1.13E+03	5.44E-01	5.44E-01	1.50E+00	3.37E-01	2.77E-01
1.46E+03	5.02E-01	5.02E-01	8.02E-01	1.80E-01	1.64E-01
1.90E+03	4.55E-01	4.55E-01	4.36E-01	9.79E-02	9.81E-02
2.48E+03	4.02E-01	4.02E-01	2.38E-01	5.34E-02	5.88E-02
3.22E+03	3.43E-01	3.43E-01	1.27E-01	2.85E-02	3.46E-02
4.18E+03	2.84E-01	2.84E-01	6.63E-02	1.49E-02	1.99E-02
5.44E+03	2.29E-01	2.29E-01	3.44E-02	7.74E-03	1.14E-02
7.07E+03	1.80E-01	1.80E-01	1.80E-02	4.04E-03	6.54E-03
9.18E+03	1.37E-01	1.37E-01	9.49E-03	2.13E-03	3.77E-03
1.19E+04	9.95E-02	9.95E-02	4.80E-03	1.08E-03	2.08E-03
1.55E+04	6.60E-02	6.60E-02	2.15E-03	4.83E-04	1.02E-03
2.02E+04	4.24E-02	4.24E-02	9.40E-04	2.11E-04	4.93E-04
2.62E+04	2.66E-02	2.66E-02	4.09E-04	9.19E-05	2.36E-04
3.41E+04	1.62E-02	1.62E-02	1.76E-04	3.96E-05	1.12E-04
4.43E+04	9.36E-03	9.36E-03	7.40E-05	1.66E-05	5.11E-05
5.76E+04	4.92E-03	4.92E-03	2.91E-05	6.55E-06	2.18E-05
7.48E+04	2.06E-03	2.06E-03	9.46E-06	2.13E-06	7.59E-06
9.73E+04	2.23E-04	2.23E-04	8.24E-07	1.85E-07	7.00E-07
1.00E+05	7.24E-05	7.24E-05	2.63E-07	5.91E-08	2.25E-07

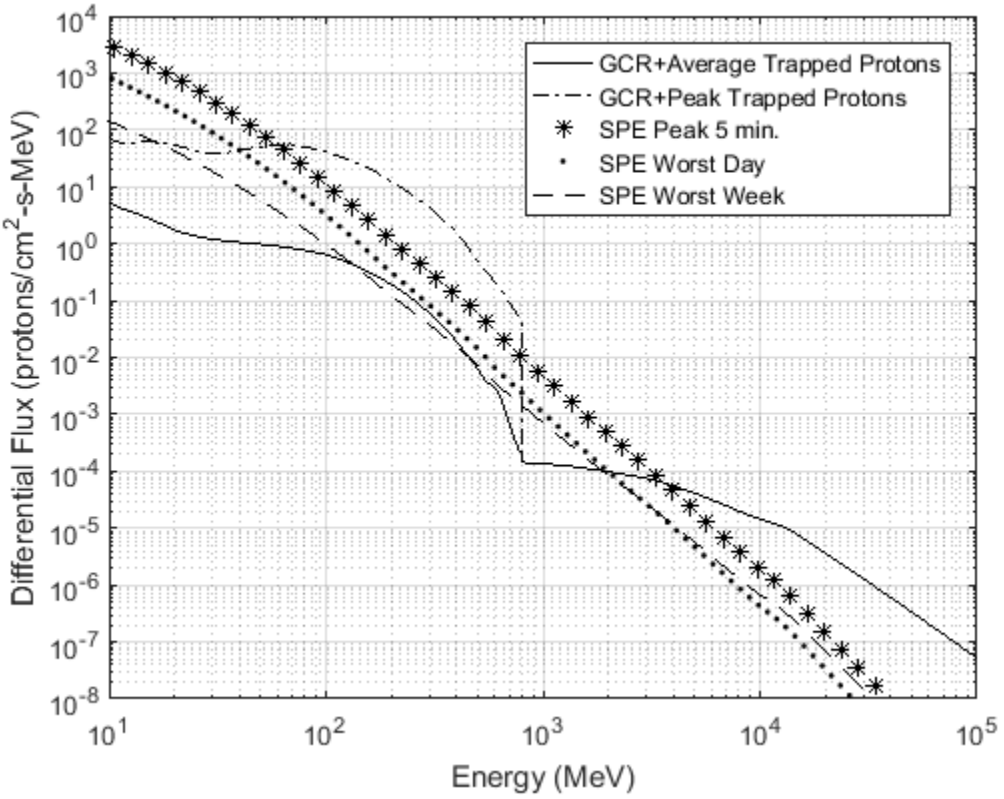

Figure 3.3.2.1-4. Differential Proton Flux for ISS SPE and Solar Minimum GCR

Table 3.3.2.1-4. Differential Proton Flux for an ISS SPE, Solar Minimum GCR, Average Trapped Protons and Peak Trapped Protons

Proton Energy	GCR + Average Trapped	GCR + Peak Trapped	SPE Worst 5 Minutes	SPE Worst Day	SPE Worst Week
MeV	p+/cm^2-s-MeV	p+/cm^2-s-MeV	p+/cm^2-s-MeV	p+/cm^2-s-MeV	p+/cm^2-s-MeV
1.00E+01	5.40E+00	7.37E+01	3.24E+03	8.29E+02	1.41E+02
1.31E+01	3.48E+00	6.19E+01	2.00E+03	5.17E+02	9.12E+01
1.70E+01	2.33E+00	5.94E+01	1.18E+03	3.10E+02	5.72E+01
2.21E+01	1.54E+00	5.41E+01	6.75E+02	1.79E+02	3.48E+01
2.87E+01	1.23E+00	4.98E+01	3.70E+02	9.91E+01	2.04E+01
3.73E+01	1.08E+00	4.95E+01	1.93E+02	5.23E+01	1.15E+01
4.85E+01	9.84E-01	4.92E+01	9.66E+01	2.65E+01	6.30E+00
6.30E+01	8.80E-01	4.12E+01	4.64E+01	1.28E+01	3.32E+00
8.19E+01	7.54E-01	3.95E+01	2.14E+01	5.95E+00	1.69E+00
1.06E+02	5.94E-01	3.82E+01	9.38E+00	2.61E+00	8.15E-01
1.38E+02	4.02E-01	2.64E+01	3.99E+00	1.11E+00	3.81E-01

Proton Energy	GCR + Average Trapped	GCR + Peak Trapped	SPE Worst 5 Minutes	SPE Worst Day	SPE Worst Week
MeV	p+/cm^2-s-MeV	p+/cm^2-s-MeV	p+/cm^2-s-MeV	p+/cm^2-s-MeV	p+/cm^2-s-MeV
1.80E+02	2.43E-01	1.60E+01	1.62E+00	4.45E-01	1.69E-01
2.34E+02	1.29E-01	8.58E+00	6.99E-01	1.88E-01	7.82E-02
3.04E+02	5.67E-02	4.11E+00	3.09E-01	8.02E-02	3.62E-02
3.95E+02	2.01E-02	1.63E+00	1.34E-01	3.31E-02	1.60E-02
5.13E+02	5.41E-03	4.36E-01	5.57E-02	1.29E-02	6.69E-03
6.67E+02	1.19E-03	1.23E-01	2.00E-02	4.49E-03	2.55E-03
8.67E+02	1.40E-04	1.40E-04	7.89E-03	1.77E-03	1.11E-03
1.13E+03	1.31E-04	1.31E-04	3.15E-03	7.07E-04	4.90E-04
1.46E+03	1.16E-04	1.16E-04	1.26E-03	2.83E-04	2.16E-04
1.90E+03	1.01E-04	1.01E-04	5.16E-04	1.16E-04	9.79E-05
2.48E+03	8.58E-05	8.58E-05	2.20E-04	4.93E-05	4.61E-05
3.22E+03	7.06E-05	7.06E-05	9.48E-05	2.13E-05	2.20E-05
4.18E+03	5.23E-05	5.23E-05	3.86E-05	8.68E-06	9.89E-06
5.44E+03	3.65E-05	3.65E-05	1.54E-05	3.46E-06	4.36E-06
7.07E+03	2.43E-05	2.43E-05	6.10E-06	1.37E-06	1.90E-06
9.18E+03	1.61E-05	1.61E-05	2.47E-06	5.54E-07	8.51E-07
1.19E+04	1.17E-05	1.17E-05	1.13E-06	2.53E-07	4.30E-07
1.55E+04	6.88E-06	6.88E-06	4.24E-07	9.52E-08	1.79E-07
2.02E+04	3.57E-06	3.57E-06	1.43E-07	3.22E-08	6.66E-08
2.62E+04	1.82E-06	1.82E-06	4.83E-08	1.09E-08	2.48E-08
3.41E+04	9.22E-07	9.22E-07	1.63E-08	3.67E-09	9.26E-09
4.43E+04	4.62E-07	4.62E-07	5.51E-09	1.24E-09	3.45E-09
5.76E+04	2.30E-07	2.30E-07	1.86E-09	4.18E-10	1.29E-09
7.48E+04	1.14E-07	1.14E-07	6.28E-10	1.41E-10	4.81E-10
9.73E+04	5.62E-08	5.62E-08	2.12E-10	4.76E-11	1.79E-10
1.00E+05	5.21E-08	5.21E-08	1.89E-10	4.25E-11	1.62E-10

Model Inputs

None

Limitations

Probability that the ISS SPE Peak Flux will not be exceeded is estimated at 97%.

Technical Notes

All environment models were run for the assumed ISS orbit of 500 km circular orbit at 51.6° inclination. The ISS SPE LET, and trapped proton integral and differential flux specifications

were developed using CREME96 assuming a stormy magnetosphere. All SPE fluxes were multiplied by 2 for model uncertainty. CREME96 generates trapped proton fluxes using the AP8MIN model. All trapped proton fluxes are multiplied by 2 for AP8MIN model uncertainty, and by another factor of 2 for the known AP8MIN model underestimation of fluxes at the altitude of the ISS orbit.

A spherical shield model with radius set equal to the minimum shield thickness provides very conservative results. CREME96 can also model flux inside other 3D shield geometries if the distribution of shielding thicknesses is known.

An industry accepted radiation transport code that provides a semi-infinite slab model should be used to define flux at selected depths within surface coatings and materials.

Not all passes through the SAA will constitute a worst-case pass. The worst-case pass is one that traverses the center of the SAA where the proton flux is at a maximum. The duration of one of these passes is nominally 10 minutes but may be as long as 20 minutes. These worst-case passes constitute approximately 3.6% of the LEO Mission time.

3.3.2.2 Staging and Transit Orbits

3.3.2.2.1 Low Earth Orbit 185 x 1806 km

The orbit does stay inside the Earth's geomagnetic field during the orbit and the environment contains exposure to the trapped protons. Therefore, the SEE environment model parameters for LEO 185 x 1806 km orbit are the trapped protons, geomagnetic shielded GCR and shielded Solar Particle Event.

Figure 3.3.2.2.1-1 and Table 3.3.2.2.1-1 present the SPE peak rate LET flux inside selected aluminum shield thicknesses as a function of LET. Each thickness value is identical to the radius of the assumed spherical shielding.

Figure 3.3.2.2.1-2 and Table 3.3.2.2.1-2 provide the SPE worst day average fluxes for the same shield geometry and thicknesses.

Figure 3.3.2.2.1-3 and Table 3.3.2.2.1-3 present integral proton flux of the peak trapped protons.

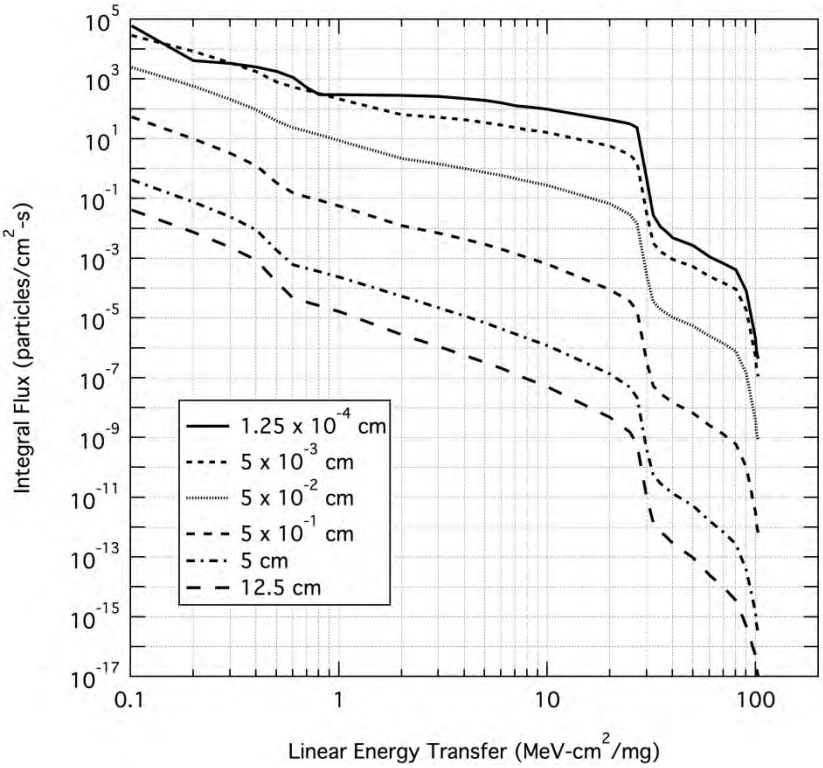

Figure 3.3.2.2.1-1. SPE Integral Peak LET Flux for Selected Al Shielding Thickness as a Function of LET

Table 3.3.2.2.1-1. SPE Integral Peak LET Flux for Selected Al Shielding Thickness as a Function of LET

LET	Shield Thickness 1.25 x 10^{-4} cm	Shield Thickness 5 x 10^{-2} cm	Shield Thickness 5 x 10^{-1} cm	Shield Thickness 5 cm	Shield Thickness 12.5 cm
MeV-cm^2/mg	Particles/cm^2-s	Particles/cm^2-s	Particles/cm^2-s	Particles/cm^2-s	Particles/cm^2-s
1.01E-01	6.04E+04	2.48E+03	5.37E+01	4.21E-01	4.12E-02
2.00E-01	4.14E+03	5.76E+02	1.01E+01	7.71E-02	7.52E-03
3.01E-01	3.33E+03	2.12E+02	3.26E+00	2.43E-02	2.34E-03
4.02E-01	2.55E+03	9.47E+01	1.26E+00	8.94E-03	8.56E-04
5.01E-01	1.82E+03	3.98E+01	3.40E-01	1.86E-03	1.65E-04
6.03E-01	1.13E+03	2.38E+01	1.53E-01	6.09E-04	4.61E-05
7.01E-01	5.19E+02	1.78E+01	1.14E-01	4.61E-04	3.40E-05
8.05E-01	3.03E+02	1.35E+01	8.68E-02	3.54E-04	2.57E-05
9.04E-01	3.03E+02	1.07E+01	6.90E-02	2.85E-04	2.04E-05
1.00E+00	3.03E+02	8.75E+00	5.58E-02	2.36E-04	1.66E-05

LET	Shield Thickness 1.25×10^{-4} cm	Shield Thickness 5×10^{-2} cm	Shield Thickness 5×10^{-1} cm	Shield Thickness 5 cm	Shield Thickness 12.5 cm
MeV-cm^2/mg	Particles/cm^2-s	Particles/cm^2-s	Particles/cm^2-s	Particles/cm^2-s	Particles/cm^2-s
2.01E+00	2.85E+02	2.18E+00	1.22E-02	5.23E-05	2.78E-06
3.02E+00	2.59E+02	1.43E+00	6.92E-03	2.20E-05	1.09E-06
4.04E+00	2.24E+02	1.01E+00	4.35E-03	1.15E-05	5.56E-07
5.03E+00	1.90E+02	7.50E-01	2.89E-03	6.81E-06	3.22E-07
6.06E+00	1.60E+02	5.86E-01	1.98E-03	4.33E-06	2.01E-07
7.04E+00	1.26E+02	4.65E-01	1.41E-03	2.92E-06	1.32E-07
8.00E+00	1.18E+02	3.80E-01	1.04E-03	2.07E-06	9.12E-08
8.99E+00	1.08E+02	3.26E-01	8.10E-04	1.56E-06	6.78E-08
1.01E+01	9.75E+01	2.75E-01	6.18E-04	1.15E-06	4.88E-08
2.00E+01	4.35E+01	6.71E-02	9.07E-05	1.36E-07	4.68E-09
2.49E+01	3.17E+01	2.89E-02	3.56E-05	4.88E-08	1.52E-09
2.70E+01	2.34E+01	1.46E-02	1.73E-05	2.17E-08	6.02E-10
3.00E+01	4.44E-01	2.73E-04	3.36E-07	3.89E-10	1.00E-11
3.22E+01	2.85E-02	3.61E-05	5.37E-08	5.58E-11	1.45E-12
3.49E+01	1.12E-02	1.95E-05	2.96E-08	2.89E-11	7.22E-13
3.70E+01	8.19E-03	1.50E-05	2.22E-08	2.09E-11	4.93E-13
4.01E+01	4.88E-03	1.04E-05	1.48E-08	1.34E-11	2.85E-13
5.00E+01	2.66E-03	5.53E-06	6.62E-09	5.28E-12	9.47E-14
6.02E+01	1.11E-03	2.45E-06	2.52E-09	1.59E-12	2.45E-14
7.00E+01	6.83E-04	1.42E-06	1.28E-09	6.81E-13	9.84E-15
8.04E+01	4.10E-04	7.66E-07	6.02E-10	2.75E-13	3.56E-15
9.03E+01	8.03E-05	1.40E-07	1.02E-10	3.63E-14	4.84E-16
1.00E+02	1.95E-06	3.59E-09	2.99E-12	1.39E-15	4.88E-17
1.01E+02	8.68E-07	1.60E-09	1.34E-12	6.00E-16	2.11E-17
1.03E+02	4.28E-07	7.80E-10	6.46E-13	2.89E-16	1.02E-17

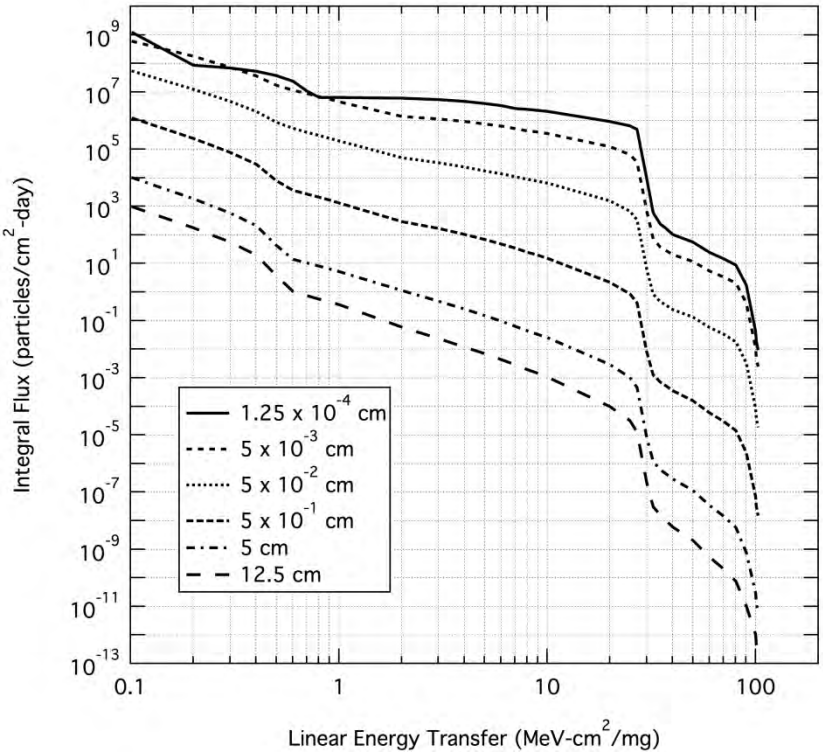

Figure 3.3.2.2.1-2. SPE Worst Day Integral Flux for Selected Al Shielding Thickness as a Function of LET

Table 3.3.2.2.1-2. SPE Worst Day Integral Flux for Selected Al Shielding Thickness as a Function of LET

LET	Shield Thickness 1.25 x 10^{-4} cm	Shield Thickness 5 x 10^{-2} cm	Shield Thickness 5 x 10^{-1} cm	Shield Thickness 5 cm	Shield Thickness 12.5 cm
MeV-cm^2/mg	Particles/cm^2-day	Particles/cm^2-day	Particles/cm^2-day	Particles/cm^2-day	Particles/cm^2-day
1.01E-01	1.26E+09	5.45E+07	1.25E+06	1.01E+04	9.72E+02
2.00E-01	8.68E+07	1.27E+07	2.36E+05	1.85E+03	1.77E+02
3.01E-01	6.98E+07	4.66E+06	7.62E+04	5.80E+02	5.51E+01
4.02E-01	5.32E+07	2.09E+06	2.95E+04	2.14E+02	2.00E+01
5.01E-01	3.80E+07	8.79E+05	7.95E+03	4.35E+01	3.79E+00
6.03E-01	2.36E+07	5.29E+05	3.60E+03	1.38E+01	1.02E+00
7.01E-01	1.09E+07	3.95E+05	2.69E+03	1.04E+01	7.50E-01
8.05E-01	6.44E+06	3.00E+05	2.05E+03	7.96E+00	5.65E-01
9.04E-01	6.42E+06	2.40E+05	1.63E+03	6.39E+00	4.47E-01
1.00E+00	6.40E+06	1.96E+05	1.32E+03	5.24E+00	3.62E-01
2.01E+00	6.04E+06	5.02E+04	2.92E+02	1.13E+00	5.87E-02

LET	Shield Thickness 1.25×10^{-4} cm	Shield Thickness 5×10^{-2} cm	Shield Thickness 5×10^{-1} cm	Shield Thickness 5 cm	Shield Thickness 12.5 cm
MeV-cm^2/mg	Particles/cm^2-day	Particles/cm^2-day	Particles/cm^2-day	Particles/cm^2-day	Particles/cm^2-day
3.02E+00	5.46E+06	3.29E+04	1.66E+02	4.75E-01	2.31E-02
4.04E+00	4.72E+06	2.34E+04	1.04E+02	2.48E-01	1.18E-02
5.03E+00	4.00E+06	1.74E+04	6.93E+01	1.47E-01	6.84E-03
6.06E+00	3.36E+06	1.36E+04	4.75E+01	9.29E-02	4.26E-03
7.04E+00	2.66E+06	1.08E+04	3.38E+01	6.25E-02	2.80E-03
8.00E+00	2.50E+06	8.84E+03	2.51E+01	4.42E-02	1.93E-03
8.99E+00	2.28E+06	7.63E+03	1.95E+01	3.33E-02	1.44E-03
1.01E+01	2.06E+06	6.42E+03	1.48E+01	2.45E-02	1.04E-03
2.00E+01	9.18E+05	1.57E+03	2.18E+00	2.89E-03	9.92E-05
2.49E+01	6.64E+05	6.77E+02	8.56E-01	1.04E-03	3.21E-05
2.70E+01	4.88E+05	3.40E+02	4.15E-01	4.60E-04	1.28E-05
3.00E+01	9.28E+03	6.37E+00	8.01E-03	8.23E-06	2.12E-07
3.22E+01	5.96E+02	8.48E-01	1.27E-03	1.18E-06	3.08E-08
3.49E+01	2.36E+02	4.60E-01	7.00E-04	6.15E-07	1.53E-08
3.70E+01	1.73E+02	3.53E-01	5.24E-04	4.44E-07	1.04E-08
4.01E+01	1.04E+02	2.45E-01	3.50E-04	2.83E-07	6.02E-09
5.00E+01	5.66E+01	1.31E-01	1.56E-04	1.12E-07	2.01E-09
6.02E+01	2.38E+01	5.78E-02	5.92E-05	3.36E-08	5.22E-10
7.00E+01	1.46E+01	3.37E-02	2.98E-05	1.44E-08	2.08E-10
8.04E+01	8.76E+00	1.81E-02	1.40E-05	5.84E-09	7.54E-11
9.03E+01	1.73E+00	3.30E-03	2.37E-06	7.72E-10	1.03E-11
1.00E+02	4.20E-02	8.50E-05	6.91E-08	2.94E-11	1.04E-12
1.01E+02	1.87E-02	3.79E-05	3.11E-08	1.27E-11	4.47E-13
1.03E+02	9.20E-03	1.85E-05	1.50E-08	6.12E-12	2.15E-13

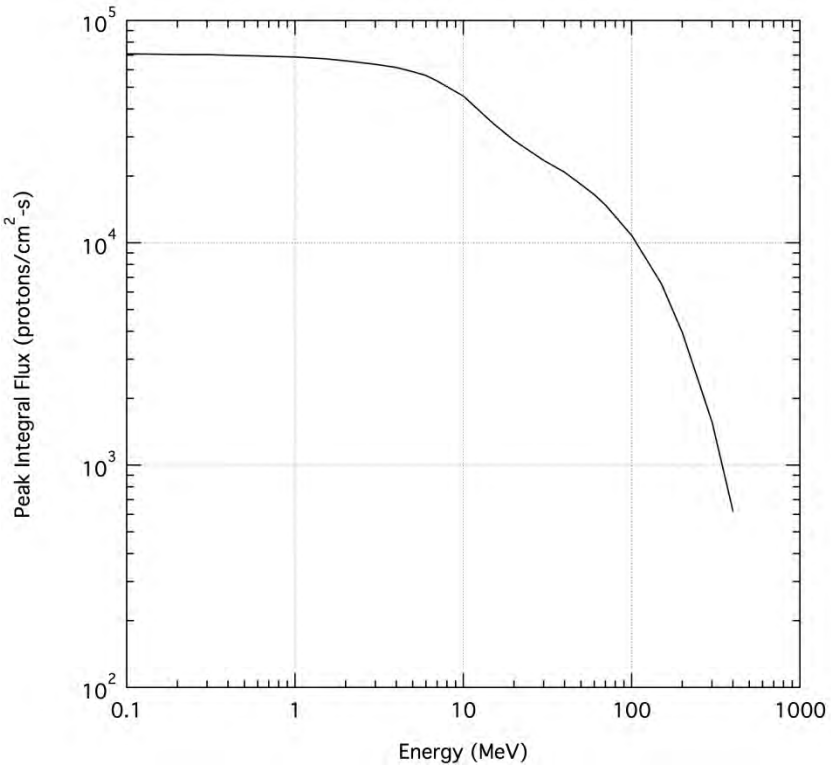

Figure 3.3.2.2.1-3. Integral Peak Trapped Proton Flux

Table 3.3.2.2.1-3. Integral Proton Flux for the Peak Trapped Protons

Proton Energy	Integral Peak Trapped Protons
MeV	p+/cm^2-s
0.1	7.08e+04
0.15	7.07e+04
0.2	7.05e+04
0.3	7.03e+04
0.4	7.00e+04
0.5	6.97e+04
0.6	6.94e+04
0.7	6.92e+04
1	6.86e+04
1.5	6.73e+04
2	6.60e+04
3	6.37e+04
4	6.15e+04

Proton Energy	Integral Peak Trapped Protons
MeV	p+/cm^2-s
5	5.90e+04
6	5.66e+04
7	5.35e+04
10	4.58e+04
15	3.45e+04
20	2.89e+04
30	2.35e+04
40	2.08e+04
50	1.83e+04
60	1.65e+04
70	1.48e+04
100	1.08e+04
150	6.54e+03
200	3.94e+03
300	1.56e+03
400	6.21e+02

3.3.2.2.2 Radiation Belt Transit

The SEE environment model parameters for Radiation Belt Transit trajectory are the geomagnetic unshielded GCR and Solar Particle Event. While the orbit does traverse inside the Earth's geomagnetic field, a SPE while outside constitutes the worst-case environment. Also, during the orbit the environment contains exposure to the trapped protons. However, very little time is spent in the trapped proton belt and those fluxes would be dominated by the levels of a SPE. Therefore, for Radiation Belt Transit trajectory, SEE environments use those presented in Section 3.3.2.10.2 Geomagnetic Unshielded.

3.3.2.2.3 Low Earth Orbit 241 km Circular

The SEE environment model parameters for LEO 241 km circular are bounded by those used for the LEO-ISS. For LEO 241 km circular SEE environments use those presented in Section 3.3.2.1 LEO-ISS Orbit.

3.3.2.2.4 High Earth Orbit 407 x 233,860 km

The SEE environment model parameters for HEO orbit are the geomagnetic unshielded GCR and Solar Particle Event. While the orbit does go back inside the Earth's geomagnetic field, a SPE while outside constitutes the worst-case environment. Also, during the orbit the environment contains exposure to the trapped protons. However, due the highly elliptical nature

of the orbit, very little time is spent in the trapped proton belt and those fluxes would be dominated by the levels of a SPE. Therefore, for HEO orbit SEE environments use those presented in Section 3.3.2.10.2 Geomagnetic Unshielded.

3.3.2.2.5 High Earth Orbit to Near Earth Asteroid Transit

The SEE environment model parameters for HEO to NEA transit are bounded by those used for the GEO. For HEO to NEA transit SEE environments use those presented in Section 3.3.2.3 Geosynchronous Earth Orbit (GEO).

3.3.2.2.6 Low Earth Orbit 407 km Circular

The SEE environment model parameters for LEO 407 km circular are the same as those used for the LEO-ISS. For LEO 407 km circular SEE environments use those presented in Section 3.3.2.1 LEO-ISS Orbit.

3.3.2.2.7 Low Perigee-High Earth Orbit 407 x 400,000 km

The SEE environment model parameters for LP-HEO orbit are the geomagnetic unshielded GCR and Solar Particle Event. While the orbit does go back inside the Earth's geomagnetic field, a SPE while outside constitutes the worst case environment. Also, during the orbit the environment contains exposure to the trapped protons. However, due the highly elliptical nature of the orbit, very little time is spent in the trapped proton belt and those levels would be dominated by the levels of a SPE. Therefore, for LP-HEO orbit SEE environments use those presented in Section 3.3.2.10.2 Geomagnetic Unshielded.

3.3.2.2.8 High Perigee-High Earth Orbit Spiral to 60,000 x 400,000 km

The SEE environment model parameters for HP-HEO spiral are the geomagnetic unshielded GCR and Solar Particle Event. For HP-HEO spiral SEE environments use those presented in Section 3.3.2.10.2 Geomagnetic Unshielded.

3.3.2.3 Geosynchronous Earth Orbit (GEO)

The SEE environment model parameters for geosynchronous earth orbit are the geomagnetic unshielded GCR and Solar Particle Event. For GEO SEE environments, use those presented in Section 3.3.2.10.2 Geomagnetic Unshielded.

3.3.2.4 Interplanetary

The SEE environment model parameters for interplanetary space are the geomagnetic unshielded GCR and Solar Particle Event. For interplanetary space SEE environments, use those presented in Section 3.3.2.10.2 Geomagnetic Unshielded.

3.3.2.5 Lunar Orbit

The SEE environment model parameters for lunar orbit are the geomagnetic unshielded GCR and Solar Particle Event. For lunar orbit SEE environments, use those presented in Section 3.3.2.10.2 Geomagnetic Unshielded.

3.3.2.6 Lunar Surface

The SEE environment model parameters for the lunar surface are the geomagnetic unshielded GCR and Solar Particle Event. For lunar surface SEE environments, use those presented in Section 3.3.2.10.2 Geomagnetic Unshielded.

3.3.2.7 Near Earth Asteroid

The SEE environment model parameters for Near Earth Asteroid (NEA) are the geomagnetic unshielded GCR and Solar Particle Event. For NEA SEE environments, use those presented in Section 3.3.2.10.2 Geomagnetic Unshielded.

3.3.2.8 Mars Orbit

The SEE environment model parameters for Mars orbit are the geomagnetic unshielded GCR and Solar Particle Event. For Mars orbit SEE environments, use those presented in Section 3.3.2.10.2 Geomagnetic Unshielded.

3.3.2.9 Mars Surface

Reserved.

3.3.2.10 GCR and Solar Particle Event

3.3.2.10.1 Geomagnetic Shielded

The geomagnetic shielded environments are defined in the above sections, as required, since the shielding levels are orbit specific.

3.3.2.10.2 Geomagnetic Unshielded

Figure 3.3.2.10.2-1 and Table 3.3.2.10.2-1 present the SPE peak rate LET flux inside selected aluminum shield thicknesses as a function of LET. Each thickness value is identical to the radius of the assumed spherical shielding.

Figure 3.3.2.10.2-2 and Table 3.3.2.10.2-2 provide the SPE worst day average fluxes for the same shield geometry and thicknesses.

Figure 3.3.2.10.2-3 and Table 3.3.2.10.2-3 present integral proton flux of a SPE and of GCR.

Figure 3.3.2.10.2-4 and Table 3.3.2.10.2-4 present differential proton flux for the SPE and solar minimum GCR.

Figure 3.3.2.10.2-5 and Table 3.3.2.10.2-5 present the GCR LET flux (at solar minimum) inside selected aluminum shield thicknesses as a function of LET. Each thickness value is identical to the radius of the assumed spherical shielding.

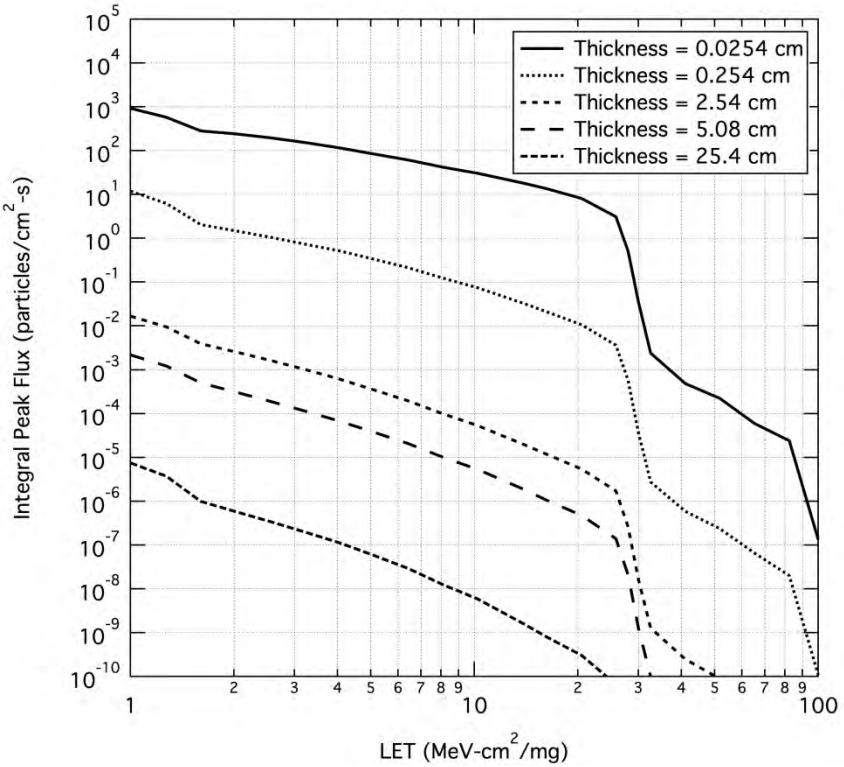

Figure 3.3.2.10.2-1. SPE Integral Peak LET Flux for Selected Al Shielding Thickness as a Function of LET

Table 3.3.2.10.2-1. SPE Integral Peak LET Flux for Selected Al Shielding Thickness as a Function of LET

LET	Shield Thickness 0.0254 cm (0.0686 g/cm^2)	Shield Thickness 0.254 cm (0.6858 g/cm^2)	Shield Thickness 2.54 cm (6.858 g/cm^2)	Shield Thickness 5.08 cm (13.72 g/cm^2)	Shield Thickness 25.40 cm (68.58 g/cm^2)
MeV-cm^2/mg	Particles/cm^2-s	Particles/cm^2-s	Particles/cm^2-s	Particles/cm^2-s	Particles/cm^2-s
1.00	9.278068E+02	1.18E+01	1.68E-02	2.19E-03	7.49E-06
1.27	5.767910E+02	6.33E+00	9.45E-03	1.22E-03	3.73E-06
1.60	2.85291E+02	2.06E+00	3.95E-03	5.03E-04	9.99E-07
2.01	2.423055E+02	1.50E+00	2.60E-03	3.15E-04	5.86E-07
2.54	1.968288E+02	1.07E+00	1.66E-03	1.93E-04	3.44E-07
3.20	1.541016E+02	7.51E-01	1.03E-03	1.16E-04	2.00E-07
4.04	1.176227E+02	5.18E-01	6.20E-04	6.79E-05	1.13E-07
5.09	8.527328E+01	3.38E-01	3.52E-04	3.78E-05	5.82E-08
6.42	6.183368E+01	2.15E-01	1.96E-04	2.07E-05	2.93E-08

LET	Shield Thickness 0.0254 cm (0.0686 g/cm^2)	Shield Thickness 0.254 cm (0.6858 g/cm^2)	Shield Thickness 2.54 cm (6.858 g/cm^2)	Shield Thickness 5.08 cm (13.72 g/cm^2)	Shield Thickness 25.40 cm (68.58 g/cm^2)
MeV-cm^2/mg	Particles/cm^2-s	Particles/cm^2-s	Particles/cm^2-s	Particles/cm^2-s	Particles/cm^2-s
8.09	4.210883E+01	1.25E-01	9.98E-05	1.02E-05	1.26E-08
10.21	3.085149E+01	7.51E-02	5.36E-05	5.35E-06	5.92E-09
13.96	1.816732E+01	3.27E-02	1.96E-05	1.84E-06	1.57E-09
16.23	1.364277E+01	2.12E-02	1.17E-05	1.06E-06	7.91E-10
20.47	8.133233E+00	1.06E-02	5.46E-06	4.78E-07	3.03E-10
25.81	3.098470E+00	3.62E-03	1.71E-06	1.41E-07	6.58E-11
28.00	5.097848E-01	5.73E-04	2.61E-07	2.08E-08	8.02E-12
30.01	3.486533E-02	3.67E-05	1.63E-08	1.25E-09	4.24E-13
32.55	2.383645E-03	2.77E-06	1.28E-09	9.87E-11	4.20E-14
41.05	4.881448E-04	5.84E-07	2.48E-10	1.83E-11	6.70E-15
51.76	2.253378E-04	2.37E-07	8.88E-11	6.31E-12	1.82E-15
65.28	5.940075E-05	6.56E-08	1.95E-11	1.32E-12	3.05E-16
82.32	2.389753E-05	2.01E-08	4.83E-12	3.03E-13	5.57E-17
100.25	1.230390E-07	1.00E-10	2.24E-14	1.91E-15	4.18E-18

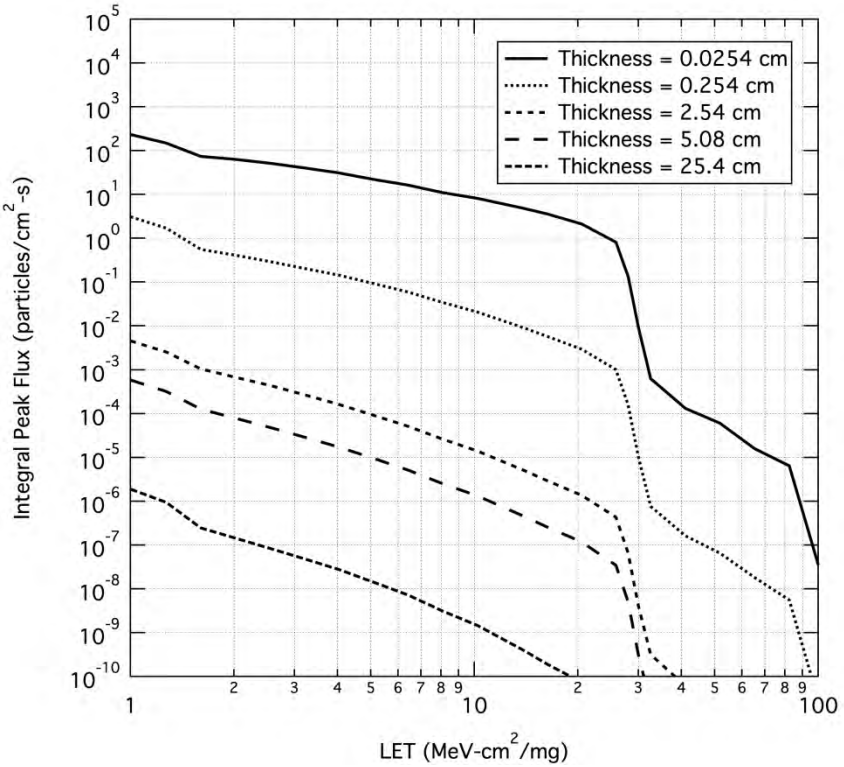

Figure 3.3.2.10.2-2. SPE Worst Day Integral Flux for Selected Al Shielding Thickness as a Function of LET

Table 3.3.2.10.2-2. SPE Worst Day Integral Flux for Selected Al Shielding Thickness as a Function of LET

LET	Shield Thickness 0.0254 cm (0.0686 g/cm^2)	Shield Thickness 0.254 cm (0.6858 g/cm^2)	Shield Thickness 2.54 cm (6.858 g/cm^2)	Shield Thickness 5.08 cm (13.72 g/cm^2)	Shield Thickness 25.40 cm (68.58 g/cm^2)
MeV-cm^2/mg	Particles/cm^2-s	Particles/cm^2-s	Particles/cm^2-s	Particles/cm^2-s	Particles/cm^2-s
1.00	2.36E+02	3.14E+00	4.58E-03	5.82E-04	1.90E-06
1.27	1.48E+02	1.70E+00	2.55E-03	3.22E-04	9.42E-07
1.60	7.47E+01	5.65E-01	1.04E-03	1.27E-04	2.45E-07
2.01	6.34E+01	4.12E-01	6.85E-04	7.97E-05	1.44E-07
2.54	5.15E+01	2.94E-01	4.37E-04	4.87E-05	8.43E-08
3.20	4.04E+01	2.07E-01	2.71E-04	2.92E-05	4.90E-08
4.04	3.09E+01	1.43E-01	1.63E-04	1.71E-05	2.77E-08
5.09	2.24E+01	9.33E-02	9.24E-05	9.49E-06	1.43E-08
6.42	1.63E+01	5.95E-02	5.13E-05	5.17E-06	7.20E-09
8.09	1.11E+01	3.46E-02	2.59E-05	2.53E-06	3.10E-09

LET	Shield Thickness 0.0254 cm (0.0686 g/cm^2)	Shield Thickness 0.254 cm (0.6858 g/cm^2)	Shield Thickness 2.54 cm (6.858 g/cm^2)	Shield Thickness 5.08 cm (13.72 g/cm^2)	Shield Thickness 25.40 cm (68.58 g/cm^2)
MeV-cm^2/mg	Particles/cm^2-s	Particles/cm^2-s	Particles/cm^2-s	Particles/cm^2-s	Particles/cm^2-s
10.21	8.18E+00	2.08E-02	1.39E-05	1.32E-06	1.45E-09
13.96	4.82E+00	9.09E-03	5.02E-06	4.52E-07	3.86E-10
16.23	3.62E+00	5.88E-03	2.98E-06	2.60E-07	1.94E-10
20.47	2.16E+00	2.96E-03	1.38E-06	1.17E-07	7.44E-11
25.81	8.20E-01	1.01E-03	4.33E-07	3.46E-08	1.61E-11
28.00	1.35E-01	1.59E-04	6.59E-08	5.10E-09	1.97E-12
30.01	9.25E-03	1.02E-05	4.06E-09	3.06E-10	1.04E-13
32.55	6.35E-04	7.71E-07	3.16E-10	2.42E-11	1.03E-14
41.05	1.31E-04	1.63E-07	6.09E-11	4.49E-12	1.64E-15
51.76	6.04E-05	6.60E-08	2.18E-11	1.55E-12	4.47E-16
65.28	1.60E-05	1.82E-08	4.77E-12	3.24E-13	7.48E-17
82.32	6.42E-06	5.58E-09	1.19E-12	7.42E-14	1.37E-17
100.25	3.31E-08	2.79E-11	5.48E-15	4.70E-16	1.03E-18

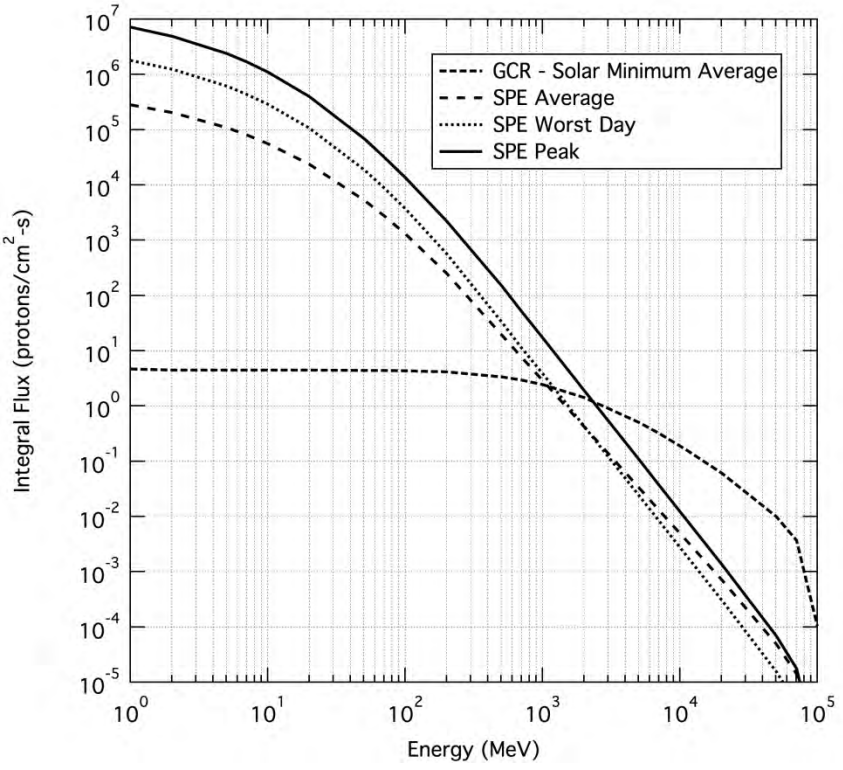

Figure 3.3.2.10.2-3. Integral Proton Flux of a SPE and GCR

Table 3.3.2.10.2-3. Integral Proton Flux of a SPE and GCR

Proton Energy	GCR In-Space (solar min)	SPE Average	SPE Worst day	SPE Peak Rate
MeV	p+/cm^2-s	p+/cm^2-s	p+/cm^2-s	p+/cm^2-s
1.00	4.638E+00	2.839E+05	1.791E+06	7.239E+06
2.03	4.491E+00	2.023E+05	1.230E+06	4.903E+06
5.04	4.452E+00	1.081E+05	6.097E+05	2.373E+06
7.02	4.449E+00	8.055E+04	4.373E+05	1.684E+06
10.05	4.447E+00	5.589E+04	2.887E+05	1.098E+06
20.03	4.442E+00	2.373E+04	1.080E+05	4.011E+05
50.50	4.420E+00	5.272E+03	1.881E+04	6.812E+04
70.33	4.396E+00	2.769E+03	8.881E+03	3.210E+04
100.69	4.347E+00	1.295E+03	3.679E+03	1.339E+04
200.77	4.125E+00	2.527E+02	5.733E+02	2.200E+03
506.17	3.358E+00	1.941E+01	3.310E+01	1.480E+02
704.94	2.934E+00	7.528E+00	1.107E+01	5.094E+01
1,009.20	2.418E+00	2.795E+00	3.709E+00	1.650E+01
2,012.30	1.422E+00	4.159E-01	4.246E-01	1.890E+00
5,003.80	5.092E-01	3.362E-02	2.429E-02	1.081E-01
7,065.60	3.175E-01	1.296E-02	8.219E-03	3.657E-02
11,142.00	1.609E-01	3.680E-03	1.965E-03	8.743E-03
20,170.00	6.084E-02	7.081E-04	3.030E-04	1.349E-03
50,153.00	1.007E-02	4.963E-05	1.554E-05	6.914E-05
70,819.00	3.679E-03	1.405E-05	3.991E-06	1.776E-05
100,000.00	1.040E-04	3.223E-07	8.477E-08	3.772E-07

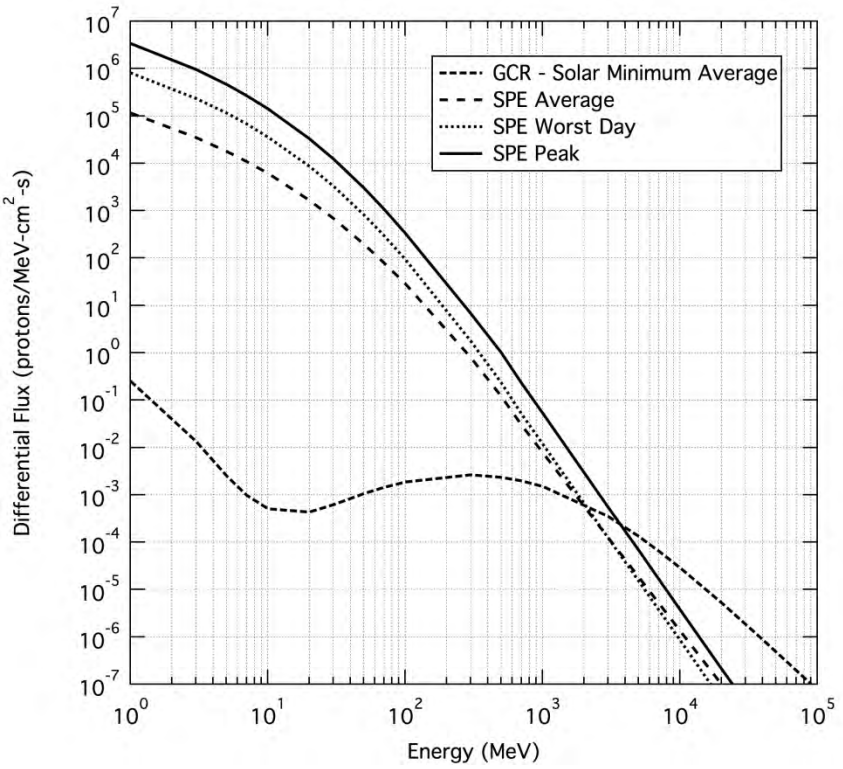

Figure 3.3.2.10.2-4. Differential Proton Flux for SPE and Solar Minimum GCR

Table 3.3.2.10.2-4. Differential Proton Flux for a SPE and Solar Minimum GCR

Proton Energy	GCR Solar Minimum Interplanetary Space	SPE Rate (average/180-hr event)	SPE Worst Day (average-worst 18 hrs)	SPE Peak Rate (Peak 5-minute average)
MeV	protons/cm^2-s-MeV	protons/cm^2-s-MeV	protons/cm^2-s-MeV	protons/cm^2-s-MeV
1.00	2.542E-01	1.165E+05	8.120E+05	3.406E+06
3.02	1.329E-02	3.518E+04	2.324E+05	9.489E+05
5.04	2.475E-03	1.787E+04	1.134E+05	4.556E+05
7.02	9.831E-04	1.092E+04	6.711E+04	2.663E+05
10.05	5.037E-04	6.081E+03	3.577E+04	1.399E+05
20.03	4.359E-04	1.657E+03	8.695E+03	3.297E+04
30.31	6.237E-04	6.726E+02	3.219E+03	1.198E+04
50.50	1.064E-03	1.934E+02	8.029E+02	2.925E+03
70.33	1.436E-03	7.942E+01	2.957E+02	1.067E+03
100.69	1.857E-03	2.818E+01	9.220E+01	3.310E+02
299.59	2.636E-03	7.968E-01	1.774E+00	6.818E+00

Proton Energy	GCR Solar Minimum Interplanetary Space	SPE Rate (average/180-hr event)	SPE Worst Day (average-worst 18 hrs)	SPE Peak Rate (Peak 5-minute average)
MeV	protons/cm^2-s-MeV	protons/cm^2-s-MeV	protons/cm^2-s-MeV	protons/cm^2-s-MeV
499.23	2.360E-03	1.213E-01	2.351E-01	1.012E+00
704.94	1.963E-03	2.913E-02	5.025E-02	2.236E-01
1009.20	1.481E-03	7.555E-03	1.137E-02	5.061E-02
3002.80	3.498E-04	1.251E-04	1.245E-04	5.540E-04
5003.80	1.333E-04	1.833E-05	1.503E-05	6.687E-05
7065.60	6.394E-05	5.007E-06	3.601E-06	1.602E-05
10116.00	2.818E-05	1.299E-06	8.149E-07	3.626E-06
20170.00	5.191E-06	9.689E-08	4.679E-08	2.082E-07
40216.00	8.677E-07	7.230E-09	2.687E-09	1.196E-08
89546.00	1.022E-07	3.561E-10	9.766E-11	4.346E-10

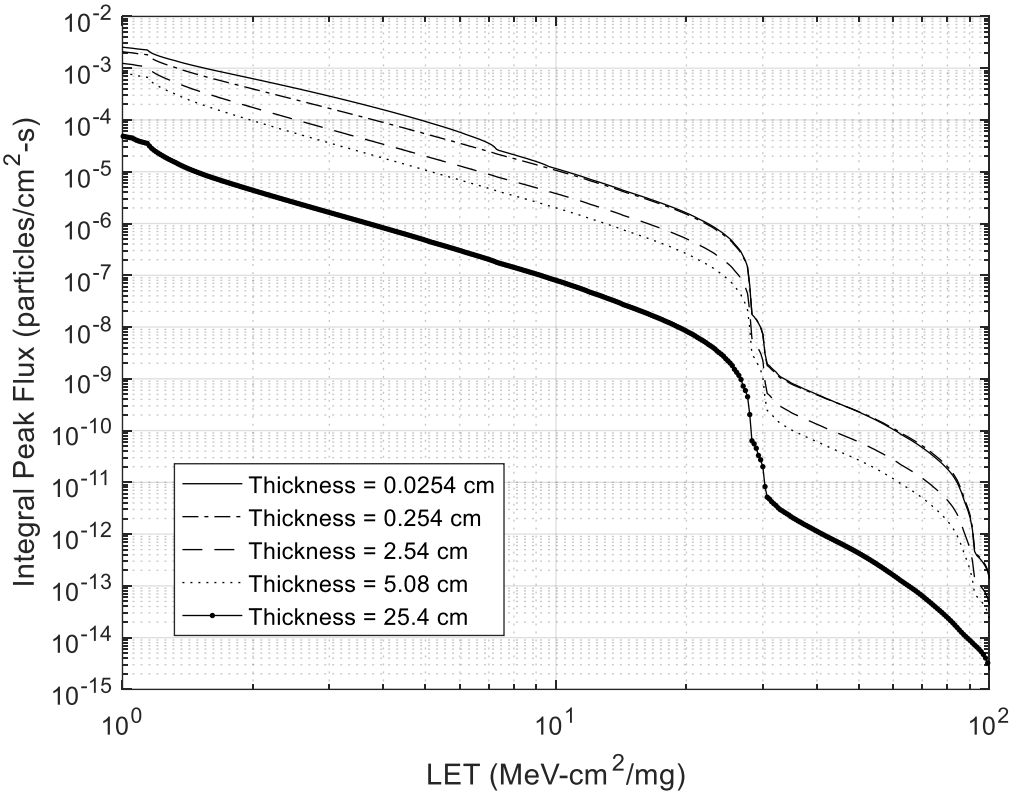

Figure 3.3.2.10.2-5. GCR Integral LET at Solar Minimum for Selected Al Shielding Thickness as a Function of LET

Table 3.3.2.10.2-5. GCR Integral LET at Solar Minimum for Selected Al Shielding Thickness as a Function of LET

LET	Shield Thickness 0.0254 cm (0.0686 g/cm^2)	Shield Thickness 0.254 cm (0.6858 g/cm^2)	Shield Thickness 2.54 cm (6.858 g/cm^2)	Shield Thickness 5.08 cm (13.72 g/cm^2)	Shield Thickness 25.40 cm (68.58 g/cm^2)
MeV-cm^2/mg	Particles/cm^2-s	Particles/cm^2-s	Particles/cm^2-s	Particles/cm^2-s	Particles/cm^2-s
1.00	2.54E-03	2.08E-03	1.24E-03	7.97E-04	4.89E-05
1.18	1.91E-03	1.50E-03	8.43E-04	5.20E-04	2.69E-05
1.38	1.26E-03	9.10E-04	4.60E-04	2.69E-04	1.26E-05
1.63	9.11E-04	6.20E-04	2.91E-04	1.65E-04	7.51E-06
1.91	6.79E-04	4.37E-04	1.94E-04	1.08E-04	4.90E-06
2.25	5.04E-04	3.10E-04	1.31E-04	7.21E-05	3.27E-06
2.64	3.71E-04	2.20E-04	8.90E-05	4.87E-05	2.21E-06
3.11	2.69E-04	1.55E-04	6.09E-05	3.31E-05	1.50E-06
3.66	1.91E-04	1.09E-04	4.17E-05	2.26E-05	1.02E-06
4.30	1.33E-04	7.59E-05	2.85E-05	1.54E-05	6.91E-07
5.06	9.08E-05	5.25E-05	1.94E-05	1.04E-05	4.60E-07
5.95	5.96E-05	3.61E-05	1.32E-05	7.09E-06	3.08E-07
6.99	3.55E-05	2.47E-05	8.95E-06	4.78E-06	2.03E-07
8.22	1.99E-05	1.68E-05	6.05E-06	3.22E-06	1.33E-07
9.67	1.25E-05	1.15E-05	4.11E-06	2.18E-06	8.70E-08
11.37	8.30E-06	7.75E-06	2.74E-06	1.44E-06	5.58E-08
13.37	5.33E-06	5.02E-06	1.75E-06	9.20E-07	3.40E-08
15.73	3.38E-06	3.20E-06	1.10E-06	5.75E-07	2.03E-08
18.50	2.09E-06	1.98E-06	6.70E-07	3.46E-07	1.15E-08
21.75	1.14E-06	1.08E-06	3.58E-07	1.82E-07	5.56E-09
25.58	4.45E-07	4.22E-07	1.37E-07	6.78E-08	1.74E-09
30.08	6.50E-09	6.46E-09	2.02E-09	9.52E-10	1.79E-11
35.37	7.86E-10	7.53E-10	2.10E-10	9.77E-11	2.01E-12
41.59	4.34E-10	4.27E-10	1.15E-10	5.24E-11	9.53E-13
48.91	2.47E-10	2.49E-10	6.51E-11	2.91E-11	4.72E-13
57.52	1.28E-10	1.33E-10	3.33E-11	1.45E-11	2.05E-13
67.64	5.70E-11	6.13E-11	1.47E-11	6.17E-12	7.97E-14
79.54	1.91E-11	2.11E-11	4.77E-12	1.90E-12	2.55E-14
93.54	3.86E-13	4.08E-13	1.18E-13	6.22E-14	6.58E-15
100.00	1.42E-13	1.51E-13	4.38E-14	2.31E-14	2.44E-15

Model Inputs

None

Limitations

Probability that the SPE Peak Flux will not be exceeded is estimated at 97%.

Technical Notes

All SPE fluxes - peak (5 minutes), worst day, average (worst week) are generated using the CREME96 model, selecting the near Earth interplanetary orbit option of the FLUX module. All model-generated SPE fluxes are multiplied by 2 for model uncertainty. The GCR peak integral flux vs. LET is also generated using CREME96, again for the near Earth interplanetary orbit option, at solar minimum conditions. Z=1-92 for all LET plots, and Z=1 for all proton plots.

A spherical shield model with radius set equal to the minimum shield thickness provides very conservative results. CREME96 can also model flux inside other 3D shield geometries if the distribution of shielding thicknesses is known.

An industry accepted radiation transport code that provides a semi-infinite slab model should be used to define flux at selected depths within surface coatings and materials.

3.3.3 Plasma Charging

Plasma interactions with the spacecraft are complex, vary significantly between the different regions of space, and are highly dependent on the spacecraft design and mission timeline. Interactions within each region also vary hourly, daily, and seasonally due to changes in geomagnetic and solar activity. Plasma charging effects include solar array/power system degradation, contamination, ionospheric scintillation, and spacecraft charging, both surface charging and deep dielectric charging (also known as bulk or internal charging). The following sections specify the charging effects, analysis models, and mitigation techniques that should be employed for each region of space. Table 3.3.3-1 identifies the regions of space that are applicable for each Design Reference Mission. For the “Staging and Transit Orbits” column, subsections of 3.3.3.2 are called out as applicable, since not all may be applicable for each DRM.

In general, spacecraft charging is more serious in GEO than in LEO and in Cis-lunar. Plasma interactions can be quite complicated, and there are significant differences between a space vehicle’s interactions with the relatively low energy plasma in the ionosphere and at very high orbits, and in the auroral regions where the higher energy plasma characteristic of higher altitudes penetrates to LEO. Examples of plasma interaction effects with space vehicle are solar array/power system degradation, contamination, ionospheric scintillation, and spacecraft charging.

Table 3.3.3-1. Plasma Charging Applicability Matrix for the Design Reference Missions by Regions of Space

	LEO (3.3.3.1)	Staging and Transit Orbits (3.3.3.2)	GEO (3.3.3.3)	Interplanetary (3.3.3.4)	Lunar Orbit (3.3.3.5)	Lunar Surface (3.3.3.6)	NEA (3.3.3.7)	Mars Orb it (3.3.3.8)	Mars Surface (3.3.3.9)	Polar Orbit (3.3.3.10)
Distant Retrograd e Orbit	X	3.3.3.2.1 3.3.3.2.2		X	X					
Crewed Lunar Orbit	X	3.3.3.2.1 3.3.3.2.2		X						
Low Lunar Orbit	X	3.3.3.2.6 3.3.3.2.2		X	X					
Initial Capability NEA	X	3.3.3.2.4 3.3.3.2.5 3.3.3.2.2		X			X			
Advanced NEA	X	3.3.3.2.4 3.3.3.2.5 3.3.3.2.2		X			X			
Full Capability NEA	X	3.3.3.2.6 3.3.3.2.7 3.3.3.2.8 3.3.3.2.5 3.3.3.2.2		X			X			
Lunar Surface Sortie	X	3.3.3.2.6 3.3.3.2.2		X	X	X				
ISS Crew Delivery Backup	X	None								X
GEO Vicinity	X	3.3.3.2.6 3.3.3.2.2	X							
Martian Moon	X	Reserve d		X				X		
Martian Landing	X	Reserve d		X				X	X	

3.3.3.1 LEO-ISS Orbit

Design Limits

Table 3.3.3.1-1 provides electron densities (Ne, #/m3) and electron temperatures (Te, eV) of the ionospheric plasma in low Earth orbit for use in evaluating current collection on vehicle conducting surface areas such as solar arrays. Surfaces that are not biased with a net potential relative to the plasma environment will only charge a few volts negative at night and a few tens of volts positive in daylight. Biased solar arrays operating in the relatively dense plasmas in LEO will experience a current drain on the power system, as a result of losses through coupling to the plasma. High voltage solar arrays (with operating voltages exceeding approximately 55 volts) can result in significant charging and require special attention to design to avoid destructive arcing or current collection that exceeds design requirements. The design environments shown in Table 3.3.3.1-1 represent extreme high and low values for both density and temperatures which bound the conditions spacecraft will encounter in LEO environments for both day and night.

Table 3.3.3.1-1. Ambient Plasma Environment for less than 1000 km Altitude

	Low	High
Ne (m^{-3})	1.0e+8	1.0e+13
Te (eV)	0.03	1.0

Model Inputs

None

Limitations

This environment applies for low Earth orbits less than 1000 km.

Technical Notes

These environments are derived from Minow, 2004. Surface charging is relatively benign in LEO low inclination orbits unless high voltage solar arrays or other exposed high voltage systems are used.

3.3.3.2 Staging and Transit Orbits

3.3.3.2.1 Low Earth Orbit 185 x 1806 km

For surface charging, low inclination, refer to Section 3.3.3.1 for environment parameters.

For surface charging, high inclination, refer to Section 3.3.3.10 for environment parameters.

For internal charging, refer to Section 3.3.3.2.2 for environment parameters.

3.3.3.2.2 Radiation Belt Transit Environment

Figure 3.3.3.2.2-1 and Table 3.3.3.2.2-1 specify the electron integral flux environment for use in analyses of bulk (internal) charging of insulating materials and isolated conductors.

Analysis of discharge events on spacecraft in geostationary or geostationary transfer orbits has shown that in order to generate electric fields exceeding the dielectric strength of materials, the electron flux must typically be sufficient to provide a fluence of approximately 10^{10} electrons/cm^2 in 10 hours. However, it must be noted that the temperature of the dielectric is important since time constants for charging and discharging are much longer at low temperatures, and evaluation of charging must include the operational temperatures of the materials.

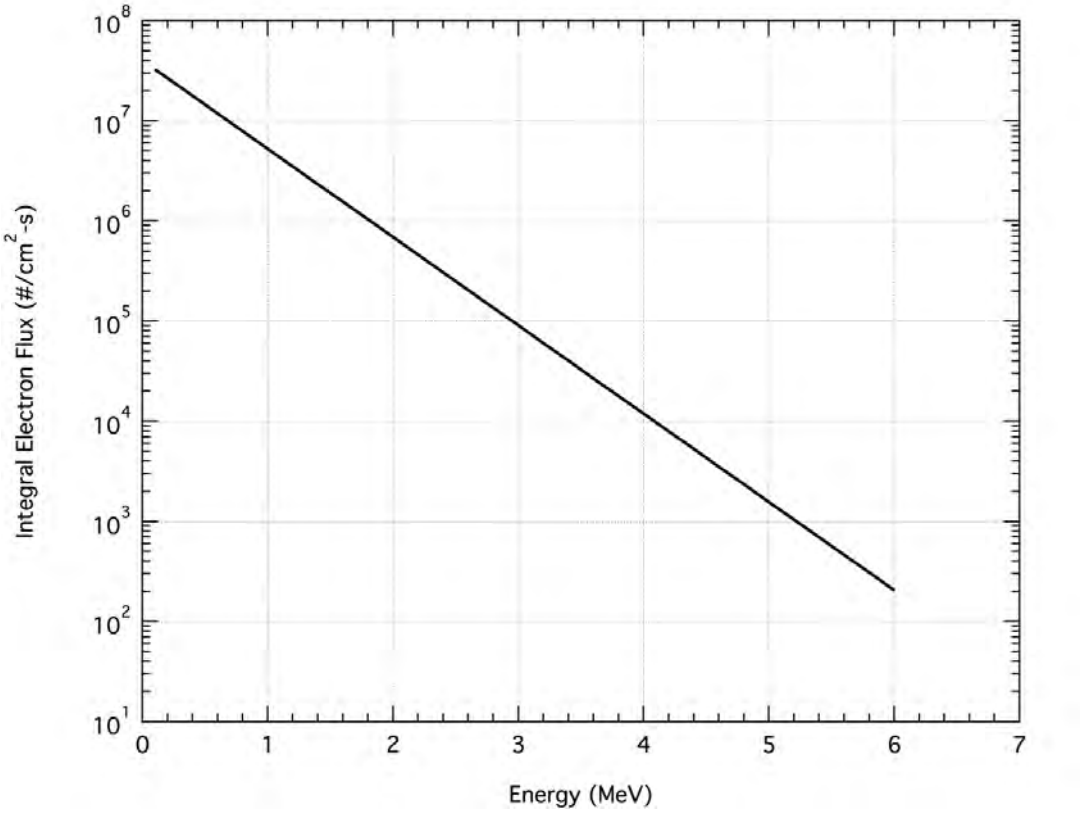

Figure 3.3.3.2.2-1. Radiation Belt Transit Average Integral Electron Flux

Table 3.3.3.2.2-1. Radiation Belt Transit Average Integral Electron Flux

Energy	Integral Flux
MeV	electrons/cm^2-sec
0.1	3.27E+07
0.2	2.67E+07
0.4	1.78E+07

Energy	Integral Flux
MeV	electrons/cm^2-sec
0.6	1.18E+07
0.8	7.88E+06
1	5.25E+06
1.2	3.50E+06
1.4	2.33E+06
1.6	1.55E+06
1.8	1.04E+06
2	6.90E+05
2.2	4.60E+05
2.4	3.06E+05
2.6	2.04E+05
2.8	1.36E+05
3	9.06E+04
3.2	6.04E+04
3.4	4.02E+04
3.6	2.68E+04
3.8	1.79E+04
4	1.19E+04
4.2	7.93E+03
4.4	5.28E+03
4.6	3.52E+03
4.8	2.35E+03
5	1.56E+03
5.2	1.04E+03
5.4	6.94E+02
5.6	4.62E+02
5.8	3.08E+02
6	2.05E+02

Refer to Section 3.3.3.3 Geosynchronous Earth Orbit for surface charging environment parameters.

Model Inputs

The orbit averaged flux is to be multiplied by the exposure period determined by the time required to transit the radiation belts (but not less than 4 hours) to determine the appropriate total electron fluence to be used in bulk charging analyses.

Surface charging analyses for radiation belt transits should be run with the correct solar illumination.

Limitations

None

Technical Notes

Radiation belt transit environment was derived from Fennell et al. 2000.

3.3.3.2.3 Low Earth Orbit 241 km Circular

Refer to Section 3.3.3.1 for environment parameters.

3.3.3.2.4 High Earth Orbit 407 x 233,860 km

Refer to Section 3.3.3.2.2 for environment parameters.

3.3.3.2.5 High Earth Orbit to Near Earth Asteroid Transit

Refer to Section 3.3.3.2.2 for environment parameters.

3.3.3.2.6 Low Earth Orbit 407 km Circular

Refer to Section 3.3.3.1 for environment parameters.

3.3.3.2.7 Low Perigee-High Earth Orbit 407 x 400,000 km

Refer to Section 3.3.3.2.2 for environment parameters.

3.3.3.2.8 High Perigee-High Earth Orbit Spiral to 60,000 x 400,000 km

Reserved.

3.3.3.3 Geosynchronous Earth Orbit

Table 3.3.3.3-1 provides worst case surface charging in Geosynchronous Earth Orbit (GEO). Given in the Table are parameters for a single Maxwellian or bi-Maxwellian plasma population. This allows for a quick analysis using the single Maxwellian or the added fidelity of modeling the plasma environment as a bi-Maxwellian distribution, which is more representative of the actual GEO plasma environment. Either distribution is acceptable to use. The data are from the Spacecraft Charging at High Altitudes (SCATHA) spacecraft.

Table 3.3.3.3-1. Geosynchronous Orbit (GEO) Plasma Environment Parameters

Parameter	SCATHA "Worst Case" Environment	
	Electrons	Ions
Single Maxwellian		
Number density (#/cm^3)	3.00	3.00

Parameter	SCATHA "Worst Case" Environment	
	Electrons	Ions
Temperature (eV)	12,000	30,000
Current density (nA/cm^2)	0.501	0.016
Double Maxwellian		
Number density, population 1 (#/cm^3)	0.87	0.97
Temperature, population 1 (eV)	600	333
Number density, population 2 (#/cm^{-3})	1.73	1.63
Temperature, population 2 (eV)	25,800	25,300

Model Inputs

Charging analyses should be run until surface potentials have obtained equilibrium.

Limitations

None

Technical Notes

Environment parameters were adapted from Purvis et al., 1984 and Gussenhoven and Mullen, 1982.

3.3.3.4 Interplanetary Orbit

Table 3.3.3.4-1 provides space plasma environment parameters for regions in an interplanetary orbit that one might encounter, such as: magnetosheath, plasma mantle, plasma sheet, and solar wind environments. A range of values is provided where applicable to show the variability in the plasma environment in the regime indicated. The magnetosheath environments are solar wind that has been heated when traversing the bow shock and accelerated back to solar wind speeds.

Table 3.3.3.4-1. Interplanetary Environment Plasma Parameters

	Electron Density	Electron Temperature	Ion Velocity	Ion Density	Ion Temperature
	m^{-3}	eV	km/s	m^{-3}	eV
Magnetosheath / magnetotail	10^6 - 10^8	10-2000	400-1000	10^6 - 10^8	10-10,000
Solar Wind	10^5 - 10^8	12	400-1000	10^5 - 10^8	50

Model Inputs

None

Limitations

These plasma environments are relevant for interplanetary space outside the Earth's radiation belts.

Technical Notes

Interplanetary and terrestrial magnetotail environments are derived from Paterson and Frank, 1994 and Minow et al., 2008. In addition, the solar wind environments are based on statistical analyses of Interplanetary Monitoring Platform (IMP)-6 and IMP-7 (Feldman et al., 1977).

3.3.3.5 Lunar Orbit (High and Low)

The variability in the lunar plasma environment creates challenges for evaluating the effects of the environment on spacecraft materials and systems. Spacecraft charging is the primary effect of the plasma environment and is the result of balancing currents from the environment and spacecraft. The magnitude of the charge collected on spacecraft surfaces is dependent on the energy and density of the local plasma environment, photoemission, and emission of secondary electrons. Photoemission and the emission of secondary electrons are material and design dependent. Spacecraft charging in the lunar environment is complex due to the low ambient density in the lunar environment and the tendency of electron energies being near the energy of maximum secondary electron generation. For crewed spacecraft, which tend to employ the use of dielectric surfaces, reliance on spacecraft charging simulation packages, such as Nascap-2k, is required to understand the risks to hardware and humans caused by spacecraft charging. In its orbit around the Earth, the Moon passes through the solar wind, magnetosheath, and the magnetotail, including the relatively energetic and dynamic plasma sheet. The environment for the following four regions is defined: solar wind, magnetosheath, magnetotail lobes and the plasma sheet. The solar wind region is defined as the space outside of the influence of Earth's magnetic field. The magnetotail is the region within the influence of the Earth's magnetic field, and the plasma sheet is a relatively thin region stretching across the magnetotail near the ecliptic plane. Above and below the plasma sheet are the magnetotail lobes. The magnetosheath is a transition region between the solar wind and magnetotail, where there is a pile up of plasma and solar wind is mostly diverted around the body of the magnetosphere. This region consists of a mixture of shocked solar wind and magnetosphere plasma. In the solar wind and magnetosheath, a wake structure develops in the near vacuum region on the opposite side of the Moon from the flowing solar wind. The wake structure occurs because the Moon acts as an obstacle to the flowing solar wind plasma, absorbing the solar wind plasma and leaving a density depletion on the opposite side.

Data from the THEMIS-ARTEMIS mission for the years 2012 through 2018 were consolidated and binned into these regions for analysis. The magnetotail, dayside solar wind, and dayside magnetosheath environments are independent of altitude, however there is a strong altitude dependence for the nightside in the solar wind and magnetosheath. Plasma environments are

defined according to their specific characteristics for each of the different regions of space and are provided in a form that can be used as inputs into spacecraft charging tools such as Nascap-2k. The values in Table 3.3.3.5-1 are the mean, 95%, 99.7%, and maximum environments derived from the THEMIS-ARTEMIS data in the years 2012 through 2018. The mission design environment is the maximum environment. The mean, 95%, and 99.7% values are provided for cognizance and mission planning purposes.

Table 3.3.3.5-1. Lunar Orbit Plasma Parameters

		Electron Density*	Electron Temperature	Ion Velocity	Ion Density*	Ion Temperature
		m^{-3}	eV	km/s	m^{-3}	eV
Magnetotail Lobes >100km	mean	2.0×10^5	48	170	2.0×10^5	290
	95%	1.5×10^5	160	440	1.5×10^5	1000
	99.7%	8.0×10^4	440	540	1.0×10^5	1700
	max	6.2×10^4	980	650	8.9×10^4	3400
Plasma Sheet >100km	mean	2.2×10^5	150	110	2.0×10^5	780
	95%	1.1×10^5	440	360	1.2×10^5	2000
	99.7%	6.9×10^4	970	591	9.1×10^4	3100
	max	5.0×10^4	3700	1100	6.9×10^4	4800
Magnetosheath Dayside >100km	mean	9.5×10^6	18	350	8.0×10^6	94
	95%	9.4×10^6	28	510	7.5×10^6	220
	99.7%	1.3×10^5	180	640	1.3×10^5	1100
	max	7.6×10^4	1400	930	9.9×10^4	3000
Magnetosheath Wake 100km – 2000km	mean	1.9×10^5	50	260	1.9×10^5	330
	95%	5.0×10^4	97	480	6.9×10^4	880
	99.7%	4.3×10^4	520	600	5.0×10^4	2000
	max	4.3×10^4	840	660	5.0×10^4	3600
Magnetosheath Wake 2000km – 12000km	mean	6.7×10^6	19	350	6.0×10^6	110
	95%	4.7×10^6	34	520	3.9×10^6	280
	99.7%	1.6×10^5	130	660	1.4×10^5	920
	max	6.6×10^4	920	770	9.2×10^4	2900
Magnetosheath Wake >12000km	mean	9.0×10^6	17	340	7.7×10^6	84
	95%	1.1×10^7	26	530	9.0×10^6	200
	99.7%	2.1×10^5	100	640	1.8×10^5	900
	max	7.7×10^4	710	820	1.3×10^5	1800
Solar Wind Dayside >100km	mean	6.0×10^6	11	420	6.0×10^6	7.0
	95%	1.5×10^7	17	610	1.6×10^7	20
	99.7%	4.4×10^7	28	620	4.3×10^7	40

		Electron Density*	Electron Temperature	Ion Velocity	Ion Density*	Ion Temperature
		m^{-3}	eV	km/s	m^{-3}	eV
	max	6.6×10^{7}	31	700	7.0×10^{7}	60
Solar Wind Wake 100km-500km	mean	7.3×10^{4}	60	260	8.1×10^{4}	320
	95%	3.4×10^{4}	110	490	4.4×10^{4}	820
	99.7%	4.6×10^{4}	220	610	5.7×10^{4}	1500
	max	2.3×10^{4}	430	720	3.6×10^{4}	2300
Solar Wind Wake 500km – 2000km	mean	1.7×10^{5}	50	300	1.8×10^{5}	250
	95%	4.8×10^{4}	90	520	5.9×10^{4}	670
	99.7%	5.5×10^{4}	160	650	6.5×10^{4}	1400
	max	5.0×10^{4}	350	770	6.5×10^{4}	2500
Solar Wind Wake 2000km – 12000km	mean	1.1×10^{6}	29	370	1.1×10^{6}	130
	95%	1.4×10^{5}	63	550	1.4×10^{5}	430
	99.7%	5.5×10^{4}	91	680	6.6×10^{4}	1000
	max	3.5×10^{4}	220	770	4.8×10^{4}	2100
Solar Wind Wake >12000km	mean	2.5×10^{6}	19	400	3.0×10^{6}	66
	95%	1.5×10^{6}	28	570	1.6×10^{6}	160
	99.7%	1.3×10^{6}	40	750	1.3×10^{6}	350
	max	1.5×10^{6}	64	790	1.4×10^{6}	800

* Density values are determined by taking the mean of the density data for data points with electron temperature within 25% of the statistical temperature value. This prevents pairing an unrealistically high density value with each statistical environment.

Limitations

This environment does not apply to the lunar surface. See 3.3.3.6.

Technical Notes

The environments are based on a statistical analysis using THEMIS-ARTEMIS (Time History of Events and Macroscale Interactions during Substorms – Acceleration, Reconnection, Turbulence and Electrodynamics of Moon's Interaction with the Sun) (Angelopoulos, 2010) Electrostatic Analyzer (McFadden et al, 2008b) data (from January 1, 2012 through December 31, 2018) in conjunction with the Space Physics Data Facility (SPDF)(https://spdf.gsfc.nasa.gov) web services, CDAweb (https://cdaweb.gsfc.nasa.gov), SSCweb (https://sscweb.gsfc.nasa.gov), and OmniWeb (https//omniweb.gsfc.nasa.gov).

3.3.3.6 Lunar Surface

See 3.4.3 for lunar surface plasma characteristics.

3.3.3.7 Near Earth Asteroid

Refer to Section 3.3.3.4 for environment parameters.

3.3.3.8 Mars Orbit

Reserved.

3.3.3.9 Mars Surface

Reserved.

3.3.3.10 Polar Orbit

The auroral charging environment is a combination of the ambient background plasma environment typical of low Earth orbit with an accelerated beam of energetic electrons originating in the distant magnetospheric plasma. Nascap-2k uses a Maxwellian distribution to characterize the cold ambient plasma environment for auroral charging and a Fontheim distribution to describe the energetic auroral particle population. The components of the Fontheim distribution are a power law describing the backscattered and secondary electron fluxes, a Maxwellian modeling the energetic part of the spectrum, and a Gaussian representing the monoenergetic high energy electron beam. The plasma charging environment, both the ambient and energetic populations, are shown in Table 3.3.3.10-1.

Table 3.3.3.10-1. Polar Plasma Parameters

	n (m^{-3})	kT (eV)	e^- current (A/m^2)	Width (eV)
Ambient	4.70E+05	0.2		
Power law		50	5.00E-08	
		1.60E+06		
Maxwellian		2.50E+04	5.00E-07	
Gaussian		2.50E+04	2.20E-06	5.00E+03

Model Inputs

None

Limitations

None

Technical Notes

Auroral charging analyses are performed in eclipse conditions because darkness is required to obtain the depletions in the ambient plasma environments. Formation of the accelerated electron beams (Gaussian component) is only possible when the ionosphere is in darkness.

3.3.4 Ionizing Radiation Environment for Crew Exposure

Description

This specification describes the ionizing radiation environment to be used to analyze risk to astronauts for design analyses for Orion MPCV. The radiation environments of concern to ensure crew health and safety are significantly different in scope and content than are those of concern for ensuring reliability and sustainability of flight hardware and materials. Inclusion of these environments, therefore, is not a duplication or supersedence of the environments specified in Sections 3.3.1 and 3.3.2. SPE, trapped proton, trapped electron, and GCR descriptions are established here to be used as design environments for evaluating crew exposures for all design analyses. For Gateway, the radiation environment to be used for crew exposure is in DSG-RQMT-002 Gateway Human Systems Requirements (HSR).

Design Limits

Crew radiation exposure design limits and verification requirements are defined in MPCV 70024, Orion Multi-Purpose Crew Vehicle Program Human-Systems Integration Requirements, Section 3.2.7. Exposures attributed to both SPE and GCR will be calculated for free space. Free-space quantities for LEO scenario analyses may be divided by two (2) to account for effects of the Earth's magnetic field.

Solar minimum conditions have been specified for trapped and GCR sources as a conservative basis for crew dose analysis. Solar maximum fluences will not be used.

Trapped radiation will not be considered for purposes of evaluating design analyses beyond a maximum McIlwain L value of 12.

Model Inputs

SPE Source:

The design reference SPE environment is given by the parameterization of the event total proton integral spectrum of J. H. King's "Solar Proton Fluences for 1977-1983 Space Missions." This omnidirectional proton spectrum is given in the inclusive energy range [0.01, 1,000] MeV by the following expressions:

Integral: $J(>E) = J_0 \exp[(30-E)/E_0]$

Differential: $J(E) = (J_0/ E_0) \exp[(30-E)/E_0]$

With $J_0 = 7.9 \times 10^9$ particles/cm^2, and $E_0 = 26.5$ MeV

Analysis fluences and resultant exposure values will be reported as totals per event for the analysis profile. Event total differential spectrum is listed in Table 3.3.4-1. These model spectra are available to all contractors, if they so choose, as Government Furnished Equipment (GFE).

Table 3.3.4-1. SPE Design Event Differential Spectra

Energy (MeV/n)	Free Space Differential Spectrum (particles/(MeV-cm^2)
0.01	9.244E+08
0.03	9.237E+08
0.06	9.227E+08
0.10	9.213E+08
0.30	9.144E+08
0.60	9.041E+08
1.00	8.905E+08
1.50	8.739E+08
2.00	8.575E+08
3.00	8.258E+08
4.00	7.952E+08
6.00	7.374E+08
8.00	6.838E+08
10.00	6.341E+08
14.00	5.453E+08
17.00	4.869E+08
20.00	4.348E+08
25.00	3.600E+08
30.00	2.981E+08
35.00	2.469E+08
40.00	2.044E+08
50.00	1.402E+08
60.00	9.610E+07
70.00	6.589E+07
80.00	4.518E+07
90.00	3.098E+07
100.00	2.124E+07
150.00	3.219E+06
200.00	4.879E+05
250.00	7.395E+04
300.00	1.121E+04
350.00	1.699E+03
400.00	2.574E+02
500.00	5.913E+00
600.00	1.358E-01

Energy (MeV/n)	Free Space Differential Spectrum (particles/(MeV-cm^2)
700.00	3.120E-03
800.00	7.166E-05
900.00	1.646E-06
1,000.00	3.781E-08

GCR Source:

The design reference GCR environment is given by the O'Neill-Badhwar model by P. M. O'Neill (2006). Species in the inclusive range Z = [1,26] will be included for the inclusive energy range [0.01, 50,000] MeV/n. Fluences are assumed omnidirectional in units of particles/(cm^2-MeV-day). Solar modulation for solar minimum (1977) is required, as given by a solar deceleration potential scalar parameter of Phi=748 MV (Megavolts). Analysis fluences and resultant exposure values will be reported as average per day over the duration of the analysis profile.

Differential spectra for P, C, N, O, and Fe are tabulated for reference in Table 3.3.4-2. This model is available to all contractors, if they so choose, as GFE.

Table 3.3.4-2. GCR Design Differential Spectra (Solar Minimum)

	Free Space Differential Spectrum (#/(MeV-cm^2-day)				
Energy (MeV/n)	P	C	N	O	Fe
0.01	0.168	1.89E-03	2.26E-05	1.74E-03	1.02E-04
0.03	0.168	1.89E-03	2.26E-05	1.74E-03	1.02E-04
0.06	0.168	1.89E-03	2.26E-05	1.74E-03	1.02E-04
0.13	0.212	2.40E-03	4.20E-05	2.21E-03	1.32E-04
0.23	0.354	3.94E-03	1.38E-04	3.64E-03	2.26E-04
0.37	0.549	5.99E-03	3.44E-04	5.52E-03	3.47E-04
0.55	0.817	8.71E-03	7.32E-04	8.01E-03	5.08E-04
0.81	1.189	0.013	1.42E-03	1.15E-02	7.26E-04
1.16	1.708	0.018	2.57E-03	1.63E-02	1.03E-03
1.64	2.426	0.025	4.40E-03	2.30E-02	1.45E-03
2.30	3.420	0.035	7.18E-03	3.22E-02	2.02E-03
3.22	4.801	0.049	1.12E-02	4.50E-02	2.82E-03
4.48	6.706	0.069	1.69E-02	6.27E-02	3.93E-03
6.22	9.338	0.096	2.46E-02	8.72E-02	5.45E-03
8.61	12.951	0.133	3.46E-02	0.120601	7.53E-03
11.91	17.956	0.183	4.76E-02	0.166589	1.04E-02
13.03	19.660	0.200	5.18E-02	0.182143	1.14E-02

Free Space Differential Spectrum (#/(MeV-cm^2-day)					
Energy (MeV/n)	**P**	**C**	**N**	**O**	**Fe**
14.26	21.517	0.219	5.62E-02	0.199043	1.24E-02
15.59	23.543	0.239	6.09E-02	0.217392	1.36E-02
17.03	25.718	0.261	6.59E-02	0.236987	1.48E-02
18.62	28.134	0.285	7.12E-02	0.258632	1.62E-02
20.36	30.769	0.310	7.69E-02	0.282072	1.76E-02
22.25	33.636	0.338	8.28E-02	0.307379	1.92E-02
24.33	36.765	0.368	8.92E-02	0.334734	2.09E-02
26.59	40.178	0.401	9.59E-02	0.364246	2.28E-02
29.07	43.897	0.436	0.103065	0.396016	2.48E-02
31.78	47.951	0.474	0.110625	0.430143	2.70E-02
34.75	52.363	0.514	0.118615	0.466664	2.93E-02
37.99	57.158	0.557	0.127045	0.505601	3.18E-02
41.53	62.364	0.602	0.135923	0.546956	3.45E-02
45.40	68.005	0.651	0.145247	0.590662	3.73E-02
49.62	74.105	0.701	0.155012	0.636618	4.03E-02
54.24	80.677	0.754	0.165186	0.684581	4.35E-02
59.29	87.769	0.809	0.175791	0.734536	4.68E-02
64.83	95.398	0.866	0.186781	0.786167	5.02E-02
70.91	103.606	0.925	0.198142	0.83928	5.38E-02
77.62	112.424	0.985	0.209833	0.893525	5.76E-02
84.93	121.769	1.045	0.221652	0.94784	6.14E-02
92.93	131.636	1.104	0.233496	1.001645	6.52E-02
101.67	142.006	1.162	0.245243	1.05426	6.91E-02
111.30	152.908	1.218	0.257	1.105	7.29E-02
121.91	164.260	1.271	0.268	1.153	7.66E-02
133.59	175.964	1.321	0.279	1.198	8.02E-02
146.46	187.901	1.364	0.288	1.237	8.35E-02
160.61	199.872	1.401	0.297	1.271	8.64E-02
176.14	211.664	1.431	0.304	1.297	8.89E-02
193.35	223.188	1.451	0.310	1.315	9.08E-02
212.40	234.153	1.461	0.314	1.324	9.22E-02
233.50	244.267	1.459	0.316	1.323	9.27E-02
256.79	253.180	1.444	0.315	1.309	9.25E-02
282.74	260.628	1.416	0.312	1.283	9.14E-02
311.58	266.282	1.373	0.306	1.244	8.94E-02

Free Space Differential Spectrum (#/(MeV-cm^2-day)					
Energy (MeV/n)	**P**	**C**	**N**	**O**	**Fe**
343.46	269.895	1.317	0.298	1.193	8.67E-02
379.24	271.317	1.247	0.287	1.130	8.32E-02
419.35	270.361	1.166	0.273	1.057	7.90E-02
464.39	266.941	1.077	0.257	0.976	7.43E-02
514.90	261.065	0.984	0.240	0.891	6.92E-02
571.55	252.814	0.891	0.221	0.805	6.39E-02
635.50	242.252	0.798	0.202	0.720	5.84E-02
707.95	229.516	0.705	0.182	0.637	5.27E-02
790.30	214.806	0.614	0.162	0.558	4.71E-02
883.74	198.443	0.529	0.143	0.483	4.15E-02
991.34	180.534	0.451	0.124	0.414	3.62E-02
1,114.78	161.600	0.382	0.107	0.349	3.11E-02
1,256.49	142.228	0.320	9.04E-02	0.292	2.65E-02
1,418.86	123.069	0.265	7.57E-02	0.241	2.23E-02
1,608.53	104.400	0.215	6.23E-02	0.196	1.85E-02
1,829.20	86.986	0.171	5.05E-02	0.157	1.52E-02
2,086.76	71.267	0.134	4.02E-02	0.124	1.22E-02
2,388.20	57.399	0.104	3.14E-02	9.64E-02	9.58E-03
2,741.57	45.380	7.94E-02	2.41E-02	7.38E-02	7.37E-03
7,575.78	5.939	8.12E-03	2.44E-03	7.85E-03	8.90E-04
12,554.78	1.835	2.18E-03	6.42E-04	2.24E-03	2.76E-04
17,687.42	0.787	8.85E-04	2.46E-04	9.23E-04	1.19E-04
22,870.16	0.412	4.43E-04	1.16E-04	4.63E-04	6.22E-05
28,131.87	0.243	2.52E-04	6.23E-05	2.63E-04	3.63E-05
33,480.56	0.155	1.57E-04	3.66E-05	1.63E-04	2.31E-05
38,911.09	0.104	1.05E-04	2.30E-05	1.10E-04	1.58E-05
44,418.88	0.074	7.47E-05	1.52E-05	7.80E-05	1.14E-05
50,000.00	0.054	5.53E-05	1.04E-05	5.77E-05	8.52E-06

Trapped Radiation Sources:

The design reference for trapped particle environments for protons and electrons is given by the AP-8 and AE-8 minimum (Sawyer and Vette, 1976, and Vette, 1991 respectively) using the International Geomagnetic Reference Field (IGRF) magnetic field (epoch 1965) for calculations of magnetic field magnitude |**B**| and the McIlwain L parameter as input.

LEO analysis will be determined using circular orbits at 51.6° inclination and 500 km altitude. LEO analysis fluences and resultant exposure values will be reported as average per day over the duration of the analysis profile.

Translunar insertion trajectory analysis fluences and resultant exposure values will be reported as totals per transit for the analysis profile. These model trapped spectra are available to all contractors, if they so choose, as GFE.

Limitations

None

Technical Notes

Crew exposure will be managed As Low As Reasonably Achievable (ALARA) per CxP 70024, Section 3.2.7.1.1, Cradle ID-HS3085.

A technical description of the LEO environment and free-space GCR environment applicable to crew health concerns may be found in the National Council on Radiation Protection and Measurements (NCRP) Report Number 132, Radiation Protection Guidance for Activities in Low-Earth Orbit, Chapter 3, and in NCRP Report Number 142, Operational Radiation Safety Programs for Astronauts in Low-Earth Orbit: A Basic Framework, Chapter 4.

GCR and trapped proton dose contributions are greatest during the solar minimum portion of the solar cycle, roughly a factor of two (2) more than during solar maximum. Therefore, solar minimum conditions are appropriate for prediction of design requirements for crew protection.

Earth's magnetic field deflects part of the SPE and GCR radiation so that exposure in LEO is roughly a factor of two (2) less than that in free space.

Technical information on the current and historical versions of the IGRF model is available at http://www.ngdc.noaa.gov/IAGA/vmod/igrf.html.

3.3.5 Reserved

3.3.6 Meteoroid and Orbital Debris Environment

Description

This section specifies the meteoroid and orbital debris (M/OD) environments that pose an impact threat during in-space operations. Orbital debris is only of concern in Earth orbit. Meteoroids must be considered a threat during Earth orbit, lunar and interplanetary missions. Meteoroid storms are not included in this section, as they are mitigated operationally and not during the design phase. Meteoroids and orbital debris should be considered in combination, as their risk is cumulative. Mass, size, velocity, and density are used to compute penetrations and effectiveness of shielding.

Design Limits

For All Phases:

The meteoroid models for the Earth, lunar and interplanetary phases can be found in the Meteoroid Engineering Model, version 3 (MEM 3) software package. The orbital debris environment in Earth orbit is described by the Orbital Debris Engineering Model 3.0 (ORDEM 3.0).

Detailed flux, speed, and directionality limits in the M/OD environments are to be derived using precise inputs for the environment models, specifically the DRM parameters as specified in ESD 10012. Orbital Debris Engineering Model 3.0 (ORDEM 3.0) will be used for the orbital debris environment. The meteoroid environment is defined by MEM 3 for all locations in the inner Solar System between the orbit of Mercury and the main Asteroid Belt.

Orbital debris falls off rapidly beyond the sun synchronous Earth orbit altitudes, and the current data/models suggest that meteoroids dominate the penetration risk above 5000 km altitude.

Model Inputs

All Mission Phases:

Use the DRM orbital parameters and mission durations as inputs into ORDEM 3.0 to calculate the debris flux, speed, and directionality. Additional information is required for input into MEM 3 since the model requires a series of state vectors along an orbit in order to define the meteoroid environment. Construct a series of state vectors in the appropriate inertial coordinate frame for input into MEM 3. Mission durations should be chosen based on the DRM parameters.

Limitations

All Mission Phases:

ORDEM provides expectation values and uncertainties for the orbital debris environment parameters. MEM models the mass ranges from 10^{-6} grams to 10 grams (those particles considered a threat to spacecraft) and does not provide uncertainties.

The meteoroid environment is especially sensitive to the orbital plane's and/or vehicle orientation relative to the Sun. The highest flux rates occur when the orbital plane is closest to the ecliptic plane. The current DRM parameters lack specific information, making it difficult to define the design limits for the meteoroid environment. Consult the models' help files for instructions on how many state vectors/random draws are necessary to adequately sample the orbit.

The fluxes from meteor showers are not included in the values output by MEM 3.

The orbital debris model, ORDEM 3.0, models the environment up to geosynchronous orbit altitude (36,000 km altitude). However, it only models large particles (greater than or equal to 10 cm in diameter) at GEO, as there is no data on the small particle population at this altitude.

The debris environment is directional, and in LEO is generally fixed with regard to a vehicle's orbital motion reference frame, whereas the meteoroid environment is fixed relative to the Sun. This means that the perceived meteoroid environment will vary with time, as the orbit (and vehicle) changes orientation relative to the solar direction. This will require the evaluation of the

meteoroid fluxes throughout the course of the mission, as described by the DRM parameters and mission durations. The meteoroid model will evaluate the meteoroid flux throughout the course of the mission if the user defined state vectors adequately describe the vehicle's position and velocity.

3.3.7 Earth Gravitational Field

Description

Accurate gravity models are required for precision navigation, operational planning, and long-term orbit propagations; however, the use of high degree and order models are generally not needed for flight system design. It is usually sufficient for the design and development of flight hardware (for example, propulsion, telecom, and GN&C hardware) to truncate an Earth gravity field to approximately degree and order 8. As a result, in keeping with the overall objective of the DSNE, a complete description of the recommended Earth gravity model will not be provided in this document. The reader is referred to the NEDD for general gravity field formulation information.

Design Limits

Earth Gravity model, GRACE model GGM02C, is used to evaluate the gravitational field strength for use in hardware applications. The truncation to degree and order 8 is acceptable for hardware design.

Model Inputs

The gravity field is available online at the following web site:
http://www2.csr.utexas.edu/grace/gravity/ggm02/.

Limitations

As stated above, a truncated gravity field may be utilized for the design and development of flight hardware. For design applications, truncation to degree and order less than 8 require supporting error analysis.

Technical Notes

The GRACE gravity model GGM02C is a 200th spherical harmonic degree and order model that combines approximately 1 year of GRACE K-band range-rate, attitude, and accelerometer data with surface gravity and mean sea surface information. The model was released in October 2004.

3.3.8 Lunar Gravitational Field

Description

To a much greater extent than for Earth, the use of accurate gravity models is required at the Moon for precision navigation, operational planning, and long-term orbit propagations due to the complex nature of the lunar gravity field and the lower altitudes at which lunar spacecraft are

typically flown. The reader is referred to the NEDD for general gravity field formulation information.

The Gravity Recovery and Interior Laboratory (GRAIL) lunar gravity model will be used for Exploration missions. The GRAIL mission placed two spacecraft into the same orbit around the Moon. As they flew over areas of greater and lesser gravity, caused both by visible features such as mountains and craters and by masses hidden beneath the lunar surface, they moved slightly toward and away from each other. An instrument aboard each spacecraft measured the changes in their relative velocity very precisely, and this information was translated into a high-resolution map of the Moon's gravitational field. This gravity-measuring technique is essentially the same as that of the Gravity Recovery And Climate Experiment (GRACE), which began mapping Earth's gravity in 2002.

Design Limits

The GRAIL Lunar Gravity Model is needed for precise orbit determination. Adequate sensitivity analyses are needed to assure that the design will cover the range of Design Reference Missions.

Model Inputs

The GRAIL model may be truncated to fewer terms for use in different applications. It is recommended that sensitivity analyses be performed to determine if the lower fidelity field is adequate for the particular application.

The gravity field is available online at the following Planetary Data System (PDS) web site:

http://pds-geosciences.wustl.edu/grail/grail-l-lgrs-5-rdr-v1/grail_1001/shadr/

Note that there are 3 models available at this site; one from Goddard Space Flight Center (gggrx_0660pm_sha) and two developed by the Jet Propulsion Laboratory (jggrx_0420a_sha and jggrx_0660b_sha). Except for small data weighting and calibration differences the two models are nearly identical for the low degree and order generally used for mission planning and operations. The GSFC model gggrx_0660pm_sha should be used for consistency across the Exploration Programs. The binary files in the following location:

http://pds-geosciences.wustl.edu/grail/grail-l-lgrs-5-rdr-v1/grail_1001/shbdr/ also contain the covariance matrices useful for error analyses.

The models on the PDS site are tide-free and do not contain the corrections for permanent Earth tide needed by some orbit propagators. If the design team using this model determines that the added accuracy from tidal corrections is necessary, then the corrected coefficients should be calculated using

C_{20} perm tide = C_{20} tide-free -1.6541e-6 x k_2

C_{22} perm tide = C_{22} tide-free + 2.8676e-6 x k_2

Where the k_2 tidal Love number is found in the .LBL file and C_{20} tide-free and C_{22} tide-free coefficients are in the .TAB file. The proper planetary ephemeris to use with the model is also found in the .LBL file. The values of lunar radius and GM are found in the .TAB file. Refer to the .LBL file for locations of those values and description of the model format.

Limitations

The GRAIL model is a vast improvement over the previous models which had no direct measurements of the field of the lunar farside. While the SHA (ASCII) version .TAB file contains estimates of the errors for each individual model coefficients, the SHB (binary) .DAT files contain the covariance matrix for use in Monte Carlo analyses if desired. Although truncation of the model is acceptable sensitivity analyses should be performed to allow trades between computational efficiency and orbit propagation accuracy.

A different correction for the permanent tide can be computed including the Earth and the Sun but the inclusion of the Sun only adds another 0.5% to the permanent tide correction.

The GRAIL models have not been evaluated for orbit prediction and navigation performance for low-degree or truncated fields.

Technical Notes

The GRAIL mission is described at this web site:

http://pds-geosciences.wustl.edu/grail/grail-l-lgrs-2-edr-v1/grail_0001/catalog/mission.cat

For operational considerations, the accuracy of the lunar gravity field is very important. Since there is essentially no atmosphere on the Moon, spacecraft may use very low-altitude orbits (for example, 100 km or lower). At low altitudes, the variations in the lunar gravity field have a large effect on long-term orbit stability. For example, without some type of orbit maintenance or station keeping a satellite placed in a circular polar lunar orbit at 100 km altitude will impact the surface in about 160 days.

3.3.9 Thermal Environment for In-Space Hardware

Description

This section specifies the external thermal parameters that determine the spacecraft heat balance, solar irradiance, Earth and lunar albedo radiation and emitted long-wave radiation. In addition to the environmental parameters, spacecraft temperatures are dependent on internal sources of thermal energy and the spacecraft geometric configuration.

3.3.9.1 Thermal Environment for Lunar Orbital Phases

Design Limits

From the perspective of external environmental conditions, the hot extreme will occur in lunar orbit. The short-term (<1 hour) cold extreme will occur in lunar orbit during eclipse; otherwise, it will occur in the Earth-Moon transit phase.

3.3.9.1.1 Solar Constant

The solar constant, as defined in Section 3.3.9.2, applies to lunar orbit. However, there is an enhanced range of variation due to changes in Moon-Sun distance caused by the Moon orbiting the Earth. This motion adds or subtracts up to 405,504 km to the variations in the Earth-Sun distance considered in Section 3.3.9.2, so the effective solar constant range is as follows (does not include a $\pm$5 W/m^2 measurement uncertainty):

Maximum solar flux:	1,421 W/m^2	
Mean solar flux:	1,367 W/m^2	(Solar Constant)
Minimum solar flux:	1,315 W/m^2	

3.3.9.1.2 Lunar Albedo

High resolution measurements of albedo have been made by Lunar Reconnaissance Orbiter and values are available in Section 3.4.6.1. For thermal analyses of lunar orbiting spacecraft the material in this section (3.3.9.1) may be of sufficient fidelity. For more detailed orbital analyses and any surface vehicle analyses please refer to the material in 3.4.6.1.

For the near side of the Moon, average values of the normal albedo are provided by Dollfus and Bowell, 1971 for wavelengths from 0.327 μ to 1.050 μ. To convert this data to an average bolometric value, the data was averaged weighted by the solar spectrum as approximated by a blackbody curve for 5,780 K. The resulting value is:

Average bolometric normal albedo = 0.12 (lunar near side)

Local surface variations will cause an orbiting spacecraft to experience short-term variations about this value. These could range from a low of 0.07 to a high of 0.20. The average reflectivity is 164 W/m^2 with a maximum of 285 W/m^2 and minimum of 91 W/m^2 for the near side.

The surface of the far side of the Moon is dominated by "lunar highlands" terrain that tends to be somewhat brighter than the near side, which has numerous darker maria. For the far side, local normal albedo data is available for the waveband at 750-nm from UV/Vis instrument (camera) from the Clementine mission. Noting that the curve fit of albedo against wavelength for the near side data crossed 750-nm essentially right at the average value, 0.12, it can be assumed that the 750-nm normal albedo will be a close approximation to the normal bolometric albedo. Thus, the following (Lawson et al., 2000):

Average bolometric normal albedo = 0.15 (lunar far side)

Temporal variation about this value will be ±0.05. The average reflectivity is 154 W/m^2 with a maximum of 285 W/m^2 and minimum of 131 W/m^2 for the far side.

The ranges of variation quoted here should bound the values seen by low orbiting spacecraft. In higher orbits, some spatial averaging will occur and the range of variation will diminish somewhat.

3.3.9.1.3 Lunar Long-Wave Radiance

Detailed measurements of surface temperatures as a function of latitude and time-of-day as well as emissivities have been made by Lunar Reconnaissance Orbiter and values are available in Section 3.4.6.1. For thermal analyses of lunar orbiting spacecraft the material in this section (3.3.9.1) may be of sufficient fidelity. For more detailed orbital analyses and any surface vehicle analyses please refer to the material in 3.4.6.1.

Analysis of the Long-Wave Infrared Camera (LWIR) data from the Clementine mission (Lawson et al., 2000) indicates that the radiance from the Moon, as viewed by a nadir-looking spacecraft, can be well represented by a simple Lambertian thermal balance model. The term Lambertian implies equal scattering in all directions. Given the slow rotation rate of the Moon, effects of thermal inertia on the surface can be neglected for this application. On this basis, the thermal balance at the lunar sub-solar point can be expressed by the Stefan-Boltzmann law:

$$\varepsilon\sigma T_s^4 \approx (1 - \bar{a})\, S_o$$

Where:

ε is the long-wave emissivity of the surface, approximately equal to 0.95 – 0.98 (see 3.4.6.1)

σ is the Stefan-Boltzmann constant (5.67E-8 W m^{-2} K^{-4})

T_s is the lunar surface temperature at the sub-solar point

$\bar{a}$ is the average lunar normal bolometric albedo described in 3.3.9.1.2.

S_o is the solar constant at the appropriate distance from the sun.

On the sunlit side, the solar irradiance varies as cos(i), where i is the solar incidence angle (the angle between the Moon-Sun vector and the Moon-satellite vector). A good approximation for the gross lunar surface temperature variation is therefore:

$$T \approx T_s \cos^{1/4}(i)$$

As a result the lunar long-wave radiance on the sunlit side can be approximated by:

$$I_{LW} \approx \varepsilon\sigma T^4 \approx (1 - \bar{a})\, S_o \cos(i)$$

The uncertainty and range of variation due to local albedo effects is approximately 270 W/m^2 at the sub-solar point. This corresponds to a ±20 K surface temperature variation. As the solar

incidence angle increases to ~ 80°, the range of surface temperature variation increases to ~ 60 K, but the irradiance variation is much less than at the sub-solar point because of the power law.

On the nightside, the first part of this expression still applies:

$$I_{LW} \approx \varepsilon\sigma T^4$$

with the nightside temperature equal to 100, ±20 K. (The analyst may wish to add an interpolation over the small discontinuity at i = 90°.)

Space sink temperature: 3 K

3.3.9.1.4 Lunar Eclipse

A lunar eclipse occurs when the Earth is between the Sun and the Moon, and the Earth's shadow falls on the Moon. The Moon's orbit is approximately 5° inclined with respect to the Earth's orbit around the Sun. This results in a lunar eclipse occurring only when the ascending or descending nodes fall in the ecliptic during a full moon. Lunar eclipse Tables can be found at http://eclipse.gsfc.nasa.gov/lunar.html for the years 1901 through 2100. There may be up to five lunar or solar eclipses in a year but the combined total of both will never exceed seven.

There are three types of lunar eclipses: penumbral, partial, or total. During a penumbral eclipse, a portion of the sun is blocked by the Earth. A partial eclipse will have only part of the Moon going through the penumbral and umbral shadows. However, during a total eclipse, the Moon experiences all three types of events during the eclipse: penumbral, partial, and total. Light is refracted in the Earth's atmosphere and will give the Moon an orange, red, blue green, or purple hue while totally immersed in the umbra. The color is dependent on atmospheric conditions on Earth while the Moon is experiencing totality.

The stellar apparent magnitude is a numerical value of the observed brightness of a celestial object as seen from Earth. A full moon has an apparent magnitude of -12.6 (the brighter an object the lower the numerical value), while the Moon during totality ranges from -3.5 to 1.5. These numbers are derived using an eclipse model during mid-eclipse. Using these computed values, the solar flux can be calculated during an eclipse from the following equations:

$\Delta m = m_{eclipse} - m_{full\ moon} = m_1 - m_0$ Calculates the decrease in apparent magnitude during an eclipse.

$\underline{I_0} = 10^{\Delta m/2.5}$ Calculates the ratio of brightness of a full moon to the eclipsed Moon I_1

$Eclipse_{flux} = \underline{1367\ W/m^2}$ Calculates the solar flux during a lunar eclipse using the average I_0/I_1 solar flux at the Moon of 1,367 W/m^2

This corresponds to 0.03% to 0% of solar flux reaching this region. This is of concern to a spacecraft orbiting the Moon if the spacecraft is dependent on solar energy.

During the years 2018-2035, the worst case lunar eclipse occurs on June 26, 2029. Using the data from this eclipse as an example, a spacecraft in a circular orbit would experience totality for the following altitudes vs. times around the Moon and would experience worst case minimum solar flux for times indicated in Table 3.3.9.1.4-1.

Table 3.3.9.1.4-1. Projected Worst Case Minimum Solar Flux during Lunar Eclipse, Dated June 26, 2029

Orbit Altitude	Totality	No Solar Flux (Worst Case)
100 km	188 minutes	233 minutes
500 km	197 minutes	242 minutes
1,000 km	177 minutes	234 minutes

Calculations by Johnson Space Center for the Near Rectilinear Halo Orbit give expected worst case durations of eclipses by the Moon of 1.5 hours (90 minutes) duration.

3.3.9.2 Thermal Parameters for Near-Earth Phases

Limits for Earth orbit cases where spacecraft configuration, power usage, or operations differ from the lunar orbit cases such that thermal performance needs to be evaluated are given below:

Space sink temperature: 3 K

Orbital beta angle: 0 to 56° (lunar missions)

0 to 75° (ISS missions)

Maximum: Solar constant: 1,414 W/m^2

Albedo, long-wave radiance pairs per the hot cases in Table 3.3.9.2-1 for lunar missions or Table 3.3.9.2-2 for ISS missions.

Minimum: Solar constant: 1,322 W/m^2

Albedo, long-wave radiance pairs per the cold cases in Table 3.3.9.2-1 for lunar missions or Table 3.3.9.2-2 for ISS missions.

Table 3.3.9.2-1. Albedo, Outgoing Longwave Radiation (OLR) Pairs for Critical Systems in Low-Inclination Orbits

	COLD CASES		
Averaging Time	**Minimum Albedo Alb ⇔ OLR (W/m²)**	**Combined Minimum Alb ⇔ OLR (W/m²)**	**Minimum OLR Alb ⇔ OLR (W/m²)**
16 second	0.06 ⇔ 273	0.13 ⇔ 225	0.40 ⇔ 150
128 second	0.06 ⇔ 273	0.13 ⇔ 226	0.38 ⇔ 154
896 second	0.07 ⇔ 265	0.14 ⇔ 227	0.33 ⇔ 173
30 minute	0.08 ⇔ 261	0.14 ⇔ 228	0.30 ⇔ 188
90 minute	0.11 ⇔ 258	0.14 ⇔ 228	0.25 ⇔ 206
6 hr	0.14 ⇔ 245	0.16 ⇔ 232	0.19 ⇔ 224
24 hr	0.16 ⇔ 240	0.16 ⇔ 235	0.18 ⇔ 230
	HOT CASES		
Averaging Time	**Maximum Albedo Alb ⇔ OLR (W/m²)**	**Combined Maximum Alb ⇔ OLR (W/m²)**	**Maximum OLR Alb ⇔ OLR (W/m²)**
16 second	0.43 ⇔ 182	0.30 ⇔ 298	0.22 ⇔ 331
128 second	0.42 ⇔ 181	0.29 ⇔ 295	0.22 ⇔ 326
896 second	0.37 ⇔ 219	0.28 ⇔ 291	0.22 ⇔ 318
30 minute	0.33 ⇔ 219	0.26 ⇔ 284	0.17 ⇔ 297
90 minute	0.28 ⇔ 237	0.24 ⇔ 275	0.20 ⇔ 285
6 hr	0.23 ⇔ 248	0.21 ⇔ 264	0.19 ⇔ 269
24 hr	0.22 ⇔ 251	0.20 ⇔ 260	0.19 ⇔ 262
Mean Albedo: 0.18		Mean OLR: 246	

Albedo and OLR values are referenced to the "top of the atmosphere," R_e + 30 km.

Table 3.3.9.2-2. Albedo, OLR Pairs for Critical Systems in Medium-Inclination Orbits

	COLD CASES		
Averaging Time	**Minimum Albedo Alb ⇔ OLR (W/m^2)**	**Combined Minimum Alb ⇔ OLR (W/m^2)**	**Minimum OLR Alb ⇔ OLR (W/m^2)**
16 second	0.06 ⇔ 273	0.15 ⇔ 213	0.40 ⇔ 151
128 second	0.06 ⇔ 273	0.15 ⇔ 213	0.38 ⇔ 155
896 second	0.08 ⇔ 262	0.17 ⇔ 217	0.34 ⇔ 163
30 minute	0.12 ⇔ 246	0.18 ⇔ 217	0.27 ⇔ 176
90 minute	0.16 ⇔ 239	0.19 ⇔ 218	0.30 ⇔ 200
6 hr	0.18 ⇔ 238	0.19 ⇔ 221	0.31 ⇔ 207
24 hr	0.19 ⇔ 233	0.20 ⇔ 223	0.25 ⇔ 210
	HOT CASES		
Averaging Time	**Maximum Albedo Alb ⇔ OLR (W/m^2)**	**Combined Maximum Alb ⇔ OLR (W/m^2)**	**Maximum OLR Alb ⇔ OLR (W/m^2)**
16 second	0.48 ⇔ 180	0.31 ⇔ 267	0.21 ⇔ 332
128 second	0.47 ⇔ 180	0.30 ⇔ 265	0.22 ⇔ 331
896 second	0.36 ⇔ 192	0.28 ⇔ 258	0.22 ⇔ 297
30 minute	0.34 ⇔ 205	0.28 ⇔ 261	0.21 ⇔ 282
90 minute	0.31 ⇔ 204	0.26 ⇔ 257	0.22 ⇔ 274
6 hr	0.31 ⇔ 212	0.24 ⇔ 248	0.21 ⇔ 249
24 hr	0.28 ⇔ 224	0.24 ⇔ 247	0.21 ⇔ 245
Mean Albedo: 0.22		Mean OLR: 234	

Albedo and OLR values are referenced to the "top of the atmosphere," R_e + 30 km.

Model Inputs

For the near-Earth phases, the design verification to thermal environments specified in this requirement shall account for variations in inclination, altitude, and SZA as described below. Note, in particular, that the Table values are referenced to the top of the atmosphere and that the Albedo values must be corrected for SZA.

Orbital Altitude and "Top of Atmosphere"

The OLR and albedo radiation received on a satellite surface diminishes as its altitude increases, i.e., as the satellite moves away from the source. This effect is accounted for as part of the "view factor" in thermal calculations. Derived OLR and albedo data measurements from satellites at several altitudes (610, 815, and 849 km) were corrected to the apparent source surface (30 km above Earth surface) or "top of atmosphere." Thus, in applying this data the analyst should

assume a source at R_e + 30 km, where R_e is the Earth's radius, 6378.140 km equatorial. Failure to do so leads to a slight underestimate of the OLR and albedo radiation by a factor of:

$$F_a = (R_e + A)^2/(R_e + 30 \text{ km} + A)^2 \qquad (7.1)$$

where A is the orbital altitude. The error is quite small (F_a = 0.9911 at A = 300 km) and decreases (F_a approaches one) with increased altitude.

Orbital Inclination, Beta Angle, and Solar Zenith Angle

Orbital "inclination" refers to the angle between the Earth's polar vector and the vector normal to the satellite's orbit plane. Thus, an equatorial orbit has an inclination of zero; a perfect polar orbit has an inclination of 90°. The orbital "beta" angle is the minimum angle between the satellite's orbit plane (the closest to a Sun-pointing vector possible in the plane) and the Sun-Earth vector. The beta angle can be thought of as the solar elevation angle with respect to the orbit plane. The angle between the Sun-Earth vector and the Earth-satellite vector is termed the "Solar Zenith" Angle (SZA). The SZA is zero when the Sun is directly above the satellite (Earth-satellite-Sun in a straight line) and 90° when a satellite is directly over the terminator. Except for special Sun synchronous cases, the SZA varies rapidly over an orbit; the minimum SZA is equal to the absolute value of the beta angle.

Limitations

None

Technical Notes

None

3.3.10 Solar Illumination Environment for In-Space Hardware

Description

This section describes the solar spectrum, including ultraviolet radiation, which can cause deterioration of materials.

Design Limits

Hardware configuration, orientation relative to the Sun, and exposure time must be considered for solar irradiation for the Space Vehicle Segment. Intensity is specified in Table 3.3.10-1.

Table 3.3.10-1. Solar Spectral Irradiance-Standard Curve, Abridged Version

λ = wavelength, micron
E_λ = solar spectral irradiance averaged over small bandwidth centered at λ, $W \cdot m^{-2} micron^{-1}$
$D_{0\lambda}$ = percentage of the solar constant (1366.1 $W \cdot m^{-2}$) associated with wavelengths shorter than λ
Note 1 – Double lines indicate change in wavelength interval of integration. Each column continues to next page.

λ	E_λ	$D_{0\lambda}$	λ	E_λ	$D_{0\lambda}$
0.14	9.833×10^{-2}	0.0	0.57	1,797	31.39

λ = wavelength, micron
E_λ = solar spectral irradiance averaged over small bandwidth centered at λ, $W \cdot m^{-2} micron^{-1}$
$D_{0\lambda}$ = percentage of the solar constant (1366.1 $W \cdot m^{-2}$) associated with wavelengths shorter than λ
Note 1 – Double lines indicate change in wavelength interval of integration. Each column continues to next page.

λ	E_λ	$D_{0\lambda}$	λ	E_λ	$D_{0\lambda}$
0.16	0.3195	3.1×10^{-4}	0.58	1,801	32.71
0.18	2.042	2.0×10^{-3}	0.59	1,758	34.01
0.20	10.83	1.1×10^{-2}	0.60	1,745	35.29
0.22	44.93	5.2×10^{-2}	0.62	1,663	37.78
0.23	49.64	8.7×10^{-2}	0.64	1,610	40.18
0.24	51.83	0.12	0.66	1,527	42.48
0.25	59.81	0.16	0.68	1,485	44.68
0.26	129.1	0.23	0.70	1,438	46.82
0.27	222.1	0.36	0.72	1,360	48.87
0.28	212.9	0.52	0.75	1,272	51.76
0.29	441.0	0.76	0.8	1,132	56.16
0.30	526.0	1.12	0.9	882.6	63.53
0.31	634.5	1.54	1.0	719.7	69.40
0.32	746.5	2.05	1.2	487.1	78.23
0.33	948.7	2.67	1.4	342.5	84.30
0.34	947.3	3.36	1.6	243.5	88.59
0.35	969.5	4.06	1.8	167.1	91.60
0.36	985.2	4.78	2.0	115.0	93.66
0.37	1,129	5.55	2.2	81.73	95.10
0.38	1,091	6.36	2.4	58.78	96.13
0.39	1,093	7.16	2.6	43.86	96.88
0.40	1,518	8.12	2.8	33.43	97.45
0.41	1,712	9.30	3.0	25.93	97.88
0.42	1,740	10.56	3.2	20.45	98.22
0.43	1,625	11.79	3.4	16.36	98.49
0.44	1,826	13.06	3.6	13.26	98.71
0.45	2,030	14.47	3.8	10.87	98.89
0.46	2,077	15.97	4.0	8.977	99.03
0.47	2,049	17.48	4.5	5.674	99.30
0.48	2,057	18.98	5	3.691	99.47
0.49	1,955	20.45	6	1.879	99.68
0.50	1,948	21.88	7	1.022	99.78
0.51	1,911	23.29	8	0.6041	99.84

λ = wavelength, micron
E_λ = solar spectral irradiance averaged over small bandwidth centered at λ, $W \cdot m^{-2} micron^{-1}$
$D_{0\lambda}$ = percentage of the solar constant (1366.1 $W \cdot m^{-2}$) associated with wavelengths shorter than λ
Note 1 – Double lines indicate change in wavelength interval of integration. Each column continues to next page.

λ	E_λ	$D_{0\lambda}$	λ	E_λ	$D_{0\lambda}$
0.52	1,806	24.65	10	0.2663	99.90
0.53	1,861	26.00	15	6.106×10^{-2}	99.96
0.54	1,861	27.36	20	1.755×10^{-2}	99.98
0.55	1,867	28.72	50	1.769×10^{-3}	100.00
0.56	1,808	30.07			

Model Inputs

None

Limitations

None

Technical Notes

None

3.3.11 In-Space Neutral Atmosphere (Thermosphere) Density

Description

The In-Space atmosphere begins at about 90 km altitude and extends to approximately 2,000 km. Atomic oxygen (AO) in the thermosphere drives selection of external materials. Atmospheric density and its variations are critical to the design of the entry thermal protection systems and entry guidance systems. Ascent environments are assumed to be considered as part of the integrated launch system analysis and are not included here.

Design Limits

The Mass Spectrometer Incoherent Scatter (MSIS) module of Earth GRAM should be used to calculate Atomic Oxygen fluence for the particular orbit and mission lifetime. The maximum conditions of solar flux F10.7 and geomagnetic index Ap from Table 3.3.11-1 should be used to provide a conservative estimate of the fluence.

Model Inputs

System performance will be evaluated through analysis of 1,000 or more Earth-GRAM 2010 (see note in 2.1.2 Applicable Models/Data Sets) (includes Marshall Engineering Thermosphere (MET)) random profiles for each of the three cases in Table 3.3.11-1.

Table 3.3.11-1. Earth-GRAM 2010 Inputs for Thermosphere Parameter Calculations

Parameter	Earth-GRAM 2010 Variable Name	Minimum	Nominal	Maximum
Solar flux $F_{10.7}$	f10 f10b	67 67	148 148	245 245
Geomagnetic index Ap	ap	7.2	16	55
Date	mn, ida, iyr	July 15	June 1	Jan 10 for systems most sensitive to heights below 90 km Oct 27 for systems most sensitive to heights above 90 km
Local time (does not affect results below 90 km)	ihro, mino, seco	03:00:00	08:00:00	14:00:00
Random perturbations	rpscale, ruscale, rwscale	1.0	1.0	2.0
Small scale perturbations	patchy	0	0	1

Limitations

Although uncertainties are not specifically determined for the Earth-GRAM 2010 (see note in 2.1.2 Applicable Models/Data Sets) model, it is generally accepted that the thermospheric density is modeled to within no better than 15% accuracy (1 standard deviation) by the MET and similar models (for example, the Mass Spectrometer Incoherent Scatter model). Perturbations on the aloft region are statistically derived and are generated using the input variables in Table 3.3.11-1.

Technical Notes

Hardware configuration, orientation relative to ram (velocity vector) direction, and exposure time must be considered. The $F_{10.7}$ and Ap values were taken from the NEDD, 7.1.4, Solar and Geomagnetic Indices. The minimum values are the minima of the minimum profiles. Nominal solar flux and geomagnetic index values are the maxima of the mean solar cycle profile. Maximum solar flux and geomagnetic index values were selected to produce a 95 percentile global maximum exospheric temperature and corresponding neutral density for a maximum solar cycle profile "Bin 5" conditions per "Ninety-day Solar and Geomagnetic Activity Input Files for Thermospheric Variation Simulation: Simulation Data Files Release 2," (Hickey and Smith, 1992).

3.3.12 Geomagnetic Fields (Reserved)

3.4 Lunar Surface Operational Phases

Characteristics of the lunar surface environment are identified in this section. The material herein represents global characteristics to be used for surface hardware design and verification. Mission planning and analysis should consider site-specific characteristics available from published and on-line resources as described in the appropriate sections.

Design Limits

Tabular values in this section are to be used for design. Figures are provided for illustration only.

3.4.1 Lunar Surface Geological and Geomorphological Environment

Rationale: All lunar surface systems are influenced by lunar surface geology and geotechnical properties, so it is required for design of surface systems.

3.4.1.1 Crater Size-Frequency Distribution

The areal number density (number per unit area) of craters on the Moon is a function of surface age, as craters accumulate with time. For a surface of a given age, the crater density will follow the production function until the frequency crosses the equilibrium curve, then tracks the equilibrium density. As an illustration, for a 3.5 billion year old (Ga) surface typical of the lunar maria, the cumulative number of craters of diameter $\geq D$ per km^2 can be summarized as:

Table 3.4.1.1-1. Number density (also called frequency) of craters equal to or larger than diameter D per km^2 for a 3.5 Ga surface.

***D* (km)**	# $\geq D$ (per km$^{2)}$	*D* (km)	# $\geq D$ (per km$^{2)}$	*D* (km)	# $\geq D$ (per km$^{2)}$
0.01	7.94E+02	0.1	7.94E+00	1	4.79E-03
0.0126	5.01E+02	0.126	5.01E+00	1.259	2.16E-03
0.0158	3.16E+02	0.158	3.16E+00	1.585	1.02E-03
0.0200	2.00E+02	0.200	1.72E+00	1.995	5.12E-04
0.0251	1.26E+02	0.251	7.73E-01	2.512	2.75E-04
0.0316	7.94E+01	0.316	3.39E-01	3.162	1.59E-04
0.0398	5.01E+01	0.398	1.46E-01	3.981	9.92E-05
0.0501	3.16E+01	0.501	6.17E-02	5.012	6.61E-05
0.0631	2.00E+01	0.631	2.60E-02	6.310	4.67E-05
0.0794	1.26E+01	0.794	1.10E-02	7.943	3.46E-05

Large craters here come from the production function of Neukum et al. (2001); surfaces older than 3.5 Ga will have accumulated more large craters than given in Table 3.4.1.1-1; younger surfaces will have fewer. Values for craters ≤200m in this Table follow

$$N_{equilibrium-Trask}(\geq D) = 0.079433D^{-2}$$

For sub-100m craters, this Trask equilibrium function is a valuable upper limit for the number of craters on a surface of any age. Craters in this size range have reached equilibrium on every part of the Moon with the exception of very rare regions that were the site of large recent impacts (i.e., floors of large young craters). This equilibrium function is always an upper limit because surfaces with non-negligible topographic slope retain fewer craters. Figure 3.4.1.1-1 provides an illustration of the crater density in this table.

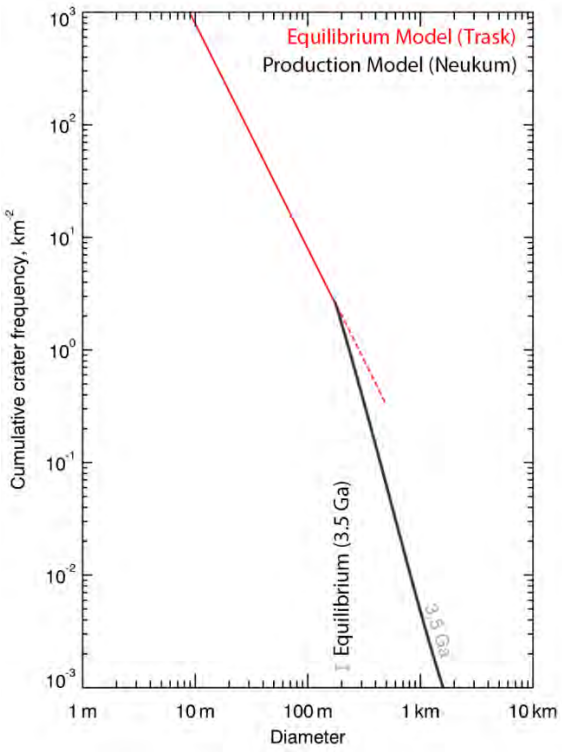

Figure 3.4.1.1-1. Cumulative crater density (number of craters of diameter ≥X per km^2) on a lunar surface of 3.5 Ga. (Ga=billions of years/surface age).

Design Limits

These series are generalizations that should be refined during detailed landing site characterization with direct observations of the crater population. The number density of craters can locally be highly affected by secondary craters and impact ejecta that will cause deviations in the number density of craters from the function. Secondary craters are usually recognizable from morphological considerations during detailed landing site characterization.

3.4.1.2 Crater Topography

Description

This section provides characteristics of individual craters' topography. See 3.4.1.3 for additional discussion on lunar topography and slope distributions.

Topography generated by craters provides most of the relief on the Moon. The topographic characteristics of individual craters vary strongly as a function of size and their age (as a result of the period of their exposure to the lunar surface environment). Larger craters remain minimally degraded for longer time periods. Morphologically fresh primary craters smaller than 10 km have floor-to-rim depth/diameter ratios given in Table 3.4.1.2-1.

Table 3.4.1.2-1. Depth/diameter ratios for fresh lunar craters (after Stopar et al., 2017).

Diameter Range	40-100m	100-200 m	200 m-400 m	400 m – 10 km
Fresh crater depth/diameter Ratio	0.12-0.14	0.14-0.16	0.16-0.17	0.19-0.22

Craters less than a few kilometers in size maintain their original depth for a geologically short period of time. For craters in the equilibrium part of the size distribution ($D \leq$100-m sizes, see 3.4.1.1), most craters are reduced to less than <50% of their initial depth. Characteristics of sub-km craters on a typical surface are:

Table 3.4.1.2-2. Crater morphological characteristics (for D<1 km; modified after Basilevsky, 1976).

	Freshest craters		→		Degraded Craters
Fraction of population	0.5%	2.5%	17%	30%	50%
Crater Characteristics	Very steep slopes, pronounced blocky ejecta, optically immature	Steep slopes, blocks common	Moderate slopes, most blocks on rim	Gentle slopes, rim mostly eroded	Very gentle slopes, no rim
Typical depth/diameter ratio	0.12-0.2+	0.12-0.2	0.1-0.15	0.07-0.1	<0.07
Max. Wall Slope	35˚+	25-35˚	15-25˚	10-15˚	<10˚

Because small craters degrade rapidly, most slope hazards at landing sites are from large craters ($D \geq$0.4 km) and/or fresh craters that are obvious during detailed landing site characterization.

Limitations

This description of craters' topography does not apply to large craters (≥10 km); craters larger than 15-20 km are in the complex crater regime and have more variable depth/diameter ratios at a given size even when fresh. Consideration of the topography of individual ≥10 km craters thus needs to be made on a case-by-case basis during landing site characterization.

Technical Notes

For individual site characterization, a high quality suite of topographic observations exists for the Moon's surface, from Lunar Orbiter Laser Altimeter, Kaguya Terrain Camera, Lunar Reconnaissance Orbiter Camera, and other missions and instruments. These data are available in the Planetary Data System (e.g., http://imbrium.mit.edu/DATA/SLDEM2015_SLOPE/) or can be visualized with ArcGIS, JMars, or Quickmap.

3.4.1.3 Lunar Surface Topography, Slope Distributions, and Roughness

The topography of a site on the lunar surface is a function of the location's cratering history and age, local geology, terrain type (mare vs. highlands), and geographic location. Individual landing site data thus should guide mission planning where possible. However, because of the rich topographic data available for the Moon, statistical characterization of lunar surface topography is readily possible at decameter-to-hectometer baselines (see Figure 3.4.1.3-1).

Very steep slopes: A very small fraction (~0.25%) globally on the Moon have slopes steeper than 32˚ at 25-m baseline. Slopes steeper than this value are almost always associated with young impact craters (Kreslavsky and Head, 2016).

Median slopes vary regionally and differ between the highlands (6-10˚) and maria (2-4˚) (e.g., Smith et al., 2010; Rosenburg et al., 2011; Kreslavsky et al. 2015). See Figure 3.4.1.3-2.

On planetary surfaces, slope is a function of relevant measurement baseline (length scale). For example, the median slopes at the scale of ~meters (lander leg separations) can be higher than at scales of tens of meters. This is particularly true on the maria, which are often relatively flat at large length, but shorter baselines sample the more variable local relief (e.g., Figure 3.4.1.3-2). Lunar highland terrains have comparable slopes at both decameter and hectometer scales (Figure 3.4.1.3-2, highlands).

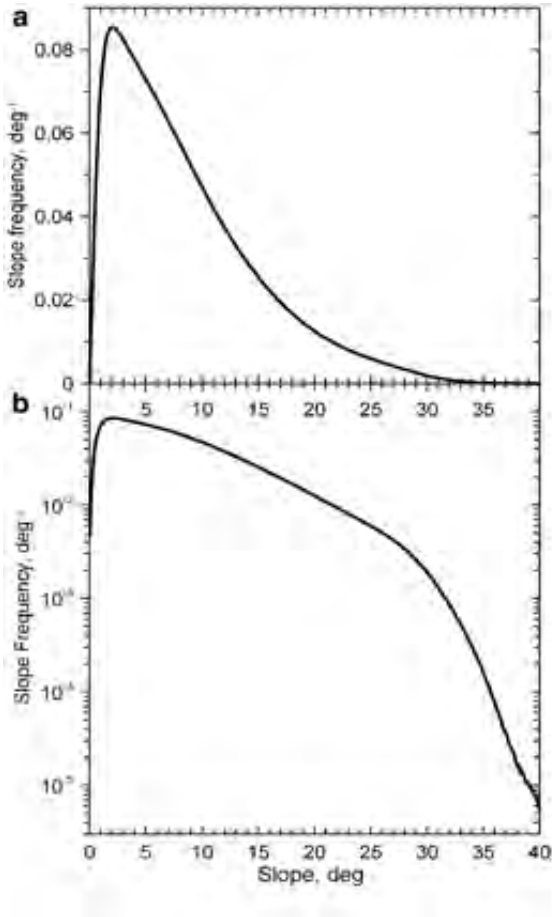

Figure 3.4.1.3-1. Frequency of slopes across the lunar surface at 25-m baseline from LOLA, shown with a linear frequency axis and logarithmic frequency axis (Kreslavsky and Head 2016)

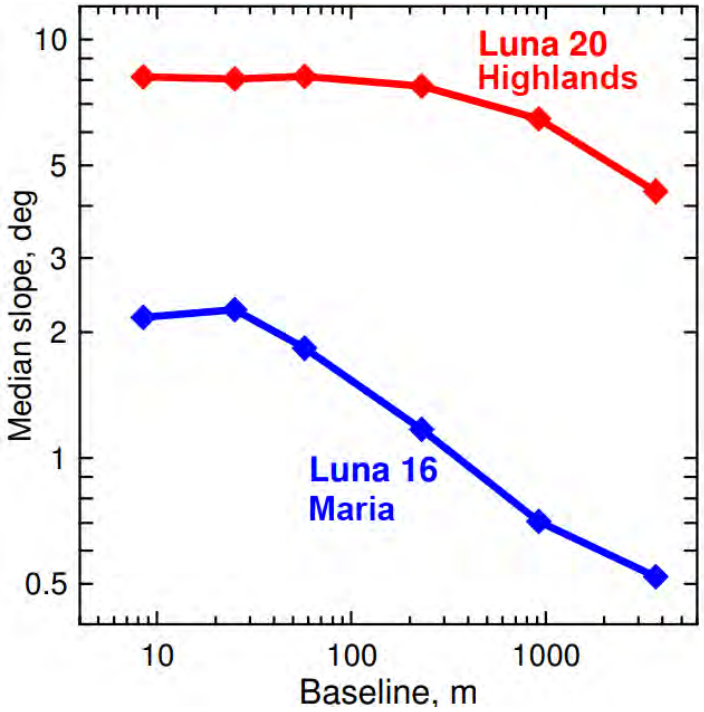

Figure 3.4.1.3-2. Median slopes at two landing sites from a combination of lola (24 m baselines and above) and lroc narrow angle camera digital terrain models. Modified from Kreslavsky et al. (2015)

Slopes at a consistent 17 m baseline were computed globally (Rosenburg et al., 2011) from LOLA data. Table 3.4.1.3-1 and Figure 3.4.1.3-3 illustrate the results. The highlands and poles are rougher than the maria, with both higher median slopes and a broader distribution (interquartile range) of observed slope values.

Table 3.4.1.3-1. Median slopes in different regions, with +/- values representing the 25th and 75th percentiles.

	Highlands	Maria	South Pole-Aitken Basin: All	South Pole-Aitken Basin: Floor	South Pole
Median slope at ~17 m baseline (degrees)	$7.5\ ^{+12.3}_{-4.2}$	$2.0\ ^{+4.1}_{-1.0}$	$7.2\ ^{+12.0}_{-3.0}$	$5.8\ ^{+10.5}_{-3.0}$	$7.6\ ^{+12.4}_{-4.2}$

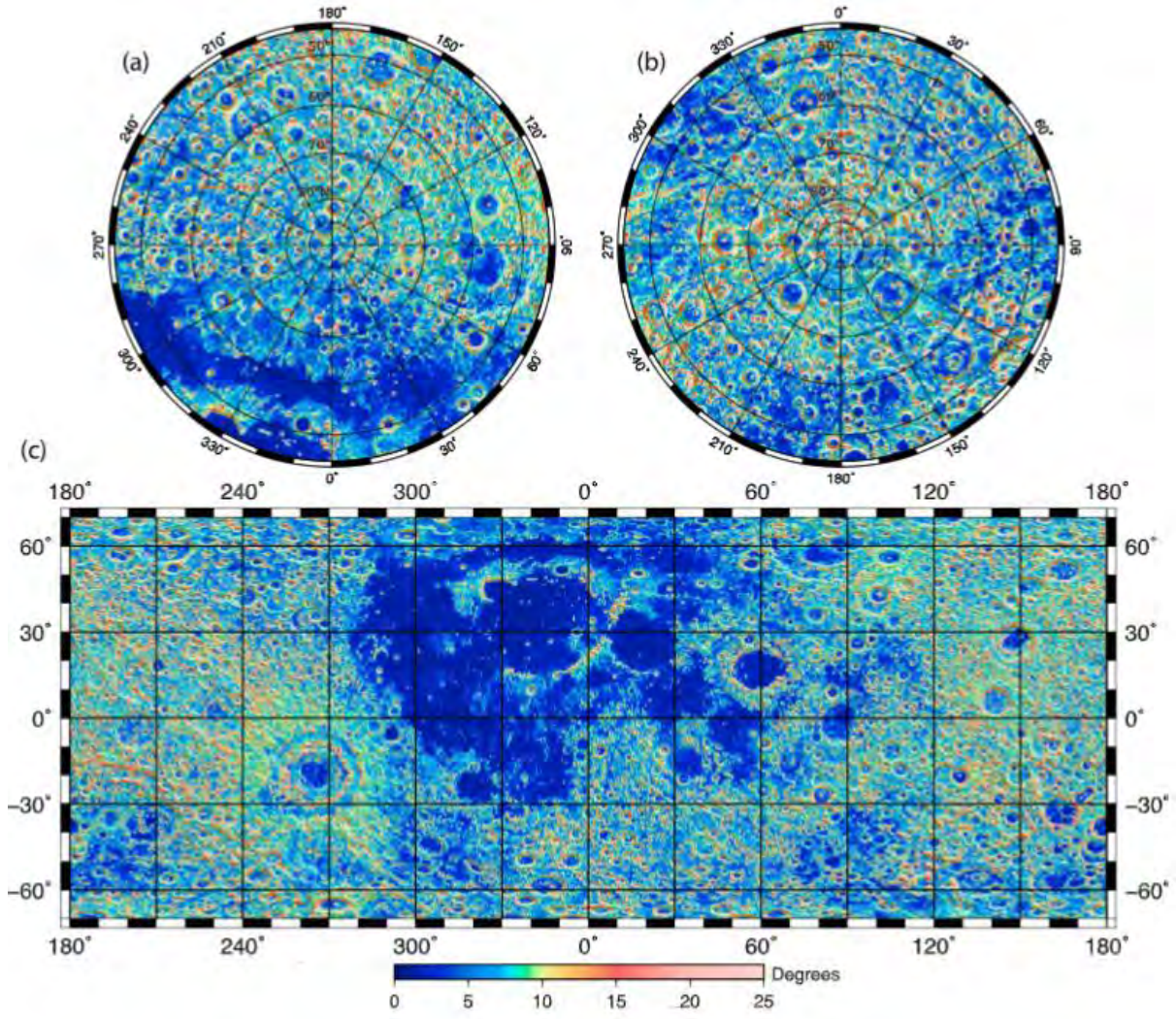

Figure 3.4.1.3-3. Median slopes from LOLA (17 m) (see Rosenburg et al. 2011). (a) North Pole, (b) South Pole, and (c) equatorial regions.

Limitations

The best available topography has posting with 2 m/px resolution, so slopes less than a few meters are currently unresolvable.

Technical Notes

For individual site characterization, a high quality suite of topographic observations exists for the Moon's surface, from Lunar Orbiter Laser Altimeter, Kaguya Terrain Camera, Lunar Reconnaissance Orbiter Camera, and other missions and instruments. These data are available in the Planetary Data System (e.g., http://imbrium.mit.edu/DATA/SLDEM2015_SLOPE/) or can be visualized with ArcGIS, JMars, or QuickMap. A detailed example of these data for the poles are shown in Figure 3.4.1.3-4.

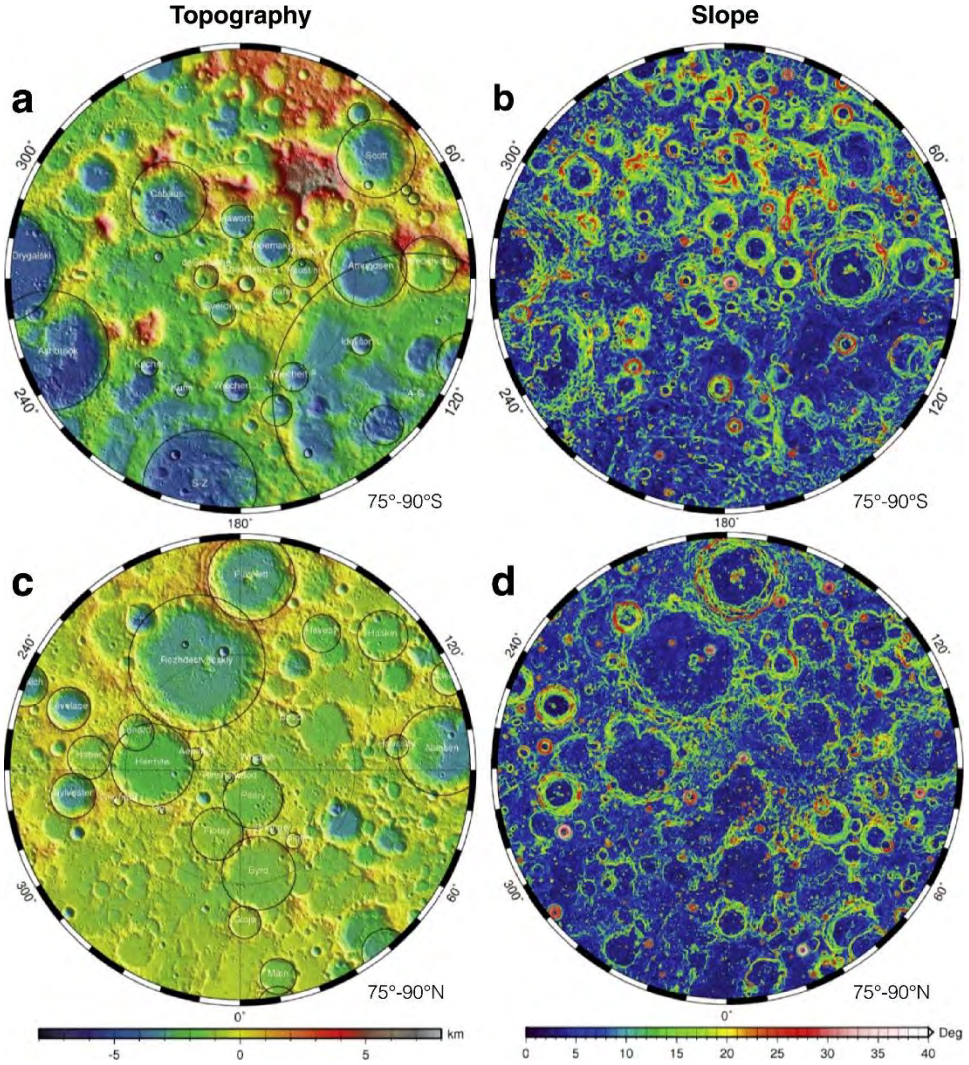

Figure 3.4.1.3-4 LOLA topography (a, c) and surface slopes (b, d) at 100-m baseline for the lunar south (top) and north poles (bottom). Both maps extend from their respective pole to 75° latitude (from Smith et al., 2017).

3.4.1.4 Rocks and Rock Size Distribution

Rocks (>10 cm) are relatively rare on the lunar surface – the fractional area covered by rocks is typically <1% (Hayne et al., 2017) and the average fractional area of the surface covered by rocks is 0.3% (e.g., Figure 3.4.1.4-1). However, rocks are not randomly distributed, and the fraction of the surface covered by rocks reaches high values (10-20%), albeit rarely (<0.01% of the surface). For this reason, hazards due to high rock abundances need to be locally assessed during detailed landing site characterization. The locations with the highest rock abundances are the ejecta of fresh craters, the interior of sizable and/or fresh craters, and on or beneath other steep slopes (e.g., rille walls). In addition to these locations, occasional rocks without an obvious source are observed; most of these are ejecta from distant impact craters. Highlands and polar

regions are generally less rocky than the maria, as smaller fresh craters are able to excavate bedrock in the maria (see Figure 3.4.1.4-3).

Rock size-distributions have been characterized from both *in situ* and orbital data. Where rocks are present, small rocks are much more common than large ones. It is common to fit observed rock size-frequency distributions with a power law (see Figure 3.4.1.4-2), where the cumulative number of rocks larger than size D is expressed as:

$$N_{>D} = CD^{-\gamma}$$

Example results are given in Table 3.4.1.4-1, with all literature results normalized so that D is in m and N is the cumulative number density of rocks ≥D in an area of 100 m^2.

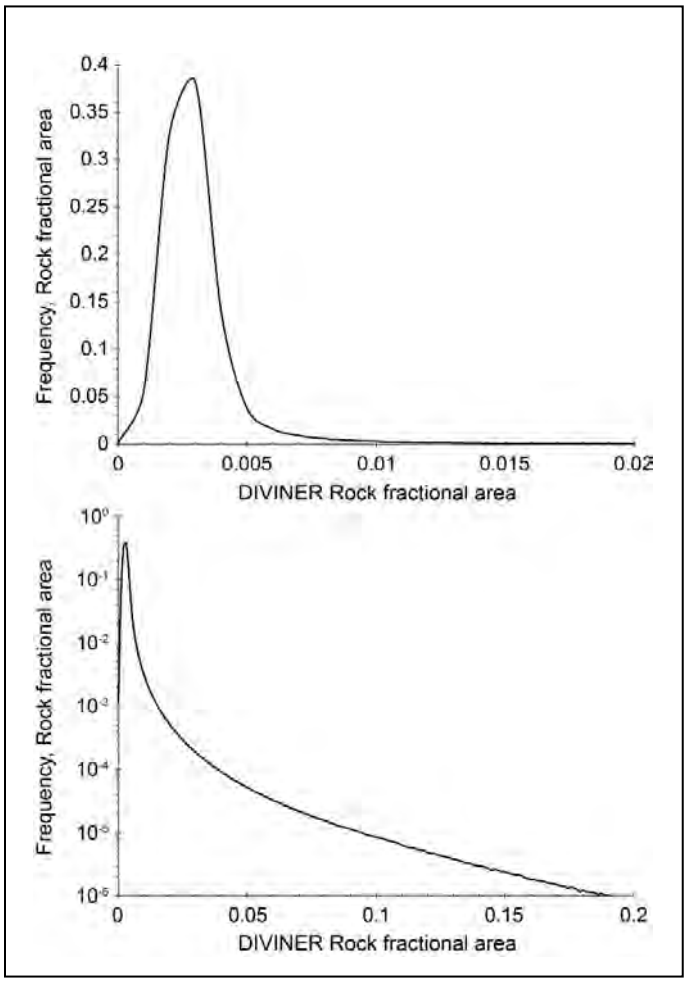

Figure 3.4.1.4-1. Frequency of fractional area covered by rocks from Diviner, shown with a linear frequency axis (top) and logarithmic frequency axis (bottom). From PDS Diviner rock abundance grid, which is calculated at 236 m/px resolution.

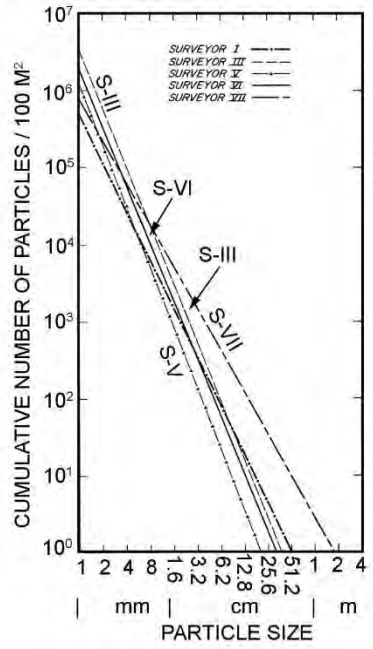

Figure 3.4.1.4-2. Cumulative size-frequency distributions for rocks near the Surveyor spacecraft derived from surface images (from Shoemaker and Morris, 1970).

Table 3.4.1.4-1. Landing site analysis of rock abundance. All of these sites with the exception of Surveyor 7 – an extreme case on the rim of Tycho crater – have fractional rock area of <~1% in Diviner.

Landing Site	C (# ≥1 m / 100 m^2)	γ	# ≥10 cm / 100 m^2	# with *height* ≥ 1 m / 100 m^2	Source Reference
Surveyor 1	0.234	-2.11	30.1	0.08	Shoemaker and Morris, 1970
Surveyor III	0.069	-2.56	25	0.02	Shoemaker and Morris, 1970
Surveyor V	0.014	-2.65	6.26	0.00	Shoemaker and Morris, 1970
Surveyor VI	0.058	-2.51	18.2	0.02	Shoemaker and Morris, 1970
Surveyor VII	2.739	-1.82	181	1.08	Shoemaker and Morris, 1970
Apollo 16 Site 4	0.217	n/a	43.2	0.07	Muehlberger et al., 1972
Apollo 16 Site 5	0.384	n/a	76.6	0.12	Muehlberger et al., 1972
Apollo 16 Site 6	0.189	n/a	37.7	0.06	Muehlberger et al., 1972
Chang E'3	0.085	n/a	17	0.03	Di et al., 2016

The height of rocks (h), on average, is less than their visible diameter (D). Measurements at the Apollo and Lunokhod landing sites suggest an average ratio of h/D=0.60 with σ=0.28 (Demidov and Basilevsky, 2014). Rock shape and angularity of rocks on the Moon is variable and site specific. The predominant rock shape can range from mostly rounded to mostly angular at different locations on the lunar surface. An abundance of angular rocks is most common in areas where immature material has been recently excavated from depth, e.g., by a fresh impact crater.

Technical Notes

Knowledge of rock distributions comes primarily from three sources (1) Diviner thermophysical observations and modeling (e.g., Bandfield et al., 2011), (2) direct observation of rock abundance in Lunar Reconnaissance Orbiter Camera Narrow Angle Camera (LROC NAC) data (or earlier high resolution orbital observations) that can directly resolve boulders larger than ~2 m (e.g., Li et al., 2017), and (3) surface observations from past landing sites (e.g., Shoemaker and Morris, 1970; Muehlberger et al., 1972; Di et al., 2016).

LROC NAC data and Diviner data are available and can be used for detailed characterization of specific landing sites. The agreement of Diviner observations with direct observations of past landing sites (e.g., Li et al., 2017) suggests that it is reliable for characterizing potential hazards due to rocks. Note that Diviner rock abundance models are not computed for the poles.

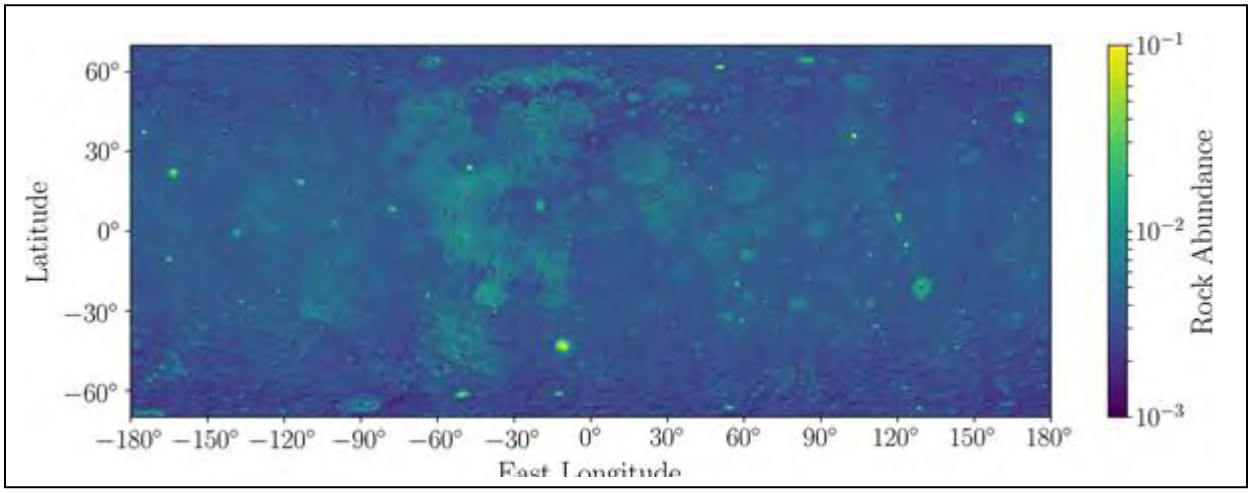

Figure 3.4.1.4-3. Spatial distribution of rock abundance (note logarithmic scale) on the Moon (Hayne et al., 2017). The maria stand out in this map as having modestly enhanced rock abundance over the highlands; mean values in the maria are 0.005% compared to 0.003% for the highlands. The brightest spots in this map are individual large craters.

3.4.2 Lunar Regolith Properties

3.4.2.1 General Description of the Lunar Regolith

The lunar regolith is the surficial layer of fragmented material (rocks, soil, and dust) that covers virtually the entire surface of the Moon. The regolith is produced by the bombardment of originally solid rock surfaces by meteoroids of various size over billions of years into a fine-grained, reworked surface deposit. Two processes dominate the formation of regolith; 1) mechanical breakdown by impacts that grind the particles into finer and finer sizes over time, and 2) melting and fusing particles together with glass formed through impact into particles known as agglutinates. The term "regolith" is used interchangeably with the more colloquial term "soil", is poorly-sorted by grain sizes, and has particle sizes ranging from sub-micron to tens of meters in diameter. The regolith is variably cohesive, and particle shapes can range from spherical beads to highly angular and fractal; particularly for small particles, more fractal shapes are common. The median thickness of the regolith is approximately 10-15 m thick in highlands regions, and 3-5 m thick in mare regions. Figure 3.4.2.1-1 shows a schematic cross section of the lunar surface. However, even in a given location, the regolith is expected to have significant natural variability in thickness as a result of the distribution of craters as seen in Figure 3.4.2.1-2 from Hirabayashi et al., 2018. Exposures of bedrock – where regolith is not present – is extremely rare on the Moon and generally found only on steep slopes.

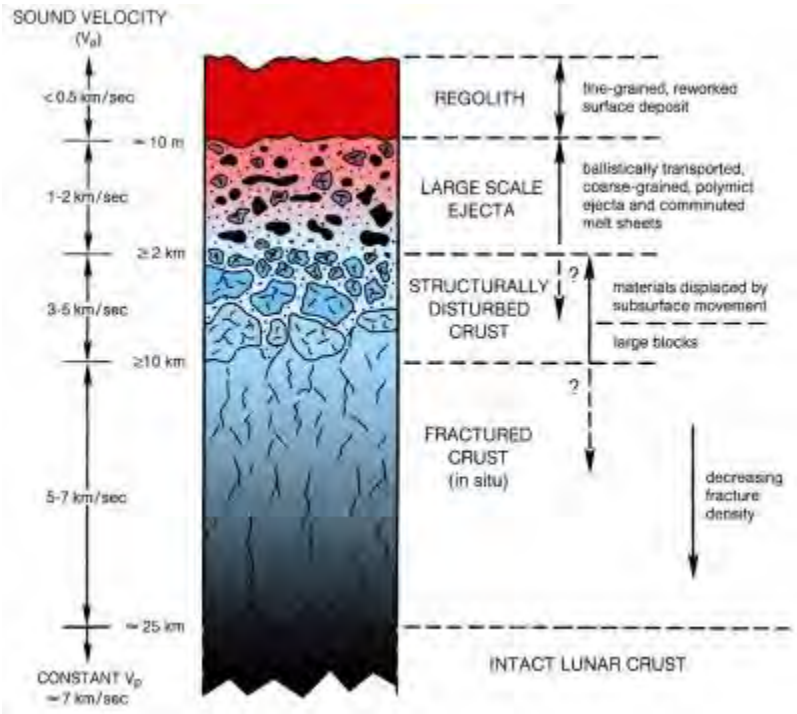

Figure 3.4.2.1-1 A schematic cross section of the lunar surface to a depth of 25 km. The uppermost surface is the lunar regolith, with a depth of approximately 0 – 15 m, depending on location and maturity of the surface. (Modified from Lunar Sourcebook, Heiken et al., 1991, and LunaRef website, Lunar and Planetary Institute).

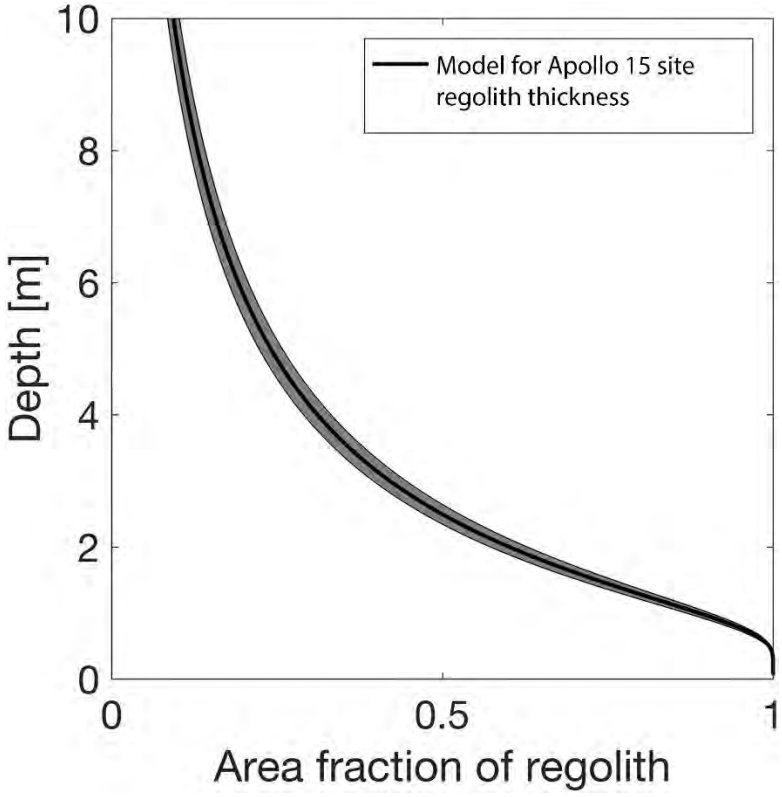

Figure 3.4.2.1-2. Model distribution of regolith thicknesses at the Apollo 15 site based on observations of the crater population (Hirabayashi et al., 2018). This illustrates the expected variability at a particular site on the Moon.

Design Limits
The following sections describe the characteristics of the lunar regolith which must be considered in hardware design.

3.4.2.1.1 Composition of the Lunar Regolith

The lunar regolith is composed of loose, clastic material derived from the mechanical disintegration of basaltic and anorthositic rocks made up of predominantly silicate minerals (those containing SiOx anions). Therefore, the soils range in composition from basaltic to anorthositic, although they can include a small (<2%) meteoritic compositional component.

Five basic particle types make up the lunar soils: mineral fragments, pristine crystalline rock fragments, breccia fragments, volcanic and impact-generated glasses, and agglutinates. Agglutinates are a unique lunar particle, and represent soil grains bonded together by impact-melted glass (fusing of other particles by micro-meteorite bombardment). Agglutinates make up a high proportion of lunar soils, about 25–30% on average, although their abundances may range from a rare 5% to about 65% (McKay, 1991). Agglutinates are highly angular and irregular in shape. Agglutinates have a wide range of sizes, from tens of microns to (rarely) millimeters, with

most common size ~175 microns. Agglutinates contain an appreciable amount of nanophase metallic Fe° in their glass, which has formed by the reduction of Fe-silicates in the soils.

Although the chemical compositions of lunar soils show considerable variation (due to the continual mixing through impact processes), physical properties such as grain size, density, packing, and compressibility are rather uniform (McKay et al., 1991; Carrier et al., 1991). Abundances for several Apollo samples are shown in Figure 3.4.2.1.1-1.

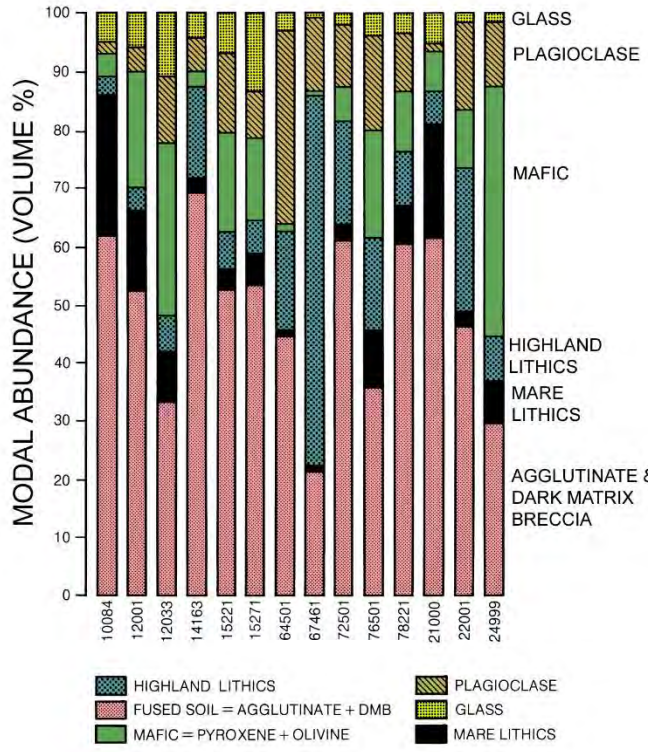

Figure 3.4.2.1.1-1 Modal (volume) abundance of different components of the regolith. Data are from each of the Apollo missions and represent the 1 mm to 90 micron size fraction. Modified from Figure 7.1 Lunar Sourcebook (from LunaRef Website, Lunar and Planetary Institute).

3.4.2.2 Particle Size and Shape

3.4.2.2.1 Particle size distribution

Description

The particle size distribution in an unconsolidated material, such as lunar soil, is a variable that controls to various degrees the strength and compressibility of the material, as well as its optical, thermal, and seismic properties (Carrier, 1973). The phi (ϕ) scale is a logarithmic transformation of millimeters into whole integers, according to the formula: $\varphi = -\text{Log}_2 d$, where d = grain diameter in millimeters.

Definition of particle size distribution parameters (Carrier et al., Lunar Sourcebook 1991): The convention of defining a percentile is such that, at the n-th percentile, n% of the sample is coarser than the n-th percentile particle size. In practice, a size class is really a size interval; let the midpoint of any size class be m (ϕ) in phi units, p the percent fraction in that size interval, and (ϕ) the n-th percentile size; then:

$$Mean(\overline{x}) = \frac{\Sigma pm\phi}{100} \backsimeq \frac{\phi_{16} + \phi_{50} + \phi_{84}}{3} = M_Z$$

$$Sorting(\sigma) = \sqrt{\frac{\Sigma p(m\phi - \overline{x}^2)}{100}} \backsimeq \frac{\phi_{84} - \phi_{16}}{4} + \frac{\phi_{95} - \phi_5}{6.6} = \sigma_1$$

The weight distribution of various Apollo samples is given in Table 3.4.2.2.1-1.

Table 3.4.2.2.1-1 Weight Distribution in size-fractions of representative scooped surface soils (data from Morris et al., 1983, data emphasize coarser fractions). (Table adapted from Heiken et al., 1991: Lunar Sourcebook, Table 9.1, pg. 478.)

	Size Fraction					Mean Size, M_z	
Soil	>1 cm	4-10 mm	2-4 mm	1-2 mm	<1 mm	<1 cm (μm)	<1 mm (μm)
		(weights in grams)					
10002*	18.5	7.6	11.0	14.7	424.5	—	52
12001			UNAVAILABLE			—	60
14003	23.0	33.0	31.8	42.1	947.9	129	99
14141	0.0	7.4	6.7	5.4	28.5	616	123
14163*	0.0	196.5	197.1	288.7	4444.0	76	56
15220	0.0	7.0	5.8	2.4	290.0	—	43
15270*	0.0	4.4	13.7	20.7	798.3	—	94
15400	513.1	7.9	6.1	4.8	86.4	330	61
61180	0.0	6.1	6.2	9.4	156.2	94	64
61220	5.1	10.6	9.6	6.4	61.0	216	68
62280	12.0	14.3	13.1	21.7	218.5	134	70
64500*	31.2	24.2	24.1	28.4	495.7	104	65
68500	1.3	17.3	25.1	37.8	521.1	106	68
70180	466.6	1.7	3.1	4.6	157.1	67	58
71500	52.3	13.1	17.6	22.7	600.9	83	65
72140	1.3	2.7	1.9	5.3	225.9	57	50
72500*	3.1	8.0	12.9	24.1	687.2	67	57
73240	1.6	22.3	14.4	14.9	192.7	127	51
74220†	0.0	0.98	0.17	0.68	7.77	—	41
78220*	0.0	1.5	2.7	5.2	227.1	50	45
78500	109.3	19.2	16.1	21.4	718.7	46	41

* Reference suite soil (*Papike et al.,* 1982).
† Orange soil; this is not a typical soil but likely represents fire fountain deposits on the Moon (see section 6.1.7).

Overall, the regolith can be considered a pebble- or cobble-bearing silty sand (using *ASTM D2487* nomenclature). The majority of lunar soil samples (< 1mm sieve) fall in a fairly-narrow range of particle-size distributions (*Carrier,* 1973; 1991). In general, the soil is a poorly-sorted (well-graded), silty-sand to sandy-silt (SW-SM to ML in the Unified Soil Classification System, *ASTM D2487,* 1987). The mean grain size of analyzed soils ranges from about 40 μm to about 800 μm and averages between 60 and 80 μm. The median particle size is 40 to 130 μm, with an

average of 70 μm (i.e. approximately half of the soil by weight is finer than the human eye can resolve). Roughly 10% to 20% of the soil is finer than 20 μm. (McKay et al., 1991; Carrier et al., 1991).

In general, for a given Apollo landing site, both the grain size of the finest-grained soil collected, as well as the average mean grain size of all soil samples collected are different from those at any other Apollo site (McKay, 1991). Grain size and sorting can even vary within a single landing site locality, based on regolith thickness and proximity to impact craters. An older, more mature lunar soil will more likely consist of fine-grained material and have a smaller mean grain size. A particle size distribution shown in Figure 3.4.2.2.1-1 and Table 3.4.2.2.1-2 from Carrier 2003 includes data from Apollo 11, 12, 14, 15, 16, 17 and Luna 24. Mean particle size as a function of depth for an Apollo 15 core sample is shown in Figure 3.4.2.2.1-4. Characteristics of the finest particle fraction are given in 3.4.2.2.3.

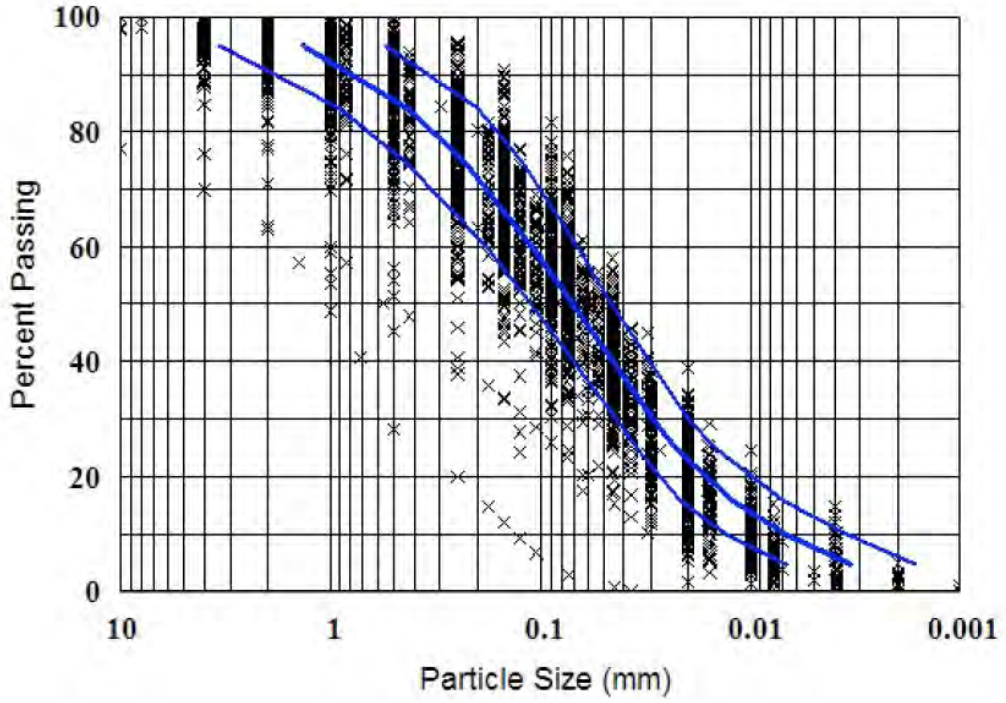

Figure 3.4.2.2.1-1 Geotechnical particle size distribution: middle curve showing the average distribution; left-hand and right-hand curves showing ± 1 standard deviation (from Carrier 2003).

Table 3.4.2.2.1-2 Average geotechnical particle size distribution from middle curve of figure 3.4.2.2.1-1 (Carrier 2003).

Size	Percent passing
mm	(smaller than)
1.3	94.9
1.0	91.8
0.4	83.5
0.3	78.7
0.2	72.1
0.1	58.0
0.07	50.5
0.05	40.8
0.04	35.0
0.03	30.2
0.02	23.6
0.01	13.9
0.005	7.8
0.003	4.8

Carrier 2005 provides plots of the particle size distribution of submillimeter regolith material for the Apollo 16 site (highlands) and all other sites (mare) as shown in figures 3.4.2.2.1-2 and -3.

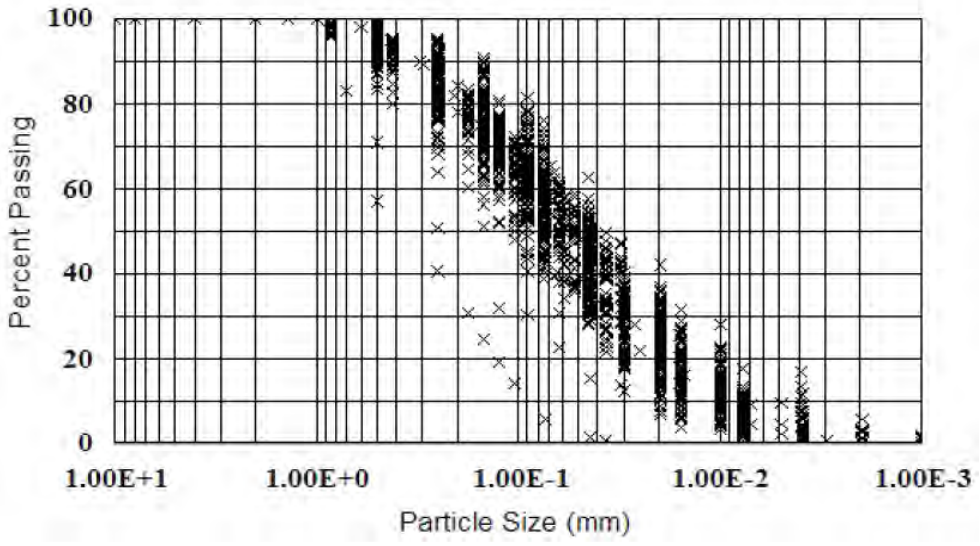

Figure 3.4.2.2.1-2 Particle size distribution of submillimeter particles for all Apollo and Luna sites except Apollo 16 (Carrier 2005).

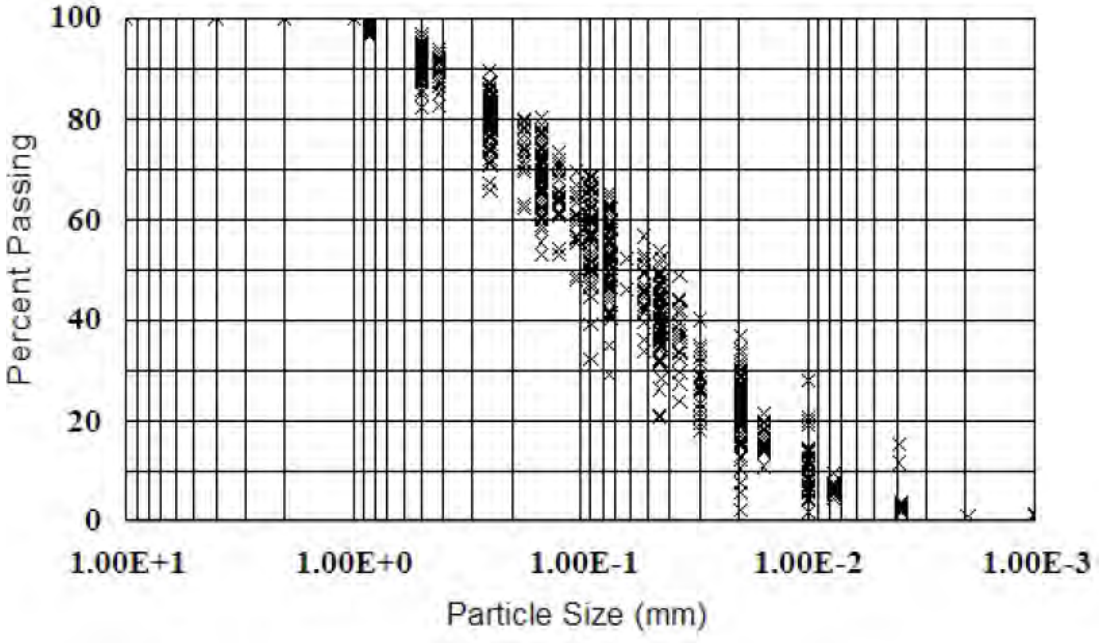

Figure 3.4.2.2.1-3 Particle size distribution of submillimeter particles for all Apollo 16 site (Carrier 2005).

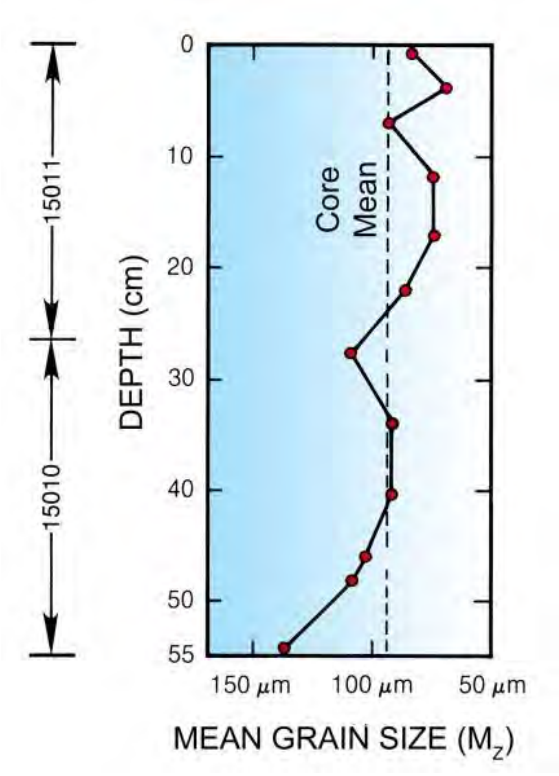

Figure 3.4.2.2.1-4 Grain-size as a function of depth at the Apollo 15 site. Sample 15010/11 collected close to the edge of Hadley Rille where the regolith is thin and immature. Modified from Figure 7.17 Lunar Sourcebook (figure from LunaRef website, Lunar and Planetary Science Institute).

Limitations

When considering laboratory analyses of the regolith, it is critical to recognize that the data were compiled from very small samples of specific size-fractions. Most regolith samples were sieved into the following size fractions: >10mm, 10-4mm, 4-2mm and <1mm. Most laboratory analyses have been collected using particles <1mm. Study of the >1mm particle size fraction is very limited and cannot be compared to the <1mm.

Technical Notes

The size-frequency distribution for the lunar regolith was determined by analysis of the samples at JSC as well as by a variety of individual investigators. The procedures followed during sample collection on the Moon and then on Earth after each mission were somewhat different. Regolith material was sieved at the Lunar Receiving Laboratory into various size fractions. Samples from Apollo 14-17 were sieved into >1 cm, 4-10 mm, 2-4 mm, 1-2 mm and <1 mm size fraction which were then weighed and assigned a sample number. The <1 mm size fraction was wet-sieved into 500, 250, 125, 62.5 and 31 micron size fractions; some samples were sieved at 500, 250, 150, 90, 75, 45 and 20 microns. Below 20 microns the size analysis was done with an optical microscope and particles counted in the 20-16, 16-8, 8-4, 4-2 and 2-1 micron size range.

On Apollo 15-17, core material was inspected and larger fragments were removed; the remainder was put through a 1 mm sieve. Fragments larger than 1 cm are treated as separate rock samples.

3.4.2.2.2 Particle Shape

Regolith particles exhibit a range of sizes and shapes due to the combination of mechanical breakdown and fusing of particles by impact processes. The following section summarizes the grain-specific properties of the <1 mm diameter size fraction of sieved lunar soil samples returned by Apollo. Figures 3.4.2.2.2-1 and 3.4.2.2.2-2 show examples of soil particle shapes and sizes. Table 3.4.2.2.2-1 provides a summary of grain-specific properties in the <1mm size fraction. In general, the particles are somewhat elongated and are subangular to angular, but can range from spherical (in the case of pyroclastic glass beads) to extremely angular.

Table 3.4.2.2.2-1 Summary of grain-specific properties (<1mm size-fraction)

Property	Value	Units	Notes	Section	Sources
Sorting	1.99 - 3.73: range	ϕ	Very poorly sorted	3.4.2.2.2.1	Heiken et al. 1991
Elongation	1.32 - 1.3835: range; 1.35: avg	-	Somewhat elongated	3.4.2.2.2.2	
Aspect ratio	0.3 - 0.9: range; 0.55: avg	-	Slightly to medium elongation	3.4.2.2.2.3	
Roundness	0.19 - 0.29: range; 0.21: avg	-	Subangular to angular	3.4.2.2.2.4	
Volume Coefficient	0.32 - 0.35: range; 0.3: avg	-	-	3.4.2.2.2.5	
Specific Surface Area	0.4 - 0.78: range; 0.5: avg	$m^2\ g^{-1}$		3.4.2.2.2.6	

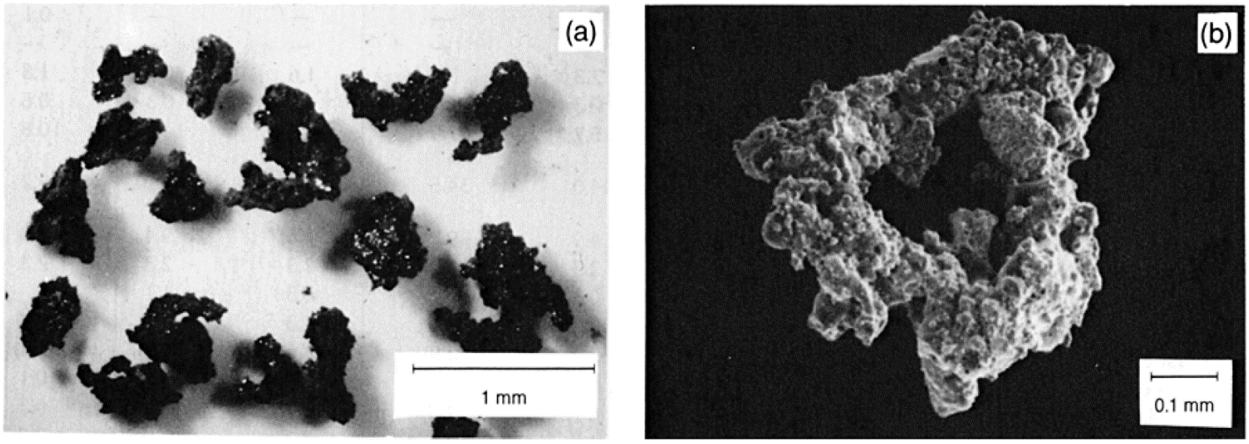

Figure 3.4.2.2.2-1 Typical lunar soil agglutinates. (a) Optical microscope photograph displaying the irregular shape variation in agglutinates (separated from Apollo 11 soil sample 10084, NASA photo S69-54827). (b) scanning electron photomicrograph of a doughnut-shaped agglutinate. Particle has a glassy surface coated with small soil fragments (NASA photo S87-38812). (Figure modified from Figure 7.2 in Carrier et al., 1991).

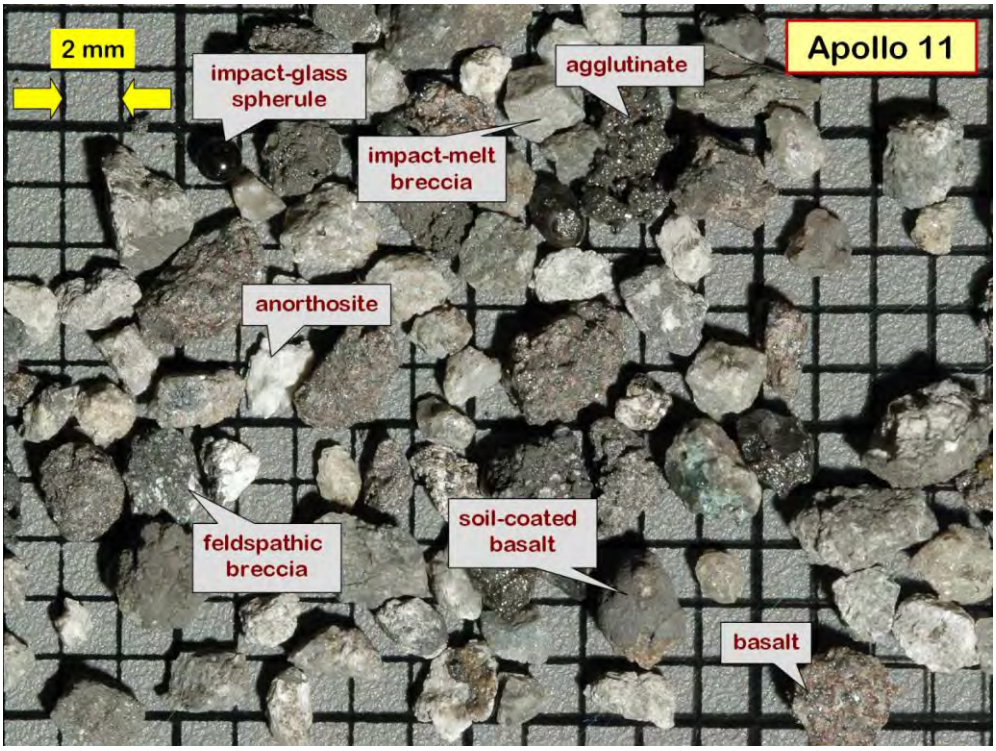

Figure 3.4.2.2.2-2 Apollo 11 regolith fragments from the 2-4 mm grain-size fraction. Note the diversity in shapes and angularity, including two impact-glass spherules. (Photo Credit: Randy Korotev, http://meteorites.wustl.edu/lunar/regolith_breccia.htm).

3.4.2.2.2.1 Sorting

Sorting values range from 1.99 ϕ to 3.73 ϕ. The phi (φ) unit is a logarithmic transformation of millimeters into whole integers, according to the formula: $\phi = -Log_2 d$, where d = grain diameter in millimeters. In other words, the lunar regolith is poorly to very poorly sorted. The more poorly sorted, the coarser the average grain size.

3.4.2.2.2.2 Elongation

Elongation is defined as the ratio of the major to intermediate axes of the particle, or length to width. Particles with values of the ratio <1.3 are considered equant, and particles whose ratio is >1.3 are elongate. Measurements of elongation on individual particles (sized 44–2,300 μm) ranged from 1.31 to 1.39.

3.4.2.2.2.3 Aspect ratio

In geotechnical studies, aspect ratio is inversely related to elongation. It is defined as the ratio of the minor axis to the major axis of an ellipse fitted to the particle by a least-squares approximation. Measurements of the aspect ratio of individual particles (sized 1.25–30 μm) range from 1 (equant) to 0.1 (very elongate), with most values falling in the range 0.4 to 0.7 (slightly to moderately elongated).

3.4.2.2.2.4 Roundness

Roundness is defined as the ratio of the average of the radii of the corners of the particle image to the radius of the maximum inscribed circle. Measurements of roundness on individual particles (sized 44–2,300 μm) had average roundness values from 0.19 to 0.26.

3.4.2.2.2.5 Volume coefficient

Volume coefficient is defined as the volume of a particle divided by the cube of the diameter of the circle that encloses the same area as the particle profile. Measurements of volume coefficient of individual particles (sized 60–733 μm) range from 0.24 to 0.37, with an average value of approximately 0.3; this value corresponds approximately to a prolate spheroid with a major-to-minor axis ratio of 3:1. The volume coefficient for a sphere is >0.52, well above the measured values for lunar particles.

3.4.2.2.2.6 Specific surface area

Specific surface area (SSA) is defined as the surface area of a particle divided by its mass. It is a measure of both the size and the shape of the particle. A ‘soil’ consisting of spheres with the same submillimeter particle size distribution as lunar soil would have an SSA of approximately 0.065 m2/g. Lunar soil particles have measured SSA values of 0.02 to 0.78 m2/g, with a typical value of 0.5 m2/g. The relatively large SSA of lunar soils is indicative of the extremely irregular, reentrant particle shapes.

3.4.2.2.3 Lunar Fine Fraction

Rationale: Properties of lunar fine fraction are required for engineering systems to operate in dusty lunar environments and for defining system requirements for removing dust from human habitats.

Description
The characteristics of the fine fraction in the lunar regolith is important to consider, because these grains are subject to electrostatic charging and interparticulate forces unimportant for larger grains. This can cause dust to be lofted above the lunar surface by charging and stick to objects on the lunar surface. All lunar dust fines less than 10 microns in diameter are relevant from an inhalation and crew health risk perspective, with particles less than 2.5 microns posing the greatest likelihood of being deeply respirable. For other systems there is no agreed upon upper size limit for the size of dust grains that might pose an environmental hazard, and this likely varies depending on the nature of the engineering concern being considered. A size threshold for dust of 100 microns was used by Colwell et al. (2007), which would include the majority of the mass in lunar regolith (Table 3.4.2.2.1-2) as a potential dust hazard. However, smaller particles, particularly those smaller than 20 microns, are most susceptible to electrostatic forces because of their higher charge-to-mass ratios.

Design Limits
Tabular values in this section are to be used for design. Figures are provided for illustration only.

3.4.2.2.3.1 Size and shape

The mean sizes of lunar soil particles are from 45-100 μm; however ~20% by mass of the particles are smaller than 20 μm (McKay et al., 1991; Carrier et al., 1991). The smallest, less than 10 μm, are the grains that are susceptible to electrostatic forces that result in levitation or lofting (Colwell et al. 2007). The majority of lunar dust grains are highly angular and elongated in shape (Heywood, 1971; Carrier et al., 1991). The ratio of the specific surface area for lunar soil to a sample of spheres with the same size distribution is nearly a factor of 8, reflecting the angular complex shapes of the particles (Colwell et al., 2007, Cadenhead et al., 1977; Carrier et al., 1991). Dust size distributions for particles smaller than 10 μm from Park et al., 2008 are shown in Figure 3.4.2.2.3.1-1 and Table 3.4.2.2.3.1-1.

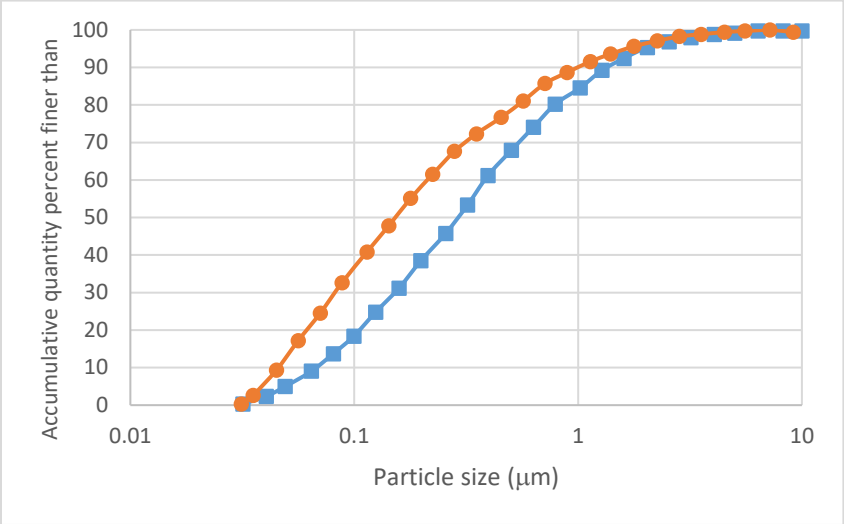

Figure 3.4.2.2.3.1-1 Cumulative percentile of dust particles (less than 10 microns) smaller than the plotted size for Apollo 11 (sample 10084, orange line) and Apollo 17 (sample 70051, blue line) after Park et al., 2008.

Table 3.4.2.2.3.1-1 Cumulative percentile of dust particles (less than 10 microns) smaller than the plotted size for Apollo 11 (sample 10084) and Apollo 17 (sample 70051) Park et al., 2008.

	Apollo 11 #10084	Apollo 17 #70051
Particle diameter (μm)	Percent finer	Percent finer
0.03	0.3	0.3
0.04	2.6	2.3
0.04	9.3	5.0
0.06	17.2	9.0
0.07	24.5	13.7
0.09	32.7	18.4
0.11	40.8	24.8
0.14	47.8	31.2
0.18	55.1	38.5
0.22	61.5	45.8
0.28	67.6	53.4
0.35	72.3	61.2
0.45	76.7	67.9
0.57	81.0	74.1
0.71	85.7	80.2

	Apollo 11 #10084	Apollo 17 #70051
Particle diameter (μm)	Percent finer	Percent finer
0.89	88.6	84.5
1.13	91.5	89.2
1.40	93.6	92.4
1.78	95.6	95.3
2.26	97.1	96.8
2.83	98.3	98.0
3.55	98.8	98.8
4.51	99.4	99.1
5.57	99.7	99.7
7.19	99.8	99.7
9.14	100.0	100.0

3.4.2.2.3.2 Altitude and spatial variations of charged dust grains

Dust grains that are above the surface of the moon can be levitated or lofted. Levitated grains are found less than 1 meter above the surface of the moon where the electrostatic and gravitational forces balance while lofted grains may reach altitudes up to 100 km due to acceleration in the lunar sheath region (Stubbs et al., 2006, Stubbs et al., 2007), Figure 3.4.2.2.3.2-1 shows the altitude and longitudinal distribution of dust grains color coded for grain size. The levitated and lofted dust altitudes peak behind the dawn terminator with smaller diameter grains achieving higher altitudes.

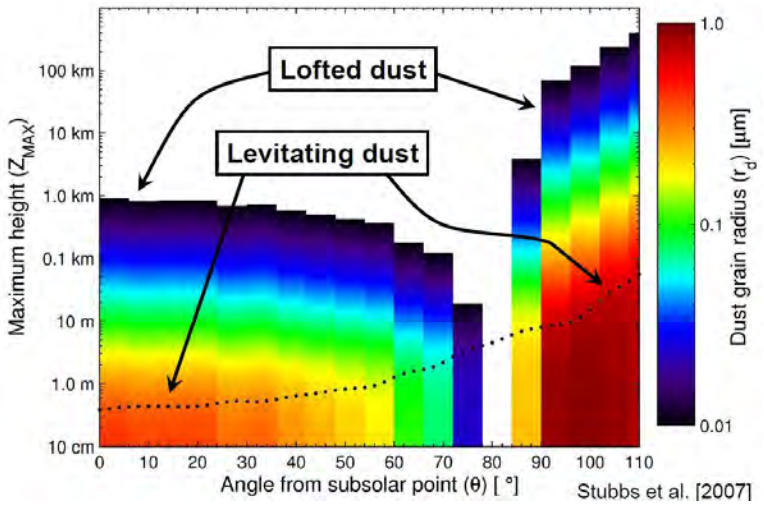

Figure 3.4.2.2.3.2-1 Altitude versus longitudinal distribution of dust grains that is color coded for grain size

3.4.2.2.3.3 Charge on dust grains

Figure 3.4.3.2.2.3.3-1 shows the results of experiments using JSC-1 which were performed using three methods of charging; 1) Tribocharging, 2) Photoemission, and 3) Photoelectron Layer (Sickafoose et al., 2001. Charge on dust grains may be either positive or negative and for 100 μm grains was on the order of 10^5 electrons per particle, corresponding to charging potentials in the range of +2 V to -2 V (Colwell et al., 2007).

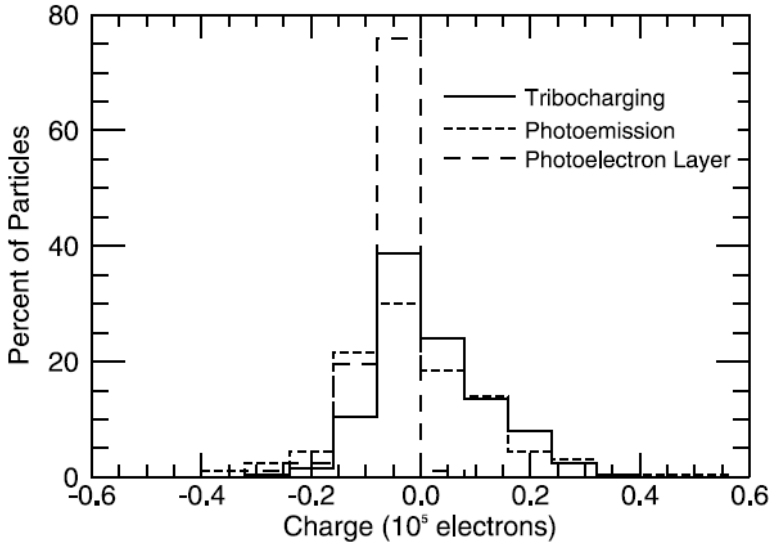

Figure 3.4.2.2.3.3-1 Experimental results using JSC-1 simulant for a 1) Tribocharging, 2) Photoemission, and 3) Photoelectron Layer (From Colwell et al., 2007 and Sickafoose et al., 2001)

3.4.2.2.3.4 Number density of charged dust

Figure 3.4.2.2.3.4-1 shows preliminary predictions of dust concentrations from Stubbs et al., Workshop on Science Associated with the Lunar Exploration Architecture in 2007. The upper, middle, and bottom panels show the surface potential, the column abundance of dust grains and the altitude distribution of dust concentration, respectively, all versus angle from the subsolar point.

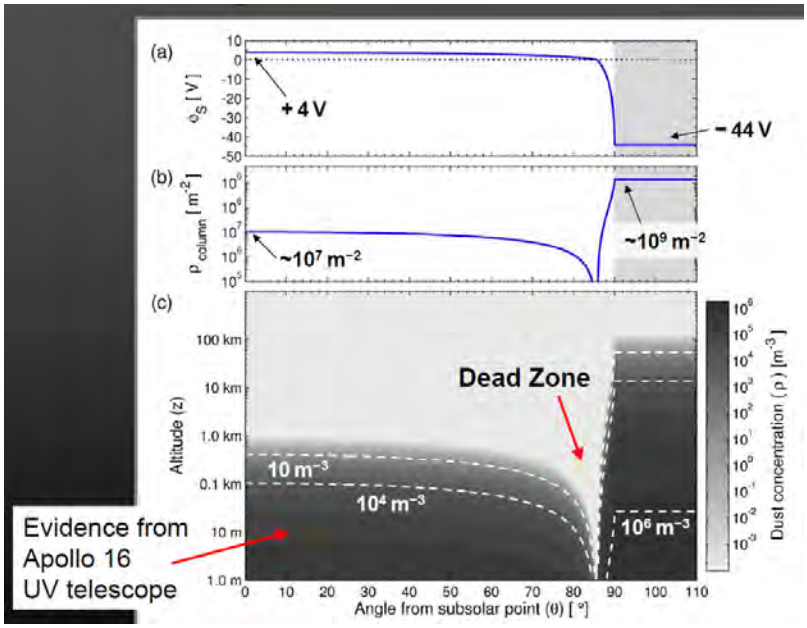

Figure 3.4.2.2.3.4-1. Modeled dust concentrations from Stubbs et al., Workshop on Science Associated with the Lunar Exploration Architecture in 2007.

Limitations

The charging experiment results shown in Figure 3.4.2.2.3.3-1 are for 100 µm grains; however levitated or lofted dust grains are less than 10 µm.

3.4.2.3 Mechanical Properties of Lunar Regolith

The following sections describe the mechanical properties of the lunar regolith. The standard reference volume for the geotechnical properties of the lunar soil and complied from Apollo Program data is Chapter 9 of the Lunar Sourcebook (Carrier et al., 1991 in Heiken et al., 1991).

The mechanical properties of the lunar regolith have been established by a combination of in-situ measurements on the lunar surface, laboratory measurements of returned lunar samples, and theoretical analysis. Table 3.4.2.3-1 summarizes the main bulk regolith parameters and each is described in the subsequent paragraphs.

Table 3.4.2.3-1 Summary of bulk regolith properties taken as representative of typical lunar characteristics based on prior landed missions and sample properties.

Property	Value	Units	Notes	DSNE Section	Sources
Bulk Density (ρ)	1.58 ± 0.05: 0-30 cm 1.74 ± 0.05: 30-60 cm	g cm^{-3}	Intercrater areas	3.4.2.3.1	Carrier et al. 1991
Relative Density (D_R)	74 ± 3: 0-30 cm 92 ± 3: 30-60 cm	%	Intercrater areas	3.4.2.3.2	Carrier et al. 1991
Specific Gravity (G)	3.1	-	Based on limited number of bulk samples	3.4.2.3.3	Carrier et al. 1991
Porosity (n)	49 ± 2: 0-30 cm 44 ± 2: 30-60 cm	%	Calculated	3.4.2.3.4	Carrier et al. 1991
Void Ratio (e)	0.96 ± 0.07: 0-30 cm 0.78 ± 0.07: 30-60 cm	-	-	3.4.2.3.4	Carrier et al. 1991
Permeability (Q)	1-7 x 10^{12}	m^2	Firing of Surveyor vernier engines on surface	3.4.2.3.5.1	Choate et al. 1968
Diffusivity	7.7 He, 2.3 Ar, 1.8 Kr	cm^2 s^{-1}	Measured on simulant function of gas species	3.4.2.3.5.2	Martin et al., 1973
Friction Angle (φ)	30-50	°	-	3.4.2.4.6	Carrier et al. 1991
Cohesion (c)	0.1 - 1	kPa	-	3.4.2.4.7	Carrier et al. 1991
Compression index (C_c)	0.3: loose 0.05: dense 0.01 - 0.11: range	-	Lab measurement on 1.2 to 200 g samples	3.4.2.4.2	Langseth et al. 1973
Recompression index (C_r)	0.003: avg 0 - 0.013: range	-	Lab measurement on 1.2 to 200 g samples	3.4.2.4.2.1	Carrier et al. 1991
Coefficient of lateral stress (K_0)	0.45: normally consolidated 3-5: below a few meters 0.7: recompacted	-	Lab measurement on 1.2 to 200 g samples	3.4.2.4.3	Carrier et al. 1991
Modulus of subgrade reactions (k)	8: avg 1-100: range	kPa cm^{-1}	Based on in situ observations of boot prints	3.4.2.4.5	Carrier et al. 1991

3.4.2.3.1 Bulk density

The bulk density (ρ) of the regolith is defined as the mass of material in a given volume usually expressed as g/m^3 or kg/m^3. Bulk density, porosity, and specific gravity are interrelated as:

$$\rho = \rho_p(1 - n) \ \ or$$

$$\rho = G\rho_w(1 - n)$$

Where:

ρ = bulk density
ρ_p = particle (or grain) density
G = specific gravity
ρ_w = density of water
n = porosity (see 3.4.2.3.4).

The density of the regolith has been determined by analysis of the returned core and drill tubes, by analysis of boot, boulder and rover tracks, penetration resistance, and in situ measurements by Surveyor, Luna, and Lunokhod spacecraft. Bulk density is 1.58 ± 0.05 g/cm^3 in the upper 30 cm of the regolith, and increases to 1.74 ± 0.05 g/cm^3 between 30 – 60 cm depth. Curve fits of data from Apollo 15, 16 and 17 give the following expression for density versus depth (Carrier et al. 1991).

$$\rho = 1.92 \left(\frac{z + 12.2}{z + 18}\right)$$

Where:

ρ = bulk density in g/cm^3

z = depth in cm

Figure 3.4.2.3.1-1 illustrates the density as a function of depth for several Apollo drill cores. Bulk density generally increases with depth. These values represent minimum values. If larger volumes were considered, intact rocks would be incorporated into the volume and the net bulk density would be greater.

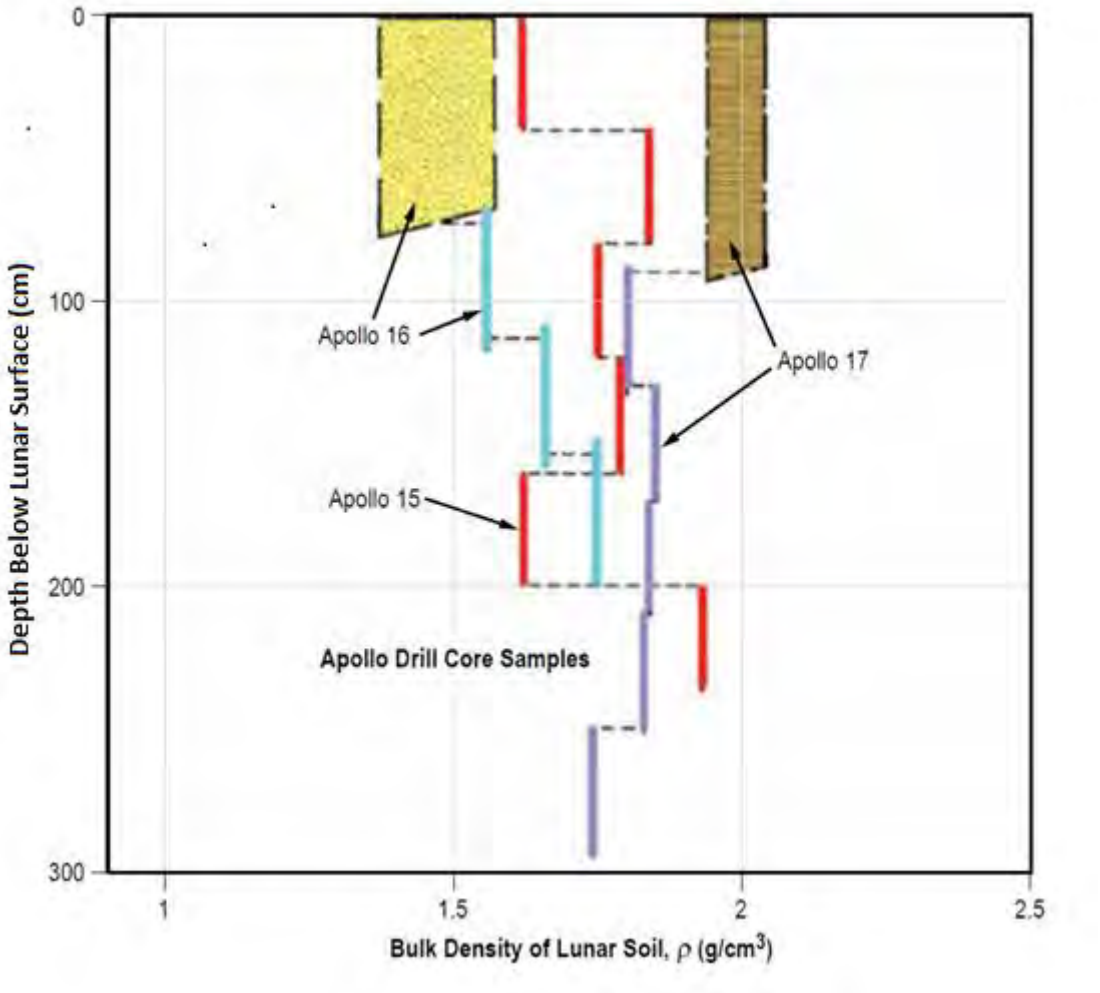

Figure 3.4.2.3.1-1 In situ bulk density of the regolith based on drill core samples from the Apollo 15, 16, and 17 missions. The abrupt increases and decreases result from different layers at different depths (Lunar Sourcebook 1991).

3.4.2.3.2 Relative density

The relative density (DR) is a function of the degree of packing of the individual particles in a granular medium. For mass of spherical particles, the relative density would be a minimum if the particles were arranged in face-centered packing and a maximum in a hexagonal close packing. Figure 3.4.2.3.2-1 illustrates the average relative density as a function of depth. The parameter is expressed as a percentage:

$$D_R = \left[\frac{e_{max} - e}{e_{max} - e_{min}}\right] x100\%$$

Where:

e = void ratio of regolith in its present configuration

e_{max} = maximum void ratio at which the regolith can be placed
e_{min} = minimum void ratio at which regolith can be placed

The relative density of the lunar regolith is 74 ± 3 % in the upper 30 cm, 92 ± 3 % between 30 and 60 cm depth.

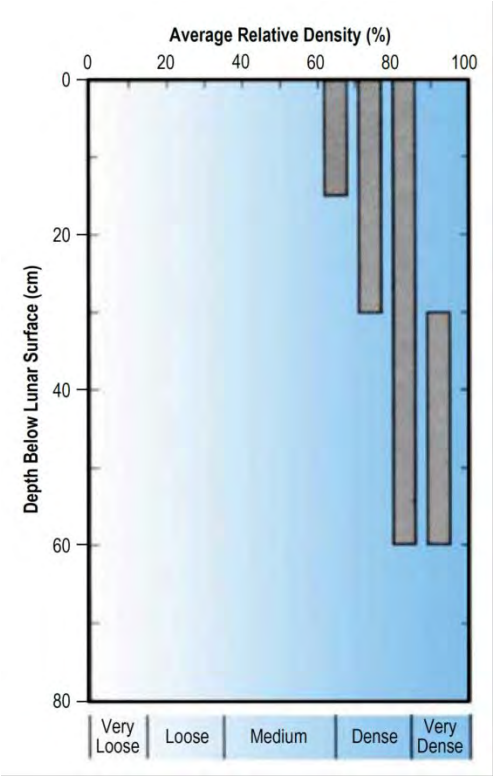

Figure 3.4.2.3.2-1 Relative density as a function of depth (modified from Figure 9.20 in Lunar Sourcebook)

3.4.2.3.3 Specific Gravity

Specific Gravity of a soil is defined as the ratio of its mass to the mass of an equal volume of water at 4° C. Various investigators have measured the specific gravity of lunar soils, breccias, and individual rock fragments (see Carrier et al., 1991 and references therein). Values for lunar soils range from 2.3 to >3.2, but a value of 3.1 for general scientific and engineering analyses of lunar soils is recommended (Carrier et al., 1991). That is, the density of the individual soil particles ρ_P is 3.1 g/cm^3, or 3.1 times that of water (1 g/cm^3).

3.4.2.3.4 Porosity

The porosity of the lunar regolith is determined by the free space between individual grains (the inter-granular porosity) and the open free space inside the grains. The porosity directly influences the value (bulk density volume weight) of the regolith. The relation between the

porosity of the lunar regolith (*n*) and its bulk and specific density is determined by the following analytical expression (Carrier et al., 1991; Slyuta, 2014). The parameter is expressed as percent:

$$n = 1 - \left[\frac{\rho_b}{\rho_p}\right] = \frac{V_v}{V_t}$$

Where:

ρ_b = bulk density
ρ_p = particle density
V_v = void volume
V_t = total volume

In the upper regolith layer about 15 cm thick, the mean porosity exceeds 50%, while it decreases to 44% within the depth interval from 30 to 60 cm. Table 3.4.2.3.4-1 gives the porosity and average void ratio for various depths.

Void ratio: The void ratio (*e*) is the volume of the void space between particles to the volume of the solid particles (including subgranular porosity). Void ratio is also referred to as a porosity factor (designated as ε or *e*) The parameter is unitless:

$$e = \left[\frac{n}{1-n}\right]$$

Where:

n = porosity.

The relationship between void ratio (*e*), relative density (*DR*), and porosity is illustrated in Figure 3.4.2.3.3-1 for a number of lunar samples, a lunar simulant, and for uniform spheres with different packing.

Table 3.4.2.3.4-1 Porosity for various depths.

Depth Range	Average Porosity, n	Average Void Ratio, e
cm	%	
0 - 15	52 ± 2	1.07 ± 0.07
0 - 30	49 ± 2	0.96 ± 0.07
30 - 60	44 ± 2	0.78 ± 0.07
0 - 60	46 ± 2	0.87 ± 0.07

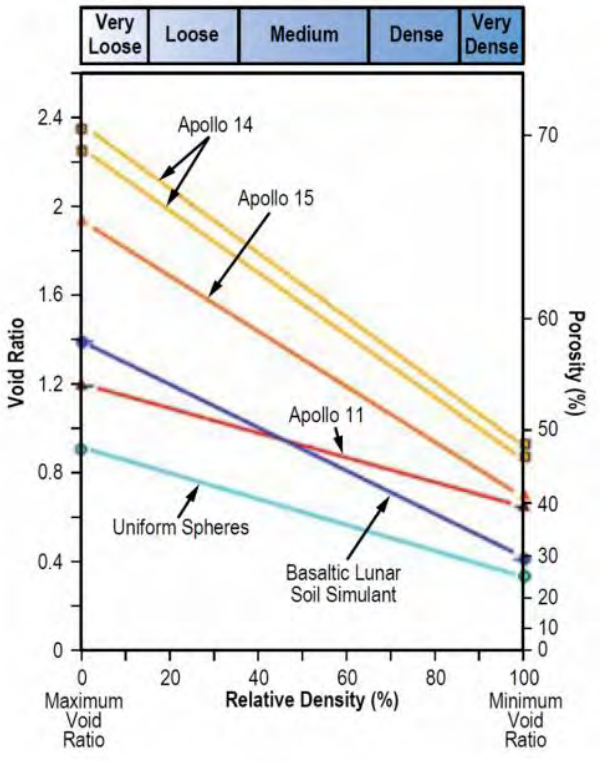

Figure 3.4.2.3.3-1 Void ratio and porosity as a function of relative density for lunar samples. Also shown is a function for ideal, variably packed uniform spheres. There is considerable scatter among the lunar samples (Modified from Figure 9.18 in ref. Lunar Sourcebook).

3.4.2.3.5 Permeability and diffusivity

These parameters relate to the movement of a fluid (either liquid or gas) through the regolith. These values have not been directly measured on lunar regolith but rather are inferred from other observations.

3.4.2.3.5.1 Permeability

The coefficient of permeability defines the flow quantity through the regolith as a function of the fluid pressure gradient. The value cited in Table 3.4.2.3-1 was derived from the test firing of the Surveyor 5 vernier engine on the lunar surface and the permeability to depth of 25 cm was deduced. This value is considered to be consistent with the fine-grained nature of the regolith.

The simplest case is an incompressible, nonreactive fluid and is given by Darcy's law:

$$Q = K\left[\frac{\rho g_m}{\mu}\right] iA$$

Where:

Q = flow rate (m^3/s)
K = absolute permeability (m^2)
ρ = density of the fluid (kg/m^3)
g_m = gravity (m/s^2)
μ = fluid viscosity (Ns/m^2)
i = hydraulic gradient
A = cross-sectional area normal to fluid flow direction (m^2)

3.4.2.3.5.2 Diffusivity

Gas diffusivity defines molecular flow through the regolith in response to a gradient in the concentration of a species. Diffusivity depends on the species composition, pressure, and temperature and the particle size and shape distribution. Data in Table 3.4.2.3-1 were derived using He, Ar, and Kr in with a lunar simulant under vacuum conditions (Martin et al., 1973). These data indicate that the diffusivity for these gases is proportional to the absolute temperature and molecular weight of the gas.

3.4.2.3.6 Particle Hardness

Hardness is generally defined as the resistance to plastic deformation. In a geologic context, the hardness of minerals (rocks are aggregates of minerals) have traditionally been measured by a scratch test comparing a minerals ability to scratch (or be scratched) by a series of incrementally harder minerals. This test is the foundation of the known as the Mohs Hardness scale, a linear relationship of mineral hardness (softest materials are 1 (e.g. Talc), hardest minerals 10 (e.g. Diamond), and is basic data available in any manual of mineralogy. The failure mode of a mineral can be categorized in two ways, those controlled by crystal lattice (cleavage) or those independent of orientation (fracture). Cleavage is the tendency to preferentially break and be oriented with respect to the mineral's crystal lattice. Minerals with perfect or good cleavage will fragment more easily than minerals with poor or no cleavage. Fracture is the term used for breaks that are not oriented with respect to the crystal lattice orientation, and are observed to form a limited number of shape patterns (e.g. hackly (i.e. jagged) or splintery). Of special interest for those interested in abrasion are those minerals that have conchoidal fracture, which has a tendency to make sharp serrated edges (for example glass).

Lunar regolith shows a very distinct and regular variation in composition as a function of particle size, and smaller particles have a higher probability of being one of the feldspars (anorthite, bytownite, labradorite), (Carrier et al., 1991; Rickman and Street, 2008). Feldspars are approximately as hard as steel, but will break down into smaller particles because of perfect cleavage. Olivine will not break down as easily and will behave much like the garnet abrasive in sandpaper, that is as it breaks down it will produce new sharp edges (Rickman and Street, 2008). Other minerals, such as spinel, are minor in abundance but are very hard with sharp edges. Table 3.4.2.3.6-1 provides a list of significant minerals in the lunar soil. Not listed in this Table are agglutinates, fractal-shaped welded glass and mineral fragment particles that can make up a

significant fraction of the soil. The Dana number is a unique identifier expressing chemical and crystallographic relationships. Mohs scale hardness for most lunar regolith constituents ranges from ~4 (e.g. Troilite, an iron sulfide) to ~8 (e.g. spinel). Percentage refers to an approximation of the abundance of the mineral in lunar soil (A-abundant, M-major, m-minor, t-trace). The relationship between Mohs hardness and the Knoop scale is shown in Figure 3.4.2.3.6-1.

Table 3.4.2.3.6-1 Significant Lunar Minerals: (%: A-abundant, M-major, m-minor, t-trace)

Mineral	Dana #	Mohs	Specific Gravity	Mode: Cleavage	Mode: Fracture	%	Chemical Composition
Anorthite	76.1.3.6	6	2.75	{001} perfect, {010} good	Conchoidal to uneven fracture; brittle	A	$CaAl_2Si_2O_8$
Bytownite	76.1.3.5	6.0 - 6.5	2.73	{001} perfect, {010} good	Conchoidal to uneven fracture; brittle	M	$(Ca, Na)(Si,Al)_4O_8$
Labradorite	76.1.3.4	7	2.71	{001} perfect, {010} good	Conchoidal to uneven fracture; brittle	M	$(Ca, Na)(Si,Al)_4O_8$
Olivine	51.3.1	6.5 - 7.0	-	-	-	M	$(Mg, Fe)_2SiO_4$
Fayalite	51.3.1.1	6.5 - 7.0	4.39	{010} moderate, {100} weak {100}, {010} indistinct to good;	Conchoidal	-	Fe_2SiO_4
Forsterite	51.3.1.2	6.5 - 7.0	3.24	{001} poor to fair	Conchoidal	-	Mg_2SiO_4
Clinoenstatite	65.1.1.1	5.0 - 6.0	3.4	{110} good to perfect	Brittle	M	$Mg_2 [Si_2O_6]$
Pigeonite	65.1.1.4	6	3.3	{110} perfect	Conchoidal to uneven fracture; brittle	M	$(Mg, Fe^{+2},Ca)_2[Si_2O_6]$
Hedenbergite	65.1.3a.2	6	3.5	{110} good	Conchoidal to uneven fracture	M	$CaFe^{+2}[Si_2O_6]$
Augite	65.1.3a.3	5.5 - 6.0	3.3	{110} good	Uneven	M	$(Ca,Na)(Mg,Fe,Al,Ti)[(Si,Al)_2O_6]$

Mineral	Dana #	Mohs	Specific Gravity	Mode: Cleavage	Mode: Fracture	%	Chemical Composition
Enstatite	65.1.2.1	5.0 - 6.0	3.4	{210} good to perfect	Conchoidal	A	$Mg2[Si_2O_6]$
Spinel	7.2.1.1	7.5 - 8.0	3.56	No cleavage	Conchoidal	m	$MgAl_2O_4$
Hercynite	7.2.1.3	7.5 -8	3.93	No cleavage	Uneven	m	$Fe^{+2}Al_2O_4$
Ulvospinel	7.2.5.2	5.5 - 6.0	4.7	No cleavage	Uneven	m	$TiFe^{+2}{}_2O_4$
Chromite	7.2.3.3	5.5	4.7	No cleavage	Uneven	m	$Fe^{+2}Cr_2O_4$
Troilite	2.8.9.1	4	4.75	No cleavage	Uneven	t	FeS
Whitlockite	38.3.4.1	5	3.12	No cleavage	Uneven to sub-conchoidal	t	$Ca_9(Mg,Fe^{+2})(PO_4)_6(PO_3OH)$
Apatite	41.8.1.0	5	3.19	No cleavage	Uneven to conchoidal	t	$Ca_5(PO_4)_3(OH,F,Cl)$
Ilmenite	4.3.5.1	5.5	4.72	No cleavage	Conchoidal	m	$Fe^{+2}TiO_3$
Native Iron	2.9.1.1	4.5	7.87	{001} Imperfect to fair	Hackly	t	Fe

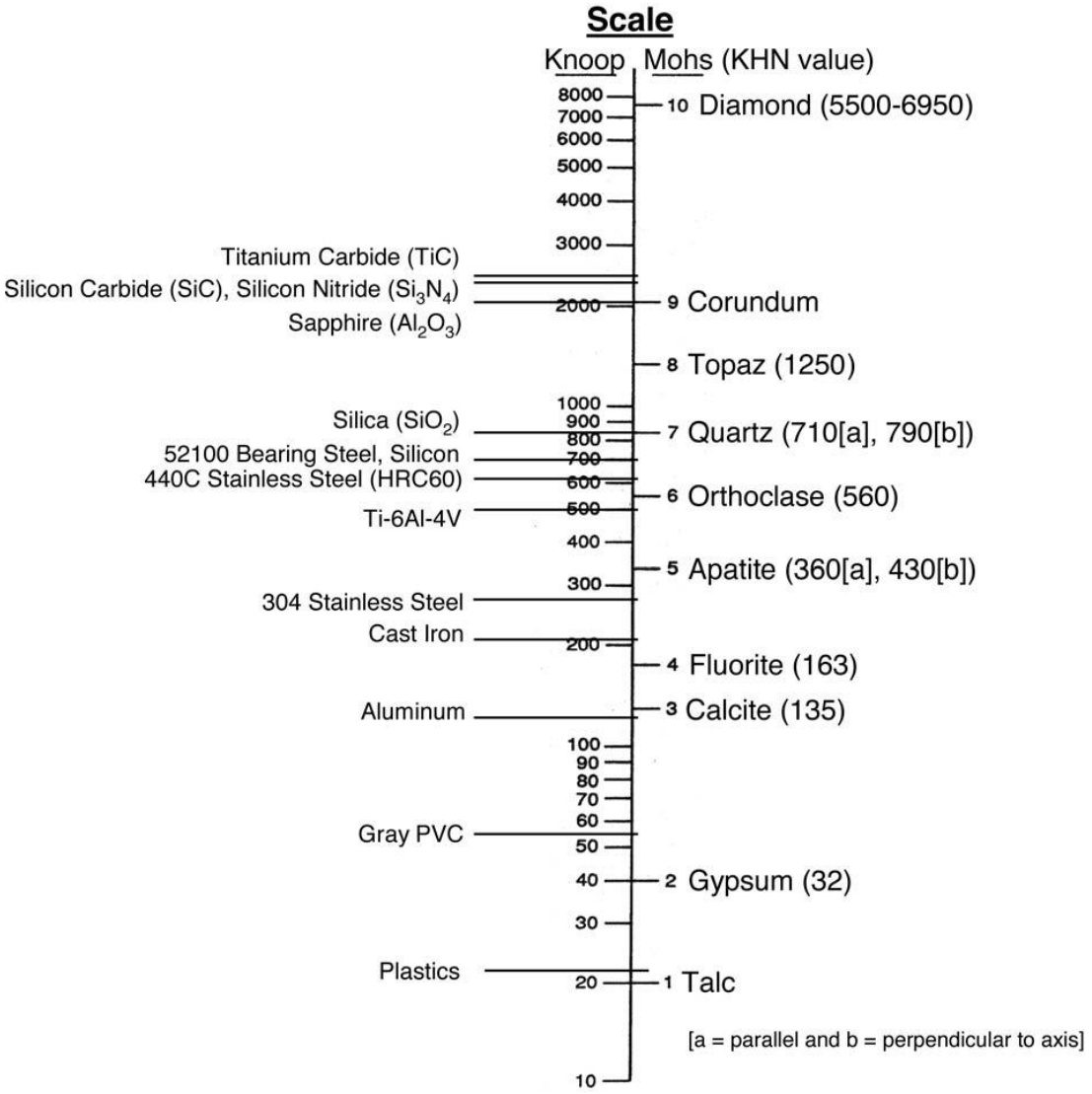

Figure 3.4.2.3.6-1: A comparison of the linear Mohs hardness and the logarithmic Knoop hardness scales. Common construction materials (left side) can be compared to Mohs reference minerals (right side) (Rickman and Street, 2008).

3.4.2.4 Derived Physical Properties

The following sections represent derived physical properties of the lunar regolith and lunar soil. The most complete summary of in situ and experimental results for geotechnical parameters can be found in Carrier et al., 1991, in Heiken et al., 1991 (The Lunar Sourcebook), which also includes comparison to some lunar soil simulants. The values presented here represent the best estimates based on Apollo data.

3.4.2.4.1 Compressibility

The compressibility of the material is an indication of the volume change that occurs when a confining stress is applied. At low stresses, the volume change is accommodated by particle movement and reorientation. At higher stresses, the volume change results from particle deformation or breakage.

3.4.2.4.2 Compression Index

The compression index (*Cc*) is defined as the decrease in void ratio when the confining stress is increased by an order of magnitude (Figure 3.4.2.4.2-1).

$$C_c = -\left[\frac{\Delta e}{\Delta\, log\sigma_v}\right]$$

Where:

Δe = change in void ratio

$\Delta \log \sigma_v$ = log change of applied vertical stress.

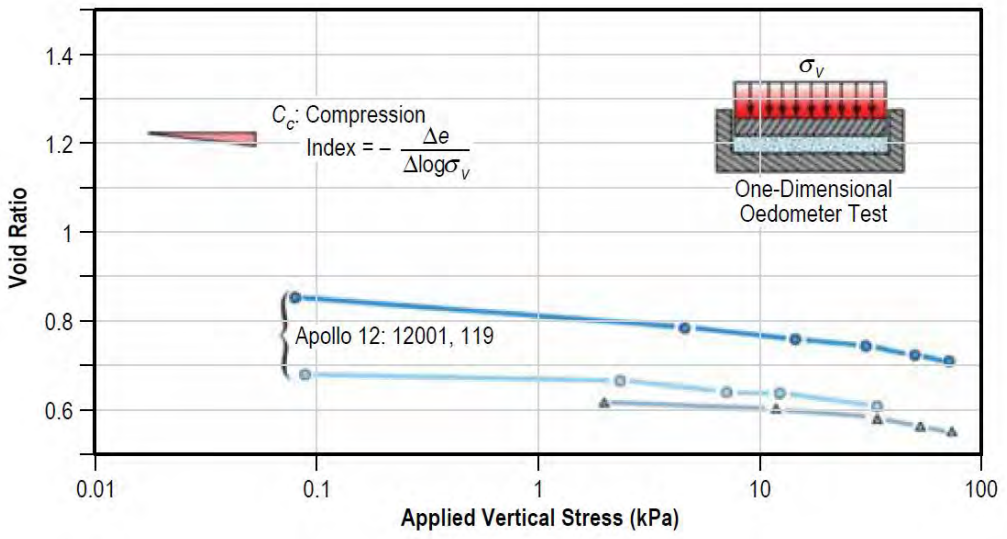

Figure 3.4.2.4.2-1 Compressibility measurements on Apollo 12 samples. Inset shows a diagram of a 1D oedometer for measuring compressibility (Lunar Sourcebook 1991).

Values are given in Table 3.4.2.3-1.

3.4.2.4.2.1 Recompression index

The recompression index (*Cr*) indicates the slope of the rebound-reload curve. It results when the sample expands after unloading and then is compressed again in the next compression cycle (Figure 3.4.2.4.2.1-1).

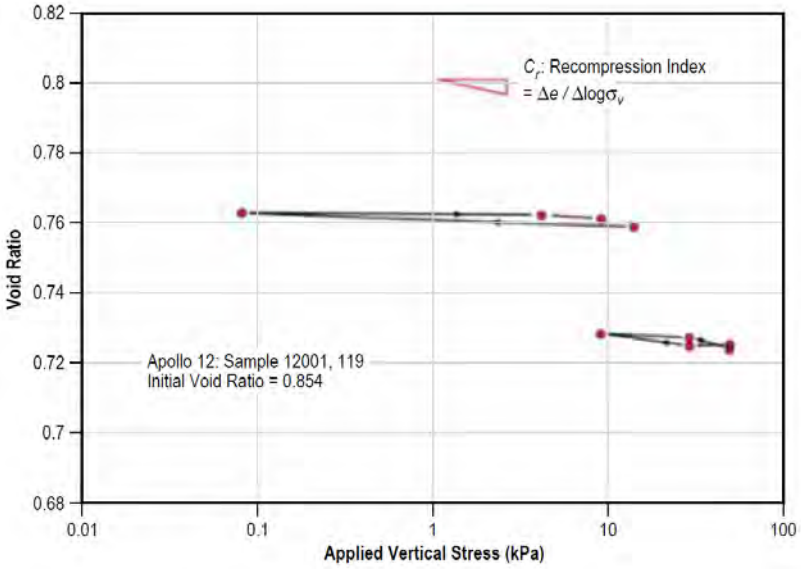

Figure 3.4.2.4.2.1-1 Change in void ratio as a function of applied vertical stress. The arrows indicate the changes in void ratio as the sample is loaded and then unloaded. (Fig 9.24 in Carrier et al., 1991; Lunar Sourcebook, 1991).

Values are given in Table 3.4.2.3-1.

3.4.2.4.3 Coefficient of lateral stress

The coefficient of lateral stress (K_0) defines the ratio of horizontal stress to vertical stress. This value has not been measured on the Moon, but the assumption is made that the lunar regolith is normally consolidated. As the parameter is a ratio, it is unitless:

$$K_0 = \frac{\sigma_h}{\sigma_v}$$

Where:

σ_h = horizontal stress
σ_v = vertical stress.

Values are given in Table 3.4.2.3-1.

3.4.2.4.4 Shear strength

The shear strength (τ) of the regolith is a measure of the stability of the regolith against failure. It is typically defined in terms of the Mohr-Coulomb equation:

$$\tau = c + \sigma \tan \varphi$$

Where:

c = cohesion (kPa)

σ = normal stress (kPa)
ϕ = friction angle (°)

3.4.2.4.5 Bearing capacity

Bearing capacity is the ability of the regolith to support a load. Bearing capacity is discussed in two categories: ultimate bearing capacity and allowable bearing capacity. Ultimate bearing capacity is the maximum possible load that can be applied without causing gross failure. For a 1-m footing, the ultimate bearing capacity is approximately 6,000 kPa. Allowable bearing capacity defines a smaller load that can be applied without exceeding a given amount of settlement. Both ultimate and allowable bearing capacity can be further defined into static and dynamic regimes. A parameter that is used to calculate the allowable static bearing capacity is the modulus of subgrade reaction (*k*). This parameter has been calculated from astronaut boot prints and has an average value of 8 kPa/cm. Values are given in Table 3.4.2.3-1.

3.4.2.4.6 Friction angle

The angle of internal friction relates the shear stress and normal stress at which failure occurs. It is a measure of the regolith's ability to withstand shear stress, and determined experimentally. The manner in which the angle is calculated is illustrated in Figure 3.4.2.4.6-1. Values are given in Table 3.4.2.3-1.

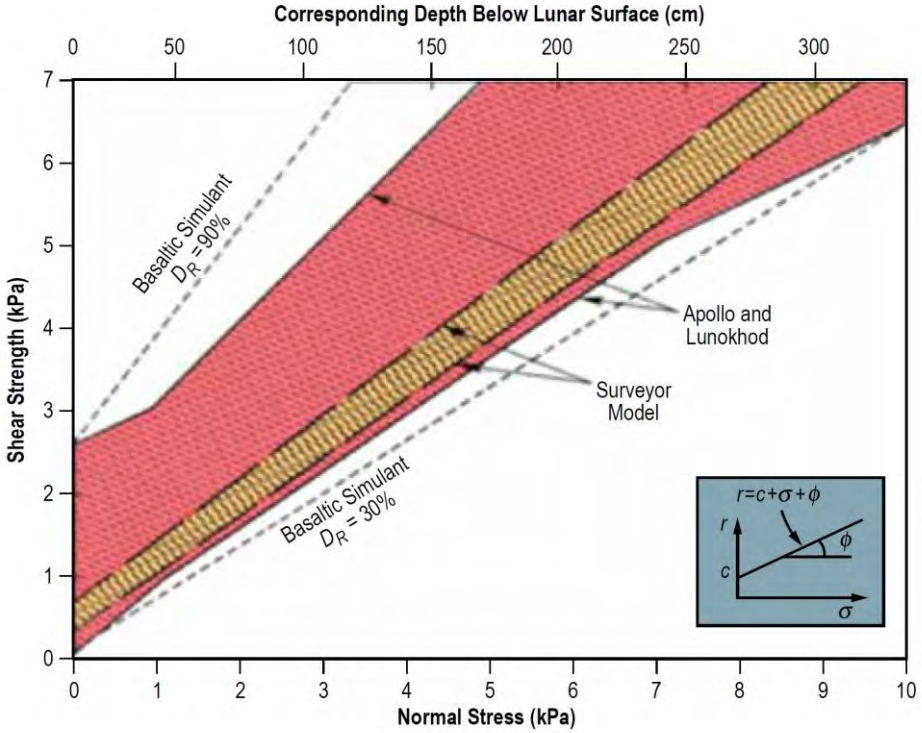

Figure 3.4.2.4.6-1 Normal shear stress versus shear strength. The slope of the relation defines the friction angle (inset) (modified from Figure 9.26, Lunar Sourcebook 1991).

3.4.2.4.7 Cohesion

Cohesion is the component of shear strength that is independent of interparticle friction; it is the strength when the confining pressure is zero. Variations in the cohesion of the regolith can be accounted for by differences in the relative density of the regolith. Values are given in Table 3.4.2.3-1.

3.4.2.4.8 Slope stability

Slope stability is a factor of consideration in construction, either in the excavation of the regolith or the construction of an embankment or pile. For stability analyses, a factor of safety (*FS*) is calculated:

$$FS = N\left[\frac{\rho g_m h}{c}\right]$$

Where:

N = stability number (function of friction angle and the slope angle)
ρ = regolith density
g_m = lunar gravity
h = slope height.
c = cohesion

3.4.3 Lunar Surface Plasma Environment

The lunar surface plasma environment requires special consideration because in addition to the variation by solar zenith angle (SZA), there are also variances due to large surface features and surface electric potentials. Near the surface of the Moon, the plasma environment is not electrically neutral due to the presence of lunar surface voltages and a photoelectron population. This non-neutral region is typically 0.5 to 1 meters (Poppe and Horanyi 2010) but can be as high as 100 meters in the plasma sheet. The nightside non-neutral region can extend to distances on the order of kilometers. The lunar orbital plasma environment is in 3.3.3.5.

Generally, in full sunlight, the lunar surface and any objects on the surface will stay at low positive electric potentials due to photoemission dominating over plasma currents. In dark areas, and possibly in sunlight during plasma sheet crossings, negative electric potentials develop which are highly dependent on material properties. The terminator is defined as the line between the dayside and nightside lunar surface.

Due to the low conductivity of the lunar surface, electric potentials can build up between objects on the surface and the surface itself resulting in electrostatic discharge that can damage materials and electronics or cause electromagnetic interference. Additionally, tribocharging is an important concern for any objects moving on the surface of the Moon. Charge transferred from the regolith to the moving object is difficult to dissipate, especially in shadowed regions with no photoemission (Jackson et. al., 2015). Models suggest the lack of dissipation could result in large buildup of electrical charge on human systems roving in shadowed regions. (Jackson et. al., 2011).

In the solar wind and the magnetotail, the dayside plasma environment is the same as higher altitudes from the lunar surface with the addition of a photoelectron population. The photoelectron population increases the electron density and can be considered an additional Maxwellian population with a density of $1x10^8$ m^{-3} and temperature of 2.2 eV (Poppe et. al. 2010 and 2011). The nightside surface magnetotail plasma environment is the same as the environment at higher altitudes. In the solar wind, starting at the terminator and moving to larger SZA, research using Lunar Prospector data shows the solar wind wake plasma densities decrease exponentially and temperatures increase linearly (Halekas et. al. 2005, Farrell et al 2008). For analysis purposes, plasma density in areas just nightside of the terminator can be approximated as an order of magnitude less than the solar wind density and plasma temperature can be assumed equal to solar wind temperature. Plasma in areas at larger SZA from the terminator on the nightside have a density that is approximately 0.001 of the solar wind density and temperature equal to ten times the solar wind temperature. The electron distribution in the solar wind wake is best approximated as a Kappa function rather than Maxwellian for use in analysis, with a Kappa value of 3.5 (Halekas et al, 2005). The Maxwellian distribution is appropriate for ions. Generally, it is acceptable to assume electron and ion densities are approximately equal, except in the region just adjacent to and downstream from the Moon where the electron density can be up to an order of magnitude higher than the ion density.

The effect of reduced plasma density and increased temperature is also applicable to wakes appearing behind large features near the terminator in the solar wind, such as mountains, or in deep craters. The solar wind flows horizontally in polar regions and cannot easily get into and around topographic obstructions creating a wake effect on the leeward side of the obstruction (Zimmerman et al. 2011, Farrell et al. 2010, Zimmerman et al., 2012). The lunar surface plasma parameters derived from the data in Table 3.3.3.5-1 are shown in Table 3.4.3-1. Electrical properties of lunar regolith are described in 3.4.4.

Table 3.4.3-1. Lunar Surface Plasma Parameters

		Electron Density	Electron Temperature	Ion Velocity	Ion Density	Ion Temperature
		m^{-3}	eV	km/s	m^{-3}	eV
Magnetotail Lobes (add photoelectron population for dayside only)	mean	2.0×10^5	48	170	2.0×10^5	290
	95%	1.5×10^5	160	440	1.5×10^5	1000
	99.7%	8.0×10^4	440	540	1.0×10^5	1700
	max	6.2×10^4	980	650	8.9×10^4	3400
	photo	1.0×10^8	2.2	N/A	N/A	N/A
Plasma Sheet (add photoelectron population for dayside only)	mean	2.2×10^5	150	110	2.0×10^5	780
	95%	1.1×10^5	440	360	1.2×10^5	2000
	99.7%	6.9×10^4	970	591	9.1×10^4	3100
	max	5.0×10^4	3700	1100	6.9×10^4	4800
	photo	1.0×10^8	2.2	N/A	N/A	N/A
Magnetosheath Dayside	mean	9.5×10^6	18	350	8.0×10^6	94
	95%	9.4×10^6	28	510	7.5×10^6	220
	99.7%	1.3×10^5	180	640	1.3×10^5	1100
	max	7.6×10^4	1400	930	9.9×10^4	3000
	photo	1.0×10^8	2.2	N/A	N/A	N/A
Magnetosheath Wake	mean	1.9×10^5	50	N/A	1.9×10^5	330
	95%	5.0×10^4	97	N/A	6.9×10^4	880
	99.7%	4.3×10^4	520	N/A	5.0×10^4	2000
	max	4.3×10^4	840	N/A	5.0×10^4	3600
Solar Wind Dayside	mean	6.0×10^6	11	420	6.0×10^6	7.0
	95%	1.5×10^7	17	610	1.6×10^7	20
	99.7%	4.4×10^7	28	620	4.3×10^7	40
	max	6.6×10^7	31	700	7.0×10^7	60
	photo	1.0×10^8	2.2	N/A	N/A	N/A
Solar Wind Terminator	mean	6.0×10^5	11	420	6.0×10^5	7.0
	95%	1.5×10^6	17	610	1.6×10^6	20
	99.7%	4.4×10^6	28	620	4.3×10^6	40
	max	6.6×10^6	31	700	7.0×10^6	60
Solar Wind Wake	mean	6.0×10^3	110	N/A	6.0×10^2	70
	95%	1.5×10^4	170	N/A	1.6×10^3	200
	99.7%	4.4×10^4	280	N/A	4.3×10^3	400
	max	6.6×10^4	310	N/A	7.0×10^3	600

The lunar surface potentials vary over the surface depending on location, environment, and surface features. Values of the lunar surface potential presented here are based on studies performed using Lunar Prospector satellite data (Halekas et al, 2007, 2008, 2009) and the Solar Storm Lunar Atmosphere Modeling (SSLAM) effort (Farrell et al 2012). The Lunar Prospector studies use measurements of upward accelerated, magnetic field aligned beams of secondary electrons emitted from the lunar surface to remotely sense the surface potential. The values are relative to the ambient plasma. Charging of the lunar surface involves currents to and from the surface due to incident and secondary electrons and ions, backscattered electrons, and photoelectrons. The surface potential modulates and is modulated by these currents. In equilibrium there is zero net current to the surface. Calculations using the Lunar Prospector data and estimated Lunar Prospector data indicate the secondary electron yield maximum, δ_m to be approximately 1.5 at an energy, E_m, of 500eV. The surface electrical conductivity is sufficiently small such that different regions of the lunar surface charge quasi-independently. At the poles, the surface potential is dynamic at the scale of the plasma temporal variations and as a function of rotational phase. In the solar wind, the trailing mini-wake regions forming anti-sunward of an obstacle will shift position based on orientation relative to pointing vector to the Sun.

Over most of the dayside in the nominal solar wind, surface potential is a small positive value. It rapidly becomes negative as the SZA approaches and then exceeds 90 degrees. The larger surface potential magnitudes occur on the lunar night side, where it is negative due to the absence of photoemission and the large electron current to the surface relative to the ion current. Typical nightside potentials in the terrestrial magnetotail lobes are approximately -100 V and several hundred volts to a kilovolt negative in the plasma sheet. On the dayside, negative charging is sometimes observed in the terrestrial plasma sheet. In the solar wind, negative potentials of approximately -200 V are observed near the boundary of the solar wind lunar wake, with smaller negative potentials in the central wake.

The largest negative surface potential values are observed during solar energetic particle (SEP) events. During these events the Moon is exposed to energetic (high temperature) plasma. Outside the magnetosphere, in the solar wind, there is a nearly one-to-one correspondence between extreme negative surface potential values and large SEP events. During these events the lunar nightside surface could reach values as low as - 4.5 kV, with negative potentials of a kilovolt or larger often observed. These potentials are far more negative than typical nightside potentials of a few hundred volts negative, and may increase the risk of electrostatic discharge and/or dust effects. The largest negative potentials are generally observed in the central lunar wake. More research is needed to understand and properly model the environment and conditions that lead to these large surface potentials.

The lunar surface potentials are summarized in Table 3.4.3-2. The values in this Table are approximate values and may vary.

Table 3.4.3-2. Lunar Surface Potentials

	Sunlight	Darkness/Shadow
	V	V
Magnetotail	0	-100
Magnetotail Plasma Sheet	0,-500 (rare)	-1000
Solar Wind	0	-500, -4500 (rare)
Solar Wind Terminator	-50	-200
Solar Wind Mini-wake	-50	-100

3.4.4 Lunar Regolith Electrical Properties

Description

The electrical and photoelectric properties of the lunar regolith are characterized by the bulk conductivity, dielectric constant, photoelectric emission of lunar fines, and secondary electron emission of bulk regolith. These parameters are required for evaluation of charging hazards on the lunar surface due to interactions of the space plasma and radiation environment with the lunar regolith. The lunar surface plasma environment is described in 3.3.3.6. The lunar regolith is composed of dust and broken rock that is produced from the impact of large and small meteorites, micrometeoroid impacts and solar and galactic charged particles. Heat from impacts melt or partially vaporizes dust particles so that refreezing results in welding particles together into glassy agglutinates. The lunar regolith covers most of the surface and ranges in thickness from 4-5 meters in mare areas and 10-15 meters in the highland regions. The density of regolith taken at the Apollo 15 landing site averages ~ 1.35 g/cm^3 for the top 30 cm and ~ 1.85 g/cm^3 at 60 cm depth.

Design Limits

Tabular values in this section are to be used for design. Figures are provided for illustration only.

Table 3.4.4-1 Regolith electrical properties

Parameter		Units	Notes	Section	Reference
DC Electrical Conductivity	$<10^{-10}$ @ 400 K $<10^{-25}$ @ 100 K $<10^{-9}$ @ upper 5 km	Mho/m	For rocks; values will be lower for soil. Temperature dependent lab analysis and in situ	3.4.4.1	Carrier et al. 1991 Dyal et al. 1974
Relative Dielectric Permittivity (k)	2.8 @ 1.58 g cm^{-3} 3.11 @ 1.58 g cm^{-3}	-	Function of density, temperature, and frequency	3.4.4.2	Carrier et al. 1991 Olhoeft and Strangway, 1975
Loss Tangent	0.0057 @ 1.58 g cm^{-3} 0.0066 @ 1.58 g cm^{-3}	-	Function of density, temperature, frequency, and chemistry	3.4.4.3	Langseth et al. 1973

3.4.4.1 Bulk conductivity

Description

The electrical conductivity of lunar regolith is the effectiveness of the regolith at allowing current to flow through it.

Design Limits

Olhoeft et al. (1974) measured the conductivity of Apollo 15 soil samples and found slightly different temperature dependencies.

Figure 3.4.4.1-1 shows the electrical conductivity versus temperature in vacuum for Lunar sample 12002,85 (basalt) from Figure 3 of Olhoeft et al. (1974). The exponential theoretical fit to the data is described by

$$\sigma = 6\ x\ 10^{-18} exp^{0.037T}$$

where σ is in units of Siemens per meter and T is the temperature in Kelvin. Figure 3.4.4.1-2, corresponding to Figure 4 in Olhoeft et al. (1974) is for lunar sample 65015,6 (highly recrystallized breccia) with an exponential fit given by

$$\sigma = 6\ x\ 10^{-18} exp^{0.023T}$$

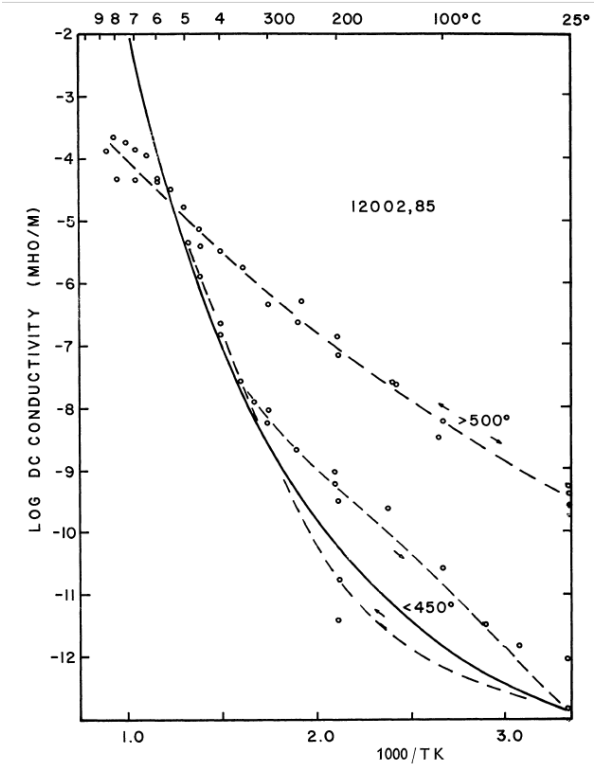

Figure 3.4.4.1-1. Figure 3 from Olhoeft et al. (1974) showing the electrical conductivity versus temperature in vacuum for Lunar sample 12002,85 (basalt).

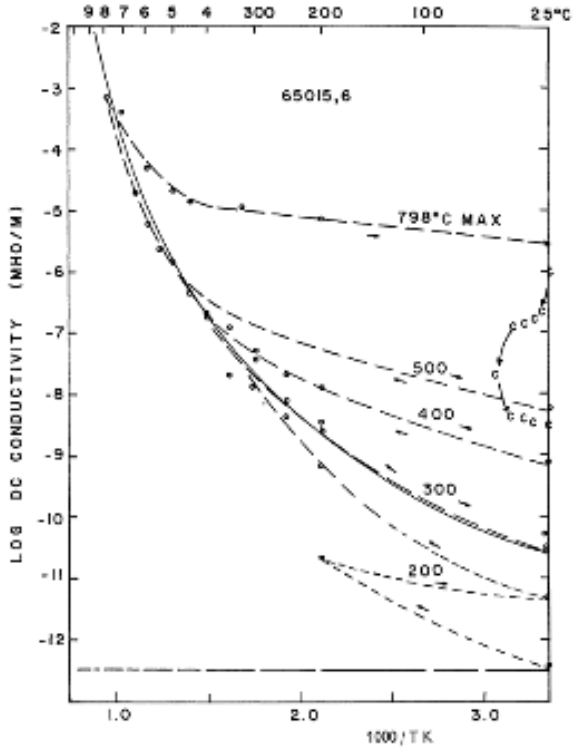

Figure 3.4.4.1-2. Taken from Figure 4 in Olhoeft et al. (1974) is for lunar sample 65015,6 (highly recrystallized breccia).

3.4.4.2 Dielectric constant

Description

The dielectric constant is the relative permittivity of the soil, where the permittivity is the effectiveness of a material at keeping charge carriers within separated and the relative permittivity is the ratio of the absolute permittivity to the permittivity in vacuum.

Design Limits

The dielectric constant, or relative permittivity, is given by

$$K = \frac{\varepsilon(\omega)}{\epsilon_0}$$

where $\varepsilon(\omega)$ is the complex frequency-dependent permittivity of the material and ε_0 is the vacuum permittivity. Olhoeft and Strangway (1975) studied measurements of lunar samples dielectric constant versus density at frequencies above 100 kHz and gave the relation

$$K' = (1.93 \pm 0.17)^{\rho}$$

where ρ is the density in g/cm^3.

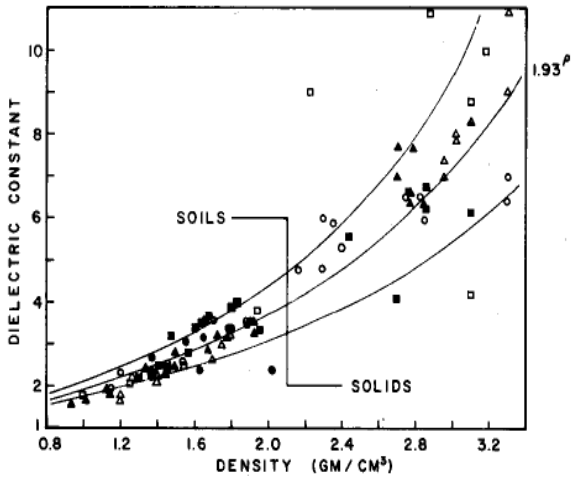

Figure 3.4.4.2-1 from Olhoeft and Strangway (1975) gives the dielectric constant versus density with fitted equation from regression analysis. Open squares, triangles, and circles are data from Apollo 11, 12, and 14 samples, respectively, and close squared, triangles and circles are from Apollo 15, 16, and 17 samples respectively. This is Figure 2 in the Olhoeft and Strangway (1975) article.

The relative dielectric permittivity as a function of frequency is given in Figure 3.4.4.2-2 and Table 3.4.4.2-1. These values should be used in radar analyses.

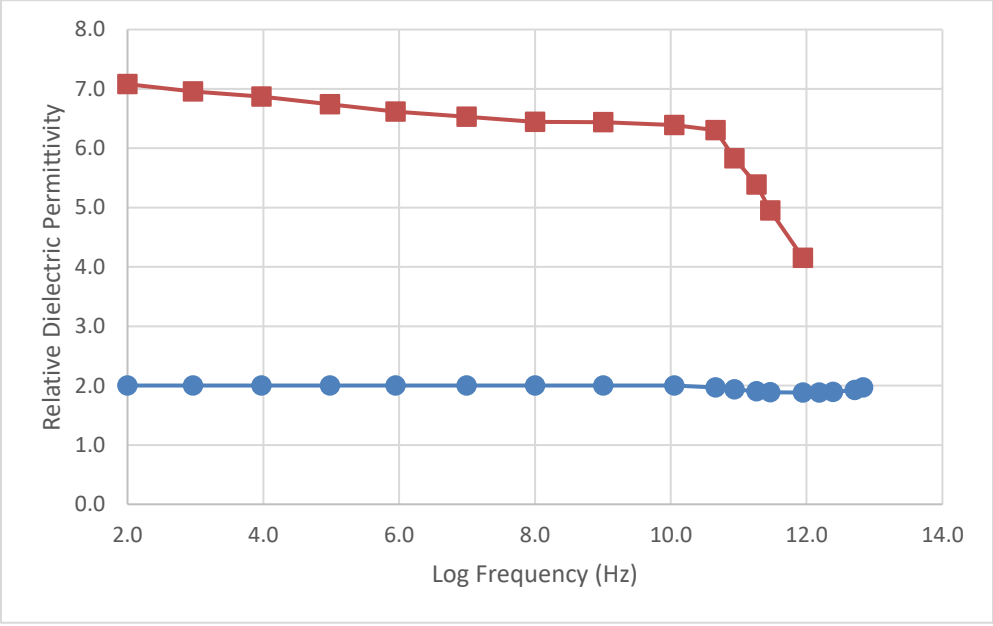

Figure 3.4.4.2-2 Relative dielectric permittivity of lunar soil (blue circles, sample 14163 fines) and rock (orange squares, sample 14310) as a function of frequency. The soil data have been normalized to a density of 1 g/cm^3. From Lunar Sourcebook figures 9.60 and 9.61.

Table 3.4.4.2-1 Numerical values of relative dielectric permittivity from figure 3.4.4.2-1. From Lunar Sourcebook figures 9.60 and 9.61.

Log Frequency	Relative Dielectric Permittivity	Relative Dielectric Permittivity
Hz	Soil sample 14163 Fines	Rock sample 14310
2.0	2.001	7.079
3.0	2.001	6.954
4.0	2.001	6.868
5.0	2.001	6.742
5.9	2.001	6.616
7.0	2.001	6.530
8.0	2.001	6.444
9.0	2.001	6.438
10.1	2.001	6.391
10.7	1.970	6.306
10.9	1.934	5.828
11.3	1.903	5.389
11.5	1.887	4.951
11.9	1.883	4.153
12.2	1.883	
12.4	1.891	
12.7	1.926	
12.8	1.970	

Model Inputs
None

Limitations
None

Technical Notes
None

3.4.4.3 Loss Tangent

Description
The loss tangent describes the dissipation of electromagnetic energy in a dielectric.

Design Limits

Table 3.4.4.3-1 gives nominal values of loss tangent for lunar regolith. Figure 3.4.4.3-1 gives the frequency dependence of the regolith loss tangent and Table 3.4.4.3-1 gives values from the curve. These have been normalized to a soil density of 1 g/cm^3. The loss tangent dependence on density is given by

$$loss\ tangent = 10^{[0.440\rho - 2.948]}$$

where ρ is the soil density (see 3.4.2.3.1).

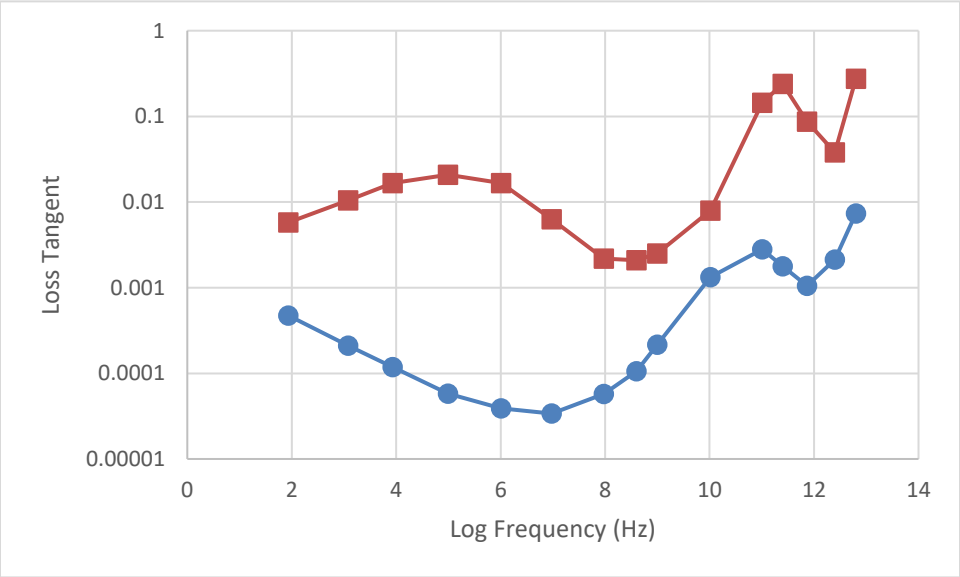

Figure 3.4.4.3-1 Loss tangent of lunar soil (blue circles, sample 14163 fines) and rock (orange squares, sample 14310) as a function of frequency from Lunar Sourcebook.

Table 3.4.4.3-1 Loss tangent of lunar soil (blue circles, sample 14163 fines) and rock (orange squares, sample 14310) as a function of frequency from Lunar Sourcebook figures 9.60 and 9.61.

Log Frequency	Loss Tangent	Loss Tangent
Hz	Soil sample 14163 Fines	Rock sample 14310
2.0	4.71E-04	5.75E-03
3.0	2.11E-04	1.05E-02
4.0	1.18E-04	1.66E-02
5.0	5.81E-05	2.09E-02
6.0	3.89E-05	1.66E-02
7.0	3.39E-05	6.31E-03
8.0	5.75E-05	2.19E-03

Log Frequency	Loss Tangent	Loss Tangent
Hz	Soil sample 14163 Fines	Rock sample 14310
8.6	1.06E-04	2.09E-03
9.0	2.16E-04	2.51E-03
10.0	1.32E-03	7.94E-03
11.0	2.80E-03	1.45E-01
11.4	1.78E-03	2.40E-01
12.0	1.05E-03	8.71E-02
12.4	2.13E-03	3.80E-02
12.8	7.37E-03	2.75E-01

Technical Notes

Lunar Sourcebook references numerous papers including Strangway and Olhoeft, 1977, Strangway et al., 1972, Gold et al., 1972, Bassett and Shackleford, 1972 and Perry et al., 1972.

3.4.5 Optical Properties

Description

Properties of photon absorption and scattering on the lunar surface and in dusty lunar environments at optical and radio wavelengths are required for design of optical and radar landing sensor systems.

Design Limits

Tabular values in this section are to be used for design. Figures are provided for illustration only.

3.4.5.1 Visible and Near-Infrared Properties

Albedo values are given in Section 3.4.6.1.1. The light scattering function is described in detail by the Hapke parameters (Sato et al. 2014), however, the Henyey-Greenstein (H-G) phase function is sufficient for engineering analyses.

$$p(g) = \frac{1+c}{2}\frac{1-b^2}{(1-2b\cos(g)+b^2)^{3/2}} + \frac{1-c}{2}\frac{1-b^2}{(1+2b\cos(g)+b^2)^{3/2}}$$

where g is the phase angle (between the incident and viewing angles), b and c are given in Table 3.4.5.1-1, etc. Note that positive values of c indicate backscattering and negative values indicate forward scattering.

Table 3.4.5.1-1 Values of H-G parameters determined by LRO for various types of regolith (Sato et al. 2014, their figure 20).

Type of soil	b	c
Highland immature ejecta	0.20	0.70
Highland mature soil	0.23	0.37
Mare mature soil	0.26	0.07
Apollo 16 highland crystalline	0.33	-0.28
Apollo 11 Mare crystalline	0.34	-0.40

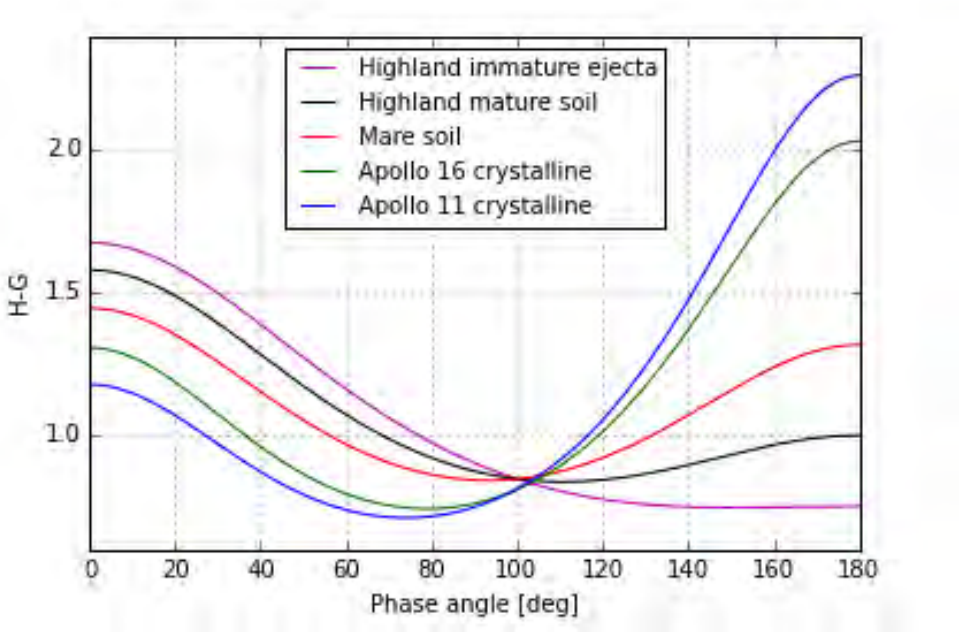

Figure 3.4.5.1-1 Henyey-Greenstein phase functions using the parameters listed in Table 3.4.5.1-1. The Apollo crystalline values are given to show possible small scale forward scattering from isolated particles. The crystalline material is not significant for engineering applications due to small number densities.

3.4.5.2 Radar Properties

Radar reflectivity can be calculated from the electrical properties of the regolith (3.4.4) and surface roughness (3.4.1.3).

3.4.6 Lunar Thermal Environment

Description

Thermal properties of the lunar regolith are required for design of lunar architecture and evaluation of thermal behavior of systems operating on the lunar surface.

The lunar thermal environment consists of radiation from the sun and lunar surface and conduction of the surface. At high latitudes local topography and seasonal (sub-solar latitude) variations are significant.

Design Limits

Tabular values in this section are to be used for design. Figures are provided for illustration only.

3.4.6.1 Lunar surface radiative environment

The space sink temperature and range of solar irradiance due to distance from the sun, S_0 is given in 3.3.9.1. Radiation from the lunar surface consists of reflected sunlight and emitted infrared radiation. The reflected sunlight is calculated from

$$I_R = S_0 \, A \cos(Z)$$

where A is the visible light (solar spectrum) albedo and Z is the solar zenith angle.
The scattering function of the lunar regolith is described in Section 3.4.5.1.
Absorptivity of the regolith is given by

$$\alpha = 1 - A$$

Emitted longwave infrared radiation is given by

$$I_L = \varepsilon \, \sigma \, T^4$$

where ε is the thermal infrared emissivity of the regolith and σ is the Stefan-Boltzmann constant. See 3.4.6.1.1 for emissivity values.
The daytime surface temperature can be approximated by

$$T(Z) = \left[\frac{S_0 \, (1 - A) \cos(Z)}{\varepsilon \sigma}\right]^{\frac{1}{4}}$$

for sensitivity analyses but the temperature extremes to be used for design purposes are given in Table 3.4.6.3-1. S_0 is the value of the solar constant scaled for distance to the sun as described in 3.3.9.1.

The daytime surface temperature variation with solar zenith angle can use the Lambertian approximation

$$T(Z) = T_S \cos^{1/4}(Z)$$

where T_S is the sub-solar temperature. Section 3.4.6.3 gives the range of temperatures observed by Lunar Reconnaissance Orbiter Diviner instrument for two regions: global and between 84 and 90 degrees south latitude. The former should be used for global access design and the latter for

analysis of polar missions only. For detailed mission-specific performance analyses, topographic effects (shadowing by mountains or proximity to solar-illuminated mountains, for example) can be performed using mission dates and digital elevation models. The analysis approach is described in the Lunar Thermal Analysis Guidebook (currently under development by the Lunar Thermal Environment Task Team). Figure 3.4.6.1.1-1 shows the variation of albedo and emissivity with longitude for the lunar equator.

3.4.6.1.1 Albedo and emissivity

The visible (solar spectrum) light albedo is not constant across the lunar surface. There are obvious differences between mare and highland regions (see Table 3.4.6.1.1-1 and Figure 3.4.6.1.1-1). The regolith visible light scattering phase function is described in 3.4.5.1.

Table 3.4.6.1.1-1 Albedo and emissivity extremes for global and south polar regions. Since the south polar region is essentially highland regolith, we use highland equatorial values for a and ε. The infrared emissivities are taken from Vasavada et al. 2012 and Hayne et al. 2017 and the global albedo is from Williams et al. 2017.

Location	Albedo a	Emissivity ε
Highland mean (0^O lat)	0.16	0.95 – 0.98
Mare mean (0^O lat)	0.07	0.95 – 0.98
South Pole (84-90^OS) nominal	0.16	None available. Use 0.95 – 0.98

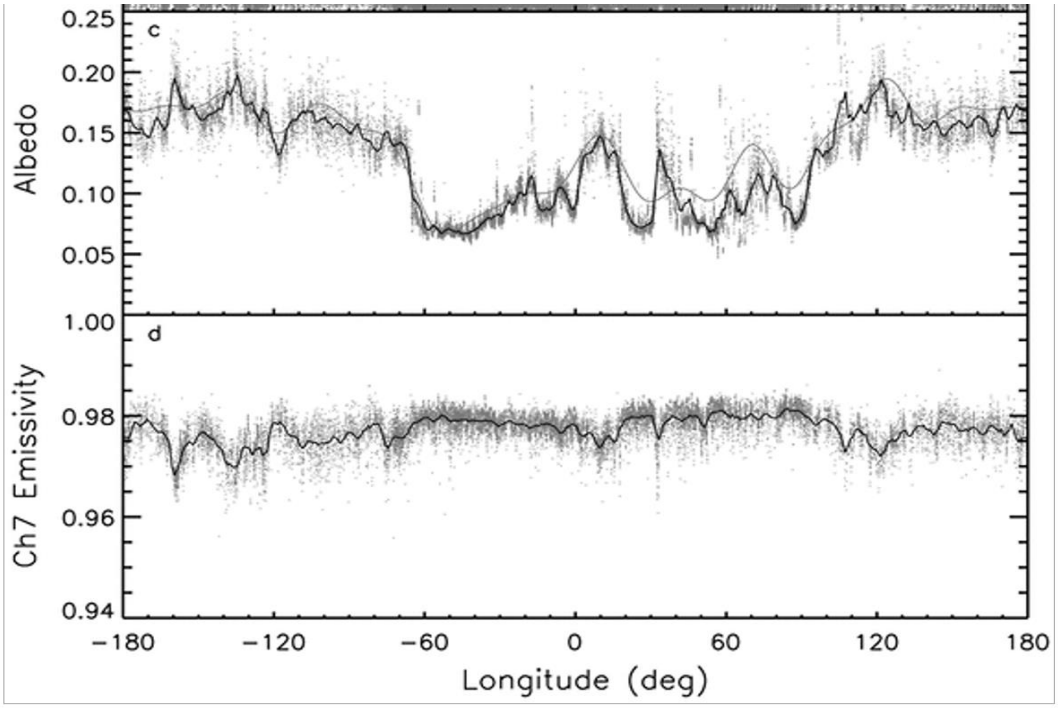

Figure 3.4.6.1.1-1 Equatorial albedo and emissivity as a function of longitude from Vasavada et al. 2012. The solid line in panel c is the albedo smoothed with a moving average of 2° of longitude every 0.05°. The gray curve is from the Clementine imagery. Panel d is from Diviner channel 7 which is near the peak of the thermal emissions. The solid line is data smoothed over 3° of longitude every 0.05°.

3.4.6.2 Lunar surface thermal properties

The following material describes lunar regolith parameters necessary for analysis of heat transfer to and from the regolith. Table 3.4.6.2-1 provides values for conductivity, diffusivity and heat capacity. Bulk density is given in Table 3.4.2.3-1 and discussed in Section 3.4.2.3.1.

Table 3.4.6.2-1 Nominal values of thermal parameters for lunar regolith.

Parameter	Value	Units	Notes	Section	Reference
Thermal Conductivity (k)	35-234cm deep: $1.4 \times 10^{-2} – 2.5 \times 10^{-2}$ (Apollo 15) 1.72×10^{-2} - 2.95×10^{-2} (Apollo 17)	W/m-K	-	3.4.6.2.1	Langseth et al. 1973a Table 9-VI
	2-15cm deep: $1.0 \times 10^{-2} – 1.5 \times 10^{-2}$ (Apollo 15 & 17)				Langseth et al. 1973b
	0-2cm deep: 0.9×10^{-3} - 1.5×10^{-3} (Apollo 15 & 17)				

Parameter	Value	Units	Notes	Section	Reference
Thermal Diffusivity (*K*)	9.9 x 10^{-5}	cm^2/s	Temperature and density dependent	3.4.6.2.3	Cremers 1972
Heat Capacity (Specific Heat)	See Table 3.4.6.2.2-1	J/kg-K	Temperature dependent	3.4.6.2.2	Woods-Robinson et al. 2019

3.4.6.2.1 Thermal conductivity

Thermal conductivity, k, is the ability of a material to conduct heat. The thermal conductivity of lunar regolith was calculated from data collected in situ during the Apollo 15 and 17 heat flow experiments, as well as on returned Apollo samples. Thermal conductivity models have been defined by fitting thermal models of the Moon's surface to these calculations, as well as to temperatures obtained from the Lunar Reconnaissance Orbiter (LRO) Diviner experiment.
The upper 1–2 cm of the regolith has extremely low thermal conductivity – about a factor of 10 lower than the bulk regolith. Overall, the bulk regolith has very low thermal conductivity. It is similar to aerogel and about a factor of 10 less than dry silica sand.
The effective thermal conductivity of lunar regolith, like other porous media in vacuum, is the sum of a solely conductive component and solely radiative component.
For disturbed regolith between 104K and 425K, Cremers et al. 1972 gives the following relationship, determined empirically from returned Apollo 12 samples of density 1970 kg/m^3:

$$k(T) = k_C + k_r T^3$$

where k_c, is the conductive component, $k_r T^3$ is the radiative component, and

$$k_C = 1.15 \times 10^{-3} \left[\frac{W}{mK}\right] \ , \ k_r = 0.159 \times 10^{-10} \left[\frac{W}{mK^4}\right]$$

For undisturbed regolith on the lunar surface, Hayne et al. 2017 presents density, ρ, dependent relationships for k_c and k_r paired with depth dependent relationships for density. These results were obtained by best matching a thermal model of the Moon's surface to global data from the LRO Diviner experiment.

$$k_r = k_C \left(\frac{2.7}{350^3}\right) \left[\frac{W}{mK^4}\right]$$
$$k_C = k_{deep\ layer} - \left(k_{surface\ layer} - k_{deep\ layer}\right)\left(\frac{\rho_{deep\ layer} - \rho}{\rho_{deep\ layer} - \rho_{surface\ layer}}\right) \left[\frac{W}{mK}\right]$$
$$k_{surface\ layer} = 7.4 \times 10^{-4} \left[\frac{W}{mK}\right] \ , \ k_{deep\ layer} = 3.4 \times 10^{-3} \left[\frac{W}{mK}\right]$$
$$\rho_{surface\ layer} = 1100 \left[\frac{kg}{m^3}\right] \ , \ \rho_{deep\ layer} = 1800 \left[\frac{kg}{m^3}\right]$$

$$\rho = \rho_{deep\ layer} - \left(\rho_{deep\ layer} - \rho_{surface}\right)e^{-\frac{z}{H}} \left[\frac{kg}{m^3}\right]$$

z = depth (from surface) [m]
H = a scaling factor, typically 0.06

Woods-Robinson et al. 2019 used a lunar simulant (crushed basalt) to empirically show that <100K, the above relations will likely over predict the thermal conductivity of lunar regolith. The authors then present thermal conductivity relations for crushed basalt that is valid at cryogenic temperatures. Updated fits for lunar regolith are not yet published.

Thermal conductivity is dependent on particle composition and shape of lunar fines and these properties vary with location. Figure 3.4.6.2.1-1 shows thermal conductivity vs. temperature for regolith samples from various Apollo landing sites and sample mass densities. The extremes from this data should be used for design purposes. These extremes are described by the coefficients of the expression for k(T) given above and are (references in figure caption):

Apollo 11 (mare), density 1640 kg/m^3:

$$k_C = 1.868 \times 10^{-3} \left[\frac{W}{mK}\right] \ , \ k_r = 2.29 \times 10^{-11} \left[\frac{W}{mK^4}\right]$$

Apollo 16 (highland), density 1500 kg/m^3:

$$k_C = 4.84 \times 10^{-4} \left[\frac{W}{mK}\right] \ , \ k_r = 1.11 \times 10^{-11} \left[\frac{W}{mK^4}\right]$$

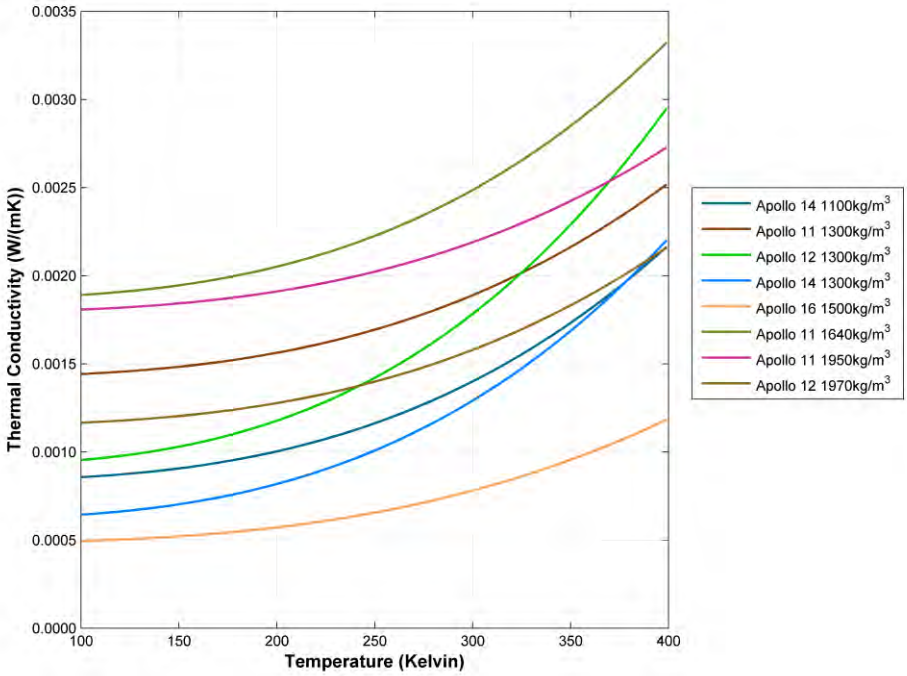

Figure 3.4.6.2.1-1 Thermal conductivity versus temperature for various Apollo samples (Cremers and Birkeback 1971, Cremers et al. 1972, Cremers 1972, Cremers and Hsia 1974)

Thermal conductivities have been calculated for several rocks returned from Apollo 11. Cremers 1974 provides a good summary of available data. Thermal conductivities vary based on rock composition and can range from 0.2 to 2.0 W/(mK) between 150K and 430K.

3.4.6.2.2 Heat capacity (specific heat)

Heat capacity (C) is a measure of the amount of heat that is required to change the temperature of a body by a given amount. Specific heat (c) capacity refers to the amount of heat required to change the temperature of a given amount of mass.
Heat Capacity is defined as:

$$C = \frac{\Delta Q}{\Delta T}$$

Specific Heat is defined as:

$$c = \frac{\Delta Q}{\mathrm{m}\,\Delta T}$$

Where:
ΔQ = amount of heat energy
ΔT = temperature change
m is the mass.

The temperature dependence of the specific heat is given in Figure 3.4.6.2.2-1 from Woods-Robinson et al. 2019. Equations for the fit are given in Woods-Robinson et al. 2019. Table 3.4.6.2.2-1 gives the values along the new fit curve.

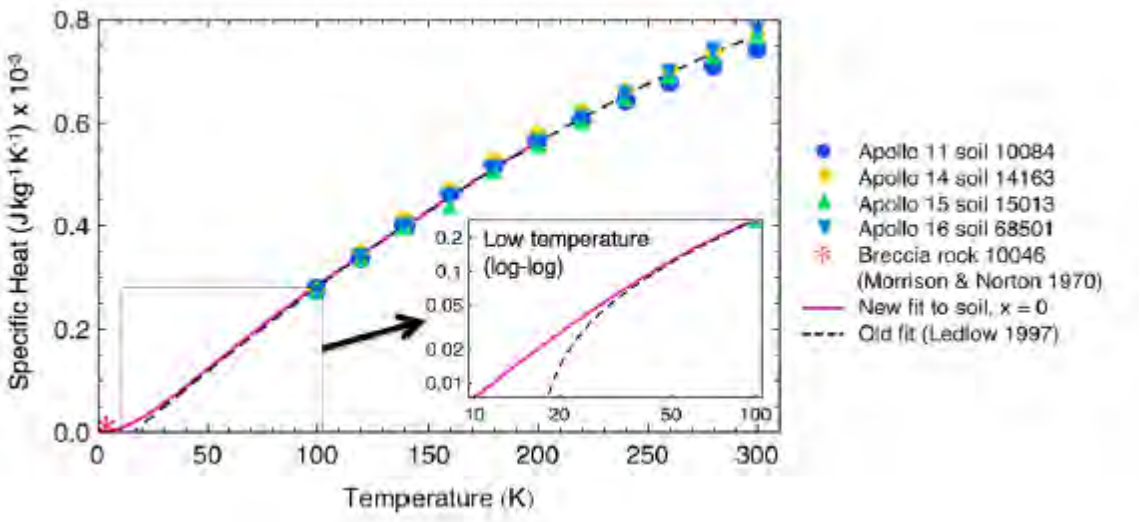

Figure 3.4.6.2.2-1 Revised estimate of the specific heat versus temperature of lunar regolith from Woods-Robinson et al. 2019. The estimate is valid between 10 and 400 K.

Table 3.4.6.2.2-1 Specific heat versus temperature extracted from Figure 3.4.6.2.2-1.

Temperature	Specific Heat
K	J/kg K x 10^{-3}
10	0.009
20	0.027
30	0.053
40	0.089
50	0.122
60	0.158
70	0.191
80	0.227
91	0.258
100	0.287
120	0.347
140	0.404
160	0.458
181	0.513
200	0.564
220	0.609

Temperature	Specific Heat
K	J/kg K x 10^{-3}
240	0.653
260	0.698
280	0.733
300	0.773

3.4.6.2.3 Thermal diffusivity

The thermal diffusivity (κ) is a measure of the rate at which material adjusts to changes in the temperature of the surroundings:

$$\kappa = \frac{k}{\rho c}$$

Where:
k = thermal conductivity (W/mK)
ρ = density (g/m3)
c = specific heat (J/kgK).

Materials with high thermal diffusivity adjust to the changes in the surrounding thermal environment rapidly. Thermal diffusivity is a function of depth as well as temperature as shown in Table 3.4.6.2.3-1.

Table 3.4.6.2.3-1 Thermal diffusivity as a function of temperature for 2 different depths. These values assume a density of 1580 kg/m^3.

Temp	Surface Thermal Diffusivity Disturbed (Cremers)	Surface Thermal Diffusivity Undisturbed (Hayne)
K	cm^2/s	cm^2/s
10	7.48E-04	6.49E-04
20	2.49E-04	2.16E-04
30	1.27E-04	1.10E-04
40	7.59E-05	6.57E-05
50	5.56E-05	4.79E-05
60	4.32E-05	3.71E-05
70	3.60E-05	3.07E-05
80	3.06E-05	2.59E-05

Temp	Surface Thermal Diffusivity Disturbed (Cremers)	Surface Thermal Diffusivity Undisturbed (Hayne)
K	cm^2/s	cm^2/s
90	2.76E-05	2.31E-05
100	2.49E-05	2.06E-05
110	2.30E-05	1.88E-05
120	2.15E-05	1.72E-05
130	2.04E-05	1.60E-05
140	1.95E-05	1.50E-05
150	1.89E-05	1.42E-05
160	1.85E-05	1.35E-05
170	1.82E-05	1.29E-05
180	1.80E-05	1.24E-05
190	1.79E-05	1.19E-05
200	1.79E-05	1.15E-05
210	1.82E-05	1.12E-05
220	1.85E-05	1.10E-05
230	1.88E-05	1.08E-05
240	1.93E-05	1.07E-05
250	1.98E-05	1.05E-05
260	2.03E-05	1.04E-05
270	2.11E-05	1.04E-05
280	2.19E-05	1.04E-05
290	2.27E-05	1.04E-05
300	2.35E-05	1.04E-05

3.4.6.3 Surface Temperature

The temperature of the lunar surface is highly dependent on the sun angle and optical properties (emissivity and absorptivity). Section 3.3.9.1 describes the calculations to approximate surface temperatures. For global access design purposes, the temperature extremes in Table 3.4.6.3-1 should be used. They have been taken from Lunar Reconnaissance Orbiter Diviner measurements (Figure 3.4.6.3-1). For situations where other variations in temperature are needed refer to Figure 3.4.6.3-2 for the standard deviation at the various latitudes and local times. At high latitudes where the solar illumination angle is near grazing, local topography and season (sub-solar latitude) are extremely important. For detailed thermal performance analysis at a specific landing site, temperatures, solar lighting conditions and local topography may be

obtained from LRO sources such as the QuickMap tool at https://quickmap.lroc.asu.edu/. Raw polar temperature data is available at http://luna1.diviner.ucla.edu/~jpierre/diviner/level4_polar/

Table 3.4.6.3-1 Lunar surface temperature extremes for various latitudes and solar illumination conditions from Williams et al. 2017. Mean temperatures are the plotted value with the max or min extremes taken from the error bars. Temperature for coldest permanently shadowed crater is from Vasavada et al. 2012.

Location	Mean Temperature K	1 Sigma Max or Min Temp K	Solar conditions
Equatorial maximum	391	394	Local noon
Equatorial minimum	96	94	Before sunrise
45 degree latitude maximum	350	357	Local noon
45 degree latitude minimum	89	83	Before sunrise
85 degree latitude maximum	182	224	Local noon
85 degree latitude minimum	61	41	Approx. 3am equivalent
Coldest permanently shadowed crater	30		

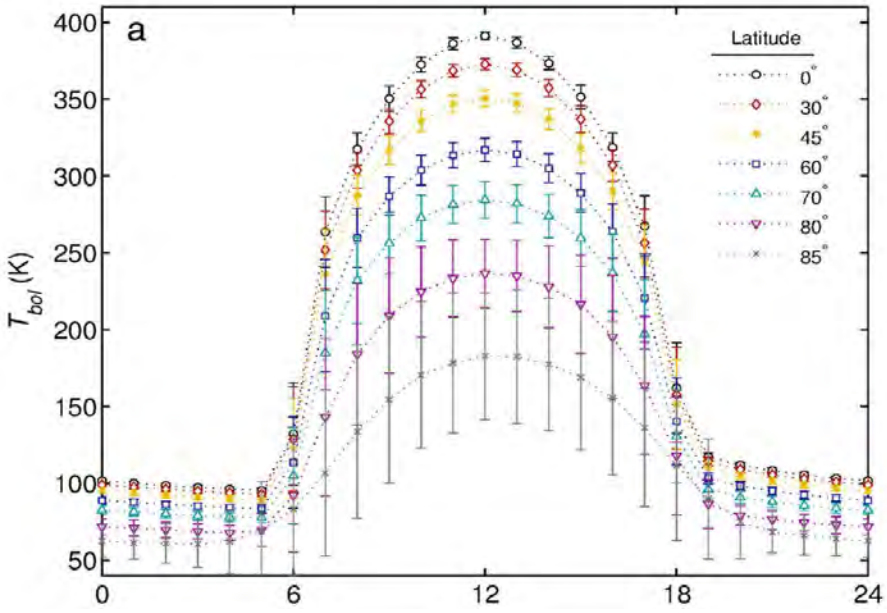

Figure 3.4.6.3-1 Zonal mean bolometric temperature as a function of latitude and 24-hour equivalent time of day from LRO Diviner (Figure 9 (a) from Williams et al. 2017).

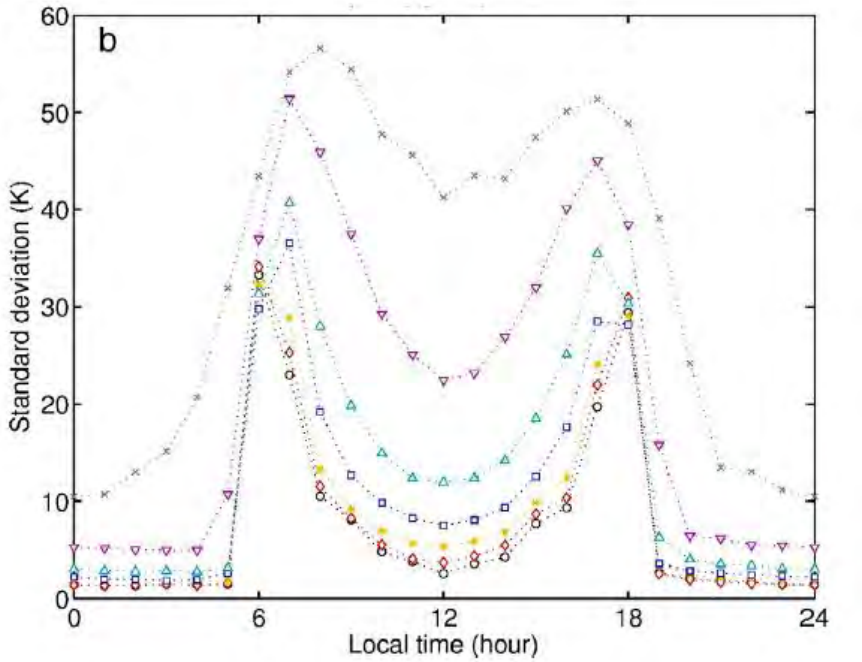

Figure 3.4.6.3-2 Zonal mean bolometric temperature standard deviation as a function of latitude and 24-hour equivalent time of day from LRO Diviner (Figure 9 (b) from Williams et al. 2017). The line symbols are the same as for Figure 3.4.6.3-1

3.4.6.4 Subsurface Temperature

The Apollo 15 and 17 heat flow experiments provided temperatures as a function of depth as seen in Figure 3.4.6.4-1. Note that these measurements are only available for some of the Apollo sites and the proximity of those sites to heating by radiogenic elements affects the temperature profiles. These results are not extensible to the lunar south pole where no measurements have been made.

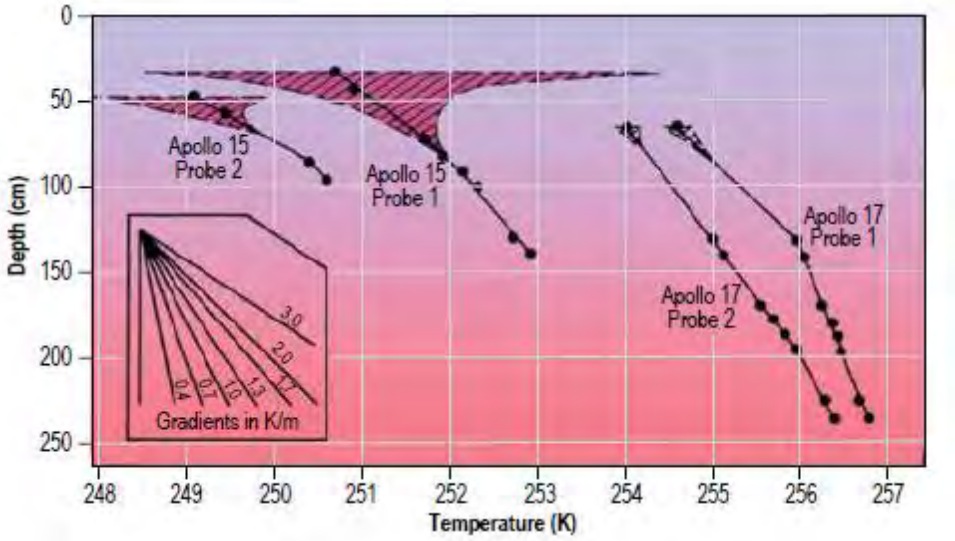

Figure 3.4.6.4-1 Temperature as a function of depth at the Apollo 15 and 17 landing sites (hatched areas show day-to-night temperature variations). From Lunar Sourcebook: A User's Guide to the Moon.

3.4.7 Lunar Ionizing Radiation Environment

Rationale: Systems operating on the lunar system must be designed to withstand the space radiation environment as well as the radiation environment due to neutrons generated by interactions of energetic solar particles and GCR.

Description

The ionizing radiation environment on the lunar surface consists primarily of solar energetic particles and galactic cosmic rays. Both of these contribute to total ionizing dose effects (3.4.7.1) and single event effects (3.4.7.2). These environments are described in detail in other paragraphs for free space exposure (see below). It is acceptable to take those particle fluxes and doses and divide them by 2 to account for the presence of the Moon which blocks the isotropic radiation for half the sky (2π steradians). Interaction of these primary energetic particles with the lunar surface can cause neutrons to be generated as described in 3.4.7.3.

Design Limits

3.4.7.1 Lunar Surface Total Ionizing Dose

Since the Moon is situated outside of the shielding afforded by the Earth's magnetic field, the total dose environment in 3.3.1.10.2 Geomagnetic Unshielded is appropriate to use for the lunar surface with a factor of 2 reduction in dose due to shielding by the Moon.

3.4.7.2 Lunar Surface Single Event Effects Environment

Since the Moon is situated outside of the shielding afforded by the Earth's magnetic field, the single event effects environment in 3.3.2.10.2 Geomagnetic Unshielded is appropriate to use for the lunar surface with a factor of 2 reduction in flux due to shielding by the Moon.

3.4.7.3 Lunar Neutron Environment

Secondary or albedo neutrons are produced when solar or galactic cosmic ray energetic particles interact with the lunar regolith. These are primarily a concern for dose to crew members (see Section 3.3.4) but also must be considered in avionics design due to possible displacement damage in the semiconductors.

Since lunar albedo neutrons are primarily generated by galactic cosmic ray (GCR) impacts with the regolith and GCR are more abundant during solar minimum, there is a solar cycle dependence of the albedo neutron flux. For design purposes the flux at solar minimum should be used. Figure 3.4.7.3-1 and Table 3.4.7.3-1 give the modeled differential neutron flux for solar maximum and solar minimum.

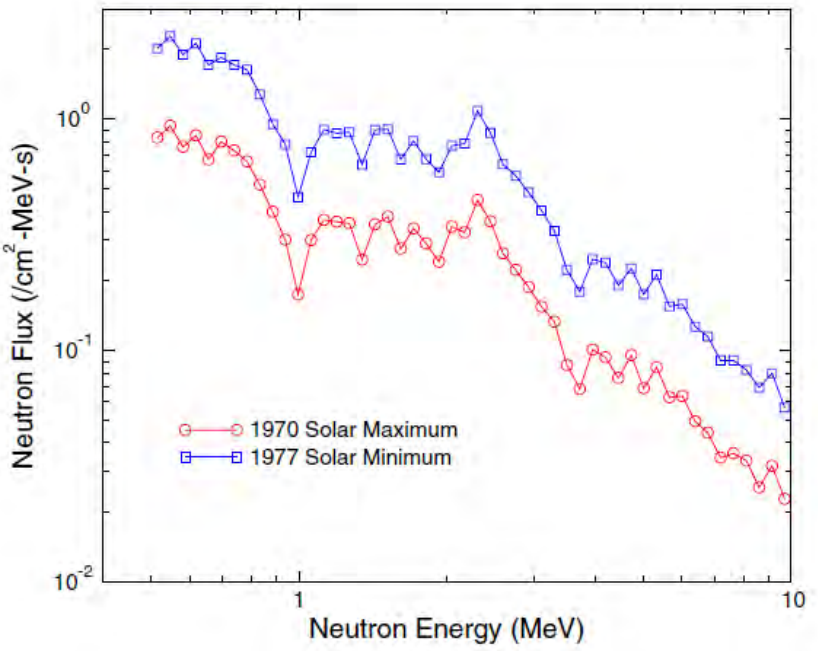

Figure 3.4.7.3-1 Differential neutron flux for solar maximum and minimum conditions (Adams et al. 2007).

Table 3.4.7.3-1 Differential neutron flux for solar maximum and minimum conditions (after Adams et al. 2007).

Neutron Energy	Neutron Flux 1977 Solar Minimum	Neutron Flux 1970 Solar Maximum
MeV	#/cm^2 MeV s	#/cm^2 MeV s
0.51	2.02	0.83
0.55	2.24	0.92
0.58	1.89	0.75
0.62	2.10	0.84
0.65	1.72	0.67
0.69	1.83	0.78
0.74	1.70	0.72
0.78	1.64	0.65
0.83	1.28	0.51
0.89	0.95	0.40
0.94	0.77	0.30
1.00	0.46	0.17
1.06	0.72	0.30
1.12	0.89	0.36
1.19	0.87	0.36
1.27	0.88	0.35
1.35	0.65	0.25
1.43	0.90	0.35
1.52	0.91	0.38
1.61	0.68	0.27
1.71	0.81	0.34
1.81	0.68	0.29
1.93	0.59	0.24
2.05	0.77	0.34
2.17	0.79	0.32
2.31	1.08	0.45
2.45	0.87	0.36
2.59	0.64	0.26
2.75	0.57	0.22
2.93	0.49	0.19
3.11	0.40	0.15
3.31	0.33	0.13

Neutron Energy	Neutron Flux 1977 Solar Minimum	Neutron Flux 1970 Solar Maximum
MeV	#/cm^2 MeV s	#/cm^2 MeV s
3.50	0.22	0.09
3.73	0.18	0.07
3.96	0.25	0.10
4.20	0.24	0.09
4.47	0.19	0.08
4.76	0.23	0.10
5.01	0.18	0.07
5.32	0.21	0.08
5.71	0.16	0.06
6.02	0.16	0.06
6.40	0.13	0.05
6.81	0.12	0.04
7.20	0.09	0.03
7.66	0.09	0.04
8.18	0.08	0.03
8.62	0.07	0.02
9.14	0.08	0.03
9.73	0.06	0.02

Technical Notes
See 3.3.1.10.2 and 3.3.2.10.2 for on the energetic charged particle environments. The albedo neutron spectra were taken from J.H. Adams, M. Bhattacharya, Z.W. Lin, G. Pendleton, and J.W. Watts (2007) Advances in Space Research 40, 338-341. Their calculations were based on CREME 96 with GEANT4 Monte Carlo simulations and comparisons with Lunar Prospector fast neutron data.

3.4.8 Lunar Meteoroid and Ejecta Environment

Rationale: Hardware operating on the lunar surface or in low lunar orbit will be exposed to primary meteoroids from space and a secondary ejecta environment produced during impacts of primary meteoroids on the lunar surface.

3.4.8.1 Primary Meteoroid Environment

The flux of primary meteoroids in the threat size range is described in Section 3.3.6 Meteoroid and Orbital Debris Environments. The Meteoroid Engineering Model (MEM) described there can be used to calculate this environment for the lunar surface by generating a state vector for a point on the lunar surface, propagating that state vector, and inputting the data into MEM. Note

that if the state vector places the target point closer than 1 lunar radius (1737.4 km) to the center of the Moon MEM will return 0 flux.

3.4.8.2 Meteoroid Ejecta Environment

The meteoroid ejecta environment is generated by larger meteoroids impacting the surface, generating a crater and ejecting pieces of regolith. The ejecta model, to characterize the flux vs size and velocity of particles, is currently under development and will be included in the next revision of this document. The existing model of this environment is documented in NASA SP-8013 Meteoroid Environment Model – 1969 [Near Earth to Lunar Surface] section 3.2 Lunar Ejecta Environment. That material should be used until the new ejecta environment is baselined herein.

3.4.9 Lunar Illumination

The illumination conditions on the Moon vary based on local topography and proximity to the lunar poles. A lunar day is the period of time for the Moon to complete one rotation on its axis with respect to the Sun. The sidereal rotational period of the Moon is 655.73 hours (~27days, 7 hours and 55 minutes). The mean synodic period of the Moon with respect to Earth (return to the same phase relative to Earth, or a full "day and night" cycle) is 708.73 hours (29 days, 12 hours and 44 minutes), but can vary slightly during the year due to the eccentricity of the elliptical orbit and variance in orbital velocity. The Moon's rotational obliquity (tilt axis) is 1.54° (relative to the Solar System ecliptic, e.g. compared to Earth's ~23.4°). The Moon's orbit is inclined 5.16° relative to the ecliptic. As a consequence of the Moon's orbital parameters, the equatorial regions of the Moon's surface are illuminated for about 15 Earth-days, followed by a 15 Earth-day long night. Polar illumination is more complex and no general statement about the duration of illumination periods can be made, though sufficient data is available to produce a high fidelity assessment of polar illumination at any future landing site. A description of polar illumination maps and links to the data is available at http://lroc.sese.asu.edu/posts/991.

In the polar regions of the Moon, solar incidence can be extremely low (grazing sunlight just above the horizon), and large local topography variations can lead to extreme illumination conditions. Areas of the poles can exist in permanent shadow (Permanently Shadowed Regions, or PSRs), receiving no direct sunlight in the year, and with minimal scattered light from surrounding areas. There are also areas of near-permanent illumination, where there are only short periods of darkness (e.g. a few Earth days). These areas are often within close proximity to each other. (Mazarico et al., 2011; Speyerer and Robinson, 2013; Glaser et al., 2014; Glaser et al., 2018).

Based on the accumulated polar imagery from the LRO – WAC camera, percentage-based and time-weighted maps of illumination have been created for the Moon's polar regions from 88° - 90° (Speyerer and Robinson, 2013). The current highest resolution time-weighted illumination maps are shown in Figure 3.4.10-1 (South Pole) and 3.4.10-2 (North Pole). These data are available in the Planetary Data System http://imbrium.mit.edu/DATA/SLDEM2015_SLOPE/. A high resolution illumination map for Shackleton crater is available here: http://lroc.sese.asu.edu/exhibits/A%20New%20Moon%20Rises/41

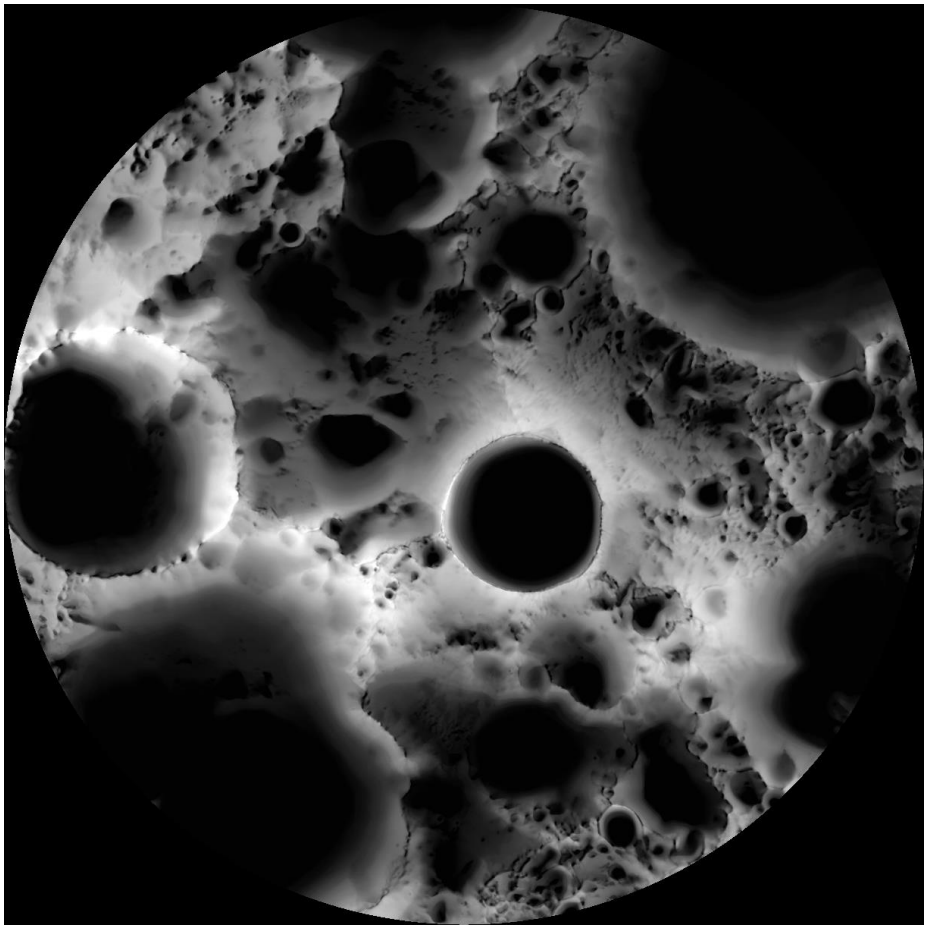

Figure 3.4.10-1 Multi-temporal illumination map of the lunar south pole, Shackleton crater (19 km diameter) is in the center, the south pole is located approximately at 10 o'clock on its rim. Mapped area extends from 88°S to 90°S [NASA/GSFC/Arizona State University].

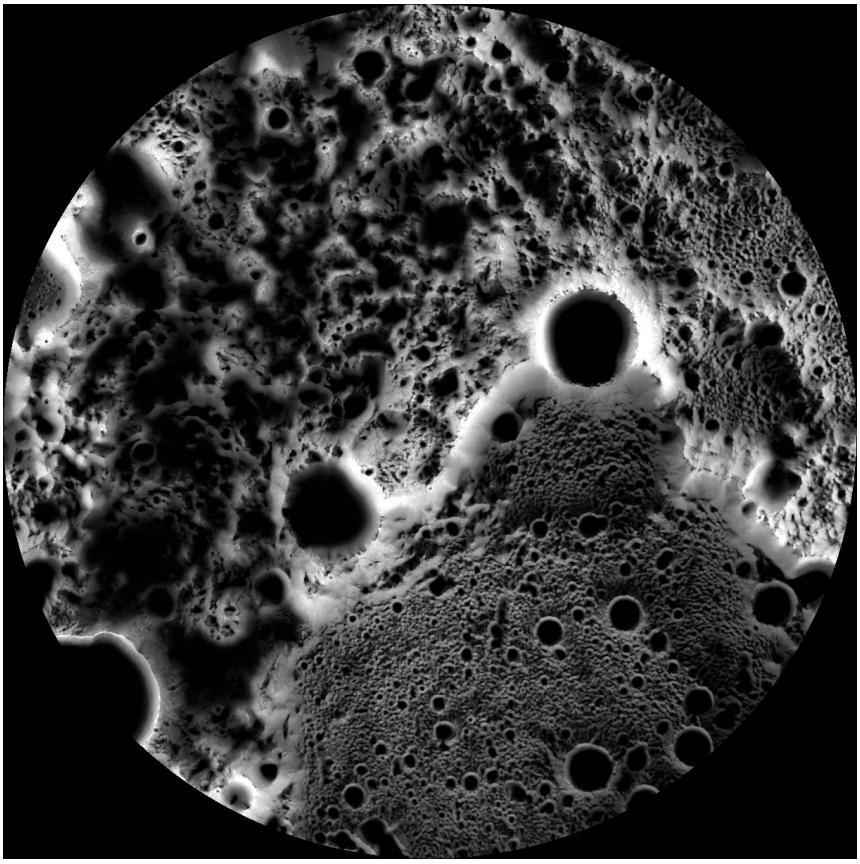

Figure 3.4.10-2. Multi-temporal illumination map of the lunar North Pole. Mapped area extends from 88°S to 90°S [NASA/GSFC/Arizona State University].

3.4.10 Lunar Neutral Atmosphere

It is not anticipated that the tenuous atmosphere of neutral atoms and molecules near the lunar surface can affect the design and operations of lunar surface systems. If any sensitivities of the hardware are identified this section can be populated.

3.4.11 Special Physical and Chemical Conditions of Regolith Inside Areas of Permanent Shadow (RESERVED)

3.5 Entry and Landing Phases

The following environments are applicable to the MPCV descent phase and also to descending Space Launch System (SLS) vehicle elements after separation from the vehicle stack during the ascent phase.

3.5.1 Re-entry Neutral Atmosphere

Description

This section defines the neutral atmosphere density, composition, and variability for various design applications. All altitude regimes and geographic locations are incorporated into the Earth-GRAM 2010 (see note in 2.1.2 Applicable Models/Data Sets) model, from the Earth surface to 2,000 km (6,561,680 ft).

Design Limits

The neutral atmosphere above 90 km (295,276 ft) is specified in Section 3.3.11, In-Space Neutral Atmosphere (Thermosphere) Density. Section 3.3.11 is also compatible with the further breakout of the specification in the various 3.5 Sections.

Model Inputs

Above 90 km (295,276 ft), 1,000 or more Monte Carlo simulations are needed per month for minimum, nominal, and maximum perturbation scale per Table 3.3.11-1. Below 90 km (295,276 ft) Earth-GRAM 2010 flight profiles with perturbations per Table 3.5.4-1 will be used. Atmospheric temperature, pressure, and density should be evaluated simultaneously in each simulation.

Limitations

None

Technical Notes

None

3.5.2 Reserved

3.5.3 Lightning During Normal Landing

Description

This section specifies the lightning environment for descent and landing operations in the normal landing zones offshore or in the western U.S. This environment is also applicable to descending launch vehicle elements after separation from the vehicle stack during the ascent phase. Design specifications include standardized voltage and current waveforms derived or characterized to represent the lightning environment at specific zones established on the vehicle.

Design Limits

See the Design Limits in Section 3.1.11, Lightning During On-pad Operations.

Model Inputs

Vehicle lightning strike zones are defined for the integrated vehicle in re-entry and landing configurations, including with and without parachutes deployed, while descending through the atmosphere or residing on land or water after landing.

Limitations

See the Design Limits in Section 3.1.11, Lightning During On-pad Operations.

Technical Notes

None

3.5.4 Aloft Winds for Normal Descent and Landing

Description

This section specifies aloft wind environments and dispersions (orbit to 300 m (984 ft) AGL) for normal vehicle descent and landing operations. This environment also applies to re-entering and descending launch vehicle elements after separation from the vehicle stack following the ascent phase.

Design Limits

System performance will be evaluated through analysis of 1,000 or more Earth-GRAM 2010 (see note in 2.1.2 Applicable Models/Data Sets) random profiles per month. Each profile is for an orbit to 300 m (984 ft) AGL flight profile into the landing site of interest with Earth-GRAM 2010 inputs per Table 3.5.4-1. Atmospheric wind, temperature, pressure, and density should be evaluated simultaneously in each simulation.

Table 3.5.4-1. Earth-GRAM 2010 Input to Generate 1,000 or More Perturbed Profiles (0 to 90 km) of Temperature, Pressure, and Density Per Monthly Reference Period

Parameter	Earth-GRAM 2010 variable name	Value
RRA data set	iyrrra	3 = 2013 RRA
RRA limits – use if near site with an RRA	sitenear	0.5
	sitelim	2.5
Random output	iopr	1= random
Non-RRA sites	NCEPyr	9008 = period of record
Random perturbations	rpscale, ruscale, rwscale	1.0
Small scale perturbations	patchy	0

Model Inputs

Earth-GRAM 2010 (see note in 2.1.2 Applicable Models/Data Sets) input is listed in Table 3.5.4-1 for each monthly reference period. The model automatically sets surface roughness for a given

location input, but the location resolution is relatively course (1 degree by 1 degree). The surface roughness input should be checked when the model is being used for applications in a region where two or more significantly different surface types exist, such as near a coastline.

The spatial and temporal increments are chosen to optimize vehicle response for performance analyses. A large increment may not capture the frequencies (and/or wavelengths) necessary to excite appropriate vehicle responses, while too small an increment can produce very large relative derivatives along the flight path. Choose increments that result in spatial steps no smaller than the length of the vehicle.

The inputs given provide random profiles with random perturbations that can be used to determine envelopes for trajectory and load variables for descent analyses. An "rpscale" setting of 1.0 represents perturbation scaling equivalent to the climatological environment. If additional analyses to study the effects of more severe perturbations/turbulence are desired, the "rpscale" can be set to a higher value, which should not exceed 2.0. For thermal and aeroheating studies, it may be desirable to design to extreme profiles (for example, 2 or 3 sigma climatological profiles) which Earth-GRAM 2010 also has the capability to produce.

Limitations

Perturbations in the aloft region are statistically derived and are generated using the input variables in Table 3.5.4-1. Earth-GRAM 2010 does not define the turbulent boundary layer in the lowest 300 m (984 ft) AGL, so separate analysis is required for winds in this region. (See Section 3.5.8, Surface Winds for Normal Landing.)

Technical Notes

None

3.5.5 Aloft Air Temperature for Normal Descent and Landing

Description

This section specifies air temperature environments and dispersions (orbit to 300 m (984 ft) AGL) for normal vehicle descent and landing operations. This environment also applies to re-entering and descending launch vehicle elements after separation from the vehicle stack following the ascent phase.

Design Limits

See Section 3.5.4, Aloft Winds for Normal Descent and Landing.

Model Inputs

See Section 3.5.4.

Limitations

Perturbations in the aloft region are statistically derived and are generated using the input variables in Table 3.5.4-1.

Technical Notes

None

3.5.6 Aloft Air Pressure for Normal Descent and Landing

Description

This section specifies air pressure environments and dispersions (orbit to 300 m (984 ft) AGL) for normal vehicle descent and landing operations. This environment also applies to re-entering and descending launch vehicle elements after separation from the vehicle stack following the ascent phase.

Design Limits

See Section 3.5.4.

Model Inputs

See Section 3.5.4.

Limitations

See Section 3.5.5, Aloft Air Temperature for Normal Descent and Landing.

Technical Notes

See Section 3.5.5.

3.5.7 Aloft Air Density for Normal Descent and Landing

Description

This section specifies air density environments and dispersions (orbit to 300 m (984 ft) AGL) for normal vehicle descent and landing operations. This environment also applies to re-entering and descending launch vehicle elements after separation from the vehicle stack following the ascent phase.

Design Limits

See Section 3.5.4.

Model Inputs

See Section 3.5.4.

Limitations

See Section 3.5.5.

Technical Notes

See Section 3.5.5.

3.5.8 Surface Winds for Normal Landing

Description

This section specifies surface wind environments (altitude range 0 to 300 m (984 ft) AGL), up to and including the maximum design limits, for normal vehicle land and water landing operations. Design specifications include peak wind-speed profile, steady state wind-speed profile, and spectral gust environment.

Design Limits

Maximum: Peak wind-speed profile (0 to 300 m (984 ft) AGL) derived from the 10 m (32.8 ft) reference level peak wind speed from any azimuth is given by:

$$u(z) = u_{10}\left(\frac{z}{10}\right)^{k}$$

where *u(z)* is the peak wind speed (m/s) at height *z* meters above natural grade (0 to 300 m (984 ft) AGL), u_{10} is the design peak wind speed (m/s) at 10 m (32.8 ft), and k is a dimensionless exponent, where k = 1/7 for land landings and k= 0.11 for water landings.

The steady state wind-speed profile is obtained from the above peak wind-speed profile by dividing the peak wind speed by a gust factor of 1.4:

$$\overline{U}(z) = \frac{u(z)}{1.4}$$

where $\overline{U}(z)$ is the steady state wind speed (m/s) at height *z* meters above natural grade and *u(z)* is the peak wind speed (m/s) at height *z* meters above natural grade (determined above). Spectral gust is obtained by using the steady state wind speed at 10 m (32.8 ft) determined above with:

$$\Phi_u(\omega, z) = \frac{2}{\pi V(z)}\left[L_{10}\left(\frac{z}{10}\right)^{q}\right]\left[\sigma_{10}\left(\frac{z}{10}\right)^{p}\right]^2 \frac{1}{1+\left\{L_{10}\left(\frac{z}{10}\right)^{q}\left[\frac{\varpi}{V(z)}\right]\right\}^2}$$

$$\Phi_w(\omega, z) = \frac{1}{\pi V(z)}\left[L_{10}\left(\frac{z}{10}\right)^{q}\right]\left[\sigma_{10}\left(\frac{z}{10}\right)^{p}\right]^2 \frac{1+3\left\{L_{10}\left(\frac{z}{10}\right)^{q}\left[\frac{\varpi}{V(z)}\right]\right\}^2}{\left\{1+\left[L_{10}\left(\frac{z}{10}\right)^{q}\right]^2\left[\frac{\omega}{V(z)}\right]^2\right\}^2}$$

where Φ_u and Φ_w are the gust spectra for the longitudinal (*u*) and lateral, vertical (*w*) components at height *z* above natural grade, *V(z)* is the magnitude of the steady state wind vector relative to the vehicle at height *z*, and ω is the frequency in units radians per second (rad/s). The gust

spectra parameters (L_{10}, σ_{10}, p, and q) are for altitudes below 300 m (984 ft) and are provided in Table 3.5.8-1.

Minimum: No wind, calm for both land and water landing sites.

Table 3.5.8-1. Dryden Gust Spectra Parameters for the Longitudinal, Lateral, and Vertical Components for the Landing Phase

Component	σ_{10}	p	L_{10}	q
	(m/s)	(non-dimensional)	(m)	(non-dimensional)
Longitudinal	2.31	0.16	21	0.65
Lateral	1.67	0.25	11	0.83
Vertical	1.15	0.36	5	1.05

Model Inputs

For vehicle descent and landing onto land, use u_{10} = 19.5 m/s (metric units must be used in the equation) for construction of the maximum design limit wind-speed profile up to 300 m (984 ft) AGL. This value of u_{10} is applicable to normal land landings. A value for off-nominal land landing has not been defined.

For normal descent and landing operations into water, the steady state design wind speed at 10.0 m (32.8 ft) height above the surface is 8.2 m/s (26.9 ft/s), which implies a peak wind u_{10} = 11.48 m/s (37.7 ft/s). This value is associated with the sea state conditions defined in section 3.5.18, Sea State for Normal Water Landing.

Technical Notes

Design limit for vehicle land landing of 19.5 m/s (64 ft/s) at the 10.0 m (32.8 ft) reference level is the 95th percentile peak wind speed for a 1-hr exposure period at Edwards Air Force Base (EAFB). The steady state wind-speed profile is the 10-minute mean wind-speed profile that could produce the peak wind-speed profile determined above.

Design steady state wind speed limit of 8.2 m/s (26.9 ft/s) at the 10.0 m (32.8 ft) reference height for vehicle water landing is associated with the sea conditions defined in section 3.5.18 Sea State for Normal Water Landing.

Longitudinal and lateral components of turbulence fluctuate with height. The longitudinal component of turbulence is parallel to the steady state wind vector with the lateral component in the horizontal plane and perpendicular to the longitudinal and vertical components.

3.5.9 Surface Air Temperature for Normal Landing

Description

This section specifies the design maximum and minimum surface air temperature for normal vehicle land and water landing environments. Zones for normal land landings are assumed to be

contained in a geographical region in the western U.S., and the zone for water landing is assumed to be contained by oceanic regions within a 685 km (370.0 nmi) radius of San Diego, California.

Design Limits

Maximum air temperature over land: 46.0 °C (114.8 °F)

Minimum air temperature over land: -38.0 °C (-36.4 °F)

Maximum air temperature over water: 26.7 °C (80.1 °F)

Minimum air temperature over water: 3.8 °C (38.9 °F)

Model Inputs

None

Limitations

For any required thermal assessment involving wind effects over land, the winds must be assumed to be steady state at 10.0 m (32.8 ft) height, with horizontal speeds ranging from 0.0 to 13.9 m/s (45.6 ft/s). This wind was determined by using the steady state wind equation and peak wind of 19.5 m/s (64.0 ft/s) for land landings given in Section 3.5.8, Surface Winds for Normal Landing.

For any required thermal assessment involving wind effects over water, the winds must be assumed to be steady state at 10.0 m (32.8 ft) height with horizontal speeds ranging from 0.0 to 8.2 m/s (26.9 ft/s). This value is associated with the sea state conditions defined in Section 3.5.18, Sea State for Normal Water Landing. The peak wind value of 11.5 m/s (37.7 ft/s) was determined by multiplying the maximum steady state wind by the 1.4 gust factor given in Section 3.5.8, Surface Winds for Normal Landing.

Technical Notes

Design limits for normal land landings represent the maximum and minimum extreme temperatures from hourly surface observations recorded at selected locations in the normal land landing area.

Design limits for normal water landings were determined using six-hourly air temperature output within the normal water landing area from a global climatology. Air temperatures were obtained from the European Centre for Medium-range Weather Forecasts (ECMWF) Re-Analysis (ERA-40), which contains air temperature records on a 2.5° x 2.5° grid every six hours for the 1979-2002 period of record. The global dataset was subsetted to only contain temperatures within the normal landing area. Design limits were determined by comparing the minimum and maximum recorded air temperatures to the 0.5^{th} and 99.5^{th} percentile temperatures with 95.0% confidence intervals applied for each month (Barbré, 2012). Design limits are the empirical minimum and maximum air temperatures during December and September, respectively.

3.5.10 Surface Air Pressure for Normal Landing

Description

This section specifies the design maximum and minimum sea level air pressure for normal vehicle landing operations.

Design Limits

Maximum: 1,051.9 hPa

Minimum: 989.4 hPa

[100 Pa = 1 hPa = 1 millibar (mbar) = 0.01450377 pound/in^2 (psi)]

Model Inputs

Design limits specify the air pressure referenced to standard sea level conditions. For applications related to on-land landings or operations, the sea level pressure must be corrected to the applicable pressure at landing site elevation. The design limits, along with temperature and humidity information, can be used to derive design limits for air pressure at other desired altitudes.

Limitations

None

Technical Notes

Design limits represent the monthly mean sea level air pressure ±3 standard deviations (maximum value of standard deviation for each month) from hourly surface observations at selected locations in the normal landing area.

3.5.11 Surface Air Humidity for Normal Landing

Description

This section specifies the design limits for surface air humidity for normal vehicle landing operations.

Design Limits

Maximum: 100% Relative Humidity

Minimum: 5% Relative Humidity

Model Inputs

None

Limitations

None

Technical Notes

None

3.5.12 Aerosols for Normal Descent and Landing

Description

This section specifies the aerosol environment for normal (on land) vehicle descent and landing operations. Aerosol environments for in water-landings are specified in Section 3.5.21, Aerosols for Water Landing.

Design Limits

Reserved (see Technical Notes)

Model Inputs

None

Limitations

None

Technical Notes

This specification will be provided if land landing for normal operations is returned to the programs.

3.5.13 Precipitation for Normal Descent and Landing

Description

This section specifies the precipitation environment for normal vehicle descent and landing operations both on land or water.

Design Limits

The maximum design rainfall rate is 7.6 mm/hr (0.30 in/hr) from non-convective clouds.

Model Inputs

None

Limitations

None

Technical Notes

The design rainfall rate is the National Oceanic and Atmospheric Administration (NOAA) maximum observational reporting value for moderate rainfall. This rate was chosen to exclude operations during heavy rainfall produced by convective clouds (thunderstorms). Flight path

avoidance of thunderstorms is desired to protect the vehicle from extreme environments such as lightning, hail, and extreme turbulence.

3.5.14 Flora and Fauna for Descent and Landing

Description

This section specifies the flora and fauna environment for all descent and landing operations, including landing operations conducted on land or sea. Normal land landings should occur at prepared sites where exposure to flora and fauna hazards has been mitigated to acceptable levels.

Design Limits

During descent and land landing operations, the design limit for an avian species is a maximum mass of 2.2 kg (4.9 lbs) up to an altitude of 0.5 km (1,640.4 ft) above ground level.

During land landing operations, the design limit includes ground brush up to 0.6 m (2.0 ft) height.

During land landing operations, the design limit includes mammals with mass up to 10 kg (22 lbs).

No flora or fauna environments are specified for water landings.

Model Inputs

None

Limitations

None

Technical Notes

Although large mammals such as deer, cattle, and wild horses are not uncommon in open range areas in the western U.S., it is impractical to protect against collision with one of significant mass. The bird mass collision criteria for descent and landing operations were selected to maintain commonality with the ascent phase criteria.

3.5.15 Surface Characteristics and Topography for Normal Land Landing

(Soil conditions at the land landing site will be provided if this option is exercised.)

Description

This section specifies the design surface characteristics for normal landing operations. Normal landings should occur at prepared sites that fall within the design limits specified below.

Design Limits

The design limit for maximum surface slope of the land landing site will be 5°. The site will be clear of solid objects projecting more than 0.3 m (1.0 ft) above the surface. The site will be clear of ditches deeper than 0.3 m (1.0 ft).

Model Inputs

None

Limitations

None

Technical Notes

The selection of surface was made based on preliminary surveys of potential land landing sites. It is anticipated that any designated site will be prepared to meet this specification.

3.5.16 Cloud Environment for Normal Descent and Landing

Description

This section defines the cloud and visibility environments for normal descent and landing operations.

Design Limits

The design range for cloud clover is up to and including 100% cloud cover, excluding convective clouds and thunderstorms. The maximum size of any liquid cloud particle is 7 mm (0.3 in) diameter. The maximum size of any frozen cloud particle is 200 μm (0.008 in).

Model Inputs

None

Limitations

None

Technical Notes

The maximum size for liquid cloud particles of 7 mm (0.3 in) allows the vehicle to traverse stratiform clouds and rain in non-convective situations. Traversing convective type clouds, such as thunderstorms, could expose the vehicle to ice particles (hail or graupel) with diameters of several centimeters or larger. Flight path avoidance of thunderstorms is assumed to protect the vehicle from extreme environments such as lightning, hail, and extreme turbulence. The maximum size for frozen cloud particles of 200 μm (0.008 in) allows for traverse through mid and high altitude layer clouds (alto and cirrus type).

3.5.17 Radiant (Thermal) Energy Environment for Normal Landing

Description

This section specifies the design radiant (thermal) energy environment and sky temperature limits for normal landing operations.

Design Limits

Table 3.5.17-1 presents design cold radiant energy and sky temperature environment for a cloudy sky.

Table 3.5.17-2 presents design hot radiant energy and sky temperature environment for a cloudy sky.

Table 3.5.17-3 presents design cold radiant energy and sky temperature environment for a partly cloudy sky.

Table 3.5.17-4 presents design hot radiant energy and sky temperature environment for a partly cloudy sky.

Table 3.5.17-5 presents design cold radiant energy and sky temperature environment for a clear sky.

Table 3.5.17-6 presents design hot radiant energy and sky temperature environment for a clear sky.

Model Inputs

None

Limitations

None

Table 3.5.17-1. Cold Design Radiant Energy and Sky Temperature as a Function of Time of Day, Cloudy Sky

Time of Day	Cold, Cloudy Conditions							
	Air Temperature		Sky Temperature		Direct Incident*		Diffuse	
Hour (LST)	°C	°F	°C	°F	W/m^2	BTU/hr/ft^2	W/m^2	BTU/hr/ft^2
00:00	13.7	56.6	13.7	56.6	0	0.0	0	0.0
01:00	13.6	56.5	13.6	56.5	0	0.0	0	0.0
02:00	13.6	56.5	13.6	56.5	0	0.0	0	0.0
03:00	13.6	56.5	13.6	56.5	0	0.0	0	0.0
04:00	13.5	56.3	13.5	56.3	0	0.0	0	0.0
05:00	13.5	56.3	13.5	56.3	0	0.0	2	0.5
06:00	13.5	56.3	13.5	56.3	0	0.0	16	4.9
07:00	13.7	56.7	13.7	56.7	0	0.0	58	18.2
08:00	13.8	56.8	13.8	56.8	0	0.0	115	36.5
09:00	14.4	57.9	14.4	57.9	0	0.0	167	52.9
10:00	14.5	58.2	14.5	58.2	0	0.0	168	53.3
11:00	14.6	58.3	14.6	58.3	0	0.0	203	64.3
12:00	14.7	58.4	14.7	58.4	0	0.0	187	59.3
13:00	14.6	58.3	14.6	58.3	0	0.0	177	56.2
14:00	14.7	58.5	14.7	58.5	0	0.0	156	49.6
15:00	14.5	58.1	14.5	58.1	0	0.0	130	41.2
16:00	14.2	57.6	14.2	57.6	13	4.1	75	23.9
17:00	14.1	57.4	14.1	57.4	0	0.0	22	7.1
18:00	14.1	57.4	14.1	57.4	0	0.0	1	0.2
19:00	14.1	57.3	14.1	57.3	0	0.0	0	0.0
20:00	14.0	57.3	14.0	57.3	0	0.0	0	0.0
21:00	13.9	57.0	13.9	57.0	0	0.0	0	0.0
22:00	13.9	57.0	13.9	57.0	0	0.0	0	0.0
23:00	13.7	56.6	13.7	56.6	0	0.0	0	0.0

* Direct Incident is to a plane normal to the sun vector.

Table 3.5.17-2. Hot Design Radiant Energy and Sky Temperature as a Function of Time of Day, Cloudy Sky

Time of Day	Hot, Cloudy Conditions							
	Air Temperature		Sky Temperature		Direct Incident*		Diffuse	
Hour (LST)	°C	°F	°C	°F	W/m^2	BTU/hr/ft^2	W/m^2	BTU/hr/ft^2
00:00	20.9	69.6	20.9	69.6	0	0.0	0	0.0
01:00	20.8	69.5	20.8	69.5	0	0.0	0	0.0
02:00	20.8	69.4	20.8	69.4	0	0.0	0	0.0
03:00	20.9	69.6	20.9	69.6	0	0.0	0	0.0
04:00	20.8	69.4	20.8	69.4	0	0.0	0	0.0
05:00	20.7	69.2	20.7	69.2	0	0.0	8	2.4
06:00	20.7	69.3	20.7	69.3	0	0.0	60	19.0
07:00	20.9	69.7	20.9	69.7	0	0.0	118	37.4
08:00	21.1	70.1	21.1	70.1	0	0.0	181	57.5
09:00	21.3	70.3	21.3	70.3	1	0.2	223	70.7
10:00	21.5	70.7	21.5	70.7	1	0.3	248	78.7
11:00	21.7	71.0	21.7	71.0	4	1.1	279	88.3
12:00	21.7	71.1	21.7	71.1	1	0.2	270	85.6
13:00	21.8	71.3	21.8	71.3	2	0.6	254	80.5
14:00	21.6	70.9	21.6	70.9	0	0.0	227	71.9
15:00	21.5	70.7	21.5	70.7	1	0.3	190	60.3
16:00	21.2	70.2	21.2	70.2	5	1.6	119	37.7
17:00	21.0	69.7	21.0	69.7	2	0.5	47	14.7
18:00	20.9	69.6	20.9	69.6	0	0.0	5	1.5
19:00	20.9	69.7	20.9	69.7	0	0.0	0	0.0
20:00	20.8	69.4	20.8	69.4	0	0.0	0	0.0
21:00	20.7	69.3	20.7	69.3	0	0.0	0	0.0
22:00	20.7	69.2	20.7	69.2	0	0.0	0	0.0
23:00	20.7	69.3	20.7	69.3	0	0.0	0	0.0

* Direct Incident is to a plane normal to the sun vector.

Table 3.5.17-3. Cold Design Radiant Energy and Sky Temperature as a Function of Time of Day, Partly Cloudy Sky

Time of Day	Cold, Partly Cloudy Conditions							
	Air Temperature		Sky Temperature		Direct Incident*		Diffuse	
Hour (LST)	°C	°F	°C	°F	W/m^2	BTU/hr/ft^2	W/m^2	BTU/hr/ft^2
00:00	9.4	48.9	2.1	35.7	0	0.0	0	0.0
01:00	8.9	48.0	-0.6	30.9	0	0.0	0	0.0
02:00	8.6	47.5	-0.4	31.2	0	0.0	0	0.0
03:00	8.3	46.9	-2.5	27.5	0	0.0	0	0.0
04:00	8.2	46.8	-2.7	27.1	0	0.0	0	0.0
05:00	7.9	46.2	-4.0	24.8	0	0.0	1	0.0
06:00	8.1	46.6	0.3	32.5	24	7.5	49	0.3
07:00	8.9	48.1	1.7	35.0	236	74.8	103	15.4
08:00	10.2	50.4	1.6	34.9	519	164.4	125	32.7
09:00	11.2	52.1	3.2	37.7	452	143.2	151	39.7
10:00	12.1	53.8	6.4	43.6	476	150.7	191	47.9
11:00	12.7	54.8	5.2	41.4	460	145.8	185	60.5
12:00	12.9	55.2	5.7	42.2	490	155.2	161	58.5
13:00	13.0	55.4	4.0	39.1	536	170.0	132	51.1
14:00	13.0	55.4	2.7	36.9	489	155.1	86	42.0
15:00	12.7	54.8	1.9	35.4	445	141.0	37	27.2
16:00	12.5	54.4	2.7	36.8	199	63.1	1	11.8
17:00	12.1	53.8	0.6	33.0	21	6.7	0	0.4
18:00	11.6	52.9	-0.2	31.6	0	0.0	0	0.0
19:00	11.2	52.1	-2.0	28.3	0	0.0	0	0.0
20:00	10.5	50.9	-2.8	27.0	0	0.0	0	0.0
21:00	10.0	50.0	-3.2	26.3	0	0.0	0	0.0
22:00	9.5	49.0	-4.2	24.5	0	0.0	0	0.0
23:00	9.0	48.3	-2.2	28.0	0	0.0	0	0.0

* Direct Incident is to a plane normal to the sun vector.

Table 3.5.17-4. Hot Design Radiant Energy and Sky Temperature as a Function of Time of Day, Partly Cloudy Sky

Time of Day	Hot, Partly Cloudy Conditions							
	Air Temperature		Sky Temperature		Direct Incident*		Diffuse	
Hour (LST)	°C	°F	°C	°F	W/m^2	BTU/hr/ft^2	W/m^2	BTU/hr/ft^2
00:00	22.4	72.3	14.8	58.7	0	0.0	0	0.0
01:00	22.3	72.1	13.9	57.1	0	0.0	0	0.0
02:00	22.2	71.9	16.1	61.0	0	0.0	0	0.0
03:00	22.0	71.6	16.9	62.4	0	0.0	0	0.0
04:00	22.0	71.5	16.4	61.6	0	0.1	0	0.0
05:00	21.9	71.5	17.4	63.3	31	9.7	13	4.1
06:00	22.6	72.7	17.7	63.8	265	84.0	97	30.7
07:00	24.4	75.8	16.1	60.9	533	169.0	134	42.6
08:00	25.8	78.4	17.3	63.2	676	214.3	157	49.8
09:00	27.1	80.7	18.1	64.5	723	229.2	171	54.2
10:00	27.8	82.0	20.0	68.0	735	233.0	206	65.2
11:00	28.4	83.1	20.5	69.0	769	243.6	195	61.9
12:00	28.2	82.7	20.1	68.1	809	256.5	174	55.0
13:00	28.4	83.2	21.4	70.5	711	225.3	202	64.1
14:00	28.2	82.7	21.2	70.1	645	204.3	202	64.0
15:00	27.8	82.0	21.0	69.7	504	159.9	180	57.1
16:00	27.0	80.6	21.3	70.4	439	139.1	126	39.9
17:00	25.7	78.2	19.2	66.6	142	45.0	75	23.8
18:00	24.8	76.7	18.7	65.7	45	14.2	4	1.3
19:00	24.7	76.5	16.9	62.5	0	0.0	0	0.0
20:00	24.6	76.2	15.9	60.6	0	0.0	0	0.0
21:00	23.7	74.6	13.2	55.8	0	0.0	0	0.0
22:00	23.7	74.6	15.7	60.3	0	0.0	0	0.0
23:00	23.3	74.0	17.4	63.3	0	0.0	0	0.0

* Direct Incident is to a plane normal to the sun vector.

Table 3.5.17-5. Cold Design Radiant Energy and Sky Temperature as a Function of Time of Day, Clear Sky

Time of Day	Cold, Clear Conditions							
	Air Temperature		Sky Temperature		Direct Incident*		Diffuse	
Hour (LST)	°C	°F	°C	°F	W/m^2	BTU/hr/ft^2	W/m^2	BTU/hr/ft^2
00:00	7.9	46.1	-14.2	6.5	0	0.0	0	0.0
01:00	7.0	44.6	-15.0	5.0	0	0.0	0	0.0
02:00	6.3	43.3	-15.7	3.8	0	0.0	0	0.0
03:00	6.1	42.9	-16.1	3.0	0	0.0	0	0.0
04:00	5.6	42.0	-16.7	2.0	0	0.0	0	0.0
05:00	5.1	41.3	-17.2	1.0	0	0.0	0	0.0
06:00	5.7	42.3	-17.1	1.3	59	18.8	3	0.8
07:00	7.3	45.1	-15.5	4.0	463	146.8	37	11.8
08:00	9.8	49.7	-12.9	8.8	724	229.4	61	19.2
09:00	11.7	53.0	-11.3	11.7	829	262.8	75	23.9
10:00	13.3	55.9	-10.0	14.1	875	277.4	88	27.9
11:00	14.3	57.7	-8.9	15.9	870	275.8	101	32.0
12:00	14.4	58.0	-8.4	16.9	868	275.2	99	31.3
13:00	14.5	58.1	-8.5	16.8	849	269.2	91	28.8
14:00	14.3	57.8	-8.5	16.8	780	247.2	73	23.1
15:00	13.9	57.1	-8.3	17.0	597	189.3	57	18.0
16:00	13.3	56.0	-8.5	16.8	267	84.6	16	5.1
17:00	12.5	54.6	-9.0	15.7	4	1.2	0	0.0
18:00	11.9	53.4	-9.9	14.2	0	0.0	0	0.0
19:00	11.1	51.9	-10.8	12.6	0	0.0	0	0.0
20:00	10.5	50.9	-11.5	11.3	0	0.0	0	0.0
21:00	9.5	49.1	-12.7	9.1	0	0.0	0	0.0
22:00	8.5	47.4	-13.7	7.3	0	0.0	0	0.0
23:00	8.0	46.5	-14.4	6.1	0	0.0	0	0.0

* Direct Incident is to a plane normal to the sun vector.

Table 3.5.17-6. Hot Design Radiant Energy and Sky Temperature as a Function of Time of Day, Clear Sky

Time of Day	Hot, Clear Conditions							
	Air Temperature		Sky Temperature		Direct Incident*		Diffuse	
Hour (LST)	°C	°F	°C	°F	W/m^2	BTU/hr/ft^2	W/m^2	BTU/hr/ft^2
00:00	19.7	67.4	1.4	34.5	0	0.0	0	0.0
01:00	19.1	66.3	0.8	33.5	0	0.0	0	0.0
02:00	18.7	65.6	0.2	32.3	0	0.0	0	0.0
03:00	18.3	65.0	-0.2	31.6	0	0.0	0	0.0
04:00	18.2	64.8	-0.9	30.4	0	0.0	0	0.0
05:00	18.2	64.7	-0.9	30.5	62	19.6	9	2.9
06:00	20.7	69.2	1.3	34.4	411	130.2	61	19.2
07:00	23.8	74.9	4.4	39.9	670	212.3	89	28.3
08:00	27.0	80.5	7.4	45.4	782	247.9	112	35.6
09:00	29.6	85.2	8.9	48.0	826	262.0	131	41.4
10:00	29.5	85.1	8.9	48.1	858	271.9	142	45.1
11:00	29.7	85.4	8.8	47.8	867	274.7	152	48.3
12:00	30.1	86.1	9.4	49.0	852	270.0	155	49.1
13:00	30.5	87.0	9.8	49.7	849	269.0	138	43.6
14:00	30.8	87.4	9.4	48.9	801	254.0	122	38.7
15:00	30.1	86.2	9.2	48.5	711	225.3	103	32.7
16:00	29.2	84.6	8.3	47.0	485	153.7	83	26.3
17:00	27.5	81.5	7.4	45.3	169	53.7	30	9.4
18:00	26.2	79.1	6.5	43.8	18	5.7	1	0.4
19:00	24.9	76.9	5.5	42.0	0	0.0	0	0.0
20:00	23.9	75.1	5.2	41.4	0	0.0	0	0.0
21:00	23.0	73.4	4.6	40.2	0	0.0	0	0.0
22:00	21.9	71.5	3.9	39.1	0	0.0	0	0.0
23:00	21.1	70.0	3.1	37.5	0	0.0	0	0.0

* Direct Incident is to a plane normal to the sun vector.

Technical Notes

Design limits are developed from the National Solar Radiation Database (http://rredc.nrel.gov/solar/old_data/nsrdb/1991-2010/) for San Diego, CA (Lindbergh Field). Cold and hot diurnal profiles are the average of the 10 coldest and warmest days for the given sky conditions (cloudy, partly cloudy, and clear). Since surface air temperature, direct incident radiant energy, diffuse radiant energy, and sky temperature are coupled and depend on sky

conditions, it is recommended that each case be used as input into thermal models to determine the worst case.

Direct incident is the solar radiant energy to a plane normal to the sun vector. The actual radiant energy absorbed by a surface would be a function of the surface optical properties and the surface geometry relative to the Sun vector. Diffuse radiant energy represents the accumulation on a horizontal surface of the scattered solar radiant energy from all directions, not including the direct incident. Sky temperature represents the temperature of the sky assuming it is radiating as a blackbody.

3.5.18 Sea State for Normal Water Landing

Description

This section specifies the design maximum and minimum wave conditions for nominal water landings. Wave height and wind speed limits were determined through examining conditions near the coast of Southern California. Wave period limits, which are conditional to wave height, were determined by examining data across the globe.

Design Limits

Minimum: Significant Wave Height (SWH): No waves.

Maximum: SWH: 2.0 m (6.6 ft)

Minimum average wave periods associated with the design maximum SWH are displayed in Table 3.5.18-1. The energy spectrum associated with the design maximum SWH is provided in Table 3.5.18-2. The energy spectrum may be truncated on the high frequency end to limit the calculated water surface slope to the dimensions of interest to the engineering application. The limit of the high frequency end of the energy spectrum can be determined using the following equation:

$$f_{max} = \sqrt{\frac{g}{2 \cdot \pi \cdot \left(\frac{L}{2}\right)}}$$

where f_{max} is the maximum frequency (Hz), g is gravity (m/s^2), and L is the smallest wavelength (m) of interest for the engineering application. The energy spectrum is used to derive water surface slope distributions using the following equations:

$$I^* = \sum_{i=1}^{n} \left\{ \left(\frac{\mu_i^2}{g} \right)^2 \cdot [A_i(\mu_i)]^2 \cdot \Delta\mu_i \right\}$$

where I^* is the omnidirectional slope variance, g is gravity, n represents the total number of frequency bins, and $[A_i(\mu_i)]^2$ and $\Delta\mu_i$ are the energy spectrum (m^2/Hz) and bandwidth (Hz), respectively, associated with the i^{-th} frequency bin.

The directional components of slope variance are determined by multiplying slope variance by the constants $f(\theta) = 0.625$ and $g(\theta) = 0.375$ (Cote et al., 1960), which are representative values of how the slope variance is divided into its directional components:

$$\sigma_{ud}^2 = I^* \cdot f(\theta)$$

$$\sigma_c^2 = I^* \cdot g(\theta)$$

where σ_{ud}^2 is the upwind-downwind slope variance component and σ_c^2 is the crosswind slope variance component. Each directional slope standard deviation component is used to run a 10,000 case (typical) Monte Carlo Simulation assuming a Gaussian distribution where r_{ud} and r_c are zero-mean, unit variance Gaussian random variables. The directional water surface slope components are determined using the following equations:

$$\mu_{ud} = arctan(\sigma_{ud} \cdot r_{ud})$$

$$\mu_c = arctan(\sigma_c \cdot r_c)$$

where μ_{ud} is the upwind-downwind water surface slope component (rad), and μ_c is the crosswind water surface slope component (rad). Each pair of directional water surface slope component values is applied to the following equation to create a water surface slope distribution:

$$\mu = arctan\left(\sqrt{tan^2\mu_{ud} + tan^2\mu_c}\right) \cdot \frac{180}{\pi}$$

where μ is the total water surface slope (degrees).

Minimum Winds: Calm, no winds.

Maximum Winds: 8.2 m/s (26.9 ft/s) steady-state wind speed at 10.0 m (32.8 ft) height above surface as referenced in Section 3.5.8, Surface Winds for Normal Landing.

Sea state characteristics and probability of occurrence: Defined by the Corrected-European Centre for Medium Range Weather Forecasts Re-Analysis (C-ERA40) database (Caires and Sterl, 2005).

Model Inputs

Table 3.5.18-1. Minimum Average Wave Period Corresponding to Given SWH

Significant Wave Height (m)	Minimum Average Wave Period(s)
0-0.5	2
0.5-1.0	2
1.0-1.5	3
1.5-2.0	4
2.0-2.5	4
2.5-3.0	5
3.0-3.5	5
3.5-4.0	5
4.0-4.5	6
4.5-5.0	6
5.0-5.5	6
5.5-6.0	7
6.0-6.5	7
6.5-7.0	7
≥ 7.0	8

The energy spectrum is listed in Table 3.5.18-2 and is used to derive water surface slope.

Table 3.5.18-2. Energy Spectrum for 2 m SWH

Frequency (Hz)	Energy (m^2/Hz)	Bandwidth (Hz)
0.025	0.00330	0.005
0.030	0.00690	0.005
0.035	0.01210	0.005
0.040	0.01130	0.005
0.045	0.02890	0.005
0.050	0.09460	0.005
0.055	0.14620	0.005
0.060	0.12900	0.005
0.065	0.20230	0.005
0.070	0.38370	0.005
0.075	0.34550	0.005
0.080	0.38370	0.005
0.085	0.42840	0.005

Frequency (Hz)	Energy (m^2/Hz)	Bandwidth (Hz)
0.090	0.61400	0.005
0.095	0.37990	0.005
0.1013	0.26110	0.0075
0.110	0.09610	0.01
0.120	0.10510	0.01
0.130	0.16900	0.01
0.140	0.45480	0.01
0.150	0.94380	0.01
0.160	1.06420	0.01
0.170	1.13560	0.01
0.180	1.35960	0.01
0.190	1.20590	0.01
0.200	0.94380	0.01
0.210	1.10760	0.01
0.220	0.59290	0.01
0.230	0.56390	0.01
0.240	0.73140	0.01
0.250	0.74990	0.01
0.260	0.46400	0.01
0.270	0.42410	0.01
0.280	0.41990	0.01
0.290	0.36680	0.01
0.300	0.44580	0.01
0.310	0.16000	0.01
0.320	0.20640	0.01
0.330	0.24840	0.01
0.340	0.11790	0.01
0.350	0.13290	0.01
0.360	0.16240	0.01
0.370	0.09850	0.01
0.380	0.10100	0.01
0.390	0.13500	0.01
0.400	0.13100	0.01
0.410	0.12270	0.01
0.420	0.07370	0.01
0.430	0.08690	0.01
0.440	0.07150	0.01

Frequency (Hz)	Energy (m^2/Hz)	Bandwidth (Hz)
0.450	0.08650	0.01
0.460	0.05830	0.01
0.470	0.04770	0.01
0.480	0.04890	0.01
0.490	0.05170	0.01
0.500	0.05430	0.01
0.510	0.03790	0.01
0.520	0.02980	0.01
0.530	0.03430	0.01
0.540	0.03250	0.01
0.550	0.01980	0.01
0.560	0.01830	0.01
0.570	0.02590	0.01
0.580	0.02030	0.01
0.590	0.01829	0.01
0.600	0.01670	0.01
0.610	0.01524	0.01
0.620	0.01392	0.01
0.630	0.01270	0.01
0.640	0.01160	0.01
0.650	0.01058	0.01
0.660	0.00966	0.01
0.670	0.00882	0.01
0.680	0.00805	0.01
0.690	0.00735	0.01
0.700	0.00671	0.01
0.710	0.00612	0.01
0.720	0.00559	0.01
0.730	0.00510	0.01
0.740	0.00466	0.01
0.750	0.00425	0.01
0.760	0.00388	0.01
0.770	0.00354	0.01
0.780	0.00323	0.01
0.790	0.00295	0.01
0.800	0.00270	0.01

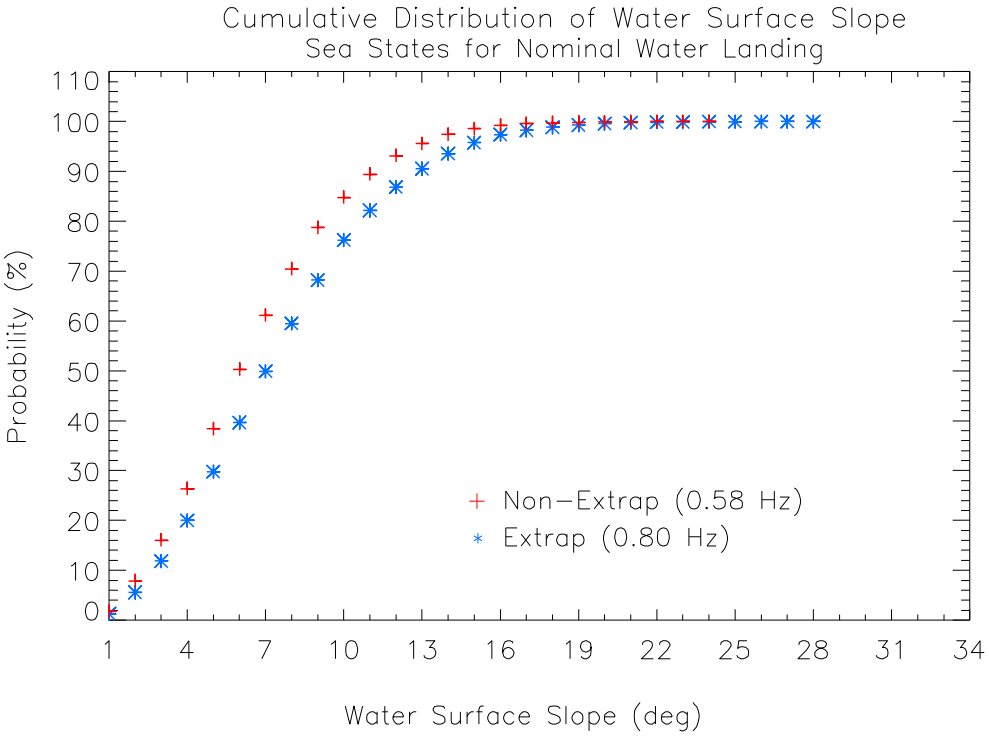

Figure 3.5.18-1. Cumulative Distributions of Water Surface Slope for 2 m SWH

Limitations

None

Technical Notes

Wave observations follow a Rayleigh distribution (Demirbilek and Vincent, 2002). An estimation of various wave heights may be determined from this distribution, where SWH corresponds to the average of the highest one-third of waves, and maximum wave height depends on the number of observed waves and the SWH.

The average wave period is defined as the average of the wave periods over the last 20 minutes of the 6-hour observation reported by the C-ERA-40 database. The minimum average wave period is the lowest average wave period associated with the specified SWH range. The C-ERA-40 database is used to determine the number of SWH observations that fall within the given SWH ranges in Table 3.5.18-1, where the first height is included in the SWH range but the second height is not included. The minimum average wave periods in Table 3.5.18-1 are identified by determining which 1-second wave period range contains the 1st percentile of wave periods observed for the given SWH range. If the 1st percentile falls between two values within the wave period range, the lower of the two wave period values is used to be conservative.

The C-ERA40 database is developed from the ECMWF atmospheric re-analysis for the POR (1957-2002) with emphasis on the POR (1971-2000). Data reported in the C-ERA-40 database is

provided every 6 hours on a 1.5º latitude x 1.5º longitude grid. Note that, although the term "C-ERA-40" refers to the SWH, wind speed, and wave period databases in this document, SWH is the only variable that was corrected.

A water surface slope distribution derived from the full energy spectrum is illustrated in Figure 3.5.18-1 with and without the energy extrapolated from 0.58 to 0.8 Hz. Both distributions represent the extreme case of 5,422 energy spectra. The x-axis represents water surface slopes that are less than the value of the x-tick.

The energy spectrum in Table 3.5.18-2 is developed using 5.0 m (16.4 ft) wind speed data from buoys 46047 and 46069, near San Nicolas Island, CA, in the NDBC network and spectral data from buoy 067, near San Nicolas Island, CA, in the Coastal Data Information Program (CDIP) buoy network. The spectral data ranges from 0.025 to 0.58 Hz and is reported every half hour, along with the corresponding SWH. This archived buoy data, when compared with the National Data Buoy Center (NDBC) spectral data, provides spectral data at higher frequencies in the area of interest. The spectral data is used from August over a 9-year POR (1999-2007) and is limited to SWH ≤ 2.0 m (6.6 ft) and wind speed ≤ 8.2 m/s (26.9 ft/s). The energy spectrum in Table 3.5.18-2 represents a single spectrum from August 23, 2001, at 03:49 Universal Time Coordinated (UTC) and is created using: (1) the energy in each frequency bin from 0.025 to 0.58 Hz, and (2) energy that is extrapolated from 0.58 to 0.80 Hz with an exponential curve ($y = 3.9708 \cdot \exp{-9.1189x}$) that is fit to the energy found in each frequency bin from 0.30 to 0.58 Hz. Here x is the desired frequency (Hz) and y is the resulting energy (m^2/Hz).

The spectrum was selected based on the distributions seen in Figure 3.5.18-1 where the spectrum not only covers the higher probabilities of steeper water surface slopes, but it also covers the water surface slopes seen at higher frequencies when the energy spectrum is extrapolated.

3.5.19 Reserved

3.5.20 Sea Surface Temperature for Water Landing

Description

This section specifies the design maximum and minimum sea surface temperatures for normal water landings. The zone for water landing is assumed to be contained by oceanic regions within a 685.0 km (370.0 nmi) radius of San Diego, California.

Design Limits

Maximum: 25.4 °C (77.7 °F)

Minimum: 10.3 °C (50.5 °F)

Model Inputs

None

Limitations

None

Technical Notes

Design limits for normal water landings were determined using weekly mean sea surface temperature output within the normal landing area from a global climatology. Sea surface temperatures were obtained from the National Centers for Environmental Prediction Optimal Interpolation (NCEP-OI) dataset, which contains weekly mean sea surface temperature records on a1.0° latitude x 1.0° longitude grid for the 1981-2012 period of record. The global dataset was subsetted to only contain temperatures within the normal water landing area. Design limits were determined by comparing the minimum and maximum recorded temperatures to the 0.5^{th} and 99.5^{th} percentile temperatures with 95.0% confidence intervals applied for each month (Barbré, 2012). Minimum and maximum design limits are the 0.5^{th} and 99.5^{th} percentile temperatures with 95.0% confidence during March and September, respectively.

3.5.21 Aerosols for Water Landing

Description

This section specifies the aerosol environment for both normal and off-nominal water vehicle descent and water landing operations.

Design Limits

The vehicle will encounter sea salt spray if landing is in the sea.

Model Inputs

None

Limitations

The vehicle may encounter volcanic dust, but this is not considered a design case.

Technical Notes

Additional information is available in NASA/TM-2008-215633, Terrestrial Environment (Climatic) Criteria Handbook for use in Aerospace Vehicle Development Environment, Section 10.

3.6 Contingency and Off-Nominal Landing Phases

This section describes the design environments for contingency (including aborts) and other off-nominal landing conditions. Typically these are along the ascent or landing trajectories where such events are most likely to occur. Where possible the same models and specifications as for normal landing operations have been applied, and the specification is simply a reference to the corresponding normal landing section.

3.6.1 Re-entry Neutral Atmosphere for Off-Nominal Descent and Landing

Same as Section 3.5.1. Apply the model to the location of interest.

3.6.2 Reserved

3.6.3 Lightning During Off-Nominal Landing

Same as Section 3.5.3.

3.6.4 Aloft Winds for Off-Nominal Descent and Landing

Same as Section 3.5.4. Apply the model to the location of interest. In the event of on-pad or near pad abort scenarios, the KSC Measured Wind Database or Earth-GRAM 2010 can be used to evaluate abort performance. All other off-nominal descent and landing scenarios should use Earth-GRAM 2010.

3.6.5 Aloft Air Temperature for Off-Nominal Descent and Landing

Same as Section 3.5.5. Apply Earth-GRAM 2010 to the location of interest.

3.6.6 Aloft Air Pressure for Off-Nominal Descent and Landing

Same as Section 3.5.6. Apply Earth-GRAM 2010 to the location of interest.

3.6.7 Aloft Air Density for Off-Nominal Descent and Landing

Same as Section 3.5.7. Apply Earth-GRAM 2010 to the location of interest.

3.6.8 Surface Winds for Off-Nominal Landing

Design Limits

Same as Section 3.5.8 with the model inputs as specified here.

Model Input:

Minimum surface wind for all off-nominal cases is calm conditions, i.e. no wind.

Maximum off–nominal land landing surface winds are not defined.

For off-nominal water landings, the maximum 10.0 m (32.8 ft) height steady state design wind is 13.9 m/s (45.6 ft/s). This value is associated with the sea state conditions defined in Section 3.6.18, Sea State for Off-Nominal Water Landing. The peak wind value of 19.5 m/s (63.8 ft/s) was determined by multiplying the maximum steady state wind by the 1.4 gust factor given in Section 3.5.8, Surface Winds for Normal Landing.

3.6.9 Surface Air Temperature for Off-Nominal Landing

Description

This section specifies the design maximum and minimum surface air temperature for off-nominal vehicle water landing environments. Currently, no off-nominal land landing zones have been defined by the Program. Zones for off-nominal water landings include the normal water landing

zone described in 3.5.9, Surface Air Temperature for Normal Landing, as well as different skip entry trajectories covering the eastern Pacific Ocean and a 29° inclination orbit from KSC to the western coast of Australia.

Design Limits

Maximum: 32.2 °C (90.0 °F)

Minimum: 3.0 °C (37.4 °F)

Model Inputs

None

Limitations

For any required thermal assessment involving wind effects over water, the winds must be assumed to be steady state at 10.0 m (32.8 ft) height with horizontal speeds ranging from 0.0 to 13.9 m/s (45.6 ft/s). This value is associated with the sea state conditions defined in Section 3.6.18, Sea State for Off-Nominal Water Landing. The peak wind value of 19.5 m/s (63.8 ft/s) was determined by multiplying the maximum steady state wind by the 1.4 gust factor given in Section 3.5.8, Surface Winds for Normal Landing.

Technical Notes

Design limits for off-nominal water landings were determined using six-hourly air temperature output within the water landing areas corresponding to 23 different skip entry trajectories provided by the Orion Program, as well as the area immediately surrounding a 29.0° inclination orbit extending over water regions from KSC to the western coast of Australia. Air temperatures were obtained from the ERA-40 dataset, which contains air temperature records on a 2.5° x 2.5° grid every six hours for the 1979-2002 period of record. The global dataset was subsetted to only contain temperatures within the off-nominal landing area. Design limits were determined by comparing the minimum and maximum recorded air temperatures to the 0.5^{th} and 99.5^{th} percentile temperatures with 95.0% confidence intervals applied for each month (Barbré, 2012). Design limits are the empirical minimum and maximum air temperatures during March and April, respectively.

3.6.10 Surface Air Pressure for Off-Nominal Landing

Reserved.

3.6.11 Surface Air Humidity for Off-Nominal Landing

Same as Section 3.5.11.

3.6.12 Aerosols for Off-Nominal Descent and Landing

Same as Section 3.5.12.

3.6.13 Precipitation for Off-Nominal Descent and Landing

Same as Section 3.5.13.

3.6.14 Flora and Fauna for Off-Nominal Descent and Landing

Reserved.

3.6.15 Surface Characteristics and Topography for Off-Nominal Descent and Landing

Reserved.

3.6.16 Cloud Environment for Off-Nominal Descent and Landing

Same as Section 3.5.16.

3.6.17 Radiant (Thermal) Energy Environment for Off-Nominal Descent and Landing

Reserved.

3.6.18 Sea State for Off-Nominal Water Landing

Description

This section specifies the design maximum and minimum wave conditions for off-nominal water landings. Wave height and wind speed limits were determined through examining conditions near the coast of Southern California and in the Atlantic Ocean. Wave period limits, which are conditional to wave height, were determined by examining data across the globe.

For pad and near-pad aborts, a capsule could land in water shallow enough such that the capsule contacts the ocean floor, which could enhance the likelihood of increased damage to the vehicle and injury to any crew onboard. Therefore, engineering assessments of capsule landings within coastal water regions must characterize the probability of the capsule contacting the ocean floor, which is partially a function of the ocean floor's depth. The area of ocean from the shoreline out to approximately 10-m water depth is the area most influenced by natural and man-made phenomena. Along the KSC coast, tides, breaking waves, and influences from storms such as hurricanes and Nor' Easters induce natural erosion. Additionally, man-made influences such as shoreline restoration efforts and near-coast construction impact the ocean's bathymetry. These influences cause the water depth at a given location to change over time. Tidal variations of roughly 1 m apply throughout the KSC/CCAFS near-shore environment. Sandbars can cause variations of roughly 1-2 m, and can change location. Shoals, which are associated with capes and other shallow areas, can also cause changes of near 2-6 m over longer time periods.

Design Limits

Minimum: Significant Wave Height (SWH): No waves.

Maximum: SWH: 4.0 m (13.1 ft)

Minimum average wave periods associated with the design maximum SWH are displayed in Table 3.5.18-1 in Section 3.5.18, Sea State for Nominal Water Landing.

The energy spectrum associated with the design maximum SWH is provided in Table 3.6.18-1. The energy spectrum may be truncated on the high frequency end to limit the calculated water surface slope to the dimensions of interest to the engineering application. The limit of the high frequency end of the energy spectrum can be determined using the following equation:

$$f_{max} = \sqrt{\frac{g}{2 \cdot \pi \cdot \left(\frac{L}{2}\right)}}$$

where f_{max} is the maximum frequency (Hz), g is gravity (m/s^2), and L is the smallest wavelength (m) of interest for the engineering application. The energy spectrum is used to derive water surface slope distributions using the following equations:

$$I^* = \sum_{i=1}^{n} \left\{ \left(\frac{\mu_i^2}{g} \right)^2 \cdot [A_i(\mu_i)]^2 \cdot \Delta\mu_i \right\}$$

where I^* is the omnidirectional slope variance, g is gravity, n represents the total number of frequency bins, and $[A_i(\mu_i)]^2$ and $\Delta\mu_i$ are the energy spectrum (m^2/Hz) and bandwidth (Hz), respectively, associated with the i^{-th} frequency bin.

The directional components of slope variance are determined by multiplying slope variance by the constants $f(\theta) = 0.625$ and $g(\theta) = 0.375$ (Cote et al., 1960), which are representative values of how the slope variance is divided into its directional components:

$$\sigma_{ud}^2 = I^* \cdot f(\theta)$$

$$\sigma_c^2 = I^* \cdot g(\theta)$$

where σ_{ud}^2 is the upwind-downwind slope variance component and σ_c^2 is the crosswind slope variance component. Each directional slope standard deviation component is used to run a 10,000 case (typical) Monte Carlo Simulation assuming a Gaussian distribution where r_{ud} and r_c are zero-mean, unit variance Gaussian random variables. The directional water surface slope components are determined using the following equations:

$$\mu_{ud} = arctan(\sigma_{ud} \cdot r_{ud})$$

$$\mu_c = arctan(\sigma_c \cdot r_c)$$

where μ_{ud} is the upwind-downwind water surface slope component (rad), μ_c is the crosswind water surface slope component (rad). Each pair of directional water surface slope component values is applied to the following equation to create a water surface slope distribution:

$$\mu = arctan\left(\sqrt{tan^2\mu_{ud} + tan^2\mu_c}\right) \cdot \frac{180}{\pi}$$

where μ is the total water surface slope (degrees).

Minimum Winds: Calm, no winds.

Maximum Winds: 13.9 m/s (45.6 ft/s) steady state wind speed at 10.0 m (32.8 ft) height above surface as referenced in Section 3.6.8, Surface Winds for Off-Nominal Landing.

Sea state characteristics and probability of occurrence: Defined by the C-ERA-40 database (Caires and Sterl, 2005).

Water depth for pad and near-pad abort landings off the KSC coast: Defined by a model to be assimilated into abort analyses. See Technical Notes.

Model Inputs

The energy spectrum is listed in Table 3.6.18-1 and is used to derive water surface slope.

Table 3.6.18-1. Energy Spectrum for 4 m SWH

Frequency (Hz)	Energy (m^2/Hz)	Bandwidth (Hz)
0.025	0.03530	0.005
0.030	0.04770	0.005
0.035	0.14190	0.005
0.040	0.16080	0.005
0.045	0.81240	0.005
0.050	4.93920	0.005
0.055	5.91320	0.005
0.060	2.06930	0.005
0.065	0.34900	0.005
0.070	0.83290	0.005
0.075	1.31280	0.005
0.080	2.24160	0.005
0.085	3.04100	0.005
0.090	2.06930	0.005
0.095	3.75160	0.005
0.1013	4.65150	0.0075

Frequency (Hz)	Energy (m^2/Hz)	Bandwidth (Hz)
0.110	7.86320	0.01
0.120	10.14720	0.01
0.130	7.07940	0.01
0.140	7.36830	0.01
0.150	6.43780	0.01
0.160	4.93920	0.01
0.170	3.13360	0.01
0.180	2.90720	0.01
0.190	2.10050	0.01
0.200	1.97820	0.01
0.210	1.66060	0.01
0.220	1.31280	0.01
0.230	1.08570	0.01
0.240	0.99220	0.01
0.250	0.56390	0.01
0.260	0.44810	0.01
0.270	0.59580	0.01
0.280	0.56680	0.01
0.290	0.26370	0.01
0.300	0.40140	0.01
0.310	0.28430	0.01
0.320	0.15520	0.01
0.330	0.16480	0.01
0.340	0.21920	0.01
0.350	0.17160	0.01
0.360	0.19340	0.01
0.370	0.12270	0.01
0.380	0.13360	0.01
0.390	0.09510	0.01
0.400	0.10460	0.01
0.410	0.09510	0.01
0.420	0.08560	0.01
0.430	0.09850	0.01
0.440	0.06700	0.01
0.450	0.06410	0.01
0.460	0.03980	0.01
0.470	0.03410	0.01

Frequency (Hz)	Energy (m^2/Hz)	Bandwidth (Hz)
0.480	0.05460	0.01
0.490	0.05250	0.01
0.500	0.05010	0.01
0.510	0.03750	0.01
0.520	0.04680	0.01
0.530	0.03640	0.01
0.540	0.03130	0.01
0.550	0.02420	0.01
0.560	0.02770	0.01
0.570	0.02250	0.01
0.580	0.02400	0.01
0.590	0.01906	0.01
0.600	0.01741	0.01
0.610	0.01591	0.01
0.620	0.01453	0.01
0.630	0.01327	0.01
0.640	0.01212	0.01
0.650	0.01107	0.01
0.660	0.01012	0.01
0.670	0.00924	0.01
0.680	0.00844	0.01
0.690	0.00771	0.01
0.700	0.00704	0.01
0.710	0.00643	0.01
0.720	0.00588	0.01
0.730	0.00537	0.01
0.740	0.00490	0.01
0.750	0.00448	0.01
0.760	0.00409	0.01
0.770	0.00374	0.01
0.780	0.00341	0.01
0.790	0.00312	0.01
0.800	0.00285	0.01

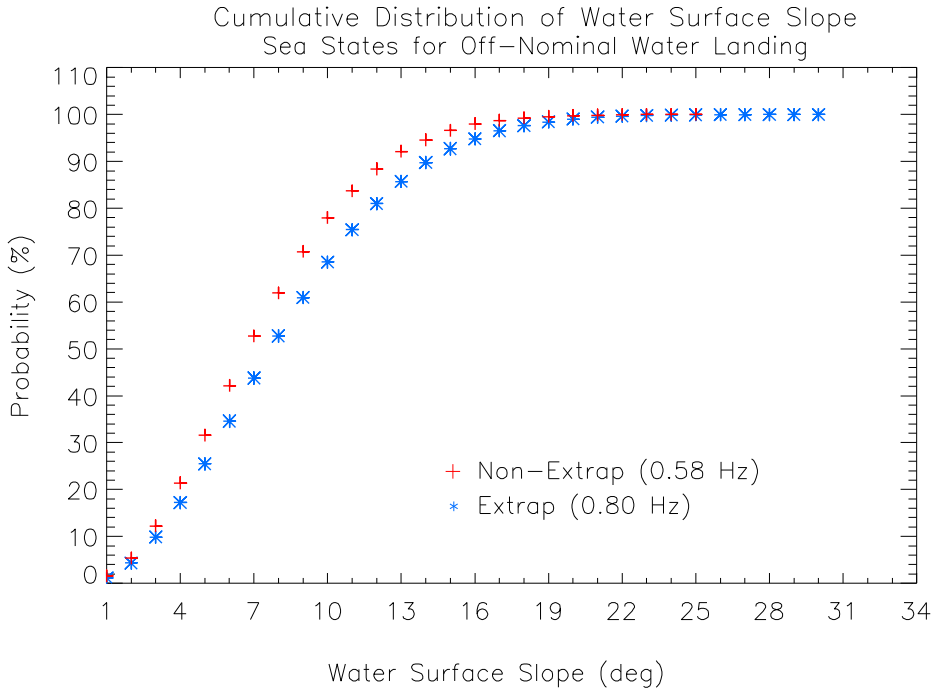

Figure 3.6.18-1. Cumulative Distributions of Water Surface Slope for 4 m SWH

Limitations

None

Technical Notes

See Section 3.5.18 on Sea State for Nominal Water Landing for on the definition of SWH and maximum wave height, the process for determining the minimum average wave period associated with the SWH, and the C-ERA-40 database, which is used to define sea state characteristics and probability of occurrence. Data reported in the C-ERA-40 database is provided every 6 hours on a 1.5º latitude x 1.5º longitude grid. Note that, although the term "C-ERA-40" refers to the SWH, wind speed, and wave period databases in this document, SWH is the only variable that was corrected.

A water surface slope distribution derived from the full energy spectrum is illustrated in Figure 3.6.18-1 with and without the energy extrapolated from 0.58 to 0.8 Hz. Both distributions represent the extreme case of 5,934 energy spectra. The x-axis represents water surface slopes that are less than the value of the x-tick.

The energy spectrum in Table 3.6.18-1 is developed using 5-meter wind speed data from buoys 46047 and 46069, near San Nicolas Island, CA, in the NDBC network and spectral data from buoy 067, near San Nicolas Island, CA, in the CDIP buoy network. The spectral data ranges from 0.025 to 0.58 Hz and is reported every half hour, along with the corresponding SWH. This

archived buoy data, when compared with the NDBC spectral data, provides spectral data at higher frequencies in the area of interest. The spectral data is used from March over a 6-yr POR (2000-2005) and is limited to SWH ≤ 4.0 m (13.1 ft) and wind speed ≤ 13.9 m/s (45.6 ft/s).

The energy spectrum in Table 3.6.18-1 represents a single spectrum from March 29, 2001, at 00:13 UTC and is created using: (1) the energy in each frequency bin from 0.025 to 0.58 Hz and (2) energy that is extrapolated from 0.58 to 0.80 Hz with an exponential curve ($y = 3.9773 \cdot \exp^{-9.052x}$) that is fit to the energy found in each frequency bin from 0.30 to 0.58 Hz. Here x is the desired frequency (Hz) and y is the resulting energy (m^2/Hz).

The spectrum was selected based on the distributions seen in Figure 3.6.18-1, where the selected spectrum not only covers the higher probabilities of steeper water surface slopes, but it also covers the water surface slopes seen at higher frequencies when the energy spectrum is extrapolated.

A water depth model used for capsule landing analyses off the coast of KSC was developed by the United States Geological Survey (USGS) using an extension of a study performed for the United States Air Force (USAF) (Thomson et al., 2015). First, sonar and lidar-based measurements dating from 1956, 2010, and 2014 were interpolated to a constant grid within a specified domain. The interpolation grid points were spaced nominally 50 m apart in the cross-shore direction and 250 m apart in the alongshore direction using a curvilinear grid that followed the contour of the shoreline. Next, the depth at each gridpoint was computed as a weighted mean between these datasets, with newer datasets being assigned a greater weight. In addition, uncertainties were calculated in Thomson et al. (2015) representing instrument uncertainties, variations over time and the short spatial scales that were filtered by the interpolation. For application to capsule landings, tidal influences on instantaneous water depth were added in a similar fashion and the root-sum-square (RSS) of all of the uncertainties were computed. This RSS parameter is used as the standard deviation of the water depth at a given gridpoint. The resulting model thus contains parameters representing the mean and standard deviation of water depths at each gridpoint within the model's domain, which specifically applies to launches from the KSC Launch Complexes.

For a given abort simulation, a water depth is randomly selected, assuming depths are Gaussian distributed, from the mean and standard deviation of the depth's distribution statistics at the closest gridpoint to the abort location.

3.6.19 Reserved

3.6.20 Sea Surface Temperature for Off-Nominal Water Landing

Description

This section specifies the design maximum and minimum sea surface temperatures for off-nominal water landings as defined in Section 3.6.9, Surface Air Temperature for Off-Nominal Landing.

Design Limits

Maximum: 32.0 °C (89.6 °F)

Minimum: 10.4 °C (50.7 °F)

Model Inputs

None

Limitations

None

Technical Notes

Design limits for off-nominal water landings were determined using weekly mean sea surface temperature output within the water landing areas corresponding to 23 different skip entry trajectories provided by the Orion Program, as well as the area immediately surrounding a 29.0° inclination orbit extending over water regions from KSC to the western coast of Australia. Sea surface temperatures were obtained from the NCEP-OI dataset, which contains weekly mean sea surface temperature records on a 1.0° latitude x 1.0° longitude grid for the 1981-2012 period of record. The global dataset was subsetted to only contain temperatures within the off-nominal water landing area. Design limits were determined by comparing the minimum and maximum recorded sea surface temperatures to the 0.5^{th} and 99.5^{th} percentile temperatures with 95.0% confidence intervals applied for each month (Barbré, 2012). Minimum and maximum design limits are the 0.5^{th} and 99.5^{th} percentile temperatures with 95.0% confidence during April and January, respectively.

3.7 Recovery and Post-Flight Processing Phases

This section describes the environments hardware and personnel will be exposed to during post-flight and recovery operations near KSC and in the normal landing sites located in the western U.S.

3.7.1 Environments for Post-Flight and Recovery at KSC

Except for the sea state specification in Section 3.7.2, Sea State for KSC Post-Flight and Recovery, specifications for post-flight and recovery operations at KSC are provided in Section 3.1, Prelaunch-Ground Processing Phases.

3.7.2 Sea State for KSC Post-Flight and Recovery

Reserved.

3.7.3 Lightning Specification for Post-Flight and Recovery

Description

Design specifications include standardized voltage and current waveforms derived or characterized to represent the lightning environment at specific zones established on the vehicle.

Design Limits

The environment in the normal landing area is such that systems will be exposed to the direct and indirect effects of lightning. Descriptions and conditions for the application of lightning environment waveforms are detailed in SAE ARP5414, and must be defined and evaluated for each applicable vehicle configuration. SAE ARP5412, Aircraft Lightning Environment and Related Test Waveforms is an applicable document. Ground support elements may have less stringent requirements to be specified at a later date.

Model Inputs

Vehicle lightning strike zones are defined for the integrated vehicle in re-entry and landing configurations, including with and without parachutes deployed, while descending through the atmosphere or residing on land or water after landing.

Limitations

Waveforms used for analysis are selected based on vehicle attachment profile and electromagnetic regions.

The most important characteristics of the standard lightning waveforms used for analysis and test are the peak current, continuing current, peak rate of rise, and the action integral, or coulomb content, of the waveform. Secondary characteristics of significance are the time to peak, and the time to fall to 50% of the peak. Peak current and continuing current levels are important for direct attachment assessment. The action integral is the amount of energy contained in the flash event, and is most important for determination of damage related to direct attachment effects. Rise and fall times are important for indirect effects assessment and analysis.

Technical Notes

None

3.7.4 Surface Winds for Post-Flight and Recovery

The ground wind environment specified in Section 3.5.8, Surface Winds for Normal Landing, is applicable to post-flight and recovery phase operations conducted in the normal landing area.

3.7.5 Surface Air Temperature for Post-Flight and Recovery

The surface air temperature limits specified in Section 3.5.9, Surface Air Temperature for Normal Landing, are applicable to post-flight and recovery phase operations in the normal landing area.

3.7.6 Surface Air Pressure for Post-Flight and Recovery

The surface air pressure limits applicable to post-flight and recovery phase operations in the normal landing area are specified in Section 3.5.10, Surface Air Pressure for Normal Landing.

3.7.7 Surface Air Humidity for Post-Flight and Recovery

The surface air humidity conditions applicable to post-flight and recovery phase operations in the normal landing area are specified in Section 3.5.11, Surface Air Humidity for Normal Landing.

3.7.8 Aerosol Environment for Post-Flight and Recovery

The aerosol environment for the normal landing area is specified in Section 3.5.12, Aerosols for Normal Descent and Landing.

3.7.9 Precipitation Environment for Post-Flight and Recovery

The precipitation environment for the normal landing area is specified in Section 3.5.13, Precipitation for Normal Descent and Landing.

3.7.10 Flora and Fauna Environment for Post-Flight and Recovery

The flora and fauna environment for the normal landing area is specified in Section 3.5.14, Flora and Fauna for Descent and Landing.

3.7.11 Surface Characteristics and Topography for Post-Flt and Recovery

Design specifications for the surface characteristics and topography of the normal landing area are specified in Section 3.5.15, Surface Characteristics and Topography for Normal Landing.

3.7.12 Cloud Environment for Post-Flight and Recovery

The cloud and fog environment in the normal landing area is specified in Section 3.5.16, Cloud and Environment for Normal Descent and Landing.

3.7.13 Radiant (Thermal) Energy Environment for Post-Flt and Recovery

The radiant energy environment in the normal landing area is specified in Section 3.5.17, Radiant (Thermal) Energy Environment for Normal Landing.

3.8 Interplanetary Space Specification

Reserved.

3.9 Mars Orbit Specification

Reserved.

3.10 Mars Atmosphere and Surface Phase Specification

Reserved.

3.11 Mars Moon Specification

Reserved.

3.12 Near Earth Asteroid Specification

Reserved.

4.0 COMPLIANCE ASSESMENT OF NATURAL ENVIRONMENTS

It is recommended that compliance assessments be developed by each integrated Program and its elements for the applicable natural environments specifications in this document. Compliance for each applicable natural environment can be met by demonstrating a robust design to the specified environment, utilizing operational mitigation strategies to reduce exposure to the natural environment, or choosing to accept the risk of exposure to all or a portion of the environment. In the latter case, each Program should acknowledge that they accept any adverse situations that may occur from exposure to the full environment.

Programs will coordinate any compliance assessments that affect other programs through the Cross-Program NEIAHT. The program representative will also keep the NEIAHT informed of internal program assessments as a courtesy.

5.0 REFERENCES

The following documents and reference materials contain supplemental information to guide the user in the application of this document.

Barbré, R.E., "Analysis of DSNE Air and Sea Surface Temperature Updates", Jacobs ESSSA Group report ESSSA-FY13-31, 2012.

Boberg PR, Tylka AJ, Adams JH Jr., Beahm LP, Fluckiger EO, Kleis T, and E. Kobel, "Geomagnetic Transmission Disturbances and Heavy-Ion Fluences Observed in Low Earth Orbit During the Solar Energetic Particle Events of October 1989", Adv Space Res. 17(2):121-5; 1996.

Caires, S. and A. Sterl, "A New Nonparametric Method to Correct Model Data: Application to Significant Wave Height From the ERA-40 Re-analysis", Journal of Atmospheric and Oceanic Technology, Vol. 22, No. 4, 2005, pp.443-459.

Changnon, S. A., Jr., "The Scales of Hail", Journal of Applied Meteorology, Vol. 16, No. 6, July 1977, pp. 626-648.

Cote, L.J., J.O. Davis, W. Markes, R.J. McGough, E. Mehr, W.J. Pierson, Jr., J.F. Ropek, G. Stephenson, and R.C. Vetter, "The Directional Spectrum of a Wind Generated Sea as Determined From Data Obtained by the Stereo Wave Observation Project", Meteorological Papers, New York University College of Engineering, 2(6), 1960, 88p.

CxP 70023, Constellation Program Design Specification for Natural Environments (DSNE), Revision C

Demirbilek, Z. and L. Vincent, "Water Wave Mechanics", In: Demirbilek, Z., Coastal Engineering Manual, Part II, Hydrodynamics, Chapter II-1, Engineer Manual, U.S. Army Corps of Engineers, Washington, DC, 2002, pp. 1110-2-1100.

Dollfus, A. and E. Bowell, "Polarimetric Properties of the Lunar Surface and its Interpretation, Part I. Telescopic Observations", Astronomy & Astrophysics, 10, 1971, pp. 29-53.

Feldman W.C., J.R. Asbridge, S.J. Bame, and J.T. Gosling, "Plasma and Magnetic Fields from the Sun", The Solar Output and its Variation, (ed.) Oran R. White, Colorado Associated University Press, Boulder, 1977.

Fennell, J. E., Harry C. Koons, Margaret W. Chen, and J. Bernard Blake, "Internal Charging: A Preliminary Environmental Specification for Satellites", IEEE Transactions on Plasma Science, Vol. 28, No. 6, December 2000, p. 2029.

Gussenhoven, M. S., and E.G. Mullen, "A "worst case" spacecraft charging environment as observed by SCATHA on 24 April 1979", AIAA Paper 82-0271, 1982.

Halekas, J.S., S.D. Bale, D.L. Mitchell, and R.P. Lin, "Electrons and magnetic fields in the Lunar Plasma Wake", J. Geophys. Res., 110, A07222, doi:10.1029/2004JA010991, 2005.

Heymsfield, A, "Properties of Tropical and Midlatitude Ice Cloud Particle Ensembles. Part II: Applications for Mesoscale and Climate Models", Journal of Atmospheric Science, Vol. 60, November 2003, pp. 2,592-2,611.

Hickey, M. P., Robert E. Smith, "Ninety-day Solar and Geomagnetic Activity Input Files for Thermospheric Variation Simulation: Simulation Data Files Release 2", Physitron Company report PHY-92R031, 1992.

Johnston, A. H., "Radiation Effects in Optoelectronic Devices", IEEE Transactions On Nuclear Science, pp. 2054 – 2073, Vol. 60, No. 3, June 2013.

King, J.H., "Solar Proton Fluences for 1977-1983 Space Missions", Journal of Spacecraft & Rockets, 11, 1974, p. 401.

Lawson, Stefanie L., Bruce M. Jakosky, Hye-Sook Park, and Michael T. Mellon, "Brightness Temperatures of the Lunar Surface: Calibration and Global Analysis of the Clementine Long-Wave Infrared Camera Data," J. of Geophysical Research, 105, No. E2, 2000, pp. 4,273-4,290.

Messenger, S. R., R. J. Walters, E. A. Burke, G. P. Summers, and M, A. Xapsos, "NIEL and Damage Correlations for High-Energy Protons in Gallium Arsenide Devices", IEEE Transactions On Nuclear Science, pp. 2121 – 2126, Vol. 48, No. 6, December 2001.

MIL-STD-810G, Change 1, Test Method Standard for Environmental Engineering Considerations and Laboratory Tests.

Miles, N. L., et al, "Cloud Droplet Size Distributions in Low-Level Stratiform Clouds", Journal of Atmospheric Science, Vol. 57, January 2000, pp. 295-311.

Minow, J.I., "Development and implementation of an empirical ionosphere variability model", Advances in Space Research, 33, 2004, pp. 887-892.

Minow, J.I., L. N. Parker, and W.C. Blackwell, Jr., "Extreme space weather events and charging hazard assessments in lunar environments", presented at 37th COSPAR Scientific Assembly, Montreal, Canada, 13-20 July 2008.

NASA-HDBK 1001, Terrestrial Environment (Climatic) Criteria Handbook for use in Aerospace Vehicle Development Environment.

NASA MSFC Memo EV44 (15-007), KSC Avian Environment, 17 August 2015.

NASA/TM-2008-215633, Terrestrial Environment (Climatic) Criteria Handbook for use in Aerospace Vehicle Development Environment, 2008 Revision.

NASA/TM 2016-218229, Natural Environment Definition for Design (NEDD).

NCRP Report 132, Radiation Protection Guidance for Activities in Low-Earth Orbit.

NCRP Report 142, Operational Radiation Safety Programs for Astronauts in Low-Earth Orbit: A Basic Framework.

NOAA, Federal Meteorological Handbook No. 1, Surface Weather Observations and Reports, FCM-H1-2005, September 2005.

NSTS 07700, Vol. X, Book 2, Space Shuttle Flight and Ground System Specification-Environment Design, Weight and Performance, and Avionics Events, Appendix 10.10, Section 11.1.4.2.

NSTS 16007, Space Shuttle Launch Commit Criteria (LCC) and Background, Section 4, Weather Rules.

O'Neill, P., and Badhwar M. O'Neill, "Galactic Cosmic Ray Model Update Based on Advanced Composition Explorer (ACE) Energy Spectra from 1997 to Present", Advances in Space Research, Vol. 37, 2006, pp 1727-1733.

Paterson, W.R., and L.A. Frank, "Survey of Plasma Parameters in Earth's Distant Magnetotail with the Geotail Spacecraft", Geophys. Res. Lett., 21, 1994, pp. 2971-2974.

Purvis, C.K., H.B. Garrett, A.C. Whittlesey, and N.J. Stevens, Design Guidelines for Assessing and Controlling spacecraft Charging Effects, NASA-TP-2361, 1984.

SLS-PLAN-008, SLSP Configuration Management Plan

SLS-SPEC-048, Cross-Program Integrated Coordinate Systems.

Sawyer, D.M., J.I. Vette," The AP-8 Trapped Proton Environment for Solar Maximum and Solar Minimum", NSSDC/SDC-A-R&S 76-06, NASA Goddard Space Flight Center, Greenbelt Maryland, 1976.

Space Shuttle Operations and Maintenance Requirements and Specifications Document, File II, Volume I, Rule S00L00.010, June 6, 2006.

Srour, J. R., IEEE, C. J. Marshall, and P. W. Marshall, "Review of Displacement Damage Effects in Silicon Devices", IEEE Transactions On Nuclear Science, pp. 653 – 670, Vol. 50, No. 3, June 2003.

Tattelman, P. and Willis, P., "Model Vertical Profiles of Extreme Rainfall Rate, Liquid Water Content, and Drop-Size Distribution", AFGL-TR-85-0200, September 6, 1985.

Tylka, A.J., J.H. Adams, Jr., P. Boberg, B. Brownstein, W.F. Dietrich, E.O. Flueckiger, E.L. Petersen, M.A. Shea, D.F. Smart, and E.C. Smith, "CREME96: A Revision of the Cosmic Ray Effects on Micro-Electronics Code," IEEE Transactions on Nuclear Science, volume 44, 1997a, pp. 2150-2160.

Tylka, A.J., W.F. Dietrich, and P.R. Boberg, "Probability Distributions of High-Energy Solar-Heavy-Ion Fluxes from IMP-8: 1973-1996," IEEE Transactions on Nuclear Science, volume 44, 1997b, pp. 2140-2149.

Vette, J.I., The AE-8 Trapped Electron Model Environment, NSSDC WDC-A-R&S 91-24, NASA Goddard Space Flight Center, Greenbelt Maryland, November, 1991.

References for 3.3.3:

Angelopoulos, V., Cruce, P., Drozdov, A. et al.,2019, The Space Physics Environment Data Analysis System (SPEDAS), Space Sci Rev 215: 9. https://doi.org/10.1007/s11214-018-0576-4.

Angelopoulos, V., 2010, The artemis mission, The ARTEMIS mission. Springer, pp. 3-25.

Artemyev, A. V., Angelopoulos, V., & McTiernan, J. M. (2018). Near-Earth solar wind: Plasma characteristics from ARTEMIS measurements. Journal of Geophysical Research: Space Physics, 123, 9955-9962. https://doi.org/10.1029/2018JA025904

Farrell, W. M., Halekas, J. S., Killen, R., Delory G. T., Gross, N., Bleacher, L., Krauss-Varben, D., Travnicek, P., Hurley, D., Stubbs, T. et. al., 2012, Solar-storm/lunar atmosphere model (sslam): An overview of the e_ort and description of the driving storm environment, Journal of Geophysical Research: Planets, vol. 117, no. E10.

Farrell, W. M., Stubbs, T., Delory G. T., Vondrak, R., M. Collier, Halekas, J. S., and Lin, R. P., 2008, Concerning the dissipation of electrically charged objects in the shadowed lunar polar regions," Geophysical Research Letters, vol. 35, no. 19.

Farrell, W. M., Stubbs, T., Halekas, J. S., Killen, R., Delory G. T., M. Collier, and Vondrak, R., 2010, Anticipated electrical environment within permanently shadowed lunar craters," Journal of Geophysical Research: Planets, vol. 115, no. E3.

Farrell, W. M., Stubbs, T., Vondrak, R., Delory G. T., and Halekas, J. S., 2007, Complex electric fields near the lunar terminator: The near-surface wake and accelerated dust, Geophysical Research Letters, vol. 34, no. 14.

Halekas, J. S., Bale S., Mitchell, D., and Lin, R. P., 2005, Electrons and magnetic fields in the lunar plasma wake," Journal of Geophysical Research: Space Physics, vol. 110, no. A7.

Halekas, J. S., Delory G. T., Brain, D., Lin, R. P., M. Fillingim, Lee, C., Mewaldt, R., Stubbs, T., Farrell, W. M., and Hudson, M., 2007, Extreme lunar surface charging during solar energetic particle events," Geophysical research letters, vol. 34, no. 2.

Halekas, J. S., Delory G. T., Lin, R. P., Stubbs, T., and Farrell, W. M., 2008, Lunar prospector observations of the electrostatic potential of the lunar surface and its response to incident currents," Journal of Geophysical Research: Space Physics, vol. 113, no. A9.

Halekas, J. S., Delory G. T., Lin, R. P., Stubbs, T., and Farrell, W. M., 2009, Lunar surface charging during solar energetic particle events: Measurement and prediction," Journal of Geophysical Research: Space Physics, vol. 114, no. A5.

Halekas, J. S., Poppe, A. R., & McFadden, J. P (2014). The effects of solar wind velocity distributions on the refilling of the lunar wake: ARTEMIS observations and comparisons to one-dimensional theory. Journal of Geophysical Research: Space Physics, 119, 5133-5149.

Halekas, J. S., Saito, Y., Delory G. T., and Farrell, W. M. , 2011, New views of the lunar plasma environment," Planetary and Space Science, vol. 59, no. 14, pp. 1681-1694.

Jackson, T. L., Farrell, W. M., Killen, R., Delory G. T., Halekas, J. S., and Stubbs, T., 2011, Discharging of roving objects in the lunar polar regions," Journal of Spacecraft and Rockets, vol. 48, no. 4, pp. 700-704.

Jackson, T.L., W.M. Farrell, M.I. Zimmerman, 2015. Rover wheel charging on the lunar surface. Advances in Space Research, 55, #6, 1710-1720.

Mandell, M. J., Davis, V. A., Cooke, V, A., Wheelock, T., and Roth, C. J., 2006, Nascap-2k spacecraft charging code overview," IEEE Transactions on Plasma Science, vol. 34, no. 5, pp. 2084 - 2093.

McFadden, J. P., C. W. Carlson, D. Larson, J. Bonnell, F. Mozer, V. Angelopoulos, K.-H. Glassmeier, and U. Auster (2008b), THEMIS ESA first science results and performance issues, Space Sci. Rev., 141, 477–508, doi:10.1007/s11214-008-9433-1.

Poppe, A. R., Halekas, J. S., and Horanyi, M., 2011, Negative potentials above the day-side lunar surface in the terrestrial plasma sheet: Evidence of non-monotonic potentials, Geophysical Research Letters, vol. 38, no. 2.

Poppe, A. R., and Horanyi, M., 2010, Simulations of the photoelectron sheath and dust levitation on the lunar surface," Journal of Geophysical Research: Space Physics, vol. 115, no. A8.

Zimmerman, M. I., Farrell, W. M., Stubbs, T., Halekas, J. S., and Jackson, T., 2011, Solar wind access to lunar polar craters: Feedback between surface charging and plasma expansion," Geophysical Research Letters, vol. 38, no. 19.

Zimmerman, M. I., Jackson, T. L., Farrell, W. M., and Stubbs, T., 2012, Plasma wake simulations and object charging in a shadowed lunar crater during a solar storm," Journal of Geophysical Research: Planets, vol. 117, no. E10.

References for 3.4

Adams, J.H., M. Bhattacharya, Z.W., Lin, G. Pendelton, J.W. Watts, 2007. The ionizing radiation environment on the moon. Advances in Space Research, 40, issue 3, 338-341.

ASTM D2487, 1987. Standard Practice for Classification of Soils for Engineering Purposes (Unified Soil Classification System). ASTM International.

Bandfield, J.L., R.R. Ghent, A.R. Vasavada, D.A. Paige, S.J. Lawrence, M.S. Robinson, 2011, Lunar surface rock abundance and regolith fines temperatures derived from LRO Diviner Radiometer data, Journal of Geophysical Research, 116, E00H02.

Basilevsky, A.T., 1976. On the evolution of small lunar craters. Proceedings of the Lunar Science Conference 7th, pp. 1005-1020.

Bassett, H.L. and R.G. Shackleford, 1972. Dielectric properties of Apollo 14 lunar samples at micrometer and millimeter wavelengths. Proceedings of the Lunar Science Conference 3rd, pp. 3157-3160.

Cadenhead, D.A., M.G. Brown, D.K. Rice, J.R. Stetter, 1977. Some surface area and porosity characterizations of lunar soils. Proceedings of the Lunar Science Conference 8th, pp. 1291-1303.

Carrier, W.D. III, 1973. Lunar soil grain size distribution. The Moon, 6, 240-263.

Carrier et al., 1991, Lunar Sourcebook, Cambridge University Press.

Carrier, W. D., 2003. Particle Size Distribution of Lunar Soil, Journal of Geotechnical and Geoenvironmental Engineering, ASCE, V.129, No. 10, 956-959.

Carrier, W.D., 2005. The Four Things You Need to Know About The Geotechnical Properties of Lunar Soil, Lunar Geotechnical Institute.

Choate, R., et al., 1968, Lunar Surface Mechanical Properties, Surveyor Project. Part 1: Project Description and Performance, JPL Technical Report 32-1265, Jet Propulsion Laboratory, Pasadena, CA, p. 137-194.

Colwell, J.E., Batiste, S., Hora´nyi, M., Robertson, S., Sture, S., 2007. Lunar Surface: Dust Dynamics and Regolith Mechanics. Reviews of Geophysics, 45, RG2006.

Cremers, C.J. and R. C. Birkebak, 1971, Thermal conductivity of fines from Apollo 12, Lunar and Planetary Science Conference Proceedings, vol. 2, p. 2311, 1971. basaltic igneous rocks, microbrecias, lunar soil"

Cremers, C.J., R. C. Birkebak, and J. E. White, 1972, Thermal characteristics of the lunar surface layer, International Journal of Heat and Mass Transfer, vol. 15, no. 5, pp. 1045–1055, May 1972.

Cremers, C.J., 1972, “Thermal conductivity of Apollo 14 fines.,” Lunar and Planetary Science Conference Proceedings, vol. 3, p. 2611-2617.

Cremers, C.J., 1974, "Heat Transfer Within the Lunar Surface Layer," in Advances in Heat Transfer, vol. 10, J. P. Hartnett and T. F. Irvine, Eds. Elsevier, 1974, pp. 39–83.

Cremers, C.J. and H.S. Hsia, 1974, Thermal conductivity of Apollo 16 lunar fines, Lunar and Planetary Science Conference Proceedings, vol., 3, p. 2703.Demidov and Basilevsky, 2014.

Di K., B. Xu, M. Peng., 2016. Rock size-frequency distribution analysis at the Chang'E-3 landing site. Planetary and Space Science, 120, p. 103-112.

Dyal, P., C.W. Parkin, W.D. Daily, 1974. Magnetism and the interior of the Moon. Reviews of Geophysics and Space Physics, 12, 568-591.

Feuerbacher, B.; Anderegg, M.; Fitton, B.; Laude, L. D.; Willis, R. F.; Grard, R. J. L., 1972. Photoemission from lunar surface fines and the lunar photoelectron sheath. Proceedings of the Third Lunar Science Conference, Supplement 3, Volume 3, 2655-2663.

Glaser, P., F. Scholten, D. De Rosa, R. Marco Figuera, J. Oberst, E. Mazarico, G.A. Neumann, M.S. Robinson, 2014. Illumination conditions at the lunar south pole using high resolution Digital Terrain Models from LOLA. Icarus, 243, 78-90.

Glaser, P., J. Oberst, G.A Neumann, E. Mazarico, E.J. Speyerer, M.S. Robinson, 2018. Illumination conditions at the lunar poles: Implications for future exploration. Planetary and Space Science, 162, 170-178.

Gold, T., E. Bilson, M. Yerbury, 1972. Grain size analysis, optical reflectivity measurements and determination of high frequency electrical properties for Apollo 14 lunar samples. Proceedings of the Lunar Science Conference 3rd, pp. 3187-3193.

Halekas, J.S., Delory, G.T., Lin, R.P., Stubbs, T.J., Farrell, W.M., 2009. Lunar Prospector measurements of secondary electron emission from lunar regolith. Planetary and Space Science, 57, 78-82.

Hayne, P.O., et al., 2017, Global regololith thermophysical properties of the Moon from the Diviner lunar radiometer experiment: lunar regolith thermophysical properties, Journal of Geophysical Research: Planets, 122, no. 12, 2371-2400.

Heywood, H. 1971. Particle size and shape distribution for lunar fine sample 12057,72. Proceedings of the Second Lunar Science Conference, vol. 3, 1989-2001.

Hirabayashi, M., Howl, B. A., Fassett, C. I., Soderblom, J. M., Minton, D. A., & Melosh, H. J. (2018). The role of breccia lenses in regolith generation from the formation of small, simple craters: Application to the Apollo 15 landing site. Journal of Geophysical Research: Planets, 123, 527– 543. https://doi.org/10.1002/2017JE005377

Heiken et al., 1991, Lunar Sourcebook, Cambridge University Press.

Horai, K.-I., Winkler, J.L., Jr. (1976). Lunar Science Conference, 7th, Proceedings, 3, (A77-3465115-91), Pergamon Press, 3183-3204. – need reference.

Hora´nyi, M., Walch, B., Robertson, S., Alexander, D., 1998. Electrostatic charging properties of Apollo 17 lunar dust. J. Geophys. Res. 103, 8575–8580.

Katz, I., Parks, D.E., Mandell, M.J., Harvey,J.M., Brownell, D.H.,Wang, S.S., Rotenberg, M., 1977. A three-dimensional dynamic study of electrostatic charging in materials. NASACR 135256.

Kreslavsky, M.A. and J.W. Head, 2016, The steepest slopes on the Moon from Lunar Orbiter Laser Altimeter (LOLA) Data: Spatial Distribution and Correlation with Geologic Features, Icarus, 273, 329-336.

Kreslavsky, M.A., A.Yu. Bystrov, I.P. Karachevtseva, 2015, Frequency Distributions of Topograph Slopes on the Moon, 46th Lunar and Planetary Science Conference, No. 1832, 2848.

Langseth, M.G., S.J. Keihm, J.L. Chute Jr., 1973. Heat-flow experiment. In Apollo 17 Preliminary Science Report, pp. 9-1 to 9-24. NASA SP-330.

Li, B., Z. Ling, J. Zhang, J. Chen, 2017. Rock size-frequency distributions analysis at lunar landing sites based on remote sensing and in-situ imagery. Planetary and Space Science, 146, 30-39.

Lucey, P.G., et al. (2014), The global albedo of the Moon at 1064 nm from LOLA, J. Geophys. Res. Planets, 119, 1665-1679.

LunaRef website https://www.lpi.usra.edu/wiki/lunaref/index.php/Table_of_Contents

Lunar Sourcebook 1991 Cambridge University Press.

Martin, R.T., J.L. Winkler, S.W. Johnson, W.D, Carrier, 1973, Measurement of conductance of Apollo 12 lunar simulant taken in the molecular flow range for helium, argon, and krypton gases. Unpublished report. In Lunar Sourcebook 1991, Cambridge University Press.

Mazarico, E., G.A. Neumann, D.E. Smith, M.T. Zuber, M.H. Torrence, 2011. Illumination conditions of the lunar poles to 65 degrees latitude from Lunar Orbiter Laser Altimeter Data. Annual Meeting of the Lunar Exploration Analysis Group, Nov. 7-9, 2011, Houston, TX. LPI Contribution No. 1646, p. 51.

McKay, 1991, Lunar Sourcebook, Cambridge University Press.

Morris, R.V., T.H. See, F. Horz, 1983. Some evidence concerning the source material of large glass objects from the Moon., Lunar and Planetary Science XIV, 528-529.

Muehlberger, et al., 1972, Apollo 16: Preliminary Science Report NASA SP-315, p. 6-1.

Neukum, G., B.A. Ivanov, W.K. Hartmann, 2001. Cratering records in the inner solar system in relation to the Lunar Reference System. Space Science Reviews, 96, 55-86.

Olhoeft, G. R.; Frisillo, A. L.; Strangway, D. W.; Sharpe, H., 1974. Temperature Dependence of Electrical Conductivity and Lunar Temperatures. The Moon, Volume 9, Issue 1-2, 79-87.

Olhoeft, G.R., Strangway, D.W., 1975. Dielectric Properties of the First 100 Meters of the Moon. Earth and Planetary Science Letters, 24, 394-404.

Park, J., Liu, Y., Kihm, K., Taylor, L., 2008. Characterization of Lunar dust for Toxilogical Studies. I: Particle Size Distribution. Journal of Aerospace Engineering, October 2008, 266-271.

Perry, C.H., D.K Agrawal, E. Anastassakis, R.P. Lowndes, N.E. Tornberg, 1972. Far infrared and Raman spectroscopic investigations of lunar materials from Apollo 11, 12, 14, and 15. Proceedings of the Lunar Science Conference 3rd, pp. 3077-3095.

Rickman, D., K.W. Street, 2008. Some expected mechanical characteristics of lunar dust: a geological view. Space Technology and Applications International Forum-STAIF 2008. AIP Conference Proceedings, 969, 949-955.

Rosenburg, M.A., et al., 2011, Global surface slopes and roughness of the Moon from the Lunar Orbiter Laser Altimeter, Journal of Geophysical Research, 116, E2, 2001.

Sato, H., M.S. Robinson, B. Hapke, B.W. Denevi, A.K. Boyd, 2014. Resolved Hapke parameter maps of the Moon. Journal of Geophysical Research: Planets, 119, 1775-1805.

Shoemaker, E.M. and E.C. Morris, 1970, Geology:Physics of fragmental debris, Icarus, 12, 2, 188-212.

Sickafoose, A. A.; Colwell, J. E.; Horányi, M.; Robertson, S., 2001. Experimental investigations on photoelectric and triboelectric charging of dust. Journal of Geophysical Research, Volume 106, Issue A5, 8343-8356.

Slyuta, E.N., 2014. Physical and mechanical properties of the lunar soil (a review). Solar System Research, 48, issue 5, 330-353.

Smith, D.E. et al., 2010, Initial observations from the Lunar Orbiter Laser Altimeter (LOLA), Geophysical Research Letters, 37, 18, L18204.

Smith, D.E, M.T. Zuber, G.A. Neumann, E. Mazarico, F.G. Lemoine, J.W. Head III, P.G. Lucey, O. Aharonson, M.S. Robinson, X. Sun, M.H. Torrence, M.K. Barker, J. Oberst, T.C. Duxbury, D. Mao, L.S. Barnouin, K. Jha, D.D. Rowlands, S. Goossens, D. Baker, S. Bauer, P. Glaser, M. Lemelin, M. Rosenburg, M.M. Sori, J. Whitten, T. McClanahan 2017. Summary of the results from the lunar orbiter laser altimeter after seven years in lunar orbit. Icarus, 283, 70-91.

Speyerer, E. J., & Robinson, M. S. (2013). Persistently illuminated regions at the lunar poles: Ideal sites for future exploration. Icarus, 222(1), 122-136. doi:j.icarus.2012.10.010

Sternglass,E.J.,1954. The Theory of Secondary Emission, Sci.Pap., 1772. Westinghouse Res.Lab.,Pittsburgh, PA.

Stopar, J.D. et al., 2017, Relative depths of simple craters and the nature of the lunar regolith, Icarus, 298, 34-48.

Strangway, D.W., W.B. Chapman, G.R. Olhoeft, J. Carnes, 1972. Electrical properties of lunar soil-dependence upon frequency, temperature and moisture. Earth and Planetary Science Letters, 16, 275-281.

Stubbs, T.J., Vondrak, R.R., Farrell, W.M., 2006. A dynamic fountain model for lunar dust. Advances in Space Research, 37, 59-66.

Stubbs, T.J., Vondrak, R.R., Farrell, W.M., Halekas, J.S., Delory, G.T., Collier, M.R., 2007. Interaction of Dust and Plasma on the Lunar Surface and in the Exosphere. Workshop on Science Associated with the Lunar Exploration Architecture, Tempe, AZ, Feb. 26 – March 2.

Vasavada, A.R., Bandfield J.L., Greenhagen, B.T., Hayne, P.O., Siegler, M.A.., Williams, J.-P., Paige, D.A. (2012). Lunar equatorial surface temperatures and regolith properties from the Diviner Lunar Radiometer Experiment, J. Geophys. Res., 117, E00H18.

Whipple, E.C., 1981. Potentials of surfaces in space. Rep. Prog. Phys. 44, 1197–1250.

Williams, J.-P., D.A. Paige, B.T. Greenhagen, E. Sefton-Nash (2017), The global surface temperatures of the Moon as measured by the Diviner Lunar Radiometer Experiment, Icarus, 283, 300-325.

Willis, R.F., Anderegg, M., Feuerbacher, B., Fitton, B., 1973. Photoemission and Secondary Electron Emission from Lunar Surface Material. Photon and Particle Interactions with Surfaces in Space, Proceedings of the 6th ESLAB Symposium, Sept. 26-29, 389-401.

Woods-Robinson, R., Siegler, M.A, Paige, D.A., 2019. A Model for the Thermophysical Properties of Lunar Regolith at Low Temperatures, Journal of Geophysical Research: Planets, 124, 1989-2011.

APPENDIX A
ACRONYMS AND ABBREVIATIONS

ACE	Advanced Composition Explorer
AGL	Above Ground Level
Al	aluminum
ALARA	As Low As Reasonably Achievable
AO	Atomic Oxygen
°C	Degrees Celsius
C-ERA40	Corrected-European Centre for Medium Range Weather Forecasts Re-Analysis
CDIP	Coastal Data Information Program
cGy	centiGrays
cm	Centimeters
CR	Change Request
CREME96	Cosmic Ray Effects on Microelectronics 96
CxP	Constellation Program
DD	Displacement damage
DDD	Displacement damage dosage
DRM	Design Reference Mission
DRM ConOps	Design Reference Missions and Operational Concepts
DSH	Deep Space Habitat
DSNE	Design Specification for Natural Environments
EAFB	Edwards Air Force Base
ECMWF	European Centre for Medium Range Weather Forecasts
ER	Eastern Range
ESD	Exploration Systems Development
ESP	Emission of Solar Protons
ev	Electron Volts
EVA	Extravehicular Activity
FS	Factor of Safety
ft	Feet
ft/s	Feet per second
g/cm^2	Grams Per Square Centimeter
g/cm^3	Grams Per Cubic Centimeter

Ga	Giga-annum (billions of years)
GCR	Galactic Cosmic Radiation (Rays)
GEO	Geosynchronous Earth Orbit
GFE	Government Furnished Equipment
GGM02C	Gravity Model 02 C
GN&C	Guidance, Navigation, and Control
GRACE	Gravity Recovery and Climate Experiment
GRAIL	Gravity Recovery and Interior Laboratory
GRAM	Global Reference Atmosphere Model
GSFC	Goddard Space Flight Center
GTRN	Geomagnetic Transmission
HEO	High Earth Orbit
HP	High Perigee
hPa	hectopascal
JPCB	Joint Program Control Board
in	Inch
IEEE	Institute of Electrical and Electronic Engineers
IGRF	International Geomagnetic Reference Field
IMP	Interplanetary Monitoring Platform
ISS	International Space Station
K	Kelvin
kg	Kilograms
km	Kilometers
KSC	Kennedy Space Center
LAS	Launch Abort System
lbs	Pounds
LCC	Launch Commit Criteria
LEO	Low Earth Orbit
LET	Linear Energy Transfer
LOLA	Lunar Orbiter Laser Altimeter
LP	Low Perigee
LST	Local Standard Time
LRO	Lunar Reconnaissance Orbiter
LROC	Lunar Reconnaissance Orbiter Camera
LWIR	Long-Wave Infrared camera
m	Meters

M/OD	Meteoroid and Orbital Debris
m/s	Meters Per Second
mbar	Millibars
MEM 3	Meteoroid Engineering Model 3
MET	Marshall Engineering Thermosphere
MeV	Megaelectronvolts
mg	Milligrams
MIL-STD	Military Standard
MLP	Mobile Launch Platform
mm/hr	Millimeters Per Hour
MPCV	Multi-Purpose Crewed Vehicle
MSFC	Marshall Space Flight Center
MSIS	Mass Spectrometer Incoherent Scatter
MV	Megavolts
MVWPM	Monthly Vector Wind Profile Model
NAC	Narrow Angle Camera (on Lunar Reconnaissance Orbiter)
NASA	National Aeronautics and Space Administration
NASA-HDBK	NASA Handbook
NASA/TM	NASA Technical Memorandum
NAVD 88	North American Vertical Datum 88
NCEP-OI	National Centers for Environmental Prediction-Optimal Interpolation
NCRP	National Council on Radiation Protection and Measurements
NDBC	National Data Buoy Center
NEA	Near Earth Asteroid
NEDD	Natural Environment Definition for Design
NEIAHT	Natural Environments Integration Ad-Hoc Team
nm	nanometers
NOAA	National Oceanic and Atmospheric Administration
nmi	Nautical Mile
OLR	Outgoing Long-wave Radiation
ORDEM 3.0	Orbital Debris Engineering Model 3.0
PDS	Planetary Data System
PMBT	Propellant Mean Bulk Temperature
POR	Period of Record
psi	Pounds Per Square Inch

PSR	Permanently Shadowed Region
PSYCHIC	Prediction of Solar particle Yields for Characterizing Integrated Circuits
R_e	radius of the Earth
RAAN	Right Ascension of Ascending Node
RRA	Range Reference Atmosphere
SAA	South Atlantic Anomaly
SCATHA	Spacecraft Charging at High Altitudes
s	Second(s)
SEE	Single Event Effects
SIG	Systems Integration Group
SLS	Space Launch System
SPE	Solar Particle Event
SPENVIS	Space Environment Information System
SSA	Specific Surface Area
SSLAM	Solar Storm Lunar Atmosphere Modeling
SWH	Significant Wave Height
SZA	Solar Zenith Angle
TBD	To Be Determined
TBR	To Be Reviewed
TID	Total Ionizing Dose
THEMIS-ARTEMIS	Time History of Events and Macroscale Interactions during Substorms – Acceleration, Reconnection, Turbulence and Electrodynamics of Moon's Interaction with the Sun
TLI	Translunar Injection
TPM-1	Trapped Proton Model-1
UTC	Universal Time Coordinated
WAC	Wide Angle Camera
W/m^2	Watts Per Square Meter

APPENDIX B
NATURAL ENVIRONMENT VALIDATION MATRIX

Section	Model/Dataset/Design Limit	Validation Statement
3.1 Prelaunch - Ground Processing Phase		
3.1.1 Transportation Environments to Launch Site KSC	N/A	N/A
3.1.2 Reserved	N/A	N/A
3.1.3 Ground Winds for Transport and Launch Pad Environments 3.2.1 Ground Winds Environments during Launch	Peak Wind Profile Model	The Peak Wind Profile Model was developed through statistical analysis of KSC 500-ft wind tower data. The model is designed to envelope peak wind variability with height (to a specified sigma level) above an 18.3 m reference level. Details of the databases, processes, and physics used in developing the Peak Wind Profile Model are given in "Characteristics of Atmospheric Turbulence as Related to Wind Loads on Tall Structures," G. Fichtl et. al., Journal of Spacecraft and Rockets, Dec. 1969, Vol. 6, No. 12, pp. 1396-1403, and in NASA TM-2008-215633, Terrestrial Environment (Climatic) Criteria Handbook for Use in Aerospace Vehicle Development, 2008 Revision. Comparison of the Peak Wind Profile Model to measured data from the KSC 500-ft wind tower has been conducted (see NASA/MSFC/EV44 Memo EV13-05-007). The study showed that the model envelopes measured peak wind profiles to the appropriate probability level (sigma level). Peak Wind Profile Model was used during Space Shuttle design and operations (NSTS 07700, Vol. 10, Book 2, Space Shuttle Flight and Ground System Specification; Environment Design, Weight and Performance, and Avionics Events).
3.1.3 Ground Winds for Transport and Launch Pad Environments	Steady-State Wind Profile Model	The Steady-State Wind Profile Model is constructed by reducing the Peak Wind Profile Model by altitude dependent gust factors. The gust factors were developed through statistical analysis of KSC 500-ft wind tower data. Details of the databases, processes, and physics used in developing the gust factors and Steady-State

Section	Model/Dataset/Design Limit	Validation Statement
3.2.1 Ground Winds Environments during Launch		Wind Profile Model are given in "Characteristics of Atmospheric Turbulence as Related to Wind Loads on Tall Structures," G. Fichtl et. al., Journal of Spacecraft and Rockets, Dec. 1969, Vol. 6, No. 12, pp. 1396-1403, and in NASA TM-2008-215633, Terrestrial Environment (Climatic) Criteria Handbook for Use in Aerospace Vehicle Development, 2008 Revision. Steady-State Wind Profile Model was used during Space Shuttle design and operations (NSTS 07700, Vol. 10, Book 2, Space Shuttle Flight and Ground System Specification; Environment Design, Weight and Performance, and Avionics Events).
3.1.3 Ground Winds for Transport and Launch Pad Environments	Table 3.1.3-1 Design Peak Wind Speed Profiles	The Design Peak Wind Speed Profiles in Table 3.1.3-1 are constructed by inputting the appropriate peak wind speed at the 18.3 m level into the Peak Wind Profile Model. For the transport to/from pad case, the 18.3 m peak wind speed of 30.8 m/s is the heritage value used for Space Shuttle Mobile Launch Platform (MLP) transport operations (Space Shuttle Operations and Maintenance Requirements and Specifications Document, File II, Vol. I, Rule S00L00.010, June 6, 2006). For the on-pad unfueled case, the 18.3 m peak wind speed of 38.3 m/s is the 99th percentile value for a 180-day exposure period at KSC. For the on-pad fueled case, the 18.3 m peak wind speed of 24.2 m/s is the 99th percentile value for a 1-day exposure period at KSC. The on-pad cases values (38.3 m/s and 24.2 m/s) were used during Space Shuttle design and operations (NSTS 07700, Vol. 10, Book 2, Space Shuttle Flight and Ground System Specification; Environment Design, Weight and Performance, and Avionics Events).
3.1.3 Ground Winds for Transport and Launch Pad Environments	Table 3.1.3-2 Steady-State Wind Speed Profiles	The Steady-State Wind Speed Profiles in Table 3.1.3-2 and Table 3.2.1-2 are constructed by reducing the Peak Wind Speed Profiles in Table 3.1.3-1 and 3.2.1-1, respectively, with an altitude dependent gust factor (Steady-State Wind Profile Model). The applied gust factor is based on a 10-minute averaging period. (The steady-state wind

Section	Model/Dataset/Design Limit	Validation Statement
3.2.1 Ground Winds Environments during Launch	Table 3.2.1-2 Steady State Wind Speed Profile for Vehicle Launch	speed profile is the 10-minute mean wind speed profile that could produce the peak wind speed profile.) The steady-state wind speed profiles were used during Space Shuttle design and operations (NSTS 07700, Vol. 10, Book 2, Space Shuttle Flight and Ground System Specification; Environment Design, Weight and Performance, and Avionics Events).
3.1.3 Ground Winds for Transport and Launch Pad Environments	Table 3.1.3-3 30-second Peak Wind Speeds for Fatigue Load Assessments	Details of the 30 second peak wind speed distribution in Table 3.1.3-3 is provided in NASA MSFC Memo ES42 (92-67), "Probabilities of Ground Winds for SSP Fatigue Loads." The 30-second peak wind distribution was developed from the statistics of 170 hours of wind tower 1-second data. To better represent a long term climatology, the 170 hours worth of 30-second statistics were scaled to 1-hour statistics from a 33-year period. The 30-second peak wind distribution was used during Space Shuttle design and operations (NSTS 07700, Vol. 10, Book 2, Space Shuttle Flight and Ground System Specification; Environment Design, Weight and Performance, and Avionics Events).
3.1.3 Ground Winds for Transport and Launch Pad Environments	Table 3.1.3-4 Design Wind Speed Profiles for Thermal Assessments (Time constants less than an hour)	Design low wind profile of no wind is the extreme for the cold case. Design high wind profile is the steady-state wind speed profile, developed from the peak wind speed profile with a 17.7 m/s input wind at 18.3 m (17.7 m/s is the 95th percentile peak wind value for a 1-hour period. See section 3.2.1 Steady-State Wind Speed Profile for liftoff.). Data was vetted through the SLS Thermal Environments Task Team on 11/05/2013 and the Natural Environments Integration Ad Hoc Team on 11/07/2013.
3.1.3 Ground Winds for Transport and Launch Pad Environments	Table 3.1.3-5 Design Wind Speed Profiles for Thermal Assessments (Time constants on the order of hours)	Design low wind profile is the 1st percentile steady-state wind speed at 60-ft for a 1-hour exposure period at KSC. The steady-state value at the 60-ft level is used at all heights up to 500 ft. The 1st percentile level is chosen since it is highly unlikely the wind speed would be completely

Section	Model/Dataset/Design Limit	Validation Statement
		calm over several hours. Design high wind profile is the steady-state wind speed profile, developed from the peak wind speed profile with a 17.7 m/s input wind at 18.3 m (17.7 m/s is the 95th percentile peak wind value for a 1-hour period. See section 3.2.1 Steady-State Wind Speed Profile for liftoff.). Design low wind profile was determined through statistical analysis of KSC LC 39B 60-ft database using MATLAB. Data was vetted through the SLS Thermal Environments Task Team on 11/05/2013 and the Natural Environments Integration Ad Hoc Team on 11/07/2013.
3.1.3 Ground Winds for Transport and Launch Pad Environments	Table 3.1.3-6 Design Wind Speed Profiles for Thermal Assessments (Time constants on the order of days)	The diurnal steady-state wind speed profiles are the 1st (design low) and 99th (design high) percentile steady-state wind at each hour of the day at KSC. Percentile values were obtained from KSC Launch Complex 39B 60-ft database. MATLAB was used to determine percentile values. Details of the log wind profile are provided in Stull, R., (1988), An Introduction to Boundary Layer Meteorology, Kluwer Academic Publishers, Section 9.7. Data was vetted through the SLS Thermal Environments Task Team on 11/05/2013 and the Natural Environments Integration Ad Hoc Team on 11/07/2013.
3.1.3 Ground Winds for Transport and Launch Pad Environments	KSC Launch Complex 39B 60-ft Wind Tower Data	The KSC LC 39B Pad database consists of 5-min and hourly mean and peak wind speed and direction at the 60-ft level for the period of record of 1995 through 2007. Database has been quality controlled and vetted by the MSFC Natural Environments Branch (EV44). Quality control processes and data were vetted at the 2/22/2008 Space Shuttle Program Natural Environments Panel (Ryan Decker, "KSC LC39 Meteorological Databases").
3.1.3 Ground Winds for Transport and Launch Pad Environments	Design Spectral Gust Model	Details of the Design Spectral Gust Model are given in ""Longitudinal and Lateral Spectra of Turbulence in the Atmospheric Boundary Layer at Kennedy Space Center"", G. Fichtl and G. McVehil, J. Applied Meteorology, Vol. 9, pages

Section	Model/Dataset/Design Limit	Validation Statement
3.2.1 Ground Winds Environments during Launch		51-63, February 1970 and in NASA TM-2008-215633, Terrestrial Environment (Climatic) Criteria Handbook for Use in Aerospace Vehicle Development, 2008 Revision. The underlining physics of the spectral gust model are given in the Monin-Obuhkov Similarity Theory. Monin-Obuhkov has been used extensively in the atmospheric science community to represent mean flow and turbulence properties in the atmospheric surface layer. The spectral gust model was developed by adjusting Monin-Obuhkov Similarity Theory to measured turbulence from the KSC 500 ft wind tower. Therefore, the model provides a good representation of the actual turbulent environment used in the development. The model has been shown to agree favorably with other spectral models, such as the Dryden and Von Karman models. Spectral Gust Model was used during Space Shuttle design and operations (NSTS 07700, Vol. 10, Book 2, Space Shuttle Flight and Ground System Specification; Environment Design, Weight and Performance, and Avionics Events).
3.1.3 Ground Winds for Transport and Launch Pad Environments 3.2.1 Ground Winds Environments during Launch	Coherence Model	Details of the Coherence Model are given in NASA TM-2008-215633, Terrestrial Environment (Climatic) Criteria Handbook for Use in Aerospace Vehicle Development, 2008 Revision. (See Section 2.2.6.3)
3.1.3 Ground Winds for Transport and Launch Pad Environments 3.2.1 Ground Winds Environments during Launch	Discrete Gust Model	The “1-cosine” gust shape is an industry standard. The Discrete Gust Model was used during Space Shuttle design and operations (NSTS 07700, Vol. 10, Book 2, Space Shuttle Flight and Ground System Specification; Environment Design, Weight and Performance, and Avionics Events).

Section	Model/Dataset/Design Limit	Validation Statement
3.1.4 Radiant (Thermal) Energy Environment for Ground Ops at KSC	National Solar Radiation Database	Details of the models used to develop the National Solar Radiation Database (NSRD) are contained in National Renewable Energy Laboratory Tech Report NREL/TP-5500-5424, National Solar Radiation Database 1991-2010 Update: User's Manual, August 2012 and Maxwell, E. L. (1998) "METSTAT - The Solar Radiation Model Used in the Production of the National Solar Radiation Database (NSRDB)", Solar Energy, 62 (4). The National Solar Radiation Database is validated to multiple years of measured data, and is described in National Renewable Energy Laboratory Tech Report NREL/TP-5500-5424, National Solar Radiation Database 1991-2010 Update: User's Manual, August 2012 and Myers, D. et. al., "Broadband Model Performance for an Updated National Solar Radiation Database in the United States of American", Proc. Solar World Congress, International Solar Energy Society, 2005. All data in Section 3.1 are obtained from the Shuttle Landing Facility grid point of the NSRD.
3.1.4 Radiant (Thermal) Energy Environment for Ground Ops at KSC	Sky Temperature	All sky temperature values in Tables 3.1.4-4 through 3.1.4-9 are determined from air temperature, dew point temperature, and sky cover. Details of the calculation, along with model validation, are given in K. Wang and S. Liang, "Global atmospheric downward longwave radiation over land surface under all-sky conditions from 1973 to 2008", J. Geophysical Research, Vol. 114, D19101, 2009.
3.1.4 Radiant (Thermal) Energy Environment for Ground Ops at KSC	Table 3.1.4-1 Design High Radiant Energy as a Function of Time of Day, Table 3.1.4-2 Design Low Radiant Energy as a Function of Time of Day	Design high and low direct incident are the maximum and minimum values at each hour for the months of June and December, determined from the NSRD. Design high (low) diffuse values are those associated with the design high (low) direct incident values. MATLAB was used to determine maximum and minimum values.
3.1.4 Radiant (Thermal) Energy Environment for Ground Ops at KSC	Table 3.1.4-3 Sky Temperature Design Limits for KSC	Design high and low sky temperature limits are obtained from NASA TM-2008-215633, Terrestrial Environment (Climatic) Criteria Handbook for Use in Aerospace Vehicle Development, 2008 Revision.

Section	Model/Dataset/Design Limit	Validation Statement
		Design high and low sky temperature limits were used by the Shuttle Program according to NSTS 07700, Vol. 10, Book 2, Space Shuttle Flight and Ground System Specification; Environment Design, Weight and Performance, and Avionics Events.
3.1.4 Radiant (Thermal) Energy Environment for Ground Ops at KSC	Table 3.1.4-4 Cold Design Radiant Energy, Cloudy Sky Table 3.1.4-5 Hot Design Radiant Energy, Cloudy Sky Table 3.1.4-6 Cold Design Radiant Energy, Partly Cloudy Sky Table 3.1.4-7 Hot Design Radiant Energy, Partly Cloudy Sky Table 3.1.4-8 Cold Design Radiant Energy, Clear Sky Table 3.1.4-9 Hot Design Radiant Energy, Clear Sky	Values in Tables 3.1.4-4, 3.1.4-6, and 3.1.4-8 were determined by taking the average at each hour for the 10 coldest days with cloudy skies (100% sky cover), partly cloudy skies (40 to 60% sky cover), and clear skies (0% sky cover) from the NSRD (1991-2010). Cold days were determined by calculating the average daily temperature for each day in the period of record, and selecting the 10 coldest days that met the specific sky condition. Values in Tables 3.1.4-5, 3.1.4-7, and 3.1.4-9 were determined by taking the average at each hour for the 10 hottest days with cloudy skies (100% sky cover), partly cloudy skies (40 to 60% sky cover), and clear skies (0% sky cover) from the NSRD (1991-2010). Hot days were determined by calculating the average daily temperature for each day in the period of record, and selecting the 10 hottest days that met the specific sky condition. Data was compared to NSRD data to ensure profile properly represented the specific condition. Methodology was vetted through the SLS Thermal Environments Task Team on 11/05/2013 and the Natural Environments Integration Ad Hoc Team on 11/07/2013.
3.1.5 Air Temperature Environment for Ground Ops at KSC	Patrick Air Force Base/Shuttle Landing Facility surface observations	The Patrick Air Force Base (PAFB)/Shuttle Landing Facility (SLF) surface observations contain hourly values of various meteorological data. The period of record is 1957-2001 (1957-1977 from PAFB, and 1978-2001 from SLF). The PAFB/SLF database was quality controlled by the MSFC Natural Environments Branch (EV44) and used throughout the Space Shuttle Program.
3.1.5 Air Temperature Environment for	Max and min design limits for air temperature	Max and min design temperature limits of 38 deg C and -6 deg C, respectively, are the max and min of the PAFB/SLF meteorological database (1957-

Section	Model/Dataset/Design Limit	Validation Statement
Ground Ops at KSC		2001). MATLAB was used to determine maximum and minimum values.
3.1.5 Air Temperature Environment for Ground Ops at KSC	Table 3.1.5-1 Design Hot and Cold Diurnal Temperature Profile	The design hot and cold diurnal profiles are the 99th and 1st percentile temperatures for each hour in the hot month (July) and cold month (January), respectively, from the PAFB/SLF database. MATLAB was used to determine percentile values.
3.1.5 Air Temperature Environment for Ground Ops at KSC	Table 3.1.5-2 Design Hot and Cold Monthly Averaged Diurnal Temperature Profile	The design hot and cold monthly average diurnal profiles are the 99th and 1st percentile monthly averaged temperatures for each hour in the hot month (July) and cold month (January), respectively, from the PAFB/SLF database. MATLAB was used for averaging, and determining percentile values.
3.1.6 Air Pressure Environment for Ground Ops at KSC 3.2.3 Surface Air Pressure Environment during Launch	Max and min design limits for air pressure	Max and min design pressure limits of 1037.4 hPA and 973.9 hPa, respectively, are the max and min of the PAFB/SLF meteorological database (1957-2001). MATLAB was used to determine percentile values.
3.1.7 Humidity Environment for Ground Ops at KSC 3.2.4 Surface Humidity Environment During Launch	Table 3.1.7-1 Psychrometric Data, Dew Point Temperature Versus Temperature Envelope for KSC	Table 3.1.7-1 was determined by plotting temperature vs. dew point temperature for the entire period of record of the PAFB/SLF database, and constructing an envelope around all the data points.
3.1.8 Aerosol Environment for Ground Ops at KSC	Salt fog and sand/dust environment	The salt fog and sand/dust environment is given in MIL-STD-810G, Test Method Standard for Environmental Engineering Considerations and Laboratory Tests. Method 509.6 describes the environments/tests for salt fog. Method 510.6, Procedure1 describes the test procedure for sand/dust with particle sizes less than 150 microns. The sand/dust particle concentration is 0.177 g/m^3, per Part 3, Section 5.7 of MIL-STD-810G.

Section	Model/Dataset/Design Limit	Validation Statement
3.1.9 Precipitation Environment for Ground Ops at KSC	Table 3.1.9-1 Design Rainfall, KSC, Based on Yearly Largest Rate for Stated Durations	Design rainfall rates are described in NASA TM-2008-215633, Terrestrial Environment (Climatic) Criteria Handbook for Use in Aerospace Vehicle Development, 2008 Revision. Design rainfall rate was used during Space Shuttle design and operations (NSTS 07700, Vol. 10, Book 2, Space Shuttle Flight and Ground System Specification; Environment Design, Weight and Performance, and Avionics Events).
3.1.9 Precipitation Environment for Ground Ops at KSC	Table 3.1.9-2 Design Hail Characteristics for KSC	Design hail characteristics are described in NASA TM-2008-215633, Terrestrial Environment (Climatic) Criteria Handbook for Use in Aerospace Vehicle Development, 2008 Revision, and S. A. Changnon, "The Scale of Hail," J. Applied Meteorology, Vol. 16, No. 6, July 1977, pp. 626-648.
3.1.10 Flora and Fauna Environment for Ground Ops	Flora and fauna environment	The KSC area contains numerous wildlife, including birds, rodents, insects, wild boar, and alligators. Observations validate the presence of wildlife at KSC. Methods for testing of materials for fungus growth are given in MIL-STD-810G, Method 508.
3.1.11 Lightning Environment for Ground Ops at KSC 3.5.3 Lightning During Normal Landing 3.6.3 Lightning During Off-Nominal Landing	Lightning environment	The KSC environment is such that systems will be exposed to the direct and indirect effects of lightning. Observations validate the presence of lightning at KSC. Descriptions and conditions for the application of lightning environment waveforms are detailed in SAE ARP5414, Aircraft Lightning Zones and SAE ARP5412, Aircraft Lightning Environment and Related Test Waveforms.
3.2 Launch Countdown and Earth Ascent Phases		
3.2.1 Ground Winds Environments during Launch	Table 3.2.1-1 Peak Wind Speed Profile for Vehicle Launch	The Design Peak Wind Speed Profiles in Table 3.2.1-1 are constructed by inputting the appropriate peak wind speed at the 18.3 m level. For launch, the 18.3 m peak wind speed of 17.7 m/s is the 99th percentile value for a 1-hour exposure period at KSC. The 17.7 m/s value was

Section	Model/Dataset/Design Limit	Validation Statement
		used during Space Shuttle design and operations (NSTS 07700, Vol. 10, Book 2, Space Shuttle Flight and Ground System Specification; Environment Design, Weight and Performance, and Avionics Events).
3.2.2 Surface Air Temperature Environment During Launch	Max and min design limits for air temperature	Max and min design limits (99 deg F and 33 deg F) represent the range of temperatures for launch used by the Space Shuttle Program and listed in NSTS 16007, Space Shuttle Launch Commit Criteria and Background, Section 4, Weather Rules. The rationale for choosing this design range for launch is that redesign, retesting, recertification, etc., of legacy hardware would not be necessary.
3.2.5 Aloft Wind Environment for Vehicle Ascent 3.6.4 Aloft Winds for Off-Nominal Descent and Landing	Earth-GRAM 2010	Details of the model are provided in NASA/TM-2011-216467, The NASA Marshall Space Flight Center Earth Global Reference Atmospheric Model - 2010 Version. Verification and validation details are provided in EV44 (14-002), Verification and Validation Report, Earth GRAM 2010 Version 4.0. Earth-GRAM is a well-established model that has been used for various space programs, including Space Shuttle, Constellation, and SLS/MPCV.
3.2.5 Aloft Wind Environment for Vehicle Ascent	Monthly Vector Wind Profile Model	The Monthly Vector Wind Profile Model (MVWPM) is built with the quadravariate normal statistics from the serial complete wind profile database. The equations for calculation of the mean, standard deviation, and correlation coefficient have abundant references in the literature. Construction of the MVWPM is detailed in NASA/CR-1999-209759, User's Guide for the Monthly Vector Wind Profile Model. The MVWPM has compared favorably with long-term climatological databases (NOAA databases). For the KSC vicinity, statistics from several different measurement systems (wind profilers, balloon systems, etc.) have shown good agreement with the MVWPM dispersions and shears. Comparison of aerodynamic load indicators (ALI) in launch vehicle simulations has shown that the MVWPM sufficiently envelopes ALI determined from 1800 detailed wind profiles (S. I. Adelfang, O. E. Smith, and G. W. Batts,

Section	Model/Dataset/Design Limit	Validation Statement
		Ascent Wind Model for Launch Vehicle Design, J. Spacecraft and Rockets).
3.2.5 Aloft Wind Environment for Vehicle Ascent	Measured Wind Database (KSC Jimsphere Wind Profile Database)	Details of the Jimsphere/high-resolution (HR) balloon system are provided in: MSFC/ED41 Internal Memorandum, Jan. 1988, Resolution and accuracy of balloon wind sounding systems used in support of STS Ascent Performance Assessments. Wilfong et. al., Characteristics of High Resolution Wind Profiles Derived from Radar-Tracked Jimspheres and the Rose Processing Program, J. Atmospheric and Oceanic Technology, Vol. 14, April 1997. T. L. Wilfong, Characteristics of Wind Profiles Derived from the GPS Based Automated Meteorological Profiling System (AMPS), 9th Conference on Aviation, Range, and Aerospace Meteorology, Paper 8.2, Sept. 2000. ED44 (01-015), Automated Meteorological Profiling System High Resolution Flight Element Analysis Results, July 2001." The KSC Jimsphere Wind Profile database consists of high-resolution (HR) balloon data, and has been quality controlled and validated through statistical comparison to established climatology by the MSFC Natural Environments Branch. The Jimsphere/HR balloon system and database was used in Space Shuttle design and DOL operational assessments.
3.2.5 Aloft Wind Environment for Vehicle Ascent	Measured Wind Database (KSC DRWP Database)	Details of the KSC DRWP are provided in: Schumann et. al., Performance Characteristics of the Kennedy Space Center 50-MHz Doppler Radar Wind Profiler Using the Median Filter/First-Guess Data Reduction Algorithm, J. Atmospheric and Oceanic Technology, Vol. 16, May 1999, pages 532-549. F. J. Merceret, The Vertical Resolution of the Kennedy Space Center 50-MHz Wind Profiler, J. Atmospheric and Oceanic Technology, Vol. 16, Sept. 1999, pages 1273-1278.

Section	Model/Dataset/Design Limit	Validation Statement
		The KSC DRWP database consists of high temporal resolution wind profiles, which have been quality controlled and validated through statistical comparison to established climatology by the MSFC Natural Environments Branch. Details of the quality control process are given in R. E. Barbre, Quality Control Algorithms for the Kennedy Space Center 50-MHz Doppler Radar Wind Profiler Winds Database, J. Atmospheric and Oceanic Technology, Vol. 29, December 2012, pages 1731-1743. Details of the development of the KSC DRWP database are given in Barbre, Jr. 2015: Development of a Climatology of Vertically Complete Wind Profiles From Doppler Radar Wind Profiler Systems. American Meteorological Society. 17th Conference on Aviation, Range, and Aerospace Meteorology. Paper 8.1. Phoenix, AZ. The KSC DRWP was used as an independent check of balloon wind profiles during Space Shuttle DOL operations.
3.2.5 Aloft Wind Environment for Vehicle Ascent	Discrete Gust Model	Details of the processes and physics used to develop the Discrete Gust Model are given in F. Leahy, Discrete Gust Model for Launch Vehicle Assessments, American Meteorology Society, 12th Conference on Aviation, Range, and Aerospace Meteorology, New Orleans, LA, January 2008, paper P2.9. The Discrete Gust Model uses moderate and severe gust turbulence standard deviations as provided in section 2.3 and Table 2-71 of NASA TM-2008-215633, Terrestrial Environment (Climatic) Criteria Handbook for Use in Aerospace Vehicle Development, 2008 Revision. The moderate turbulence standard deviations result in slightly conservative estimates, while severe turbulence deviations result in extremely conservative estimates compared to gust magnitudes determined from measured wind profiles (Barbre presentation to the Cross-Program Joint Loads Task Team on 09/27/2012, "Proposed Modifications to the NASA Discrete

Section	Model/Dataset/Design Limit	Validation Statement
		Gust Model Atmospheric Turbulence Input"). The Discrete Gust Model has been used extensively in the aerospace field, including both military and NASA developed vehicles.
3.2.5 Aloft Wind Environment for Vehicle Ascent	Tables 3.2.5-1, 3.2.5-2, 3.2.5-3, and 3.2.5-4 Discrete Gust Magnitude	Gust magnitudes in Tables 3.2.5-1, 3.2.5-2, 3.2.5-3, and 3.2.5-4 are constructed by using the 1-Cosine discrete gust model, and the gust standard deviations selected from Table 2-71 of NASA TM-2008-215633. Gust magnitudes are constructed at the 99% probability level. Gust magnitudes based on moderate turbulence compare favorably to measured data, while magnitudes based on severe turbulence are conservative compared to measured data, as shown in Barbre presentation to the Cross-Program Joint Loads Task Team on 09/27/2012, "Proposed Modifications to the NASA Discrete Gust Model Atmospheric Turbulence Input".
3.2.5 Aloft Wind Environment for Vehicle Ascent	Continuous Gust Model	The Continuous Gust Model was developed with the same methodology as defined by the Aerospace Corporation. The model was vetted through the Natural Environments Integrated Ad Hoc Team, Joint Loads Task Team, and Ascent Flight Systems Integration Task Team. The Aerospace Corporation also provided independent validation.
3.2.5 Aloft Wind Environment for Vehicle Ascent 3.2.6 Aloft Air Temperature Environment for Vehicle Ascent 3.2.7 Aloft Air Pressure Environment for Vehicle Ascent 3.2.8 Aloft Air Density Environment for Vehicle Ascent	Table 3.2.5-3 Earth-GRAM 2010 Input for Monte Carlo Runs	Table 3.2.5-3 provides input to run Earth-GRAM random profiles for ascent Monte Carlo assessments. It is recommended to use the Range Reference Atmosphere data set (monthly climatology) when available, since it provides a better statistical representation of the available sites. Random perturbations are set to nominal dispersions. Patchy turbulence is turned off (patches of severe turbulence). Suggested Earth-GRAM inputs are standard inputs for typically Monte Carlo assessments. Details and background on the Range Reference Atmosphere can be found in Burns, L., “Range Reference Atmosphere 2013 Development Reports, Jacobs ESSSA Group Report ESSSA-FY13-1655, February 19, 2013.”

Section	Model/Dataset/Design Limit	Validation Statement
3.2.5 Aloft Wind Environment for Vehicle Ascent	Table 3.2.5-4 Earth-GRAM 2010 Input for Monthly Mean Profiles	Table 3.2.5-4 provides input to run Earth-GRAM to generate profiles of monthly means. It is recommended to use the Range Reference Atmosphere data set (monthly climatology) when available, since it provides a better statistical representation of the available sites. Random output is turned off (no random perturbations). Suggested Earth-GRAM inputs are standard inputs for building monthly mean profiles.
3.2.9 Cloud Environment for Launch	Size distribution of liquid cloud particles	The size distribution for liquid cloud particles, and comparison of statistical fits to observed data, is provided in Miles, et. al., Cloud Droplet Size Distributions in Low-Level Stratiform Clouds, J. Atmospheric Science, Vol. 57, Jan 2000, pages 295-311.
3.2.9 Cloud Environment for Launch	Size distribution of frozen cloud particles	The size distribution for frozen cloud particles, and comparison of statistical fits to observed data, is provided in A. Heymsfield, Properties of Tropical and Midlatitude Ice Cloud Particle Ensembles. Part II: Applications for Mesoscale and Climate Models, J. Atmospheric Science, Vol. 60, Nov 2003, pages 2592-2611.
3.2.10 Rain and Precipitation Environment for Launch	Design Rainfall rate	The design rainfall rate is the NOAA maximum observational reporting value for moderate rainfall (NOAA, Federal Meteorological Handbook No. 1, Surface Weather Observations and Reports, FCM-H1-2005, Sept 2005). This rate was chosen to exclude operations during heavy rainfall produced by convective clouds (thunderstorms). NOTE: There is currently a Cross-Program Launch Commit Criteria to not launch through precipitation.
3.2.10 Rain and Precipitation Environment for Launch	Raindrop size distribution	The raindrop size distribution function, and comparison of statistical fits to observed data, is provided in P. Tattleman and P. Willis, Model Vertical Profiles of Extreme Rainfall Rate, Liquid Water Content, and Drop-Size Distribution, AFGL-TR-85-0200, Sept 1985.
3.2.11 Flora and Fauna Environments during Launch and Ascent	Bird mass	Studies over the past twenty years in the KSC area have been consistent with respect to bird populations, however they only provide coarse detail about bird number densities with respect to height and migratory patterns. The most common larger species of birds in the KSC area are black

Section	Model/Dataset/Design Limit	Validation Statement
		vultures (mass 1.6 to 2.2 kg (3.5 to 4.9 lbs)), turkey vultures (mass ~2.0 kg (4.4 lbs)) and osprey (mass 1.4 to 2.0 kg) (3.1 to 4.4 lbs).
3.2.11 Flora and Fauna Environments during Launch and Ascent	Table 3.2.11-1 Avian Number Density	Data used to derive Table 3.2.11-1 can be found in NASA MSFC Memo EV44 (15-007), KSC Avian Environment Report.
3.2.12 Natural and Triggered Lightning during Launch and Ascent	Lightning environment	The KSC environment is such that systems will be exposed to the direct and indirect effects of lightning. Observations validate the presence of lightning at KSC. Descriptions and conditions for the application of lightning environment waveforms are detailed in SAE ARP5414, Aircraft Lightning Zones and SAE ARP5412, Aircraft Lightning Environment and Related Test Waveforms. NOTE: There is currently a Cross-Program Launch Commit Criteria to minimize the risk of triggering lightning during launch.
3.2.13 Ionizing Radiation Environment for Launch, Ascent, and Re-entry	CREME96 Table 3.2.13-1 200 km Integral LET Flux Table 3.2.13-2 200 km Differential Proton Flux Table 3.2.13-3 200 km Integral Proton Flux	The CREME 96 model was selected to calculate this environment because it is the industry standard for ionizing radiation environments which affect avionics. The Technical Notes of 3.2.13 describe the model settings used. These were selected to give a conservative but reasonable environment for hardware design. The use of the 51.6 deg inclination orbit and "stormy" geomagnetic conditions ensures some exposure to solar energetic particles and a factor of 2 is applied to the flux to provide a worst case environment. CREME 96 and its validation are described in A.J. Tylka, J. H. Adams, Jr., P. R. Boberg, B. Brownstein, W. F. Dietrich, E. O. Flueckiger, E. L. Petersen, M. A. Shea, D. F. Smart, and E. C. Smith, "CREME96: A Revision of the Cosmic Ray Effects on Micro-Electronics Code", IEEE Trans. Nucl. Sci., vol. 44, no. 6, pp. 2150-2160, Dec. 1997.
3.2.13 Ionizing Radiation Environment for Launch, Ascent, and Re-entry	Table 3.2.13-4 Flux of > 10 MeV Neutrons at Altitudes to 20 km	Table was derived from empirical data.
3.3 In-Space Phases		

Section	Model/Dataset/Design Limit	Validation Statement
3.3.1 Total Dose		The SPENVIS space environments tool was used to generate these environments. SPENVIS includes an orbit generator and industry standard radiation environments (CREME96 for galactic cosmic rays, AE8/AP8 trapped radiation, ESP/PSYCHIC solar energetic particles, and SHIELDOSE2 radiation transport). The Technical Notes of each section describe the model inputs which were selected to provide a conservative but reasonable environment for hardware design. The orbits were chosen to cover the range of Design Reference Missions in Table 3.3.1-1. SPENVIS is described at www.spenvis.oma.be. AE8/AP8 are described in Vette, J. I., The AE-8 Trapped Electron Model Environment, NSSDC/WDC-A-R&S 91-24, 1991, Vette, J. I., The NASA/National Space Science Data Center Trapped Radiation Environment Model Program (1964-1991), NSSDC/WDC-A-R&S 91-29, 1991b. ESP is described in Tylka, A. J., Dietrich, W. F. and Boberg, P. R., Probability distributions of high-energy solar-heavy-ion fluxes from IMP-8: 1973-1996, IEEE Trans. Nucl. Sci., vol. 44, no. 6, pp. 2140–2149, Dec. 1997, and Heynderickx, D., J. Lemaire, E. J. Daly, and H. D. R. Evans, Calculating Low-Altitude Trapped Particle Fluxes With the NASA Models AP-8 and AE-8, Radiat. Meas., 26, 947-952, 1996 and Sawyer, D. M., and J. I. Vette, AP-8 Trapped Proton Environment for Solar Maximum and Solar Minimum, NSSDC/WDC-A-R&S 76-06, 1976. PSYCHIC is described in Xapsos, M. A., Stauffer, C., Jordan, T., Barth, J.L., and Mewaldt, R.A., Model for Cumulative Solar Heavy Ion Energy and Linear Energy Transfer Spectra, IEEE Trans. On Nucl. Science, 54, No. 6, 2007 and SHIELDOSE in S. M. Seltzer, "SHIELDOSE: A computer code for space-shielding radiation dose calculations," National Bureau of standards Technical Note 1116, 1980.
3.3.1.1 Low Earth Orbit (LEO)-International Space Station (ISS) Orbit	Table 3.3.1.1-1 Daily Trapped Proton Fluences Table 3.3.1.1-2 Daily Trapped Electron Fluences	The 51.6 deg inclination, 500km orbit was chosen because an ISS docking mission was in the "study DRMs" list. The material was left in the DSNE because it provides a conservative LEO environment including trapped protons, galactic

Section	Model/Dataset/Design Limit	Validation Statement
3.3.1.2.6 LEO 407 km Circular	Table 3.3.1.1-3 Proton Fluences of an ISS SPE Table 3.3.1.1-4 Daily Trapped Belts TID Inside Shielding Table 3.3.1.1-5 Total SPE TID Inside Shielding AE8MAX Model AP8MIN Model ESP/PSYCHIC Model SPENVIS	cosmic rays, and solar particle events reduced by geomagnetic shielding. The Technical Notes describe the inputs to the models and probability levels selected. The models are described in the validation entry for 3.3.1.
3.3.1.2 Staging and Transit Orbits		
3.3.1.2.1 LEO 185 x 1806 km	Table 3.3.1.2.1-1 Daily Trapped Proton Fluences Table 3.3.1.2.1-2 Daily Trapped Electron Fluences Table 3.3.1.2.1-3 Daily Trapped Belts TID Inside Shielding	The 28.5 deg inclination 185 x 1806 km staging orbit was selected to represent the pre-trans-lunar injection portion of the SLS mission. The more likely orbits are more circular (see 3.3.1.2.3) but exposure to the radiation belts at the 1806 km apogee provides a conservative estimate of the dose. The models are described in the validation entry for 3.3.1 and the Technical Notes describe the model input parameters and the factor of 2 applied to account for the uncertainty in the trapped radiation models. The models are described in the validation entry for 3.3.1.
3.3.1.2.2 Radiation Belt Transit	Table 3.3.1.2.2-1 Daily Trapped Proton Fluences Table 3.3.1.2.2-2 Daily Trapped Electron Fluences Table 3.3.1.2.2-3 Daily Trapped Belts TID Inside Shielding	After the TLI burn the SLS upper stage, Orion, and other payloads will transit the high flux regions of the trapped radiation belts. The models are described in the validation entry for 3.3.1.
3.3.1.2.3 LEO 241 km Circular	Table 3.3.1.2.3-1 Daily Trapped Proton Fluences Table 3.3.1.2.3-2 Daily Trapped Electron Fluences	This section is representative of the environment for circular pre-TLI orbits. The models are described in the validation entry for 3.3.1.

Section	Model/Dataset/Design Limit	Validation Statement
	Table 3.3.1.2.3-3 Daily Trapped Belts TID Inside Shielding	
3.3.1.2.4 High Earth Orbit (HEO) 407 x 233,860 km	Table 3.3.1.2.4-1 Daily Trapped Proton Fluences Table 3.3.1.2.4-2 Daily Trapped Electron Fluences Table 3.3.1.2.4-3 Daily Trapped Belts TID Inside Shielding	This type of staging orbit is unlikely for current DRMs but is included to cover possible future missions. The models are described in the validation entry for 3.3.1.
3.3.1.2.7 Low Perigee (LP)-HEO 407 x 400,000 km	Table 3.3.1.2.7-1 Daily Trapped Proton Fluences Table 3.3.1.2.7-2 Daily Trapped Electron Fluences Table 3.3.1.2.7-3 Daily Trapped Belts TID Inside Shielding	This type of staging orbit is unlikely for current DRMs but is included to cover possible future missions. The models are described in the validation entry for 3.3.1.
3.3.1.2.8 High Perigee (HP)-HEO Spiral to 60,000 x 400,000 km	N/A	N/A
3.3.1.3 Geosynchronous Earth Orbit (GEO)	Table 3.3.1.3-1 Daily Trapped Electron Fluences Table 3.3.1.3-2 Daily Trapped Belts TID Inside Shielding	All translunar missions will pass through here. The models are described in the validation entry for 3.3.1.
3.3.1.8 Mars Orbit	N/A	N/A
3.3.1.9 Mars Surface	N/A	N/A
3.3.1.10 Solar Particle Events		
3.3.1.10.1 Geomagnetic Shielded 3.3.2.10.1 Geomagnetic Shielded	Table 3.3.1.10.1-1 Integral and Differential Proton Fluences of a Shielded SPE Table 3.3.1.10.1-2 Total Shielded SPE TID Inside Al Shielding	The solar particle event and geomagnetic shielding models are described in the validation entry for 3.3.1.

Section	Model/Dataset/Design Limit	Validation Statement
3.3.1.10.2 Geomagnetic Unshielded 3.3.1.2.5 HEO to NEA transit 3.3.1.4 Interplanetary 3.3.1.5 Lunar Orbit 3.3.1.6 Lunar Surface 3.3.1.7 Near Earth Asteroid 3.3.2.10.1 Geomagnetic Shielded	Table 3.3.1.10.2-1 Integral and Differential Proton Fluence of an Unshielded SPE Table 3.3.1.10.2-2 Daily Unshielded GCR Integral Proton Fluence Table 3.3.1.10.2-3 Total Shielded SPE TID Inside Al Shielding Table 3.3.1.10.2-4 Total Unshielded Daily GCR TID Inside Al Shielding	The solar particle event model is described in the validation entry for 3.3.1
3.3.2 Single Event Effects		The SPENVIS space environments tool was used to generate these environments. SPENVIS includes an orbit generator and industry standard radiation environments (CREME96 for galactic cosmic rays, AE8/AP8 trapped radiation, ESP/PSYCHIC solar energetic particles, and SHIELDOSE2 radiation transport). The Technical Notes of each section describe the model inputs which were selected to provide a conservative but reasonable environment for hardware design. The orbits and trajectories were chosen to cover the range of Design Reference Missions in Table 3.3.1-1. SPENVIS is described at www.spenvis.oma.be. AE8/AP8 are described in Vette, J. I., The AE-8 Trapped Electron Model Environment, NSSDC/WDC-A-R&S 91-24, 1991, Vette, J. I., The NASA/National Space Science Data Center Trapped Radiation Environment Model Program (1964-1991), NSSDC/WDC-A-R&S 91-29, 1991b. ESP is described in Tylka, A. J., Dietrich, W. F. and Boberg, P. R., Probability distributions of high-energy solar-heavy-ion fluxes from IMP-8: 1973-1996, IEEE Trans. Nucl. Sci., vol. 44, no. 6, pp. 2140–2149, Dec. 1997, and Heynderickx, D., J.

Section	Model/Dataset/Design Limit	Validation Statement
		Lemaire, E. J. Daly, and H. D. R. Evans, Calculating Low-Altitude Trapped Particle Fluxes With the NASA Models AP-8 and AE-8, Radiat. Meas., 26, 947-952, 1996 and Sawyer, D. M., and J. I. Vette, AP-8 Trapped Proton Environment for Solar Maximum and Solar Minimum, NSSDC/WDC-A-R&S 76-06, 1976. PSYCHIC is described in Xapsos, M. A., Stauffer, C., Jordan, T., Barth, J.L., and Mewaldt, R.A., Model for Cumulative Solar Heavy Ion Energy and Linear Energy Transfer Spectra, IEEE Trans. On Nucl. Science, 54, No. 6, 2007 and SHIELDOSE in S. M. Seltzer, "SHIELDOSE: A computer code for space-shielding radiation dose calculations," National Bureau of standards Technical Note 1116, 1980. CREME 96 is described in A.J. Tylka, J. H. Adams, Jr., P. R. Boberg, B. Brownstein, W. F. Dietrich, E. O. Flueckiger, E. L. Petersen, M. A. Shea, D. F. Smart, and E. C. Smith, "CREME96: A Revision of the Cosmic Ray Effects on Micro-Electronics Code", IEEE Trans. Nucl. Sci., vol. 44, no. 6, pp. 2150-2160, Dec. 1997.
3.3.2.1 LEO-ISS Orbit 3.3.2.2.3 Low Earth Orbit 241 km Circular 3.3.2.2.6 Low Earth Orbit 407 km Circular	Table 3.3.2.1-1 ISS SPE Integral Peak LET Flux for Selected Al Shielding Thickness as a Function of LET Table 3.3.2.1-2 ISS SPE Worst Day Integral Flux for Selected Al Shielding Thickness as a Function of LET Table 3.3.2.1-3 Integral Proton Flux for an ISS SPE, Solar Minimum GCR, Nominal Trapped Protons and Worst SAA Pass Table 3.3.2.1-4 Differential Proton Flux for an ISS SPE, Solar Minimum GCR, Nominal Trapped Protons and Worst SAA Pass	The 51.6 deg inclination, 500km orbit was chosen because an ISS docking mission was in the "study DRMs" list. The material was left in the DSNE because it provides a conservative LEO environment including trapped protons, galactic cosmic rays, and solar particle events reduced by geomagnetic shielding. The Technical Notes describe the inputs to the models and probability levels selected where appropriate. The models are described in the validation entry for 3.3.2.

Section	Model/Dataset/Design Limit	Validation Statement
3.3.2.2 Staging and Transit Orbits		
3.3.2.2.1 Low Earth Orbit 185 x 1806 km	Table 3.3.2.2.1-1 SPE Integral Peak LET Flux for Selected Al Shielding Thickness as a Function of LET Table 3.3.2.2.1-2 SPE Worst Day Integral Flux for Selected Al Shielding Thickness as a Function of LET Table 3.3.2.2.1-3 Integral Proton Flux for the Peak Trapped Protons	See 3.3.2 for Validation information
3.3.2.9 Mars Surface	N/A	N/A
3.3.2.10 GCR and Solar Particle Event		
3.3.2.10.2 Geomagnetic Unshielded 3.3.2.2.2 Radiation Belt Transit 3.3.2.2.4 High Earth Orbit (HEO) 407 x 233,860 km 3.3.2.2.5 High Earth Orbit to Near Earth Asteroid Transit 3.3.2.2.7 Low Perigee-High Earth Orbit 407 x 400,000 km 3.3.2.2.8 High Perigee-High Earth Orbit Spiral to	Table 3.3.2.10.2-1 SPE Integral Peak LET Flux for Selected Al Shielding Thickness as a Function of LET Table 3.3.2.10.2-2 SPE Worst Day Integral Flux for Selected Al Shielding Thickness as a Function of LET Table 3.3.2.10.2-3 Integral Proton Flux of a SPE and GCR Table 3.3.2.10.2-4 Differential Proton Flux for a SPE and Solar Minimum GCR Table 3.3.2.10.2-5 GCR Integral LET at Solar Minimum for Selected Al	This section is representative of the environment for orbits which are outside of earth's geomagnetic field such as cis-lunar and interplanetary space. There are no trapped protons and electrons, but the spacecraft is exposed to the full spectrum of energetic charged particles from Solar Particle Events (SPE) and Galactic Cosmic Rays (GCR).

Section	Model/Dataset/Design Limit	Validation Statement
60,000 x 400,000 km 3.3.2.3 Geosynchronous Earth Orbit (GEO) 3.3.2.4 Interplanetary 3.3.2.5 Lunar Orbit 3.3.2.6 Lunar Surface 3.3.2.7 Near Earth Asteroid 3.3.2.8 Mars Orbit	Shielding Thickness as a Function of LET	
3.3.3 Plasma Charging		
3.3.3.1 LEO-ISS Orbit 3.3.3.2.3 Low Earth Orbit 241 km Circular 3.3.3.2.6 Low Earth Orbit 407 km Circular	Table 3.3.3.1-1 Ambient Plasma Environment for less than 1000 km Altitude	Minow, J.I., “Development and implementation of an empirical ionosphere variability model”, Advances in Space Research, 33, 2004, pp. 887-892.
3.3.3.2 Staging and Transit Orbits		
3.3.3.2.1 Low Earth Orbit 185 x 1806 km	see Sections 3.3.3.1, 3.3.3.10, and 3.3.3.2.2	see Sections 3.3.3.1, 3.3.3.10, and 3.3.3.2.2
3.3.3.2.2 Radiation Belt Transit 3.3.3.2.4 High Earth Orbit (HEO) 407 x 233,860 km 3.3.3.2.5 High Earth Orbit to Near	Table 3.3.3.2.2-1 Radiation Belt Transit Average Integral Electron Flux	Fennell, J. E., Harry C. Koons, Margaret W. Chen, and J. Bernard Blake, "Internal Charging: A Preliminary Environmental Specification for Satellites", IEEE Transactions on Plasma Science, Vol. 28, No. 6, December 2000, p. 2029.

Section	Model/Dataset/Design Limit	Validation Statement
Earth Asteroid Transit 3.3.3.2.7 Low Perigee-High Earth Orbit 407 x 400,000 km		
3.3.3.2.8 High Perigee-High Earth Orbit Spiral to 60,000 x 400,000 km	N/A	N/A
3.3.3.3 Geosynchronous Earth Orbit	Table 3.3.3.3-1 Geosynchronous Orbit (GEO) Plasma Environment Parameters	Purvis, C.K., H.B. Garrett, A.C. Whittlesey, and N.J. Stevens, Design Guidelines for Assessing and Controlling Spacecraft Charging Effects, NASA-TP-2361, 1984. and Gussenhoven, M. S., and E.G. Mullen, "A "worst case" spacecraft charging environment as observed by SCATHA on 24 April 1979", AIAA Paper 82-0271, 1982.
3.3.3.4 Interplanetary Orbit 3.3.3.7 Near Earth Asteroid	Table 3.3.3.4-1 Interplanetary Environment Plasma Parameters	Paterson, W.R., and L.A. Frank, "Survey of Plasma Parameters in Earth's Distant Magnetotail with the Geotail Spacecraft", Geophys. Res. Lett., 21, 1994, pp. 2971-2974. Minow, J.I., L. N. Parker, and W.C. Blackwell, Jr., "Extreme space weather events and charging hazard assessments in lunar environments", presented at 37th COSPAR Scientific Assembly, Montreal, Canada, 13-20 July 2008. Feldman W.C., J.R. Asbridge, S.J. Bame, and J.T. Gosling, "Plasma and Magnetic Fields from the Sun", The Solar Output and its Variation, (ed.) Oran R. White, Colorado Associated University Press, Boulder, 1977.
3.3.3.5 Lunar Orbit (High and Low)	Table 3.3.3.5-1 Lunar Orbit Plasma Parameters	A team from MSFC/EV44 and MSFC/ST13 analyzed THEMIS-ARTEMIS satellite data, binned into the appropriate regions, to generate the Table. The data is available from the websites described in the Technical Notes of this section.
3.3.3.6 Lunar Surface	N/A	N/A
3.3.3.8 Mars Orbit	N/A	N/A
3.3.3.9 Mars Surface	N/A	N/A
3.3.3.10 Polar Orbit	Table 3.3.3.10-1 Polar Plasma Parameters	Parameters were taken from Nascap-2K charging model described in Mandell, M., Katz, I., Hilton,

Section	Model/Dataset/Design Limit	Validation Statement
		J. M., Cooke, D. L., & Minor, J. Spacecraft Charging Technology, Proceedings of the Seventh International Conference held 23-27 April, 2001 at ESTEC, Noordwijk, the Netherlands. Edited by R.A. Harris, European Space Agency, ESA SP-476, 2001., p.499
3.3.4 Ionizing Radiation Environment for Crew Exposure	Table 3.3.4-1 SPE Design Event Differential Spectra	King, J.H., "Solar Proton Fluences for 1977-1983 Space Missions", Journal of Spacecraft & Rockets, 11, 1974, p. 401.
3.3.4 Ionizing Radiation Environment for Crew Exposure	Table 3.3.4-2 GCR Design Differential Spectra (Solar Minimum)	O'Neill, P., and Badhwar M. O'Neill, "Galactic Cosmic Ray Model Update Based on Advanced Composition Explorer (ACE) Energy Spectra from 1997 to Present", Advances in Space Research, Vol. 37, 2006, pp 1727-1733.
3.3.4 Ionizing Radiation Environment for Crew Exposure	Trapped Radiation Sources	Sawyer, D.M., J.I. Vette," The AP-8 Trapped Proton Environment for Solar Maximum and Solar Minimum", NSSDC/SDC-A-R&S 76-06, NASA Goddard Space Flight Center, Greenbelt Maryland, 1976.
3.3.5 Reserved	N/A	N/A
3.3.6 Meteoroid and Orbital Debris Environment	MEM 3	Moorhead, A.V., A. Kingery, S. Ehlert, 2019, "NASA's Meteoroid Engineering Model 3 and its ability to replicate spacecraft impact rates". Accepted for publication in Journal of Spacecraft and Rockets. Preprint available at https://arxiv.org/abs/1909.05947
3.3.6 Meteoroid and Orbital Debris Environment	ORDEM 3.0	ORDEM 3 V&V consisted of peer review and an extensive study by the NESC titled "Joint Polar Satellite System (JPSS) Micrometeoroid and Orbital Debris (MMOD) Assessment - NASA Engineering and Safety Center Technical Assessment Report" which is currently in final draft.
3.3.7 Earth Gravitational Field	GRACE model GGM02C	The GGM02 Earth gravity model is based on the analysis of 363 days of GRACE in-flight data, spread between April 4, 2002 and Dec 31, 2003. GGM02C - complete to degree 200 - is based on satellite measurements and is constrained with terrestrial gravity information. The new GGM02 model builds upon the experience with the older GGM01 model, and is also derived from globally distributed, precise inter-satellite range rate

Section	Model/Dataset/Design Limit	Validation Statement
		measurements derived by the GRACE mission. This model used improved GRACE mission data and processing methods, when compared to the previously released model. As a result, the GGM02 models are more accurate than the GGM01 models at all wavelengths. The model has been extensively documented in scientific journals and peer-reviewed by the geosciences community.
3.3.8 Lunar Gravitational Field	GRAIL	The GRAIL lunar gravity model is based on measurements made by the GRAIL spacecraft. The GRAIL mission placed two spacecraft (GRAIL-A and GRAIL-B), flying in formation, into orbit around the Moon to study its internal structure. By very precisely measuring the distance of one orbiter relative to the other, the orbital perturbations caused by the Moon could be observed. Combining this with the orbiter position as determined from Earth-based observations, the mass distribution on the Moon could be determined. The GRAIL spacecraft entered lunar orbit on December 31, 2011, and January 1, 2012. The mission ended on December 17, 2012, with a controlled impact of both spacecraft on the lunar surface. The model underwent extensive peer review prior to be made available on the NASA Planetary Data Systems - Geosciences repository.
3.3.9 Thermal Environment for In-Space Hardware		
3.3.9.1 Thermal Environment for Lunar Phases	solar flux	These are standard values of the solar flux adjusted for distance from the sun.
3.3.9.1 Thermal Environment for Lunar Phases	albedo	Dollfus, A. and E. Bowell, "Polarimetric Properties of the Lunar Surface and its Interpretation, Part I. Telescopic Observations", Astronomy & Astrophysics, 10, 1971, pp. 29-53.
3.3.9.1 Thermal Environment for Lunar Phases	Lunar Long-Wave Radiance	Derived from the average bolometric albedo from Lawson, Stefanie L., Bruce M. Jakosky, Hye-Sook Park, and Michael T. Mellon, "Brightness Temperatures of the Lunar Surface: Calibration and Global Analysis of the Clementine Long-Wave Infrared Camera Data," J. of Geophysical Research, 105, No. E2, 2000, pp. 4,273-4,290.

Section	Model/Dataset/Design Limit	Validation Statement
3.3.9.1 Thermal Environment for Lunar Phases	Lunar Eclipse	Lookup of worst case lunar eclipse length from eclipse prediction Tables.
3.3.9.1 Thermal Environment for Lunar Phases	Table 3.3.9.1-1, Projected Worst Case Minimum Solar Flux during Lunar Eclipse, Dated June 11, 2029	Calculated from eclipse prediction Tables.
3.3.9.2 Thermal Parameters for Near-Earth Phases	Table 3.3.9.2-1, Albedo, Outgoing Longwave Radiation (OLR) Pairs for Critical Systems in Low-Inclination Orbits Table 3.3.9.2-2, Albedo, OLR Pairs for Critical Systems in Medium-Inclination Orbits	From Justus et al., NASA/TM-2001-21122 "Simple Thermal Environment Model (STEM) User's Guide".
3.3.10 Solar Illumination Environment for In-Space Hardware	Table 3.3.10-1 Solar Spectral Irradiance-Standard Curve, Abridged Version	From American Society for Testing and Materials Designation: E490-00a "Standard Solar Constant and Zero Air Mass Solar Spectral Irradiance Tables", ASTM International, December 2000.
3.3.11 In-Space Neutral Atmosphere (Thermosphere) Density 3.5.1 Re-entry Neutral Atmosphere 3.6.1 Re-entry Neutral Atmosphere for Off-Nominal Descent and Landing	Table 3.3.11-1 Earth-GRAM 2010 Inputs for Thermosphere Parameter Calculations	This set of inputs to the Marshall Engineering Thermosphere module of the Global Reference Atmosphere Model were selected to span the ranges of solar flux, season, and local time so conservative values of thermospheric density could be computed.
3.3.12 Geomagnetic Fields (Reserved)	N/A	N/A
3.4 Lunar Surface Operational Phases	Numerous published data sets from orbiting spacecraft and analysis of	See section 3.4 which contains reference citations for all design environment data.

Section	Model/Dataset/Design Limit	Validation Statement
	Apollo and other sample return missions were used.	
3.5 Entry and Landing Phases		
3.5.4 Aloft Winds for Normal Descent and Landing	Earth-GRAM 2010	Details of the model are provided in NASA/TM-2011-216467, The NASA Marshall Space Flight Center Earth Global Reference Atmospheric Model - 2010 Version. Verification and validation details are provided in EV44 (14-002), Verification and Validation Report, Earth GRAM 2010 Version 4.0. Earth-GRAM is a well-established model that has been used for various space programs, including Space Shuttle, Constellation, and SLS/MPCV. Verification and validation details are provided in EV44 (14-002), Verification and Validation Report, Earth GRAM 2010 Version 4.0.
3.5.4 Aloft Winds for Normal Descent and Landing 3.5.5 Aloft Air Temperature for Normal Descent and Landing 3.5.6 Aloft Air Pressure for Normal Descent and Landing 3.5.7 Aloft Air Density for Normal Descent and Landing 3.6.4 Aloft Winds for Off-Nominal Descent and Landing 3.6.5 Aloft Air Temperature for Off-Nominal	Table 3.5.4-1 Earth-GRAM 2010 Input to Generate 1,000 or More Perturbed Profiles (0 to 90 km) of Temperature, Pressure, and Density Per Monthly Reference Period	Table 3.5.4-1 provides input to run Earth-GRAM random profiles for ascent Monte Carlo assessments. It is recommended to use the Range Reference Atmosphere data set (monthly climatology) when available, since it provides a better statistical representation of the available sites. Random perturbations are set to nominal dispersions. Patchy turbulence is turned off (patches of severe turbulence). Suggested Earth-GRAM inputs are standard inputs for typically Monte Carlo assessments.

Section	Model/Dataset/Design Limit	Validation Statement
Descent and Landing 3.6.6 Aloft Air Pressure for Off-Nominal Descent and Landing 3.6.7 Aloft Air Density for Off-Nominal Descent and Landing		
3.5.8 Surface Winds for Normal Landing	Peak Wind Speed Profile	Rationale for k = 0.11 over water is found in Hsu, S.A., E.A. Meindl, and D.B. Cilhousen: 1994. Determining the Power-Law Wind-Profile Exponent under Near-Neutral Stability Conditions at Sea. Journal of Applied Meteorology. Vol. 33. pp. 757-765. Also, the following concluded that k=1/7 is valid if z0 is at least an order of magnitude smaller than the reference level height: Peterson, E. W. and J.P. Hennessey, Jr.: 1978. On the Use of Power Laws for Estimates of Wind Power Potential. Journal of Applied Meteorology. Vol 17. pp. 390-394.
3.5.8 Surface Winds for Normal Landing	Gust Factor	For locations which a gust factor has not been established, a value of 1.4 is to be used per NASA TM-2008-215633, Terrestrial Environment (Climatic) Criteria Handbook for Use in Aerospace Vehicle Development, 2008 Revision. Details of the 1.4 gust factor are presented in McVehil, G.E.; and Camnitz, H.G.: "Ground Wind Characteristics at Kennedy Space Center," NASA CR–1418, NASA Marshall Space Flight Center, AL, September 1969.
3.5.8 Surface Winds for Normal Landing	Spectral Gust Model	The Dryden Turbulence (Gust) Model is a well-established model with uses in private, civil, and military aviation. Details on the development and use for NASA programs is given in NASA TM-2008-215633, Terrestrial Environment (Climatic) Criteria Handbook for Use in Aerospace Vehicle Development, 2008 Revision. Details on the use for military applications is given in Flying Qualities of Piloted Aircraft. Department of Defense Handbook. MIL-HDBK-1797A. Washington, DC: U.S. Department of Defense, 1997.

Section	Model/Dataset/Design Limit	Validation Statement
3.5.8 Surface Winds for Normal Landing	Table 3.5.8-1 Dryden Gust Spectra Parameters for the Longitudinal, Lateral, and Vertical Components for the Landing Phase	Parameters in Table 3.5.8-1 are obtained from NASP-NEC-NERD #030194, National Aero-Space Plane (NASP), X-30 Natural Environment Requirements Document (Rev. 1.0), March 1, 1994.
3.5.8 Surface Winds for Normal Landing	Reference Level Peak Wind Speed (Land)	Reference level peak wind speed of 19.5 m/s is the 95th percentile value for a 1-hour exposure period at Edwards Air Force Base. Value is obtained from NASA TM-2008-215633, Terrestrial Environment (Climatic) Criteria Handbook for Use in Aerospace Vehicle Development, 2008 Revision.
3.5.8 Surface Winds for Normal Landing 3.7.4 Surface Winds for Post-Flight and Recovery	Reference Level Peak Wind Speed (Water)	Reference level peak wind speed of 8.2 m/s is given in Section 3.5.18
3.5.9 Surface Air Temperature for Normal Landing	Max/Min over land	Design limits for normal land landings represent the maximum and minimum extreme temperatures from hourly surface observations recorded at selected locations in the normal land landing area.
3.5.9 Surface Air Temperature for Normal Landing 3.7.5 Surface Air Temperature for Post-Flight and Recovery	Max/Min over water	Design limits for normal water landings were determined using six-hourly air temperature output within the normal water landing area from a global climatology. Air temperatures were obtained from the European Centre for Medium-range Weather Forecasts (ECMWF) Re-Analysis (ERA-40), which contains air temperature records on a 2.5° x 2.5° grid every six hours for the 1979-2002 period of record. The global dataset was subsetted to only contain temperatures within the normal landing area. Design limits are the empirical minimum and maximum air temperatures during December and September, respectively (Barbré, 2012: "Analysis of DSNE Air and Sea Surface Temperature Updates", Jacobs ESSSA Group Report ESSSA-FY13-31).
3.5.10 Surface Air Pressure for Normal Landing	Max/min design limits	Design limits represent the monthly mean sea level air pressure ±3 standard deviations (maximum value of standard deviation for each month) from hourly surface observations at selected locations in the normal land landing area.

Section	Model/Dataset/Design Limit	Validation Statement
3.7.6 Surface Air Pressure for Post-Flight and Recovery		
3.5.11 Surface Air Humidity for Normal Landing 3.6.11 Surface Air Humidity for Off-Nominal Landing 3.7.7 Surface Air Humidity for Post-Flight and Recovery	Max/min design limits	100% is the maximum relative humidity observable in the boundary layer. Although relative humidity less than 5% can occur, these events are extremely rare in the boundary layer.
3.5.12 Aerosols for Normal Descent and Landing 3.6.12 Aerosols for Off-Nominal Descent and Landing 3.7.8 Aerosol Environment for Post-Flight and Recovery	N/A	N/A
3.5.13 Precipitation for Normal Descent and Landing 3.6.13 Precipitation for Off-Nominal Descent and Landing 3.7.9 Precipitation Environment for Post-Flight and Recovery	Design Rainfall rate	The design rainfall rate is the NOAA maximum observational reporting value for moderate rainfall (NOAA, Federal Meteorological Handbook No. 1, Surface Weather Observations and Reports, FCM-H1-2005, Sept 2005). This rate was chosen to exclude operations during heavy rainfall produced by convective clouds (thunderstorms).
3.5.14 Flora and Fauna for Descent and Landing	Avian Species	The bird mass collision criteria for descent and landing operations were selected to maintain commonality with the ascent phase criteria (see section 3.2.11).

Section	Model/Dataset/Design Limit	Validation Statement
3.7.10 Flora and Fauna Environment for Post-Flight and Recovery		
3.5.14 Flora and Fauna for Descent and Landing	Ground brush	Ground brush design height of 0.6 m is used to cover typical desert vegetation, such as sagebrush.
3.5.14 Flora and Fauna for Descent and Landing	Mammals	Although large mammals such as deer, cattle, and wild horses are not uncommon in open range areas in the western U.S., it is impractical to protect against collision with one of significant mass. The design limit of 10 kg is to protect from collisions with smaller mammals.
3.5.15 Surface Characteristics and Topography for Normal Land Landing 3.7.11 Surface Characteristics and Topography for Post-Flt and Recovery	The design limit for maximum surface slope of the land landing site will be 5°. The site will be clear of solid objects projecting more than 0.3 m (1.0 ft) above the surface. The site will be clear of ditches deeper than 0.3 m (1.0 ft).	The selection of surface was made based on preliminary surveys of potential land landing sites. It is anticipated that any designated site will be prepared to meet this specification. Details can be found in NASA Constellation Program white paper, K. Altino and R. Buehrle, Kennedy Space Center Terrain and Wind Environments for Orion Pad Abort Land Landings (Task Description Statement #SIG-08-1003: Contingency Land Landing Design Criteria Development).
3.5.16 Cloud Environment for Normal Descent and Landing	Cloud Cover	Up to 100% cloud cover
3.5.16 Cloud Environment for Normal Descent and Landing 3.7.12 Cloud Environment for Post-Flight and Recovery	Liquid Cloud Particle Size	The maximum size for liquid cloud particles of 7 mm (0.3 in) allows the vehicle to traverse stratiform clouds and rain in non-convective situations. Cloud particle size data is provided in NASA TM-2008-215633, Terrestrial Environment (Climatic) Criteria Handbook for Use in Aerospace Vehicle Development, 2008 Revision.
3.5.16 Cloud Environment for Normal Descent and Landing 3.6.16 Cloud Environment for Off-Nominal	Frozen Cloud Particle Size	The maximum size for frozen cloud particles of 200 mm (0.008 in) allows for traverse through mid and high altitude layer clouds (alto and cirrus type). Cloud particle size data is provided in NASA TM-2008-215633, Terrestrial Environment (Climatic) Criteria Handbook for Use in Aerospace Vehicle Development, 2008 Revision.

Section	Model/Dataset/Design Limit	Validation Statement
Descent and Landing		
3.5.17 Radiant (Thermal) Energy Environment for Normal Landing 3.7.13 Radiant (Thermal) Energy Environment for Post-Flt and Recovery	Table 3.5.17-1 Cold Design Radiant Energy and Sky Temperature as a Function of Time of Day, Cloudy Sky Table 3.5.17-2 Hot Design Radiant Energy and Sky Temperature as a Function of Time of Day, Cloudy Sky Table 3.5.17-3 Cold Design Radiant Energy and Sky Temperature as a Function of Time of Day, Partly Cloudy Sky Table 3.5.17-4 Hot Design Radiant Energy and Sky Temperature as a Function of Time of Day, Partly Cloudy Sky Table 3.5.17-5 Cold Design Radiant Energy and Sky Temperature as a Function of Time of Day, Clear Sky Table 3.5.17-6 Hot Design Radiant Energy and Sky Temperature as a Function of Time of Day, Clear Sky	Values in Tables 3.5.17-1, 3.5.17-3, and 3.5.17-5 were determined by taking the average at each hour for the 10 coldest days with cloudy skies (100% sky cover), partly cloudy skies (40 to 60% sky cover), and clear skies (0% sky cover) from the NSRD (1991-2010). Cold days were determined by calculating the average daily temperature for each day in the period of record, and selecting the 10 coldest days that met the specific sky condition. Values in Tables 3.5.17-2, 3.5.17-4, and 3.5.17-6 were determined by taking the average at each hour for the 10 hottest days with cloudy skies (100% sky cover), partly cloudy skies (40 to 60% sky cover), and clear skies (0% sky cover) from the NSRD (1991-2010). Hot days were determined by calculating the average daily temperature for each day in the period of record, and selecting the 10 hottest days that met the specific sky condition. The Table values were determined from NSRD data for San Diego, CA (Lindbergh Field).
3.5.18 Sea State for Normal Water Landing	Min Significant Wave Height	The lowest environment physically possible is the no waves case.
3.5.18 Sea State for Normal Water Landing	Max Significant Wave Height	Availability of "sea state 3" conditions (1.25 m SWH, 8.2 m/s wind speed) were assessed at the CxP Integrated Stack TIM. At the TIM, it was shown that increasing the SWH limit to 2.0 m provided reasonable availability in the regions of interest while still being within recovery limits. Reference presentation Barbre, R.E. 2007. Integrated Stack TIM - Team 0 Land and Water Landing. Environments and Constraints Systems

Section	Model/Dataset/Design Limit	Validation Statement
		Integration Group. Presentation to CxP. Houston, TX. November 2007.
3.5.18 Sea State for Normal Water Landing 3.6.18 Sea State for Off-Nominal Water Landing	Max Frequency Equation	This equation is based on the vehicle's size and the physical relationship between frequency and wavelength.
3.5.18 Sea State for Normal Water Landing 3.6.18 Sea State for Off-Nominal Water Landing	Energy Spectrum Equation	Equation derived from conversations with oceanographers (Dr. Kaihatu, Texas A&M) and Analytical Mechanics Associates (AMA). Documented in AMA report Bose, D.M. and Toniolo: 2010. Monte Carlo Wave Modeling. Analytical Mechanics Associates, Inc. AMA Report No.: 08-09, rev G. NASA Contract NNL09AC54T- AMA Task 9009-030 Baseline study: Cox, C. S., and W. H. Munk (1956), Slopes of the sea surface deduced from photographs of sun glitter, Bull. Scripps Inst., 6, 401 – 488.
3.5.18 Sea State for Normal Water Landing 3.6.18 Sea State for Off-Nominal Water Landing	Slope Variance Components	Reference: Cote, L.J., J.O. Davis, W. Markes, R.J. McGough, E. Mehr, W.J. Pierson, Jr., J.F. Ropek, G. Stephenson, and R.C. Vetter, "The Directional Spectrum of a Wind Generated Sea as Determined From Data Obtained by the Stereo Wave Observation Project", Meteorological Papers, New York University College of Engineering, 2(6), 1960, 88p.
3.5.18 Sea State for Normal Water Landing 3.6.18 Sea State for Off-Nominal Water Landing	Water Surface Slope Components	Arctangent function is used to back out a slope given a slope for an individual MC run.
3.5.18 Sea State for Normal Water Landing	Water Surface Slope Distribution	Total slope is computed as the root sum squared of the individual slope components for an individual MC run.

Section	Model/Dataset/Design Limit	Validation Statement
3.6.18 Sea State for Off-Nominal Water Landing		
3.5.18 Sea State for Normal Water Landing 3.6.18 Sea State for Off-Nominal Water Landing	Min Winds	No wind is the lowest environment physically possible.
3.5.18 Sea State for Normal Water Landing	Max Winds	Availability of "sea state 3" conditions (1.25 m SWH, 8.2 m/s wind speed) were assessed at the CxP Integrated Stack TIM. At the TIM, it was shown that a threshold of 8.2 m/s had acceptable availability while still being within recovery limits. Reference presentation Barbre, R.E. 2007. Integrated Stack TIM - Team 0 Land and Water Landing. Environments and Constraints Systems Integration Group. Presentation to CxP. Houston, TX. November 2007.
3.5.18 Sea State for Normal Water Landing	Table 3.5.18-1 Minimum Average Wave Period Corresponding to Given SWH	The minimum average wave periods in Table 3.5.18-1 are identified by determining which 1-second wave period range contains the 1st percentile of wave periods observed for the given SWH range. If the 1st percentile falls between two values within the wave period range, the lower of the two wave period values is used to be conservative.
3.5.18 Sea State for Normal Water Landing 3.6.18 Sea State for Off-Nominal Water Landing	Table 3.5.18-2 Energy Spectrum for 2 m SWH Table 3.6.18-1 Energy Spectrum for 4 m SWH	The energy spectrum in Table 3.5.18-2 is developed using 5.0 m (16.4 ft) wind speed data from buoys 46047 and 46069, near San Nicolas Island, CA, in the NDBC network and spectral data from buoy 067, near San Nicolas Island, CA, in the Coastal Data Information Program (CDIP) buoy network. The spectral data ranges from 0.025 to 0.58 Hz and is reported every half hour, along with the corresponding SWH. This archived buoy data, when compared with the National Data Buoy Center (NDBC) spectral data, provides spectral data at higher frequencies in the area of interest. The spectral data is used from August over a 9-year POR (1999-2007) and is limited to SWH $\leq$ 2.0 m (6.6 ft) and wind speed $\leq$ 8.2 m/s (26.9 ft/s). The energy spectrum in Table 3.5.18-2 represents a single spectrum from August 23,

Section	Model/Dataset/Design Limit	Validation Statement
		2001, at 03:49 Universal Time Coordinated (UTC) and is created using: (1) the energy in each frequency bin from 0.025 to 0.58 Hz, and (2) energy that is extrapolated from 0.58 to 0.80 Hz with an exponential curve (y = 3.9708·exp-9.1189x) that is fit to the energy found in each frequency bin from 0.30 to 0.58 Hz. Here x is the desired frequency (Hz) and y is the resulting energy (m2/Hz).
3.5.18 Sea State for Normal Water Landing	Figure 3.5.18-1 Cumulative Distributions of Water Surface Slope for 2 m SWH	Figure 3.5.18-1 is a cumulative distribution of water surface slope from the CDIP buoy used to derive the energy spectrum.
3.5.18 Sea State for Normal Water Landing	C-ERA40	The C-ERA40 database is developed from the ECMWF atmospheric re-analysis for the POR (1957-2002) with emphasis on the POR (1971-2000). Data reported in the C-ERA-40 database is provided every 6 hours on a 1.5º latitude x 1.5º longitude grid. Note that, although the term "C-ERA-40" refers to the SWH, wind speed, and wave period databases in this document, SWH is the only variable that was corrected. Reference: Caires, S. and A. Sterl, "A New Nonparametric Method to Correct Model Data: Application to Significant Wave Height From the ERA-40 Re-analysis", Journal of Atmospheric and Oceanic Technology, Vol. 22, No. 4, 2005, pp.443-459. EV44 selected the 1971-2000 POR to correspond to WMO at the time and from a subjective perception of improved data collection methodologies. Also, note that we're now using ERA-Interim, but the C-ERA-40 was used to derive the numbers in the DSNE.
3.5.19 Reserved	N/A	N/A
3.5.20 Sea Surface Temperature for Water Landing 3.6.20 Sea Surface Temperature for Off-Nominal Water Landing	Max/min design limits	Design limits for normal water landings were determined using weekly mean sea surface temperature output within the normal landing area from a global climatology. Sea surface temperatures were obtained from the National Centers for Environmental Prediction Optimal Interpolation (NCEP-OI) dataset, which contains weekly mean sea surface temperature records on a1.0° latitude x 1.0° longitude grid for the 1981-2012 period of record. The global dataset was

Section	Model/Dataset/Design Limit	Validation Statement
		subsetted to only contain temperatures within the normal water landing area. Minimum and maximum design limits are the 0.5th and 99.5th percentile temperatures with 95.0% confidence during March and September, respectively. NCEP OI Reference: Reynolds, R.W., N. A. Rayner, T.M. Smith, D.C. Stokes and W. Wang. 2002. An Improved in situ and satellite SST analysis for climate. J. Climate, 15, 1609-1625. Analysis documented in: Barbre, BJ: 2012. Analysis of DSNE Air and Sea Surface Temperature Updates. Jacobs ESSSA Group report. ESSSA-FY13-31.
3.5.21 Aerosols for Water Landing	sea salt spray	The landing area is in an environment conducive to sea salt spray. Details of sea salt spray can be found in Cloud particle size data is provided in NASA TM-2008-215633, Terrestrial Environment (Climatic) Criteria Handbook for Use in Aerospace Vehicle Development, 2008 Revision.
3.6 Contingency and Off-Nominal Landing Phases		
3.6.2 Reserved	N/A	N/A
3.6.8 Surface Winds for Off-Nominal Landing 3.6.18 Sea State for Off-Nominal Water Landing	See Section 3.5.8	"Sea state 5" conditions (4.0 m SWH, 13.9 m/s wind speed) was assessed at the CxP Integrated Stack TIM. At the TIM, it was communicated that a threshold of 13.9 m/s corresponded to the maximum achievable wind by Orion. Reference presentation Barbre, R.E. 2007. Integrated Stack TIM - Team 0 Land and Water Landing. Environments and Constraints Systems Integration Group. Presentation to CxP. Houston, TX. November 2007.
3.6.9 Surface Air Temperature for Off-Nominal Landing	Max/min design limits	Design limits for off-nominal water landings were determined using six-hourly air temperature output within the water landing areas corresponding to 23 different skip entry trajectories provided by the Orion Program, as well as the area immediately surrounding a 29.0° inclination orbit extending over water regions from KSC to the western coast of Australia. Air

Section	Model/Dataset/Design Limit	Validation Statement
		temperatures were obtained from the ERA-40 dataset, which contains air temperature records on a 2.5° x 2.5° grid every six hours for the 1979-2002 period of record. The global dataset was subsetted to only contain temperatures within the off-nominal landing area. Design limits are the empirical minimum and maximum air temperatures during March and April, respectively (Barbré, 2012). Analysis documented in: Barbre, BJ: 2012. Analysis of DSNE Air and Sea Surface Temperature Updates. Jacobs ESSSA Group report. ESSSA-FY13-31. The report contains the methodology used to select limits.
3.6.10 Surface Air Pressure for Off-Nominal Landing	N/A	N/A
3.6.14 Flora and Fauna for Off-Nominal Descent and Landing	N/A	N/A
3.6.15 Surface Characteristics and Topography for Off-Nominal Descent and Landing	N/A	N/A
3.6.17 Radiant (Thermal) Energy Environment for Off-Nominal Descent and Landing	N/A	N/A
3.6.18 Sea State for Off-Nominal Water Landing	Min Significant Wave Height	The lowest environment physically possible is no waves.
3.6.18 Sea State for Off-Nominal Water Landing	Max Significant Wave Height	"Sea state 5" conditions (4.0 m SWH, 13.9 m/s wind speed) was assessed at the CxP Integrated Stack TIM. At the TIM, it was recommended that a threshold of 4.0 m SWH be instituted as "a compromise between launch availability, risk, and design feasibility". Reference presentation

Section	Model/Dataset/Design Limit	Validation Statement
		Barbre, R.E. 2007. Integrated Stack TIM - Team 0 Land and Water Landing. Environments and Constraints Systems Integration Group. Presentation to CxP. Houston, TX. November 2007.
3.6.19 Reserved	N/A	N/A
3.7 Recovery and Post-Flight Processing Phases		
3.7.1 Environments for Post-Flight and Recovery at KSC	See Section 3.1, except for sea states	
3.7.2 Sea State for KSC Post-Flight and Recovery	Reserved	N/A
3.7.3 Lightning Specification for Post-Flight and Recovery	Lightning environment	The environment in the normal landing area is such that systems will be exposed to the direct and indirect effects of lightning. Descriptions and conditions for the application of lightning environment waveforms are detailed in SAE ARP5414, Aircraft Lightning Zones and SAE ARP5412, Aircraft Lightning Environment and Related Test Waveforms.
3.8 Interplanetary Space Specification	Reserved	N/A
3.9 Mars Orbit Specification	Reserved	N/A
3.10 Mars Atmosphere and Surface Phase Specifications	Reserved	N/A
3.11 Mars Moon Specification	Reserved	N/A
3.12 Near Earth Asteroid Specification	Reserved	N/A